THE UNIVERSITY OF CALGARY

BALLOON OBSERVATIONS OF
BREMSSTRAHLUNG X-RAYS
FROM COLD LAKE, ALBERTA

by

LUDOVIT VARGA

A THESIS
SUBMITTED TO THE FACULTY OF GRADUATE
STUDIES IN PARTIAL FULFILLMENT OF THE REQUIREMENTS
FOR THE DEGREE OF DOCTOR OF PHILOSOPHY
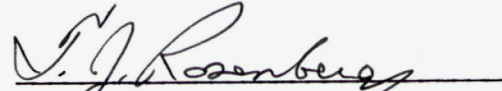

DEPARTMENT OF PHYSICS
CALGARY, ALBERTA

September 1986

THE UNIVERSITY OF CALGARY

FACULTY OF GRADUATE STUDIES
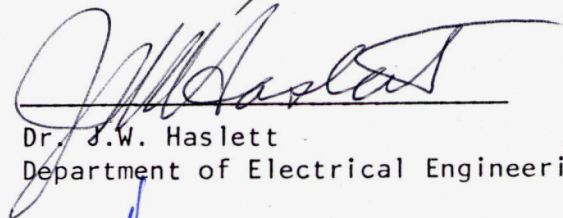
The undersigned certify that they have read and recommend to the Faculty of Graduate Studies for acceptance, a thesis entitled: "Balloon Observations of Bremsstrahlung X-Rays From Cold Lake, Alberta" submitted by Ludovit Varga in partial fulfillment of the requirements for the the degree of Doctor of Philosophy in Physics.

Dr. D. Venkatesan (Supervisor)
Department of Physics

Dr. T.J. Rosenberg (External)
University of Maryland

Dr. J.W. Haslett
Department of Electrical Engineering

Dr. Sun Kwok
Department of Physics

Dr. T.A. Clark
Department of Physics

ABSTRACT

An overview of auroral physics involves an understanding of the time and spatial variations of precipitating primary electrons at the top of the atmosphere. One can conveniently study the seconda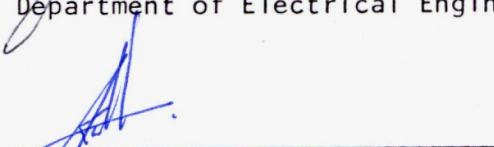ry phenomena, namely, Bremsstrahlung x-rays (or auroral x-rays in popular parlance) by balloon-borne detectors and optical (or auroral) emissions by an all-sky camera. This study uses directional and zenith-pointing x-ray detectors onboard balloons consisting of NaI(Tl) crystal cum photomultiplier assemblies. The auroral emissions are studied by a ground-based CCD camera. Such simultaneous observations enable us to explore the association between auroral x-rays and optical emissions.

The present study also involves the extensive use of a Monte Carlo program for simulating the propagation of x-rays through the terrestrial atmosphere. Several versions of such programs are available, but that of Pilkington (1970) has been used in this work. The original version of the program was modified to include the direct x-rays in the output of the program. Additional software has been developed to simulate the motion of various x-ray sources and to handle the data from the basic files. The observational data from October 14, 1982, taken at Cold Lake, Alberta, forms the major input for this thesis.

Several x-ray events were registered by the detectors.

A definite association between the magnetic bay at College (L ≈ 5) and the x-ray activity at Cold Lake (L ≈ 4.8) suggests the importance of common L-shell values while the longitudinal separation appears to be only secondary.

The results from moving simulated x-ray sources indicate the importance of scattering at the atmospheric depth of 9 g cm^{-2}. The position and the size of the x-ray sources also affect the e-folding energies of the spectra measured by the vertical and inclined detectors. Spectral observations reveal the presence of soft x-ray flux at the balloon altitude originating from the 'x-ray source which is distinct from the source responsible for the main x-ray events. The intensity variations of this soft flux have produced extensive "flapping motion" at the low energy end of the hard spectrum. It has been determined from the Monte Carlo simulation that the soft x-ray source can have an e-folding energy E_0 of only 12 keV or less. A method has been developed and applied to separate the soft and the hard components of the spectrum in the case study at 10:45 UT; the intensity and the hardness of the determined spectrum have indicated that the soft x-ray spectrum has E_0 = 5 keV. The deduced electron spectrum with E_0 = 6 keV and integral intensity of 8.60 x 10^8-1.41 x 10^9 fits well into the range of optical auroral electron spectra observed in the past from rocket and satellite measurements. The thesis concludes with some suggestions for the future.

A *time will come* when diligent research over long
periods will bring to light things which now lie hidden.

> - Seneca, *Natural Questions*
>   Book 7, *first century*

Dedicated to all of you who have encouraged me

TABLE OF CONTENTS

Chapter	Page

1 STUDY OF AURORAL X-RAYS AND OPTICAL AURORAS

3 **OBSERVATIONS OF X-RAY AURORAS**

4   STUDY OF X-RAY REGION DYNAMICS—MONTE CARLO SIMULATION

LIST OF TABLES

LIST OF FIGURES

(xx)

CHAPTER 1

STUDY OF AURORAL X-RAYS AND OPTICAL AURORAS

1.1 Introduction

Extensive satellite survey revealed that only the inner portion of the Earth's magnetic field retains the dipole field configuration, the outer part of the field is greatly distorted due to the interaction between the magnetic field and the stream of charged particles (solar wind) originating in the coronal region of the Sun. The net result of such an interaction is that the outer portion of the dipole field becomes compressed at the noon side while being stretched out into a comet tail-like structure at the night side. This is known as the Earth's magnetosphere. It is also known, that the magnetosphere acts as a reservoir of charged particles which are deposited in the high-latitude upper atmosphere during magnetospheric substorms. The location of the charged particle precipitation seems to be intimately tied to the topology of the magnetosphere as different magnetospheric regions and their boundaries are projected along the magnetic field lines down into the polar atmosphere. Survey by satellites revealed that there are basicly three matnetospheric plasma regions which are characterised by plasmas of different temperature. The cool domain, called the "plasmasphere", is located in the inner dipole of the magnetosphere; the plasmaspheric plasma being

1

of ionospheric origin.

The hot plasma domain is in the radiation belts, the region of the magnetosphere where the charged particles become trapped by the magnetic field. This region extends radially from the ionosphere out to a distance of approximately 7-9 R_E (R_E = Earth's radius). The warm plasma region is in the so called "plasma sheet" located in the equatorial region of the magnetospheric tail. The inner boundary of the plasma sheet is situated just outside the trapping region boundary (7-9 R_E). On the night-side, the magnetic field lines threading the plasma sheet project onto the auroral oval region, the bank in the high latitude ionosphere of maximum abundance of visible aurora. More specificaly, the plasma sheet in the vicinity of the equatorial plane (also called central plasma sheet or CPS) project via magnetic field lines into equatorward portion of the auroral oval while the plasma sheet region away from the equatorial plane, near the upper or lower boundary of the plasma sheet region (BPS), maps into the poleward region of the auroral oval. During the magnetospheric substorm, the plasma sheet particles are convected toward the earth and accelerated. Some are injected into the radiation belts and become magnetically trapped while others are precipitated into the atmosphere. The precipitating charged particles in the high latitude atmosphere produce phenomena such as the visual auroras, x-ray auroras, and cosmic noise absorptions, to name a few. In addition, the charged particle

precipitation also causes anomalous ionization thus providing a conducting path for the auroral zone current, the auroral electrojet. Optical and x-ray auroras are of main interest to us here.

Since in-situ simultaneous study of both temporal and extended spatial variations of the precipitating charged particles is not easily achieved it is necessary to resort to the study of the secondary effects produced when these particles lose their energy to the upper atmosphere. For example, auroral bremsstrahlung x-rays are produced when the high energy electrons, impinging on the top of the atmosphere, suffer large acceleration in the Coulomb field of the atomic nuclei of the atmospheric constituents. The spatial and temporal variations of the x-ray emissions can thus be related to the same variations of the precipitating electrons producing these x-rays. It is, however, well known that the nature of interaction of x-rays with the atmospheric constituents prevents any ground-based observations of the auroral x-rays. Hence the need to study them by means of payloads onboard balloons, rockets, or satellites.

First balloon-borne observations of auroral x-rays were carried out by Winckler et al. (1959) using Geiger counters and ionization chambers as detectors. These were later replaced by sodium iodide scintillation detectors which are much more effective in x-ray detection. The ultimate goal of these measurements is then to relate the morphology of

the x-ray emission region to that of the high energy electrons producing these x-rays. Direct measurements of high energy parent electrons using satellites is unsatisfactory since we still need to sort out the spatial and temporal variations of the electron intensity. Rocket measurements can provide good short-term temporal resolution but the data collected is over a relatively limited interval of time and hence is a very small quantity.

On the other hand, balloon-borne measurements are capable of isolating the temporal from the spatial variations of x-rays since, relatively speaking, balloons are stationary in space. But note that the electron flux producing the x-rays is being monitored by only the secondary effect. The x-ray spectrum at the float altitude of the balloon must then be related to the primary electron spectrum. An additional disadvantage of the balloon is that it provides information only about the limited position of the source region of the x-ray production and up to a radius of 150 km. Multi-balloon observations seem to be an answer to such a problem. However, these require considerable effort to coordinate and only a few have been carried out to date (Bewersdorff et al., 1968; Maral et al, 1973; and Trefall et al., 1975).

Alternatively, the solution to this spatial limitation problem is the use of polar-orbiting satellites for simultaneous extensive overview of observations of x-ray aurora, as Imhof et al. (1974) have done. Such

observations provide an opportunity to study the electron precipitation as a function of local time simultaneously, hereby sacrificing the few details available to balloons. To date however, it is fair to say that most of the advances in the field of x-ray aurora have been from balloon-borne detectors. These, as well as observations by rockets and satellites, are briefly reviewed in the following sections.

The history of optical auroral observations began centuries ago. Recent observations of the optical aurora are registered by ground-based detectors and those onboard balloons, rockets, and polar-orbiting satellites. Studies of all-sky camera photographs from the ground have revealed that the auroras on a statistical basis seem to lie along an oval (rather than circular band) around the geomagnetic pole. This is known as the auroral oval; the earliest to demonstrate the existence of such an oval was Feldstein (1963). Further investigation by Lui (1974) has demonstrated the contribution of both discrete and diffuse auroras to the oval. Later, imagers onboard satellites ISIS-2, DMSP, Dynamic Explorer and recently the Viking have confirmed the oval nature of auroral display region. A classical model of auroral substorm development has been given by Akasofu (1964) again from a statistical study of the all-sky photographs. Two substorm phases, expansion and recovery, have been recognized in the substorm. During the expansion phase the intensification of quiet arcs lying along the auroral oval are observed followed by further

intensification, distortion, and poleward movement of the arcs located around the midnight meridian. After 30 minutes the recovery phase is observed; auroral activity begins to subside and the discrete arcs in the equatorward part of the oval disintegrate. Electrons are then seen to drift eastward with speeds of 300-1000 m sec^{-1}. This pattern can repeat a few times during one night.

Rocket studies of optical aurora provide quantitative measurements such as intensity of optical emissions and intensity and spectral measurements of electrons and ions associated with the optical emissions. Again, as pointed out earlier, only a limited amount of data is obtained. Some of the results of the auroral x-ray measurements are given in the following sections.

1.2 X-Ray Aurora

1.2.1 Atmospheric Effect on the Parent X-Ray Spectrum

Propagation of x-rays from the production layer at an altitude of 90 km (0 g cm^{-2}) down to the balloon float altitude of 48-30 km (2-10 g cm^{-2}) must be understood in order to estimate the spectrum of the parent x-ray source. Monte Carlo simulations and theoretical models pertaining to propagation of x-rays through the atmosphere have been carried out, for example, by Rees (1964); Pilkington and Anger (1971); Berger and Seltzer (1972); Seltzer et al. (1973); Luhmann (1976); and Vij et al. (1980).

Seltzer et al., (1973) presented the results of Monte Carlo simulation in graphical and tabular form. Vij et al. (1980) related the Monte Carlo simulation directly to observation of x-rays at altitudes located above the balloon's float level by using rocket payloads parachuting down from 65 km height.

There appears to be some disagreement among the investigations as to whether the observed spectrum at the balloon's float level should be harder or softer than the original spectrum. Pilkington and Anger (1971), and Vij and Venkatesan (1974) have indicated a spectral softening. Rees (1964) suggests hardening and no unique conclusion about the spectral change has been indicated by Berger and Seltzer (1972). The neglect of multiple Compton scattering seems to produce harder spectra as shown in Figure 1.1. Luhmann (1976) has treated Compton scattering as an absorption event and obtained harder spectra (Figure 1.1, plots C and D) than those obtained by Berger and Seltzer (1972) and Seltzer and Berger (1974) shown in the same figure (plots c and d). All results however indicate the importance of photoelectric absorption which strongly operates at the low energy end of the spectrum. The absorption coefficient for the photoelectric interaction increases with decreasing energy as shown in Table 1.1. This results in the fast removal of low energy x-rays from the beam. Figure 1.1 shows the downward bending of the spectrum (plots B, C, D, and b, c, d) at the low energy end compared to the original spectrum

ABSORPTION AND SCATTERING OF X-RAYS

PHOTON ENERGY (keV)	PHOTOELECTRIC ABSORPTION COEFFICIENT ($cm^2\ g^{-1}$)	COMPTON SCATTERING COEFFICIENT ($cm^2\ g^{-1}$)
10	4.2	0.190
15	1.2	0.185
20	0.50	0.175
30	0.13	0.165
40	0.050	0.160
50	0.025	0.155
60	0.013	0.150
80	0.005	0.135
100	0.0025	0.125
150	-	0.105
200	-	0.093

TABLE 1.1

at the production altitude (plots A and a). Note also, (Table 1.1) that the absorption coefficient for Compton scattering is much less energy dependent.

In the case of the collimated x-ray detectors, Pilkington and Anger (1971) have indicated a strong dependence of the observed spectrum on the source geometry and relative source-detector distance. The results reveal a rather sudden spectral softening as the source goes outside the detector's field of view. Such a sudden softening is due to the fact that from outside the field of view, only the scattered component can enter the detector. The situation is much better in the case of the omnidirectional detectors, the spectrum shows little variation with the source-detector distance or with change in geometry.

As already indicated, the prime objective of auroral x-ray studies is to obtain the parent electron spectrum. Anderson (1964) gives the expression for the differential x-ray spectrum produced by electrons as follows:

$$\frac{dN(E_x)}{dE_x} = \int_{E_x}^{\infty} K(E_x,E) \frac{dN(E)}{dE} dE \qquad (1.1)$$

where $K(E_x,E)$ is a function related to the number of x-rays of energy E_x in the energy interval dE_x produced by the electron of initial energy E while coming to rest. Anderson (1964) has given a non-relativistic approximation
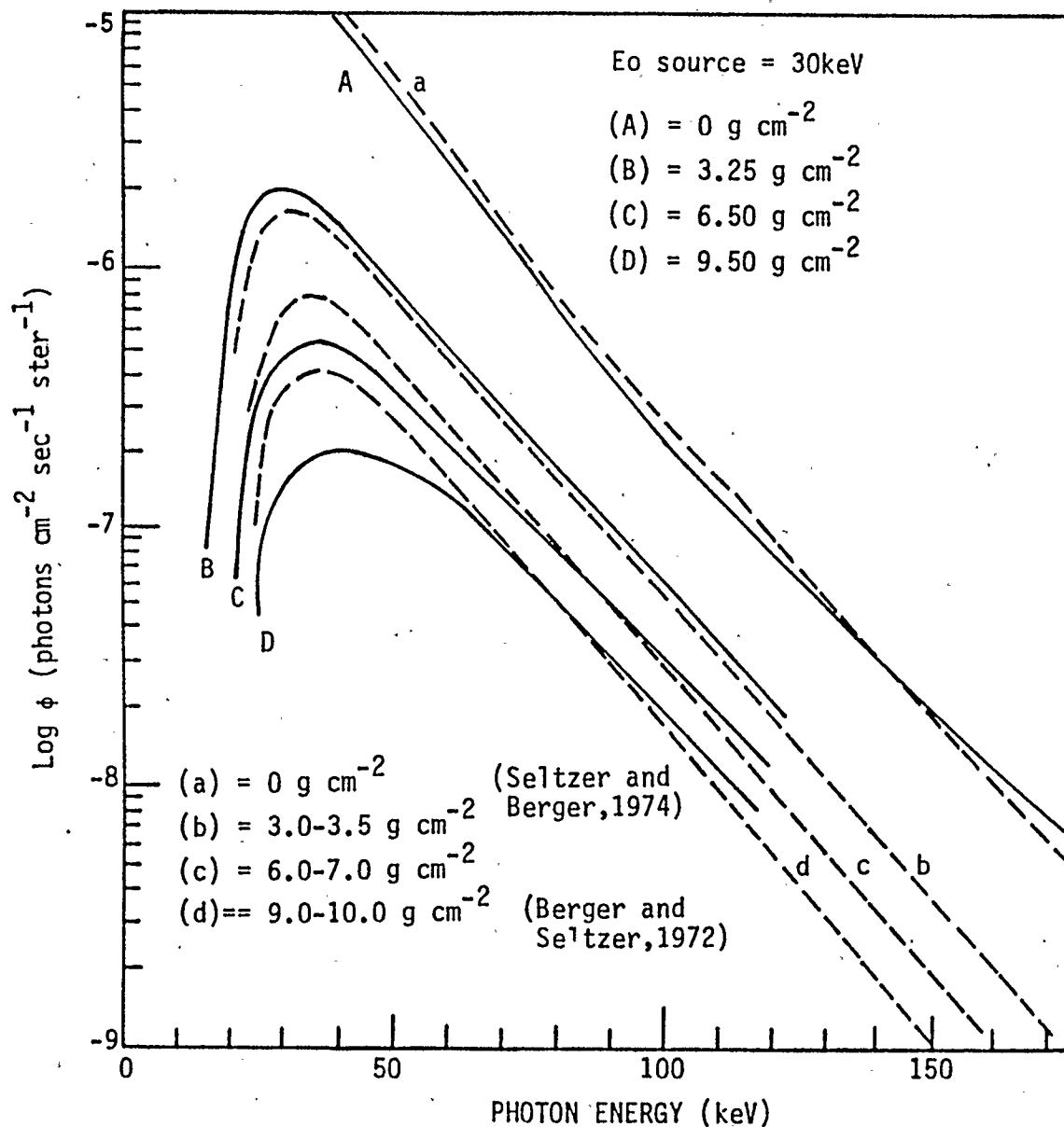
Figure 1.1 Calculated omnidirectional flux spectra of X-ray photons
at various atmospheric depths ((A,B,C,D)Luhmann,1976),
((a,b,c,d)Berger and Seltzer,1972,Seltzer and Berger,1974).
The incident electron spectrum has e-folding energy of 30keV.
(Taken from Luhmann,1976).

of $K(E_x,E)$ in the form of a polynomial

$$K(E_x,E) = \sum_{n=0}^{n=3} a_n(E_x)E^n \qquad (1.2)$$

indicating a fit within 1 percent of the calculated $K(E_x,E)$.

Evans (1955), Anderson and Enemark (1960) give a relativistic expression for $K(E_x,E)$ of the form

$$K(E_x,E) = k\left(\frac{E}{E_x} - 1\right) \qquad (1.3)$$

where k is an electron to photon conversion constant. Vij et al. (1975) have determined the value of k to be $2 \pm 0.5 \times 10^{-5}$ from simultaneous measurements of auroral electrons and x-rays. Anderson and Enemark (1960) have given a value of 1×10^{-5} photons/electron.

1.2.2 Results from Balloon-Borne Studies

Systematic single and multiple balloon-borne investigations have shown that the x-ray emissions during polar substorms can be classified into events which are characteristic to a particular magnetic local time. (See for example Barcus and Rosenberg, 1966; Parks et al., 1968; Bewersdorff et al., 1968; Sletten et al., 1971; Bjordal et al., 1971; Maral et al., 1973; and Trefall et al., 1975).

Temporal characteristics of x-ray activity in the midnight zone (22:00-02:00 LMT) shows impulsive electron precipitation events (Barcus and Rosenberg, 1966; Bjordal et al., 1971). Parks et al. (1967) has also observed 5-50 m/sec bursts superimposed over the impulsive midnight events.

A spatial association of x-ray emissions with the auroral electrojet in the midnight sector has been reported in a few studies (for example, by Clark and Anger, 1967; Bjordal et al., 1971; Sletten et al., 1971; and Maral et al., 1973). In some instances, Clark and Anger (1967) found a close relation between the observed x-ray intensity and the apparent balloon-electrojet distance. Varga and Venkatesan (1983) have also reported good correlation between the observed intensity of impulsive x-ray events and the intensity of the electrojet determined from the meridional chain of magnetic stations. Such association suggests that precipitating electrons responsible for the ionospheric conductivity increase share a common magnetic field line with the high energy electron component which produces bremsstrahlung x-ray emissions. Multiple balloon observations have shown that the x-ray emission region in the midnight sector (Bjordal et al., 1971 and Maral et al., 1973) is typically latitudinally confined but with large longitudinal eastward extension. The cause of much pre/post midnight asymmetry may be attributed to the eastward corotation of the plasma in the inner magnetosphere as

suggested by Freeman and Maguire (1968).

Dissociation between the x-ray and the bay activity can sometimes be observed in the early morning sector (02:00-06:00 LMT) and almost always observed in the morning sector (06:00-10:00 LMT). Multiple balloon observations have indicated that the x-ray activity in these sectors can be characterised by two types of electron precipitation; events associated with the bay activity and events located to the south of the electrojet activity. (Sletten et al., 1971; Kremser et al., 1973; and Trefall et al., 1975)

The latter x-ray events are also called SVA events as they have been observed to occur together with the slowly varying ionospheric absorptions measured by riometers (Kremser et al., 1973). The electron precipitation in the vicinity of the bay activity just represent an eastward extension of the activity in the midnight sector. The source of electrons for the second type of precipitation apparently comes from an eastward drifting electron cloud originating from the primary electrons injected into the inner magnetosphere in the midnight sector during the substorm. Sletten et al. (1971) points out that direct satellite observations of the drifting electron cloud was reported by Pfitzer and Winckler (1969). The electrons with larger pitch-angles can become temporarily trapped and will assume an eastward drift (the drifting rain cloud model) (Sletten et al., 1971 and Maral et al., 1973; Kremser et al., 1973; and Kangas et al., 1975). Time delays of 5 to 30

minutes between the substorm onset in the midnight sector and the onset of the SVA events have been reported for example by Kremser et al., 1973 and Kangas et al., 1975.

The temporal profile of the SVA event in the early morning and morning sector is characterized by a fast rise (20-40 minute) and a slower decay; this apparently also shows some relation to the x-ray events observed by Barcus and Rosenberg (1966) in the post-midnight sector called "slowly varying bay events". Spectral observations during SVA events show an initial rapid spectrum softening followed by more gradual hardening (Kangas et al., 1975). An energy dispersion effect has been postulated as a reason for the initial spectral softening as the higher energy electrons will arrive earlier at the point of observation. The subsequent hardening (Kangas et al., 1975) could be caused by the preferential removal of the low energy electrons.

Post-midnight x-ray measurements often indicate the presence of pulsating and microburst activity. (See for example Barcus and Rosenberg, 1966: Bewersdorff et al., 1968; and Parks et al., 1968). Bewersdorff et al. (1968) for example report a 5-10 seconds pulsating activity superimposed over the SVA events. Parks et al. (1968) report observation of pulsating activity of similar periodicity; the e-folding energy of the electron spectrum associated with the observed x-ray pulsations was estimated to be 15 keV. The foregoing discussion of diurnal precipitation pattern is summarized in Figure 1.2 a and b.

Precipitation patterns of discrete and diffuse events in the auroral zone are shown in Figure 1.2a (Hartz and Brice, 1967). The discrete events (shown by triangles) include, besides others also the midnight-like impulsive x-ray bursts while the diffuse events (indicated by dots) include SVA x-ray activity. These precipiations patterns seem to be tied directly to the topology of the magnetosphere. Apparently, the charged particles producing the discrete events originate in the plasma sheet while the particles producing the diffuse events have their origin in the outer regions of the radiation belts. Figure 1.2b (Barcus and Rosenberg, 1966) shows the diurnal pattern of characteristic x-ray activity and the typical e-folding energy associated with the individual events.

1.2.3 Satellite Studies of X-Ray Aurora

Extensive investigations of spatial and temporal variations of x-ray events using low altitude satellites have been carried out by Imhof et al., (1974, 1978, 1980, 1982, and 1985). Results from the 1972-076B satellite (Imhof et al., 1974) indicated that high energy electron precipitations were occurring over the wide range of local times and there existed a significant variation in intensity from one local time to another. In addition, no significant x-ray fluxes were observed during the polar crossings suggesting the relative absence of high energy electron precipitation over these regions.
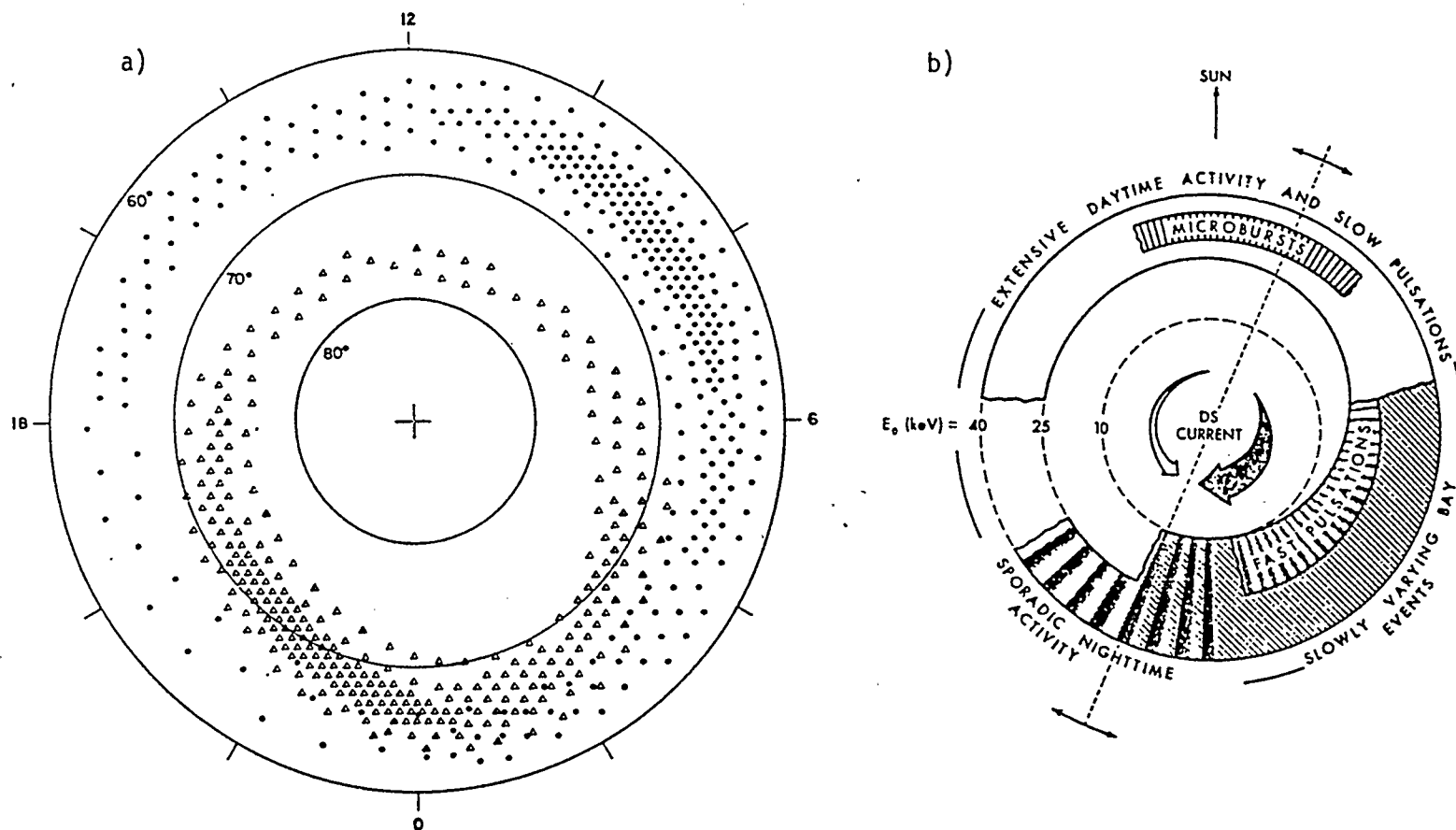
Figure 1.2 a) The general pattern of auroral particle precipitation in the auroral zone.
The discrete type of precipitation (triangles) seems to be confined to the
auroral oval region;the diffuse events (dots) form a circle equtorward of
oval.(Hartz and Brice,1967).

b) Diurnal pattern of typical electron spectrum and precipitation deduced from
X-ray observations in the auroral zone (Barcus and Rosenberg,1966).

Similar results indicating the presence of wide-spread high energy precipitation have been obtained by using the polar-orbiting satellite P78-1. The x-ray data were collected by an array of cadmium telluride sensors onboard the satellite. The output signals from the detectors were discriminated into six energy channels (21-30 keV, 30-46 keV, 46-68 keV, 68-98 keV, 98-139 keV, and >139 keV).

Detailed observation of the precipitation pattern also showed some intensity dependence with respect to local time (Imhof et al., 1985). From 09:30 to 14:00 LMT the average x-ray intensity showed a decrease with increasing local time. No such trend was observed between 22:00 to 02:00 MLT. The x-ray activity in this time zone has been found to true if the hardening had occurred within three hours of local time.

In addition to the spatial variations, temporal variations of x-rays have been investigated by Imhof et al., (1978). From more than 400 polar cap crossings, the polar-orbiting satellite 1972-076B has observed the presence of x-ray temporal spikes emanating from the vicinity of the > 155 keV electron trapping boundary. These impulsive events have displayed a relatively rapid variation as the satellite, spinning at the rate of one revolution in 5 sec, was able to detect changes in the counting rate at the times the detector was looking downward. The total duration of these events was of the order of 5 minutes or less. Wide

observation field of the detector was able to establish that these events are truly temporal in character and not some narrow precipitation region just passing through the detector's field of view. Spatially they were predominantly observed in the vicinity of the local midnight.

Even faster temporal variations in the x-ray flux measurements have been detected around the local dusk region (18:00 MLT) by Imhof et al., (1980) from the data of P78-1 satellite. The x-ray bursts have been observed to have a time duration between 30 to 100 seconds. The spatial extent of these impulsive precipitation regions was variable since some events were observed by all four detectors and some by one only. However, it has been pointed out by Imhof et al., (1980) that these events are relatively rare; only a few such impulsive events have been observed from the total of 200 southern polar-cap crossings. Such a conclusion is also supported by the balloon observations in the local dusk zone; these indicate that the auroral x-ray flux does not seem to display a large temporal variation in this time zone although Barcus and Rosenberg (1966) have encountered some impulsive events before local midnight.

Observations of x-ray emissions at the onset of the substorm (Imhof et al., 1982) show that just prior to the onset of the substorm, no significant x-ray flux was observed. This has been interpreted as due to the lack of significant energetic electron population on higher L shells. The wide field of view of the detectors enabled

investigators to conclude that no x-rays were generated at any higher L shell prior to the onset of the storm. At the onset of the substorm, the x-ray count rate has been observed to increase sharply, reaching a maximum within one minute. The main electron precipitation started at L = 5.5 and moved to higher L shells as the substorm progressed.

1.3 Optical Aurora

1.3.1 Auroral Optical Emissions

Visual aurora can be described as a luminous phenomenon caused by the precipitation of energetic charged particles, mainly electrons into the upper atmosphere. Energetic particles encountering the polar upper atmosphere will produce ions as well as excited atoms or molecules directly. The secondary electrons arising from ionization will be able to produce secondary ionization if they have enough energy. Relevant interactions of the auroral electrons with the atmospheric constituents have been discussed for example by Rees (1969), Omholt (1973), and Banks et al., (1974), to name a few. For example (Omholt 1973) has shown that relevant reactions for the excitation, ionization-excitation and dissociation-excitation are

$$M + X \longrightarrow M^1 + X \qquad (M_2 + X \longrightarrow M_2^1 + X)$$

$$M + X \longrightarrow M^{+1} + X + e \qquad (M_2 + X \longrightarrow M_2^{+1} + X + e)$$

$$M_2 + X \longrightarrow M + M^1 + X$$
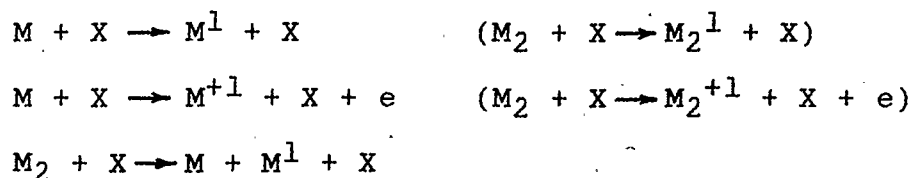
where M_2 is the diatomic molecule such as O_2 or N_2, X is the precipitating particle, M, M^+, and M^1, M^{+1} are atoms and ions in the ground and the excited states respectively and e is the secondary electron. According to Rees (1969) the ionization-excitation type of interaction dominates at higher energies of precipitating particles. The emission intensity induced by ionization-excitation therefore dominates at lower altitudes due to the larger penetration depth of the primary electrons. For example, the ionization-excitation of N_2^+ molecules results in the emission at 3914A. Interaction of O_2 with the energetic electrons may involve all the three above-mentioned processes resulting in generation of various emission lines of which the most prominent ones are at 5577A and 6300A.

Rees and Jones (1973) have pointed out that because of the long lifetime for the 6300A emission, the collisional deactivation will remove the large fraction of the excited species at low altitudes restricting the bulk of 6300A emissions to above 150 km. Banks et al., (1974) has similarly indicated that emissions at 5577A intensifies at lower altitudes. The relationship between the auroral brightness and the energy deposited into the atmosphere has been explored by Deehr et al. (1973) and Rees and Luckey (1974). Deehr et al. have reported an energy conversion factor of 27OR of 4278A N_2^+ emission per erg of incoming electron energy. However Rees and Luckey (1974) have

pointed out that the conversion factor depends on the characteristic energy of the precipitating electron flux which, according to them, can be inferred from the relative ratios of 6300A/4278A, 5577A/4278A, 6300A/5577A and the known absolute emission rates at 4278A. These authors also conclude that since the electrons with harder energy spectrum are able to penetrate deeper into the atmosphere where the molecular species such as N_2 are abundant, the emissions like 3914A and 4278A are expected to dominate over the oxygen atom emission lines such as 5577A and 6300A.

1.3.2 Visual Auroral Forms

Considering the spatial distribution of the auroral luminosity, there exist two types of visual auroral forms, namely the diffuse and the discrete aurora. Akasofu (1977) has described the discrete auroral form as a single bright strand separated from the other bright strands by a darker space. The diffuse aurora on the other hand is a broad band of auroral luminosity in general, much wider but less bright than the discrete aurora. Further subdivision of the discrete aurora based on the finer spatial forms has for example been discussed by Eather and Mende (1971) and Omholt (1973). These subforms are then termed homogeneous arcs, rayed arcs, patchy auroras, rayed bands, rays, drapery, and curls. Temporal luminosity variations of the auroral forms have given rise to terms like pulsating, flickering, and flaming auroras. Ohmolt (1973) has described the flaming

aurora as the auroral form in which the waves of luminosity sweep toward the magnetic zenith. The basic characteristic of the pulsating aurora is the quasi-periodic variation in the brightness, the periods of variation ranging between 0.9-10 sec (Davis et al., 1971).

A number of auroral patches of size of 5-10 km moving and changing in their luminosities when viewed along the magnetic field lines is the so-called flickering aurora (Oguti 1981).

1.3.3 Distribution of the Auroral Forms In the Oval

Although not easily identifiable from the ground-based all-sky camera observations, the satellite observations indicate that the diffuse aurora tend to occupy the equatorial region of the auroral oval as pointed out by Lui (1974), Lui and Anger (1973), Akasofu (1976), and Meng (1978). In the geomagnetic and local time coordinate system, the diffuse aurora is known to extend over a wide range of local magnetic times. Lui (1974) and Lui and Anger (1973), from images generated by the ISIS-2 scanning auroral photometer, have shown that the diffuse emission belt encircling the auroral oval seem to be a permanent feature even during magnetically quiet periods.

Meng (1978), using the DMSP satellite, has reported observations of diffuse aurora in the evening, morning, and late morning sectors during the quiet as well as geomagnetically disturbed periods. Meng (1978) has also

reported a drastic decrease of the diffuse auroral width from 9° in the morning sector to 3° in the afternoon sector during the geomagnetically disturbed conditions. This difference in width may however be caused by the branching into two components as previously reported by Lui and Anger (1973) who have pointed out that one branch of the diffuse aurora follows the oval whereas the second branch follows the constant geomagnetic latitude. Akasofu (1977) has indicated the high degree of conjugacy associated with the diffuse aurora, but which breaks down during the geomagnetically disturbed conditions. Characteristics of the diffuse aurora over the wide range of local time has been given by Akasofu (1976) using DMSP satellite pictures. Here, Figure 1.3 gives the summary of his observations; this shows that homogeneity of the diffuse aurora breaks down in the early morning and morning time zones into bands and patches. The discrete aurora is seen to appear as a poleward feature of the auroral oval predominantly situated in the evening sector (Akasofu, 1977). Davis (1978) has pointed out the separation from the diffuse form to be several tens of kilometers in the evening sector. He has also discussed the presence of short lived pulsating arc or arc segments in association with the discrete auroral portion in the evening sector. Oguti (1981), based on high resolution TV observations, has shown that the discrete auroral arc in the dusk sector is actually a discrete chain of vortices of various sizes. However, the location of the
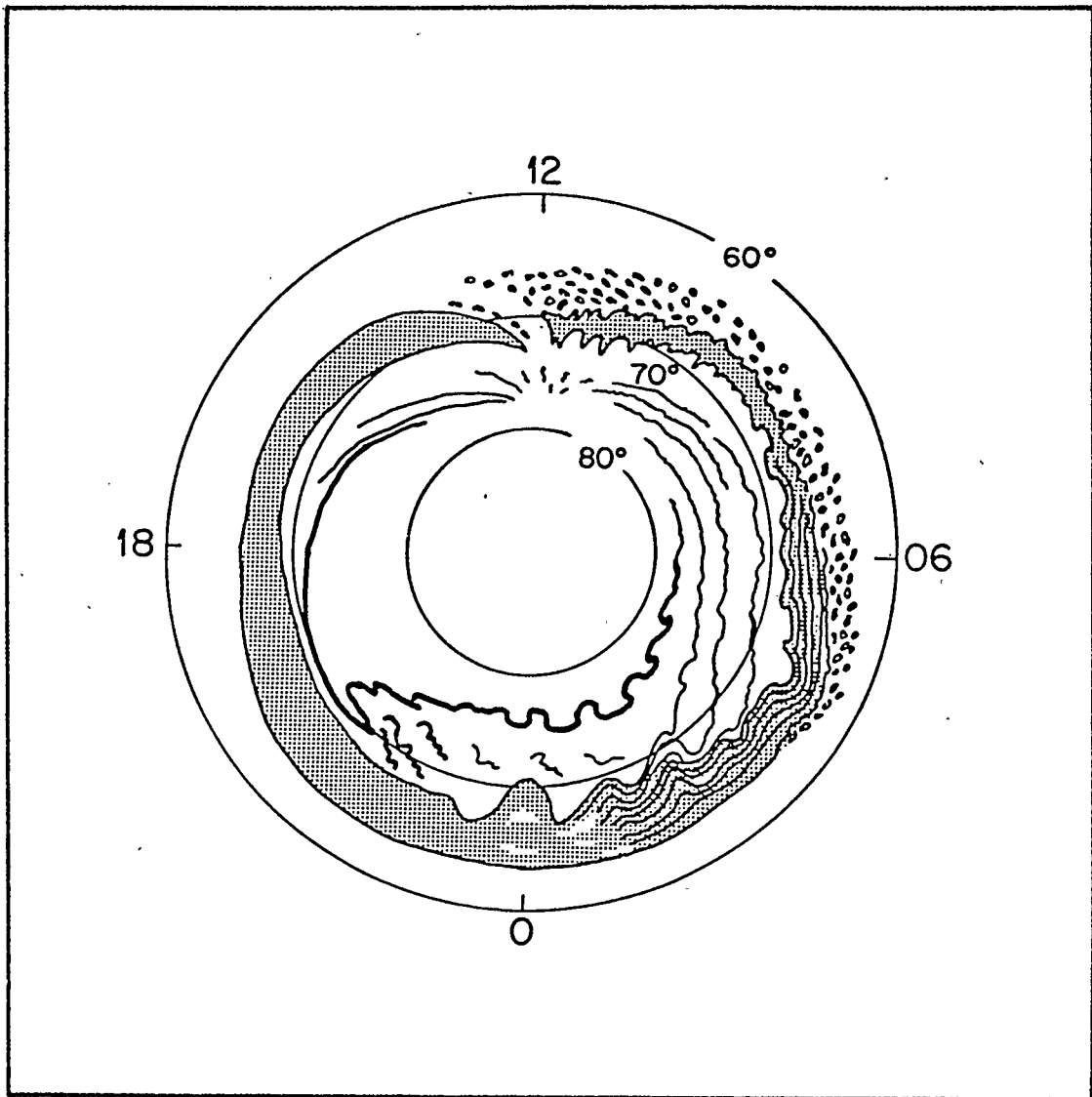
Figure 1.3 Characteristic diurnal pattern of optical auroral
display. Auroral arcs are shown by the solid lines,
the shaded areas show the location of the diffuse
aurora(Akasofu,1976).

discrete auroral arcs is not just a poleward feature of the auroral display but may also be superimposed on the diffuse aurora as pointed out by for example Murphree et al. (1981).

1.3.4 Source of Diffuse Auroral Particles

The origin of particles responsible for the diffuse aurora has been investigated in the past, for example, by a number of researchers such as Winningham et al., (1975); Lui et al., (1977); Ashour-Abdalla and Kennel (1977); Meng (1978); and Fairfield and Vinas (1984). Winningham et al., (1975) have attributed the diffuse aurora particles to the sources in the central plasma sheet (CPS). Lui et al. (1977) have pointed out that the broadness and uniformity of the diffuse aurora requires an extensive and uniform source of particles; such requirements would be satisfied by the CPS particle population. Meng (1978) using DMSP and ATS-6 satellite particle data has concluded that the spectrum and the intensity of the trapped electrons in the CPS region and those precipitating into the diffuse aurora are identical, indicating a direct electron precipitation from the CPS supporting the study of Lui et al. (1977).

1.3.5 Discrete Auroral Particles

Observations indicate that the discrete auroras are usually located within the diffuse aurora; however, they tend to lie in the poleward portion as pointed out by Lui et

al. (1977), and Murphree et al. (1981). Since Lui (1974) has demonstrated that the auroral oval is defined by the diffuse and discrete aurora put together, it is appropriate to recognize that particles responsible for the discrete aurora also originate in the plasma sheet region. For example, Winningham et al. (1975) has associated the source region of the discrete auroral particles with the boundary plasma sheet (BPS). In contrast to uniform precipitation associated with diffuse auroras, Lui et al. (1977), from satellite observations, have shown that the particle fluxes in the region of discrete auroras are highly structured. The spectrum of the structured electron fluxes show some prominent mono-energetic peaks in the range of 0.1-10 keV. Akasofu (1977) has shown the presence of mono-energetic peaks superimposed over the power law and the Maxwellian distribution. In addition, he has also pointed out that the average energy of the structured discrete auroral spectrum is higher than that of the electron flux associated with the CPS and thus into the diffuse aurora. Measurements of the pitch angle distribution of the discrete auroral electrons have also shown the presence of large, field-aligned mono-energetic fluxes embedded within the isotropically distribute population. Note for example, observations from rocket measurements by Arnoldy (1974) which have shown that the Maxwellian part of the spectrum has an isotropic distribution whereas the mono-energetic peak is highly field-aligned.

The flux of protons has been observed to be 2-3 orders of magnitude smaller than that of electrons (Akasofu, 1977).

1.3.6 Mechanism for the Discrete Aurora

Since the mono-energetic peaks seem to be absent in the energy spectrum of the equatorial plasma sheet, it is reasonable to assume that the electrons must be accelerated somewhere between the source and the precipitation region. A much debated and popular mode of acceleration is that through the magnetic field-aligned electric field situated a few thousand kilometers above the auroral arc. The importance of such parallel electric fields to the formation of discrete auroras was pointed out by Alfven as early as 1958. Observational evidence for such a localized acceleration region has been reported, for example by Mozer et al. (1977) from the S3-3 polar orbiting satellite. They observed DC electric fields of peak magnitude of 500 mV/m. Support for the field-aligned electric field has also been provided by Shelley et al. (1976) through observations of O^+ and H^+ ions of ionospheric origin proceeding upward along the magnetic field lines.

From a barium release experiment, Wescott et al. (1975 and 1976) have shown the rapid $E \times B$ movement of the ionized barium cloud to be consistent with the appearance of aurora on the same field line. They have reported the location of the electric field at an altitude of 4000 km,

with intensity of 250 mV/m. No **E** x **B** drift has been observed below 4000 km, indicating the localized nature of the accelerating field; however, the exact nature of the energizing electric field is still being debated. Models like V and S equipotential structure have been put forward for example by Kan and Lee (1981), Swift (1978), and Mozer et al. (1977).

Akasofu (1981) suggests that the limiting current-carrying capacity of the space plasma is the basic reason for the development of the field-aligned potential drop. He has also pointed out that the most popular mechanism for developing and maintaining the field-aligned electric field arises from the double layer and anomalous resistivity processes (see Akasofu, 1981 and reference therein).

1.4 In-situ Observations of Auroral Electron Spectra

Energy spectra of electrons precipitating during auroral substorms have been extensively studied by means of rockets and satellites (Meredith et al., 1958; McIllwain, 1960; Sharp et al., 1964; Rearwin, 1971; Lui et al., 1977; and Meng, 1978) to name a few. Observations have shown that the auroral electrons have continuous as well as peaked spectra. The classic study of McIllwain (1960) from two rocket flights has pointed out that the measured spectrum lies between 3 keV and 30 keV energy interval and could be fitted by an exponential function. For example, in one

particular flight into a faint aurora, the integral energy spectrum of electrons has been shown to be represented by

$$N(3<E<30 \text{ keV}) = 2.5 \times 10^9 \exp(-E/E_O) \text{ (electrons cm}^{-2}\text{sec}^{-1})$$

where E_O = 5 keV. Here E_O (also referred to as E-folding energy) is just a parameter in the exponent representing the spectrum hardness. Similarly, the exponential fit to the observed electron spectrum has also been reported in two other studies.

For example, Meredith et al. (1958) have reported Eo = 8.3 keV for the e-folding energy by observing that the electron flux at 8 keV was one order of magnitude larger than that observed at 35 keV; the observed e-folding energy has also shown variations. Ulwick et al. (1967), also from rocket observations, have measured a rather steep spectrum for auroral electrons. They have indicated a variation between 4 keV and 8 keV in the e-folding energy. A typical example of such variations is given by Sharp et al. (1964); from three polar orbiting satellite passes over the auroral zone, the e-folding energy has been between 3 keV and 8 keV, although on rare occasions it has been 15 keV. Also from rocket measurements, spectra of the form

$$\frac{dN(E)}{dE} \propto E^{-\gamma}$$

(1.4)

and

a)

b)

06-56:30 - 06-56:40 UT

$\frac{dN(E)}{d(E)} = 8.8 \times 10^7 \exp(-E/3.7) \quad 0 < E < 25 keV$

$\frac{dN(E)}{d(E)} = 2.7 \times 10^6 \exp(-E/6.8) \quad E > 25 keV$

Spectra obtained from differential electron detectors

Spectra obtained from integral detectors

T=56-75 sec.
ALT.=430 km.

T=211-225 sec.
ALT.=700 km.

T=464-483 sec.
ALT.=750 km.

T=563-577 sec.
ALT. 630 km.

ELECTRONS (cm⁻² sec⁻¹ ster⁻¹ keV⁻¹)

DIFFERENTIAL ELECTRON FLUX (FLUX / cm² - sec - Sr - keV)

Energy (keV)

Energy (keV)
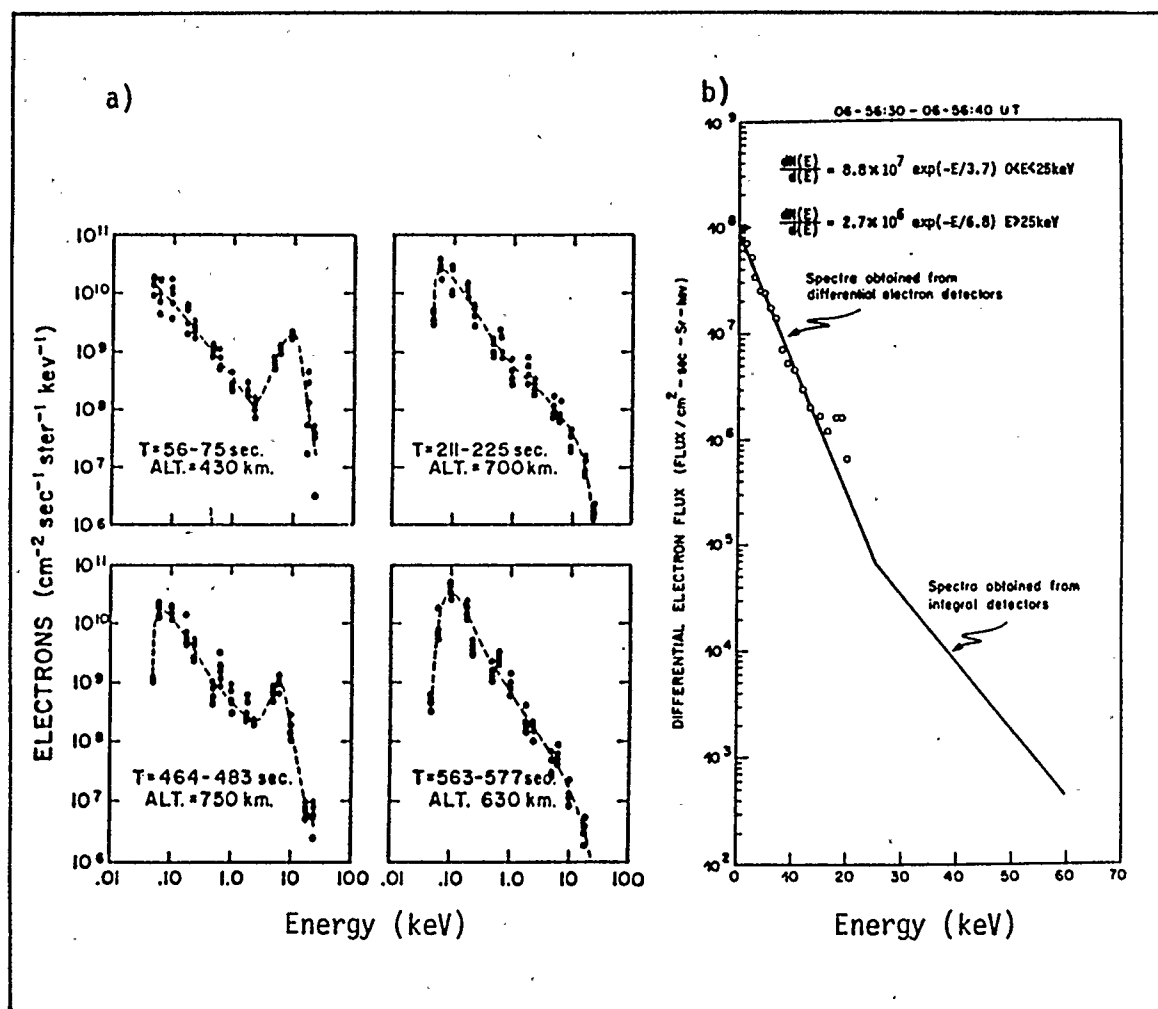
Figure 1.4   Examples of precipitated auroral electron spectra obtained from rocket measurements (Westerlund,1969 - Panel a; Vij et.al., 1975 - Panel b). The rocket at T=56 and T=464 seconds (Panel a) was located above intense auroral arcs.

$$\frac{dN(E)}{dE} \propto E^{\gamma} \exp(-E/E_0)$$

<div align="right">(1.5)</div>

respectively have been reported by Ogilvie (1968) and Westerlund (1969). The latter, from observations of 200 auroral electron spectra, has given a value of γ between 0.3 and 2.3 whereas Ogilvie places the values of γ and E_0 in the observed power-exponential law between 0.9 and 5 and 0.67 and 2.0 respectively. Rearwin (1971) however has reported a Maxwellian type electron spectrum with approximately isotropic pitch angle distribution and characteristic temperature

$$kT = 3 \pm 0.7 \text{ keV}$$

In case of either power or exponential laws (Rees 1963) the observational evidence seems to point in favour of steep energy spectra for the auroral electron primaries; this would indicate a definite absence of high energy electrons in measurements as the flux would fall below the threshold level of the detectors. Examples of power and exponential auroral electron spectra obtained from rocket measurements by Westerlund (1969) and Vij et al. (1975) are shown in Figure 1.4. Westerlund has reported a sharp cut-off of auroral electron flux at > 30 keV whereas McIllwain observed a striking absence of electrons just above the 50 keV energy region.

1.5 Simultaneous Studies of X-Ray and Optical Auroras

Investigations involving comparisons of x-ray and visible auroras have indicated only a loose association between the two phenomena. Anderson and Enemark (1960) have pointed out that the peaks of x-ray and optical activities did not coincide; but in all cases the maximum of x-ray activity preceded the maximum of the optical activity by about half an hour. In similar experiments correlating wide-spread aurora and x-ray activities, a close space-time association has been found by Anderson and DeWitt (1963); this was explained by pointing out that the auroras and x-rays are generated respectively by lower energy electrons (8-10 keV) and the high energy tail ($>$ 25 keV) of the same spectrum. They have further estimated that the total power input by the high energy electrons (E $>$ 25 keV) into the atmosphere is only 1 percent of the power input by the low energy electrons in the energy region below 25 keV.

Rosenberg et al. (1971) have observed a poor correlation between the gross variations of auroral luminosity at 5577A and the x-ray intensity. The optical data were collected by the ground-based all-sky camera and a 5577A photometer carried onboard the x-ray payload. Thus a constant geometry between the optical and the x-ray detectors was maintained.

On the other hand however, a positive correlation has been found between the fast x-ray and optical pulsations in

the morning sector. Cross-correlation analysis has indicated an average time delay of 0.5-1.0 seconds, the optical lagging the x-ray pulsations. The observed delays were attributed to the lifetime of the oxygen atom in the ^1S state.

Direct measurements of electron pulsations showed a time lag of 0.5 sec for electrons in the energy region 4 to 10 keV compared to higher energy components (Bryant et al., 1967); this was interpreted as due to the difference in transit times needed for the electrons to arrive from the equatorial plane; furthermore they have estimated from the time lag the equatorial plane as the location of the modulating source. Instead of 5577A, the utilization of 4278A N_2^+ emissions with negligible lifetime can give a better estimation of the transit time and thus the position of the modulating mechanism.

Sorensen et al. (1973) observed that the 4278A and x-ray ($E_x > 25$ keV) quasi-periodic 5-15 sec pulsations were correlated. The analysis also has shown that the x-rays lead the 4278A pulsations by 0.2-0.6 sec. They have interpreted the delay as due to the considerable distance of the modulating source from the region of observation. Hofmann and Greene (1972) report observations of simultaneous 20-50 keV x-rays and 3914A N_2^+ emission bursts, the bursts exceeding in intensity the uniform quiet time emission by 2 kR. No significant x-ray bursts were reported at energies $E > 50$ keV thus estimating the

e-folding energy of the electron spectrum to be 10 keV.

1.6 Objectives of the Thesis

The bombardment of the high latitude upper atmosphere during the polar substorms by electrons ranging in energy from a few tens of eV to a few hundred keV can be studied by means of the secondary effects they produce, namely the optical and the x-ray auroras. Observations by rockets and calculations of electron penetration into the atmosphere show that the maximum energy deposition for electrons between 2-10 keV coincide with the observed altitudes of 5577A auroral emissions. On the other hand, x-ray emissions detectable at the balloon altitudes (30 km) are produced by electrons with energy > 20 keV. It is therefore imperative to understand the relationship between these two secondary phenomena in order to determine the origins of the low and the high energy electrons which are precipitated during the magnetospheric substorm and which are responsible for the two secondary phenomena.

The development of the CCD all-sky camera at the University of Calgary, provided an opportunity for simultaneous qualitative and quantitative observations of the auroral x-rays and the optical emissions during the polar substorms. Thus the presence or absence of correlation between the two phenomena could be explored. This was done in Chapter 5, where the relationship between the soft x-ray and the optical emissions intensities is

studied. Since directional x-ray detectors will be used for this study, the imaging capability of the detector system will be explored. Chapter 4 deals with this topic involving the Monte Carlo technique.

CHAPTER 2

INSTRUMENTATION PERTAINING TO

DATA ACQUISITION AND PROCESSING

2.1 The X-Ray Detectors

2.1.1 The NaI(Tl) Detector Assembly

The x-ray detector onboard the balloon payload is an assembly of sodium iodide crystal doped with thallium impurity (NaI(Tl)) suitably coupled to a photomultiplier tube (PM) and a high-voltage power supply. The high mass absorption coefficient for energetic electromagnetic waves renders the NaI(Tl) crystal effective in the detection of x-rays. In addition, since proportionally about 10 to 13 percent of the x-ray photon energy is converted into visible photons, this property also makes the crystal suitable for differential energy counting applications. The NaI(Tl) crystal inside each detector is 1.0 inch in diameter and 1.0 inch thick. It is coupled to the PM tube via an optical medium with its index of refraction matched to that of the Na(Tl) crystal. This minimizes the reflection of the luminescent light back into the crystal and hence improves the light collection efficiency of the detector. The crystal and the PM tube are encased inside a 0.015 inch aluminum housing which also serves as the x-ray window at the front end of the crystal. Between the crystal and the aluminum window is a white magnesium oxide powder which

36

diffuses the luminescent light uniformly over the area of the photocathode. The photomultiplier is also surrounded by a μ-metal shield to prevent the perturbation of the electrons paths in the geomagnetic field. The assembly of crystal cum PM tube was purchased from Harshaw Chemicals Ltd., Cleveland, Ohio.

The high voltage (HV) power supply is attached to the back of the PM tube, and this unit is encased inside a 0.032 inch thick stainless-steel tube for mechanical protection. The voltage output from the HV power supply of 900 V provides the potential drop across the dynodes of the PM tube. A white potting compound seals and prevents any physical motion of the HV power supply within the stainless-steel tube; its high dielectric constant also prevents arcing. The analog voltage pulse output from the detector is then proportional to the energy of x-ray photon.

2.1.2 Two Versions of Balloon Payloads

Two versions of x-ray detector assemblies have been in use in the balloon payloads. The older version consists of four vertical detectors with brass tube collimators giving 0.18π ,0.25π, 0.36π, and 2π steradians of opening angles respectively. The newer version also consists of four detectors; however, only one x-ray detector is mounted vertical; the other three are inclined 30° to the zenith and with azimuthal separation of 120° from each other. The detectors are collimated with brass tubes to the same
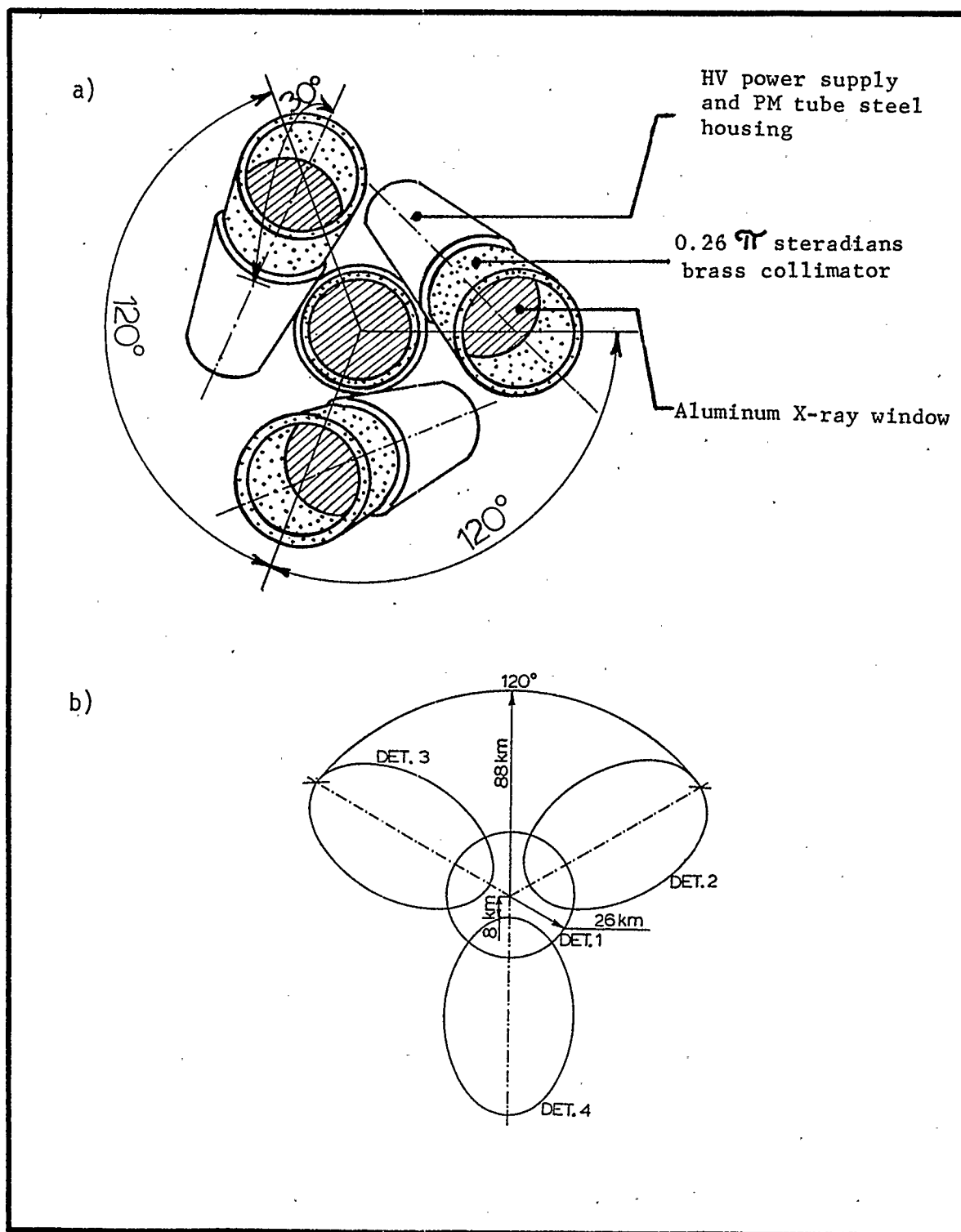
Figure 2.1 a) Relative orientation of X-ray detectors in the
newer assembly version.

b) Illumination area at 100km altitude formed by
the assembly in a).

opening angle of 0.25π steradians. Figure 2.1a gives the top view of the newer detector assembly; Figure 2.1b illustrates the illumination area at the 100 km altitude viewed by the assembly.

2.2 The Balloon X-Ray Payload

A detailed description of the x-ray package has been given earlier (Varga, 1982); however, for the sake of completeness, a brief description of the payload is given in the following sub-sections. A schematic diagram of the balloon payload is shown in Figure 2.2. The dimensions of the payload are 40 x 45 x 85 cm and the weight is 14 kilograms when flight-ready. The frame of the payload is made of 3/4 inch L profiled aluminum; on the outside, the frame is covered with 5 cm thick poly-urethane for thermal and mechanical protection of the payload contents. Inside, the poly-urethane housing is lined with aluminum foil to further increase thermal protection and to shield the equipment from time-varying magnetic fields. Generally, the payload can be divided into three parts:

1) The top portion houses the four x-ray detectors,

2) The middle part houses the associated electronics; out of the six electronic boards, of the four identical boards contain the pulse-height discriminators and the counters. Thus there is one such board for each detector.

45cm

85cm

1) 5cm polyurethane housing   6) Compass mount
2) Aluminum frame   7) Flux gate magnetometers
3) Detector assembly   8) Battery pack
4) Aluminum foil   9) Transmitter
5) Electronic boards   10) Antenna
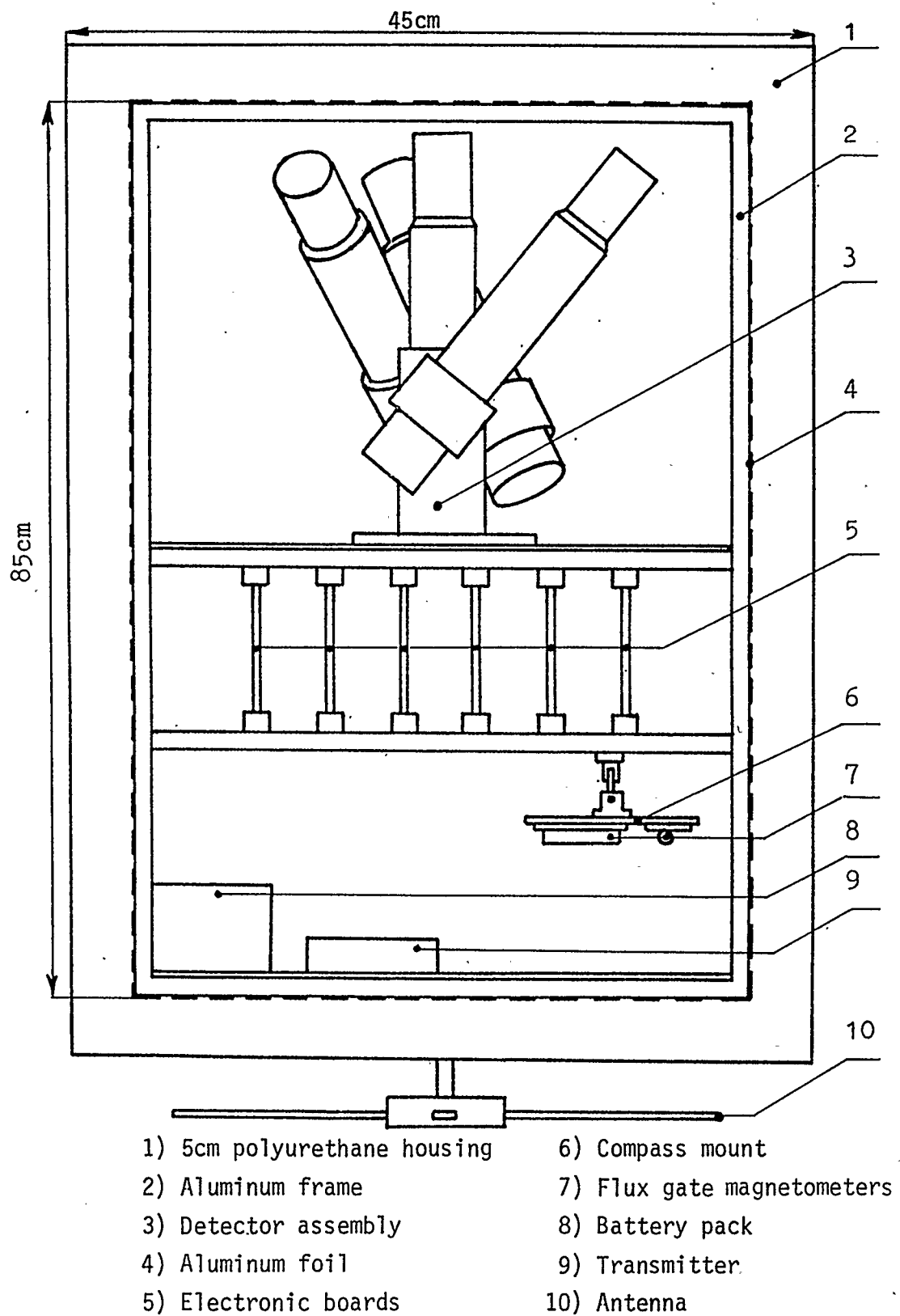
Figure 2.2   Schematic diagram of the X-ray payload.

The remaining two boards contain the control
logic and the A-D converter.

3) The bottom portion houses the power supply of
lithium organic electrolite batteries, the
transmitter and the compass.

2.2.1 Pulse Height Discrimination

The block diagram of the pulse height discriminator
circuit is shown in Figure 2.3a. The analog output signal
from the PM tube is proportional to the x-ray photon
energy. This is compared against the reference voltage of
the voltage comparators. For each detector the reference
voltage for each comparator is set by the resistive divider
network. This generates eight energy windows into which the
analog pulses from the PM tube are discriminated. The
energy windows have been set to values given below; these
apply only to the inclined detectors.

$$20 - 40 \text{ keV}$$
$$40 - 60 \text{ keV}$$
$$60 - 80 \text{ keV}$$
$$80 - 100 \text{ keV}$$
$$100 - 120 \text{ keV}$$
$$120 - 140 \text{ keV}$$
$$140 - 160 \text{ keV}$$
$$> 160 \text{ keV}$$

However, in the case of the vertical detector we do not
have the differential channel 140-160 keV and the integral
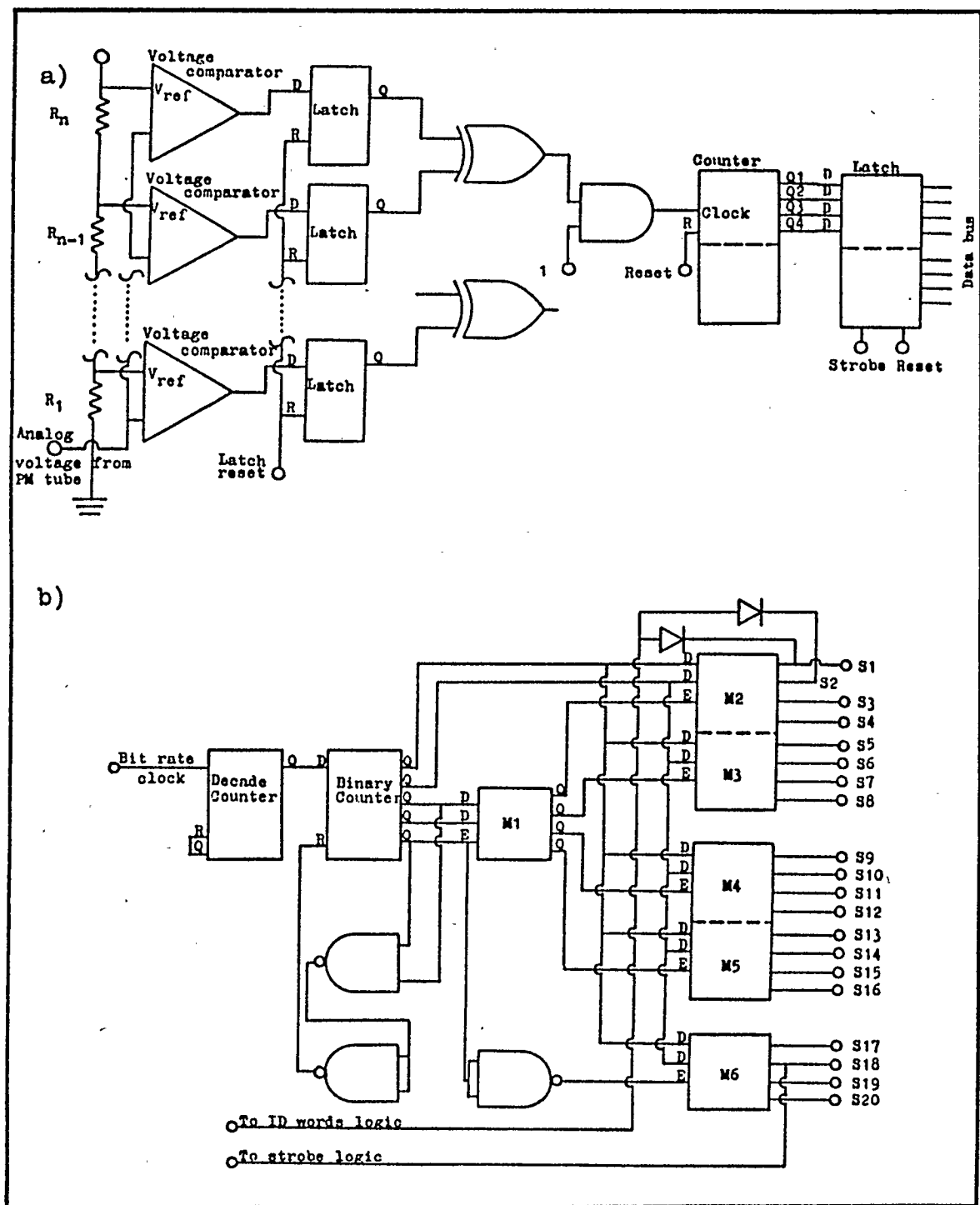
Figure 2.3 Schematic diagram of the electronic circuit boards:
   a) Voltage comparator-pulse height discriminator circuit board
   b) Select logic circuit board

channel > 160 keV since these two channels have been replaced by the integral channel which counts all x-rays with energy > 20 keV. In the case of the older version payload, three vertical detectors have windows exactly the same as the inclined detectors, and the fourth vertical one has an integral channel above 20 keV.

. Counters located on the same electronic board then keep track of the number of events in each energy window. The counts are stored in the form of a binary number.

2.2.2 PCM Encoding

The binary data of the counters, the digitized housekeeping data, and the identifier binary words are sent down to the ground station as a PCM bit stream. The frame format consists of 20 nine-bit binary words, the ninth bit being the parity bit. The beginning of each frame is marked by two identical ID words (10100110 + parity) followed by 16 words carrying information about the counts registered by the four x-ray detectors. There are four words for each detector and four bits per energy channel. The first four bits of word 19 is the housekeeping identifier word. These identifier words are arranged as follows:

Frame #1 - 0000 = high pressure transducer

Frame #2 - 0001 = low pressure transducer

Frame #3 - 0010 = temperature at the electronic boards

Frame #4 - 0011 = temperature at the detectors

Frame #5 - 0100 = positive power-supply voltage
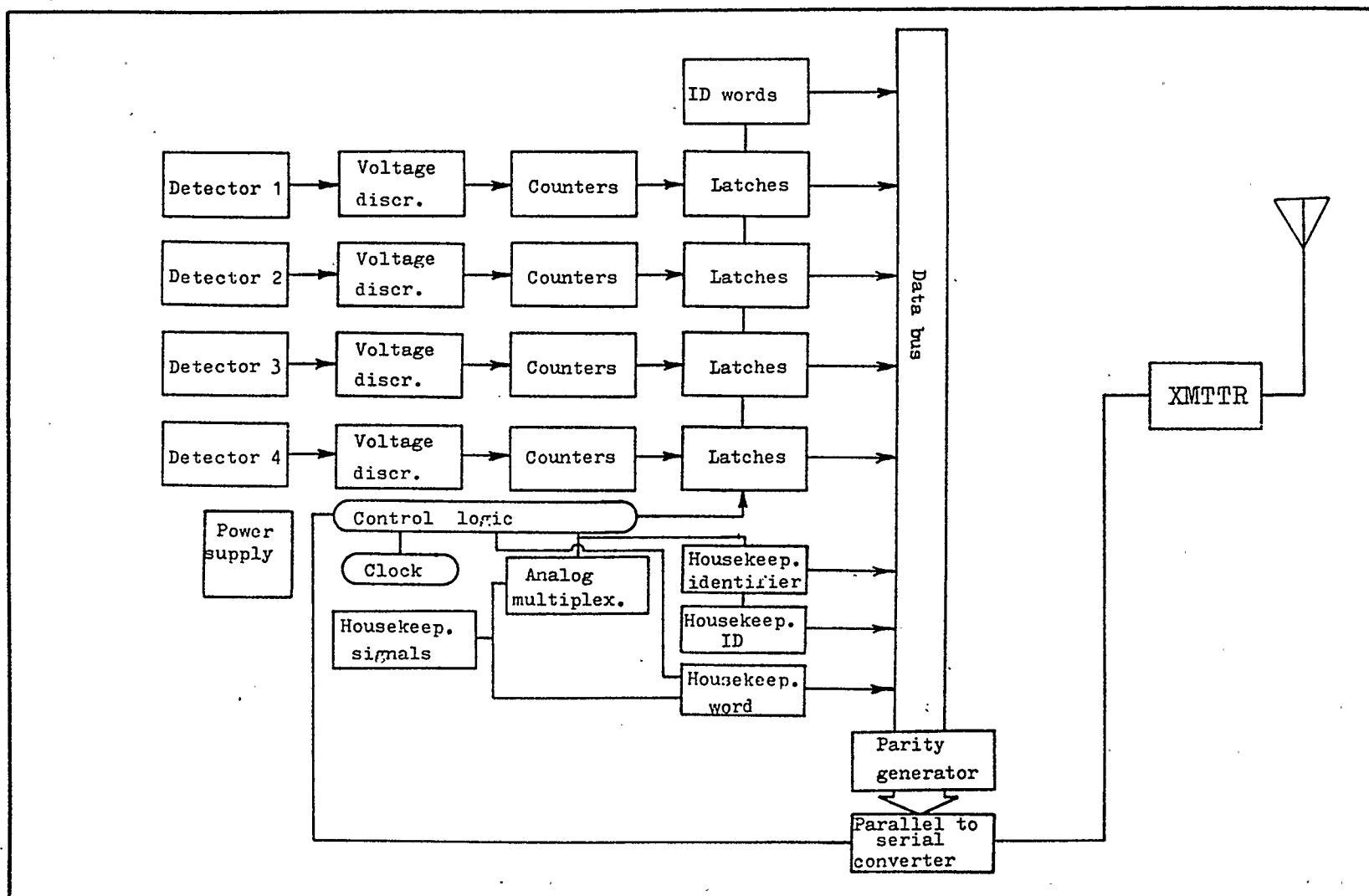
Figure 2.4 Block diagram of signal flow in the balloon payload.

Frame #6 - 0101 = negative power-supply voltage

Frame #7 - 0110 = flux gate #1 of the compass and

Frame #8 - 0111 = flux gate #2 of the compass

The sequence repeats at Frame #9. Word #20 is the housekeeping data itself. It takes 5.76 msec to transmit one frame at the bit rate of 31.25 kHZ. The proper sequence of the binary words to be placed on the bus and hence into the PCM stream is controlled by the control logic of the PCM encoding system shown in Figure 2.3b. The block diagram of the payload is shown in Figure 2.4.

2.3 Energy Resolution of the X-Ray Detectors and Gaussian Smearing

Statistical fluctuations in the number of electrons emitted from the dynodes of the PM tube give rise to deterioration of the energy resolution of the detector. The output response of such an x-ray detector to a mono-energetic photon beam can be visualized as a Gaussian curve instead of a sharp pulse. The percent energy resolution of the detector is defined as,

$$\% \text{ resolution} = \Delta E/E(\max) \times 100\% \qquad (2.1)$$

where ΔE is the width of the peak at half-maximum and $E(\max)$ is the energy at the peak maximum. Figure 2.5a shows the measured energy resolution of the detectors as a function of x-ray energy. The graph represents an average
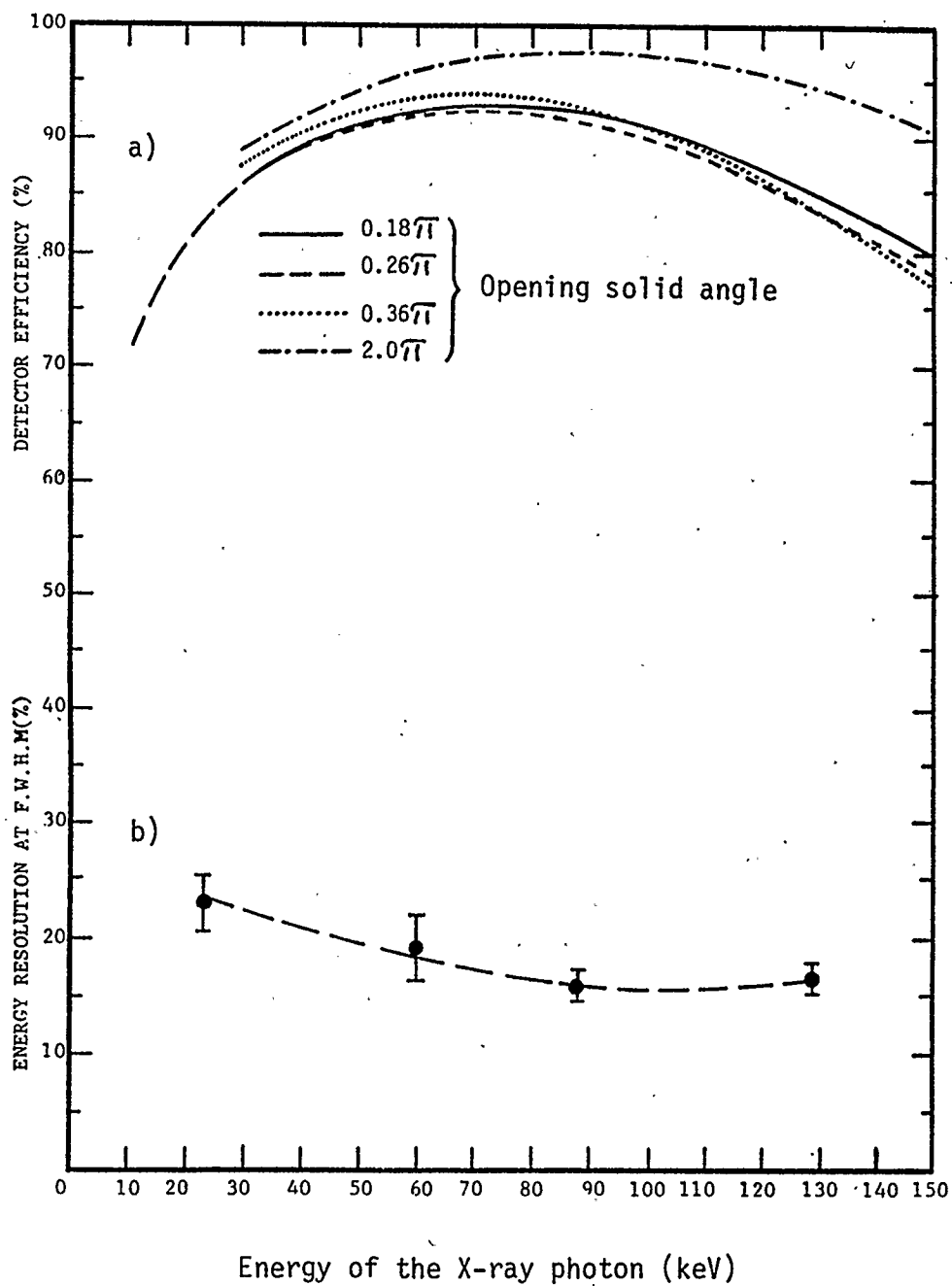
Figure 2.5 a) Percent efficiency of the detectors for a given
opening solid angle as a function of X-ray energy.

b) Dependency of the observed percent energy resolution
of the detectors on the energy of the X-ray photon.

energy resolution of four detectors selected at random from the larger population of x-ray detectors. Cadmium 109, Americium 241, and Cobalt 57 radioactive sources were used in the measurement. In all the x-ray payloads the detected x-ray photons were discriminated into energy windows of 20 keV width as pointed out in Section 2.2. The final output of this type of energy discriminating system is the convolution between the output response of the detector and the windows. The output response of the x-ray detectors is represented by the Gaussian curve with standard deviation as a function of energy resolution.

$$\delta = 4.25 \times 10^{-3} \times E(\max) \times \% \text{ resolution} \qquad (2.2)$$

The window is then a step function of unit height and 20 keV wide. Figure 2.6b is the result of a computer model of the Gaussian smearing effect indicating the relative fraction of counts spilling over into the neighboring energy windows. The examples are given for two different x-ray spectra with e-folding energies of 20 keV and 40 keV respectively. The percent resolution used in the model has been obtained from Figure 2.5b. The horizontal bars represent the fraction of counts in the energy window under investigation (horizontal axis) contributed from the energy windows shown on the vertical axis. For example, the 20-40 keV energy window retains 93 percent of its own counts while the 120-140 keV energy windows can hold only 60 percent of

its own counts, the remaining 40 percent being contributed from the higher and lower energy windows. The contributed fraction from the lower energy window also increases with decreasing e-folding energy. One of the results is that the x-ray count rate profiles for the higher energy windows will look similar.

Figure 2.6a shows the Gaussian smearing effect on the e-folding energy of the observed x-ray spectrum, where E_O represents the e-folding energy in the absence of counts spilling over into the neighboring windows. The result shows that the effect is not large; only 1 to 4 percent corrections are to be made if the observed e-folding energy is between 10 and 60 keV.

2.4 Energy Efficiency and the Dead Time of the X-Ray Detector

Figure 2.5a shows the efficiency of the detectors calculated for 0.18π, 0.25π, 0.36π, and 2π opening solid angles. The percent efficiency was determined using equation

$$\% \text{ efficiency} = \frac{\sum_{\theta = 0}^{\theta = \alpha} e^{-\mu(AL) \cdot t(w)} \left(1 - e^{-\mu(Ex) \cdot t(\theta)}\right)}{\alpha + 1} \cdot 100$$

$$(2.3)$$
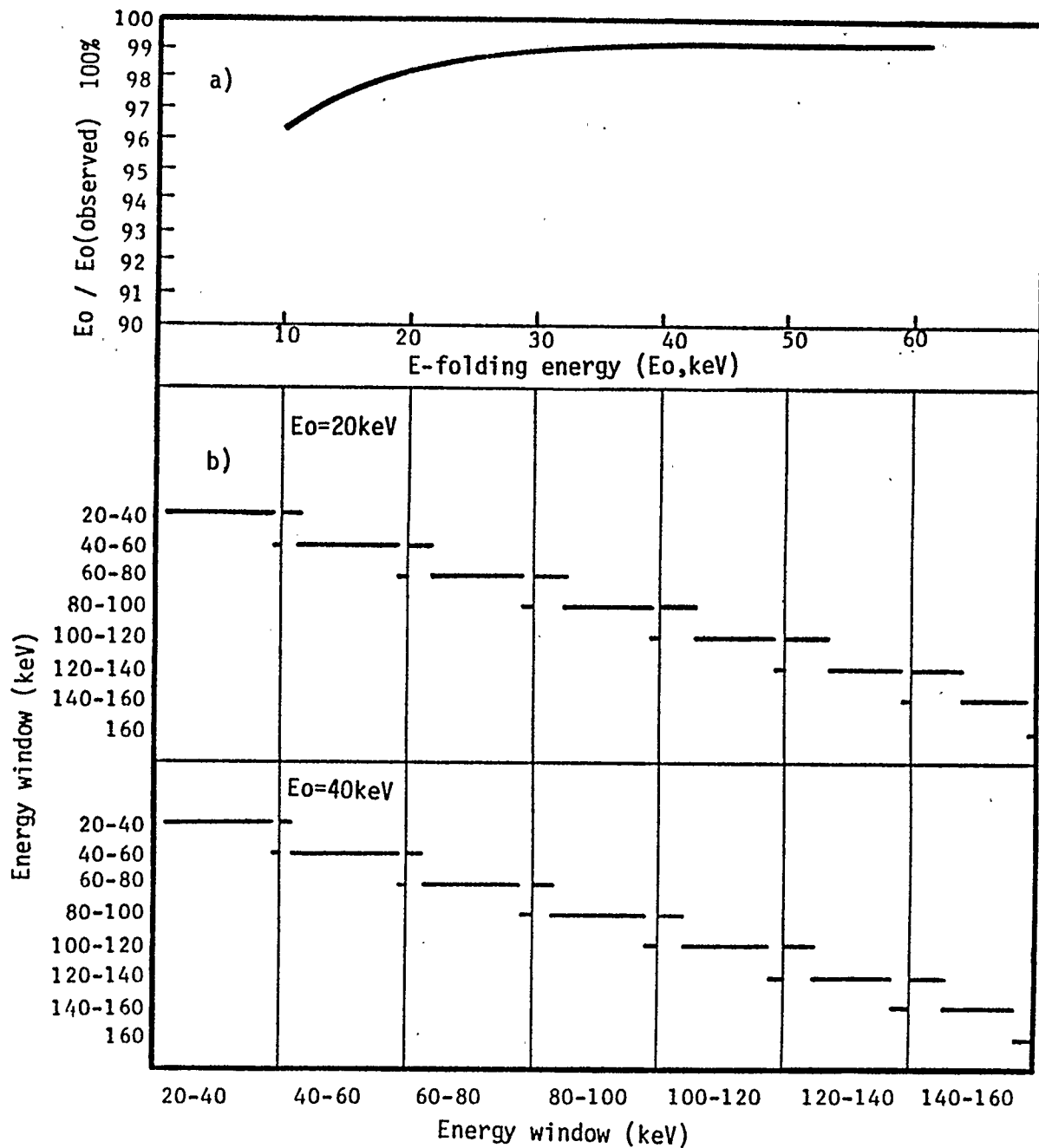
Figure 2.6 a) Changes in the original e-folding energy of the X-ray
spectrum caused by the Gaussian smearing effect.

b) The Gaussian smearing also causes spilling of counts
into the neighboring energy windows. The relative fractions
are indicated by the lengths of the horizontal segments.

where $\mu(Al)$ is the mass attenuation coefficient of the aluminum window, $\mu(E_x)$ is the total attenuation coefficient of NaI(Tl) (both taken from Price 1964), t(w) is the mass thickness (t(w) = density x thickness), $t(\theta)$ is the zenith angle dependent thickness of the NaI(Tl) crystal, α is the largest angle subtended by the crystal for the given opening angle. The four curves (Figure 2.5b) show the effect of absorption by the Al window at low photon energies, at high energies the lower efficiency is due to the x-rays "cutting" through the edges of the NaI(Tl) crystal.

After the detected x-ray pulse, the detector becomes insensitive to oncoming x-ray photons for a short period of time called "dead time". During this period, the voltage drop across the PM tube gets restored. The true count is given by

$$\text{True Count} = \frac{\text{observed count}}{1 - (\text{observed count x dead time})} \quad (2.4)$$

The value of 100μ seconds for the dead time has been adopted from Pilkington (1970) for count rate corrections done in Chapter 3.

2.5 The Azimuth and the Elevation Angle of the Auroral Portion Illuminated by the X-Ray Detectors

When the geographical coordinates of the balloon are known, the elevation angle (ϵ) and the azimuth (α) of
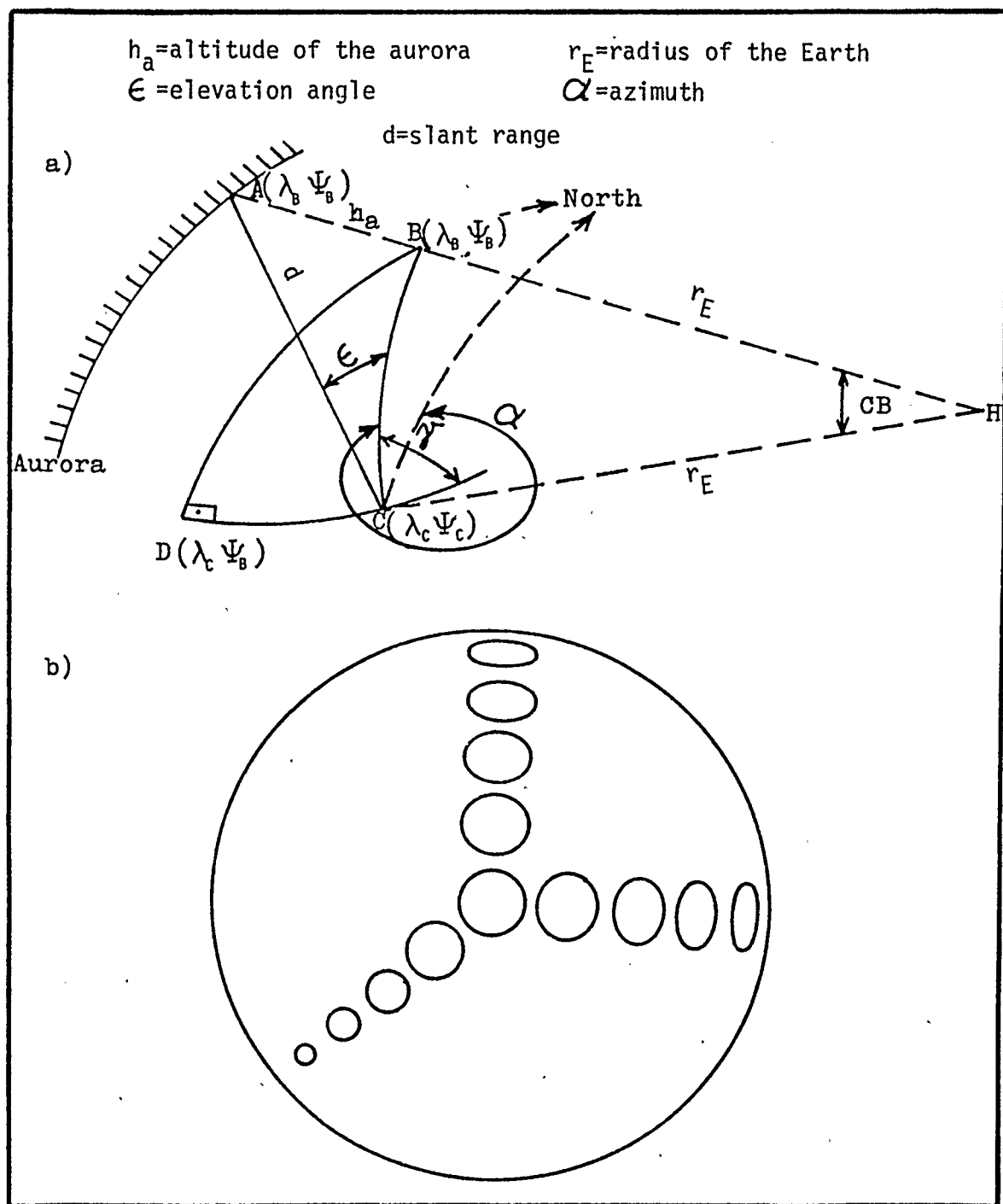
Figure 2.7 a) Geometry showing the relative positions of the balloon, balloon zenith and the all-sky camera site.

b) Barrel distortion of the image by the all-sky lens.

the auroral portion being sampled by the balloon's detectors can be determined (see also Thomas 1972). This is important to know when coordinated balloon-borne and ground based all-sky camera measurements are conducted. Figure 2.7a shows the geometry involved.

It consists of the spherical triangle BCD, each vertex having latitudinal and longitudinal coordinates as indicated. The λ_C and λ_B are the geographic latitudes, ψ_C and ψ_B are geographic longitudes of the CCD camera and the balloon respectively.

The Pythagorean triangle ACH shows the geometry between the all-sky camera (C) and the auroral section (A) viewed by the balloon-borne x-ray detectors. The vertex H is located at the Earth's centre. The azimuth (θ) measured from North over East is given by,

$$\alpha = 90^0 - \sin^{-1} \left\{ \frac{\sin (\lambda_B - \lambda_C)}{\left[1 - \cos^2 (\lambda_B - \lambda_C) \cos^2(\psi_B - \psi_C) \right]^2} \right\} \quad (2.5)$$

The elevation angle (ϵ) is given by,

$$\epsilon = \cos^{-1} \left(\frac{d^2 + r_E^2 - (r_E + h_A)^2}{2dr_E} \right) - 90^0 \quad (2.6)$$

where h_A is the altitude of the aurora and d is slant range from the camera site to the centre of the sampled auroral section given by via cosine rule of triangle ACH. CosCB is determined via cosine rule from spherical trigonometry (Thomas 1972, Velchors and Krickenberger 1957) here given by

$$cosCB = cos(\lambda_B - \lambda_C) \cdot cos\ (\Psi_C - \Psi_B) \qquad (2.7)$$

2.6 Fish Eye Projection of the Auroral Portion Sampled by the X-Ray Detector

Ideally, the imaging system should give an accurate scaled representation of the object. This is true if the image size projected by the lens is given by

$$Y = f \cdot tan\theta \qquad (2.8)$$

where Y is the distance of the image point from the optical axis, f is the focal length of the lens and θ is the angle between the object point and the optical axis.

The Soligor fisheye lens, such as one in the visual CCD camera, gives equidistant projection of the object onto the image plane (Smith, 1981). The relation between image and the object is now given by

$$Y = f\theta \qquad (2.9)$$

(Sidney 1979). This type of projection introduces a barrel type of distortion of the image. The magnification is non-linear and is governed by

$$Y = f \cdot \tan^{-1}(x/h) \qquad (2.10)$$

where x is the object size and h is the distance of the object from the lens.

The illumination area of the x-ray detectors at 100 km altitude is contained within a circle of 88 km in radius (see Figure 2.1b). The circle then contains the smaller elliptical and circular illumination areas from individual detectors. The distortion of a circular geometry along the axis of symmetry and along the diagonal is shown in Figure 2.7b.

2.7 The Bi-axial Compass Onboard the Payload

2.7.1 The Flux Gates Magnetic Sensors

The magnetic sensors of the compass are two solenoid flux-gates oriented 90° with respect to each other in the XY horizontal plane. Wound on plastic tubes, they are 5 cm long and have 0.5 cm diameter. Both flux-gates have a soft ferromagnetic core made out of μ-metal with magnetic susceptibility χ equal to 6×10^4 (Runcorn, 1960). Each flux-gate has two coils, the primary coil has 400 turns while the secondary has only 100 turns. The magnitude of the horizontal component of the Earth's magnetic field to be

measured forms a dot product between the unit vector oriented along the longitudinal axis of the flux-gates and the total horizontal magnetic component H_E and is given by

$$H(\Phi) = H_E \cos(\Phi) \qquad (2.11)$$

The magnitude of H_E is 0.12 Gauss at the Cold Lake latitude, and at the angle Φ, $H(\Phi)$ produces the initial magnetization of the core. The location of the initial magnetization on the hysteresis curve (point A; see Figure 2.8a) depends on the sign and the magnitude of $H(\Phi)$. The core is then driven toward saturation by a current passing through the primary coils of the flux-gates, this current increases with time according to

$$i(t) = \frac{V}{R} (1 - e^{-Rt/L}) \qquad (2.12)$$

where V is the applied voltage to the solenoid (12 volts), R is the DC resistance of the circuit and L is inductance of the primary coil. When magnetization of the core reaches a pre-set point P, the induced voltage across the 22 kΩ resistor of the secondary coil will have value proportional to dB_p/dt; this refers to the change of magnetic field B at the point P.

The function of the voltage comparator LM 311 (Figure 2.8b) is to disrupt the primary current at this point. The voltage corresponding to the position of point P on the hysteresis curve (Figure 2.8a) has been pre-set by the 5
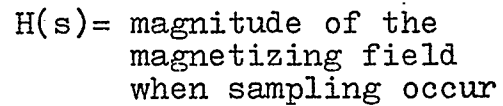
a)
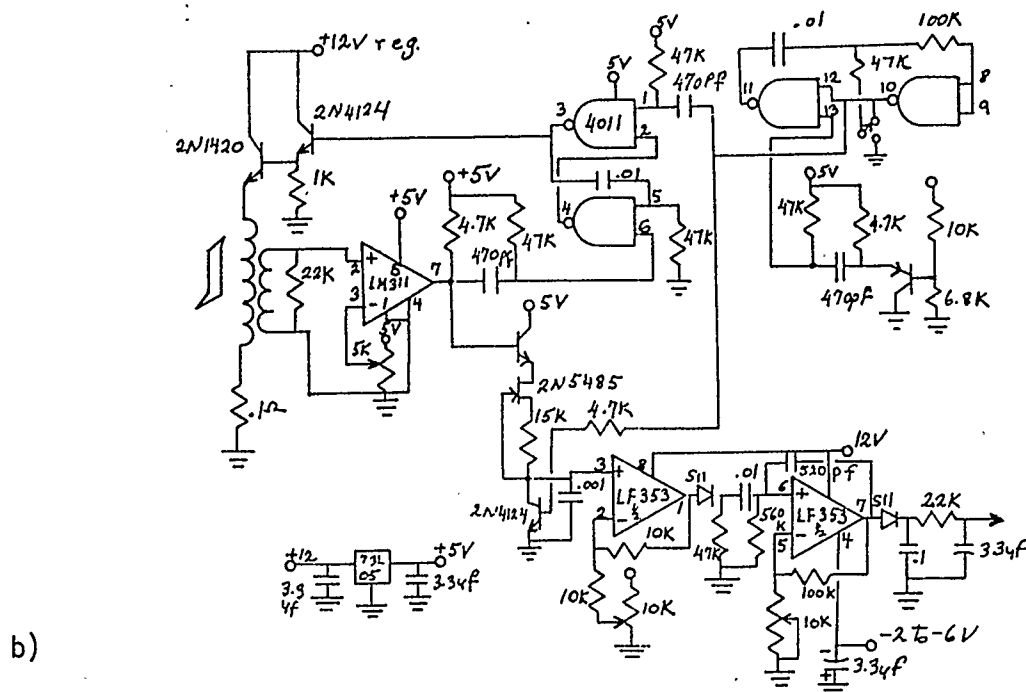
b)

Figure 2.8 Schematic diagrams showing:

   a) The hysteresis curve of the flux gate core. The points on the curve are discussed in the text.

   b) The electronic circuit of compass.

kΩ pot. The disruption of the primary current removes part of the external field H leaving only the H(Φ) component (corresponding to position A on the hysteresis curve). The cycle is then repeated.

2.7.2 The Analog Voltage Generation

Figure 2.8b is the schematic diagram of the flux-gate magnetometer and the associated control electronics. This system was built at the University of Calgary. The magnetometer output is generated by charging the 0.001 μ F capacitor with constant current. The length of time the capacitor is being charged is the same as the time needed to magnetize the core from the initial point A, set by H(Φ) to the point P on the hysteresis curve as seen in Figure 2.8a. The output low from the voltage comparator thus disrupts the charging at the same time as it disrupts the magnetizing current. The analog voltage output from the magnetometer is generated by tapping the voltage across the capacitor by the pass-through amplifier followed by low-pass filtering and further amplification.

2.7.3 The Output Data From the Compass

The digitized output voltage from the flux-gate of the compass is given by

$$D_1 = D_{01} - \left(\frac{D_{1MAX} - D_{1MIN}}{2} \cos\Phi \right) \qquad (2.13)$$

$$D_2 = D_{02} - \left(\frac{D_{2MAX} - D_{2MIN}}{2} \right) \sin \Phi \qquad (2.14)$$

where D_1 and D_2 are the observed digitized output voltages from flux-gates #1 and #2; D_{1MAX}, D_{2MAX} and D_{1MIN}, D_{2MIN} are the maximum and minimum outputs when the gates are pointing to the magnetic South and North respectively. D_{01} and D_{02} are the respective output voltages when the flux-gates are pointing to the magnetic East or West. The angle Φ (measured from magnetic North over East) is given by

$$\Phi = \tan^{-1} \left[\frac{(D_{02} - D_2)(D_{1MAX} - D_{1MIN})}{(D_{01} - D_1)(D_{2MAX} - D_{2MIN})} \right] \qquad (2.15)$$

The analog voltage output from the compass was found to be temperature dependent; the tests were carried out at the ground with the payload oriented perpendicular to H_{earth} in the horizontal plane. To obtain a wide range of temperatures, the measurements of the output voltage were made outside, commencing early in the morning and continuing till late afternoon. Using a least-squares fit, it was observed that this dependency can be approximated by the empirical relation

$$D_{01}(T) = 2.17T + 83.43$$
$$D_{02}(T) = 1.85T + 82.43 \qquad (2.16)$$

for the compass flown in September 1982 and by

$$D_{01} (T) = 1.68T + 95.00$$
$$D_{02} (T) = 1.98T + 88.00 \qquad\qquad (2.17)$$

for the compass flown in October 1982. Here D_{01} (T) and D_{02} (T) are now the digitized and temperature dependent analog voltage outputs from the respective flux-gates of the compass when oriented at 90° with respect to the horizontal magnetic field and T is the temperature in degrees Celsius in the measured range of 5° to 19°. The magnitude of the intercept can be set by the 5 kΩ pot (see Figure 2.8b) which in turn sets the control voltage of the voltage comparator. Figure 2.9 shows the decrease of the output parameters such as D_{MAX}, D_0 (September 1982 only), and D_{MIN} during the September 1982(a) and October 1982(b) flights as transmitted down in the PCM bit stream housekeeping data. This decrease of the output voltage from the compass is due to the gradual temperature drop inside the payloads during the flight. Unfortunately, the output from one of the flux-gates (September 1982 flight) became locked at constant value (D = 192) when situated between 120° and 250° range and hence only one flux-gate was used to determine the orientation in this azimuth interval. It was also necessary to estimate the value D_0 which also can be used to calculate the angle in the absence of D_{MAX}. This was carried out by first observing when the output from
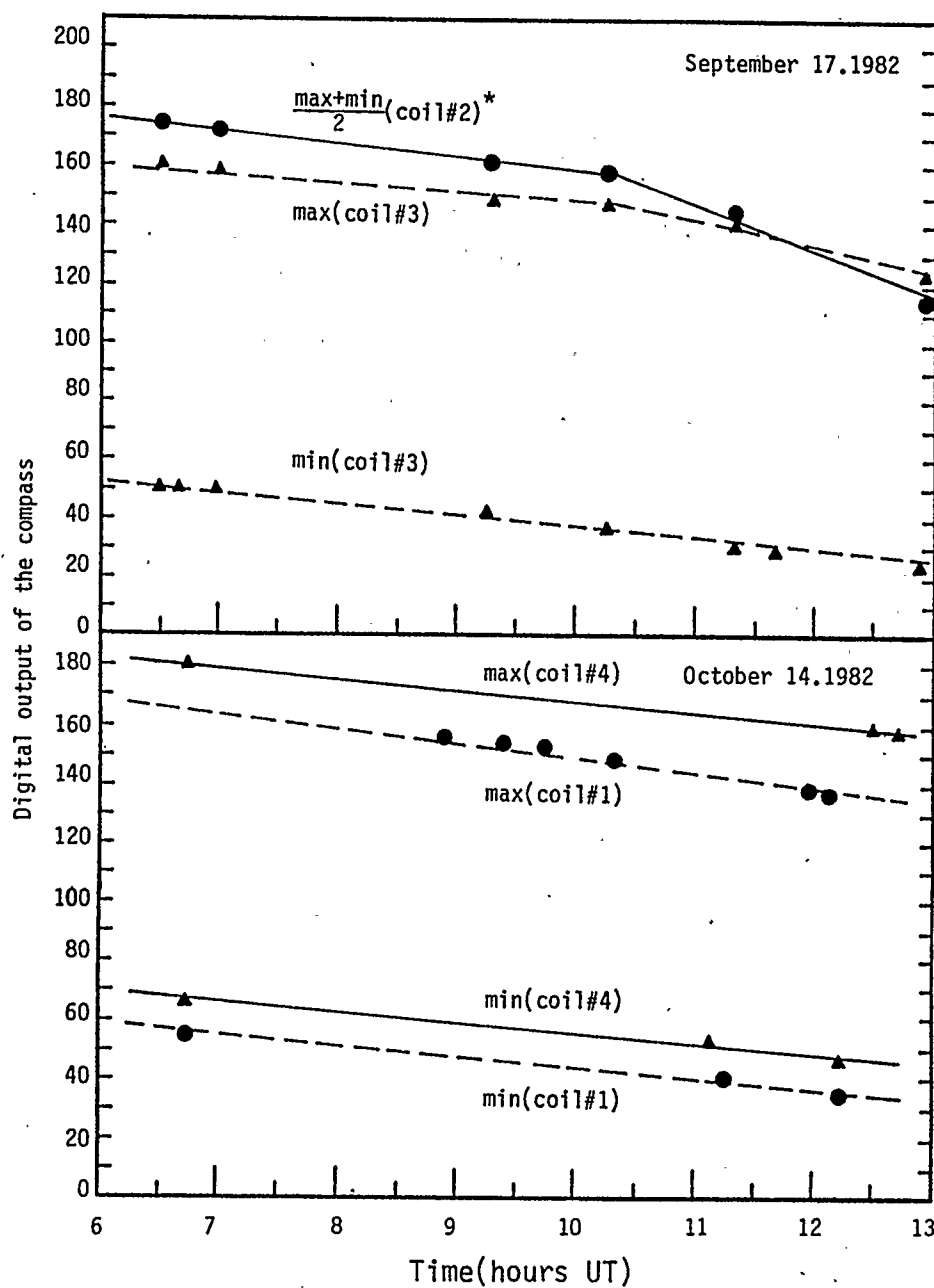
Figure 2.9 Plot showing the gradual decrease of the output voltage from the compass during the September 1982 and October 1982 balloon flights. The meanings of Dmax,Do and Dmin is discussed in the text.

the functioning flux-gate of the rotating payload was at D_{MAX} or D_{MIN} since at this point the output from the second gate is D_0. Since these parameters directly incorporated the changes due to the temperature drop during the flight, least square fitted, they were used to determine the orientation. It was possible to obtain these parameters because payloads showed complete rotations in addition to oscillations about some temporary azimuth. The periods of rotation varied between 2 sec (shortly after launch) to 30 minutes or more later at float altitudes. The azimuth was measured from magnetic North (taken as 0°) over East.

2.7.4 Uncertainty in the Orientation of the Payload

Errors in the estimation of the output parameters D_{MAX}, D_{MIN}, and D_0 as well as the presence of magnetic storms introduces uncertainty in the orientation determination of the payload. The values of D_{MAX} and D_{MIN} are relatively easy to estimate but the estimation of D_0 can be subject to errors in the range of ± 10 percent. This is due to rapid changes in the flux-gate output as it passes through the 90 and 270 degree azimuth.

The error in the orientation was therefore estimated by computer simulation. The output parameters (D_{MAX}, D_{MIN}, and D_0) of the flux-gates were disturbed by up to 20 percent. The effect of 500 and 800 Gamma magnetic storms which occurred during the September 17, 1982, and October 14, 1982, respectively, was also investigated. The result
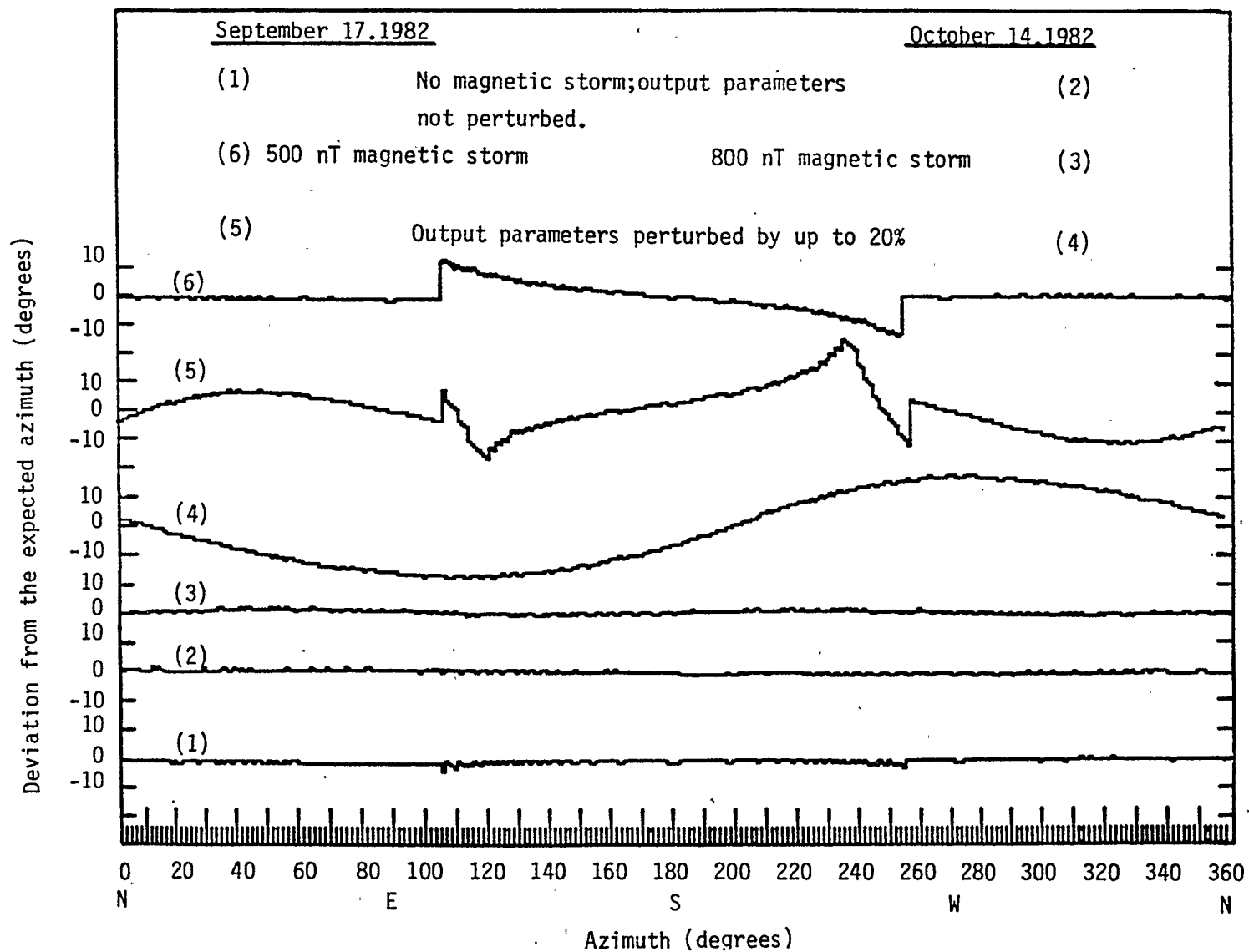
Figure 2.10 Possible magnitudes and causes of error in determining the payload orientation.

is shown in Figure 2.10. The horizontal axis represents the true angle, the vertical axis represents the deviation from the true angle. Plots (1) and (2) are the ideal outputs from the rotating compass. Plots (6) and (3) show the effect of the 500 and 800 Gamma magnetic storms on the output of the compass. The effect is dramatic between 120° and 250°, the region where only one flux is being used (September 1982). Plots (5) and (4) show that the uncertainty in the angular orientation of the payload can reach up to 20° when the output parameters are wrongly estimated by up to 20 percent.

2.8 Optical Instrumentation, Method

2.8.1 All-Sky CCD Camera

The spatial and temporal variations of the optical aurora during the CL-2 and CL-3 flights have been monitored by the ground-based CCD imaging system, operated entirely in the all-sky mode wherein the fisheye lens with 165° field of view performs the necessary light collection. Note that a narrow angle mode of operation is also available if required. A description of the system is given for the sake of completeness. For details, reference should be made to Babey et al. (1986) and Anger (1983).

Figure 2.11 is the schematic diagram of the camera showing the optical and the detection system. The 165° wide light beam entering the fisheye lens emerges as a narrow beam with divergence reduced to a half-angle of
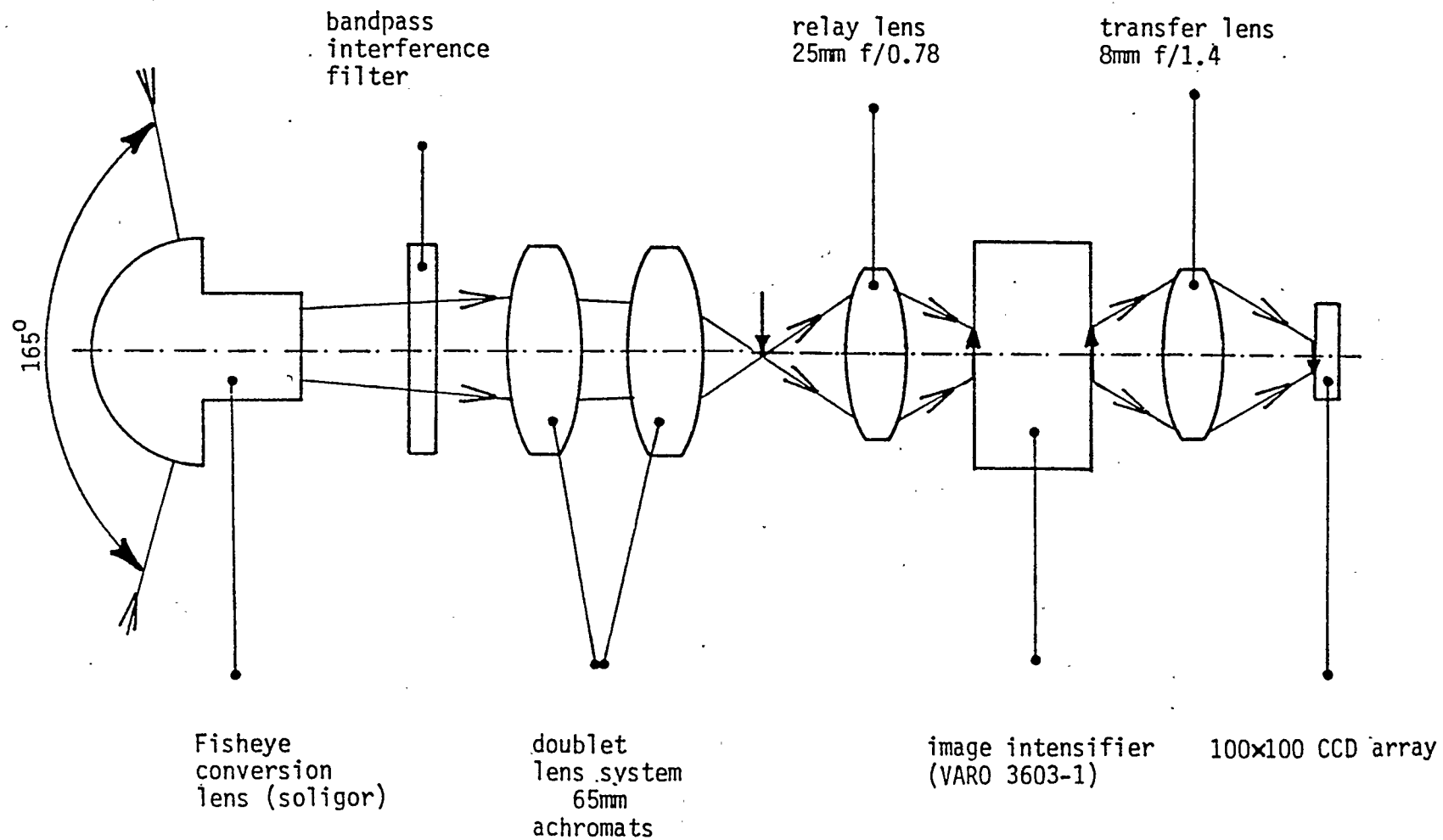
Figure 2.11 Schematic diagram of the All-Sky Camera.

10°. A zero or small divergence angle for the light beam emerging from the fisheye lens is desirable in this case, since increasing the angle of incidence of the beam on the filter from the normal direction will shift the wavelength of maximum transmittance. The small shift effect is handled here by using filters with broader bandwidth, specifically, the bandwidth of filters is 30A.

Four selectable filters are available with centre wavelengths at 6300A, 5577A, 3914A, and 4278A. The doublet lens behind the filters will generate the first image of the monochromatic sky; the image diameter here is 14 mm. The relay lens further reduces the monochromatic image of the sky to 6 mm in diameter on to the photocathode of the light intensifier, which is a single stage Varo 3603-1 25mm with a nominal luminous gain of 2.5×10^4.

The optical coupling between the image intensifier and the CCD array is through an f/1.48 converging lens, which projects a final 4 mm diameter image of the sky on the Charge Coupled Device (CCD) detector. The device is a 100 x 100 array of pixels, each pixel with dimensions of 18 μm. During actual data-taking periods, the CCD detector is cooled with crushed dry ice to reduce the thermal noise.

2.8.2 Optical Data Acquisition

The CCD all-sky camera was initially located at Primrose Lake 60 km away from the balloon launch Cold Lake. Primrose Lake was free of optical interference from

municipal lights and the availability of a trailer for housing the control and data acquisition microcomputer made this site a good choice. However, this led to an unnecessary increase in the zenith angle; furthermore the problems of communications and local weather difference also hampered the coordinated observations. Hence the shifting of the optical observation site to the balloon launch site was offered. The balloon launch site at Cold Lake was a small, private airport and permission had to be obtained from the airport management to switch off the runway lights during the collection of optical data, which was entirely in the wavelength 5577A O ^{1}S green line. The exposure time per frame was usually 6 seconds but, on several occasions during active auroras, the exposure time was decreased to 4 seconds. During the CL-2 flight (October 14, 1982) the optical data were collected over the time interval from 07:45 to 12:00 UT, the data gathering termination occurring at sunrise. During the CL-3 flight (October 2, 1983) the optical data are available from 05:30 UT to 10:30 UT. However, unfortunately, due to the loss of photographic film by the Kodak processing laboratory, only 30 minutes of data is now available to us. Because of the involvement of the main data processing computer with the Viking project the lost images will be retrieved at later times.

CHAPTER 3

OBSERVATIONS OF X-RAY AURORAS

3.1 Introduction

A program of simultaneous observations of visual and x-ray auroras using ground-based and balloon-borne instruments has been actively pursued at the University of Calgary over the past decade or more. One such attempt with considerable expectation in October 1977 eventually proved unsuccessful as the balloon drifted out of the useful visual range of the all-sky camera before reaching float altitude. The closed-circuit image intensifier TV system of the earlier period (collaborators: N.R. Parsons and F.T. Berkey) has in the past five years been replaced by the CCD all-sky camera (collaborators: C.D. Anger, L.L. Cogger and J.S. Murphree). A campaign in fall 1981 also turned out to be in vain. In general, various factors such as optimum geophysical activity, weather conditions, at ground level and at upper atmospheric levels, visibility, and dark nights all have to be simultaneously suitable for success; this is not easy, when compounded with limited financial resources.

In the fall of 1982 and 1983 three balloon flights were conducted. These occurred on:

September 17, 1982 (CL-1)

October 14, 1982 (CL-2)

TABLE 3.1

LIST OF BALLOON FLIGHTS FROM COLD LAKE IN 1982-1983.

BALLOON FLIGHT	LAUNCH DATE	LAUNCH TIME (UT) GEOGRAPHIC COORDINATES	CUT-DOWN TIME (UT) GEOGRAPHIC COORDINATES
CL-1	SEPT. 17. 1982	04:53:00	13:27:00
		$54.33^{O}N$ $110.05^{O}W$	165 miles SE of Cold Lake
CL-2	OCT. 14. 1982	06:42:00	12:40:00
		$54.33^{O}N$ $110.05^{O}W$	$53.12^{O}N$ $107.40^{O}W$
CL-3	OCT. 2. 1983	04:41:00	11:40:00
		$54.33^{O}N$ $110.05^{O}W$	$55.35^{O}N$ $103.60^{O}W$

Figure 3.1 Positions of the balloons during CL-2 (October 14.1982) and CL-3 (October 2.1983) flights.

October 1982
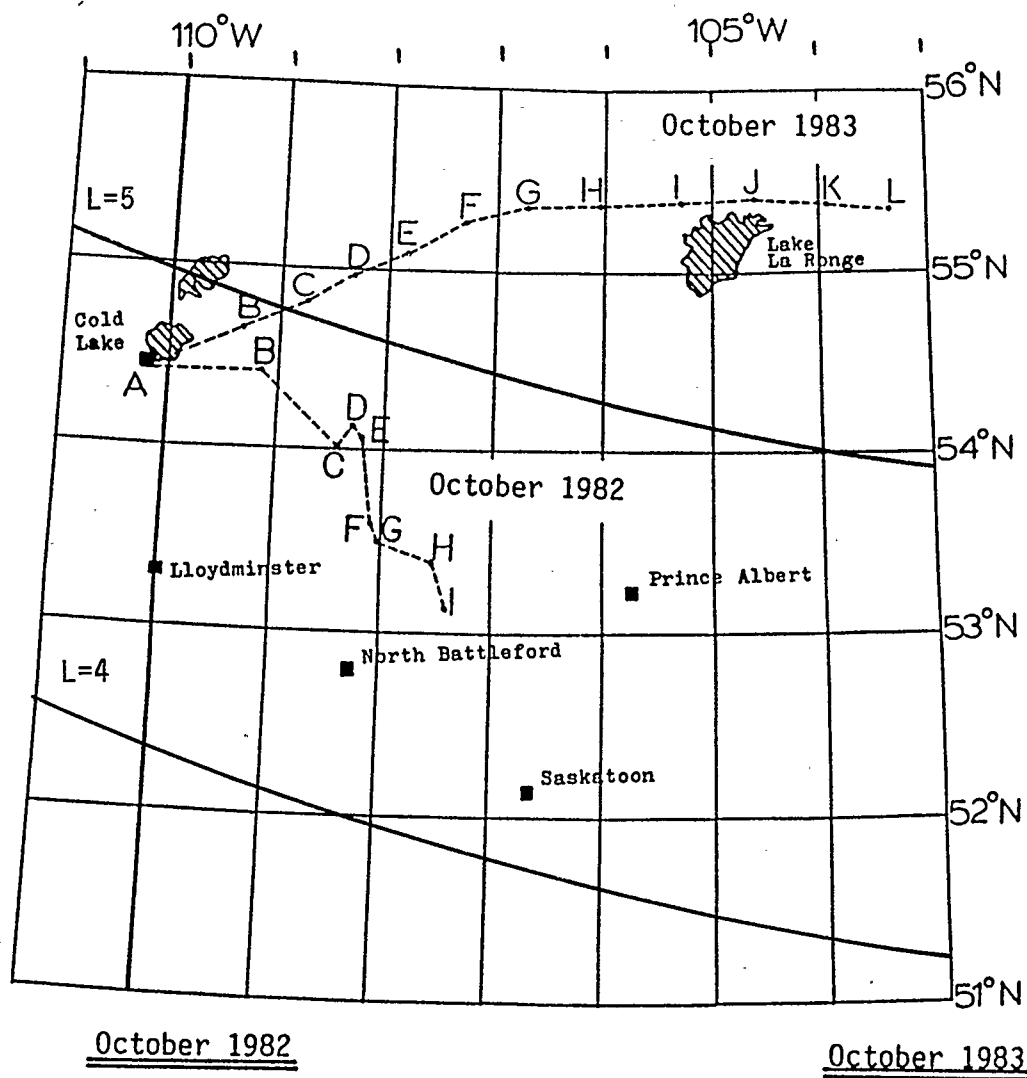
Location	Time(UT)
A	06:42
B	07:30
C	08:03
D	08:42
E	09:21
F	10:00
G	10:30
H	11:00
I	12:30

October 1983

Location	Time(UT)
A	04:41
B	07:00
C	07:30
D	08:00
E	08:30
F	09:00
G	09:30
H	10:00
I	10:30
J	11:00
K	11:30
L	12:00

and October 2, 1983 (CL-3)

The CL-2 and CL-3 flights also had successful ground support from the CCD all-sky imager group. All balloons were hand-launched from the small private airport in Cold Lake (geographical latitude 54.33°N, geographical longitude 110.2°W, L = 4.8). Over four hours of optical observations in the 5577A wavelength is available for the CL-2 and CL-3 flights. The flight paths of these flights were monitored by the 42nd Radar Squadron at Cold Lake. Unfortunately, this was not possible for the CL-1 flight; thus no exact position of the balloon was available for this. However, the cut-down telemetry system has been used to determine the range and approximate azimuth of the balloon. Figure 3.1 provides the flight paths of CL-2 and CL-3 balloons with checkpoints giving the exact position of the balloons. Based on the cut-down telemetry, the CL-1 balloon was drifting in the SE direction; the flight was terminated when the balloon was at a distance of 165 nautical miles from the launch site. Table 3.1 gives the dates, launch and cut-down coordinates of the flights during the 1982-83 Cold Lake balloon campaigns. The following sections give the results of the x-ray measurements obtained during these three flights.

3.2 Format of X-Ray Data Presentation

The observed x-ray profiles from the CL-1, CL-2, and CL-3 (see Chapter 5) balloon flights are presented mainly as

semi-log plots in Figures 3.5, 3.6, 3.18, and 3.19; some examples of plots in linear scale are also provided in Figure 3.3 and 3.17.

The semi-log plots allow presentation of a large volume of x-ray data (mostly three detectors per flight) in a relatively compact form since peaks get reduced in height thus enabling suitable stacking. The semi-log plots are one minute averaged. The linear plots refer to smoothed data, having been subjected to the moving average technique. Both averaging and smoothing have been performed on the basic six second resolution x-ray data files.

The spectral plots shown (CL-1 and CL-2 flights) have been averaged over one minute; this smooths out some of the fluctuations while still retaining the trend. The main objective here is to focus attention on the systematically observed spectral variation, especially the shape, during the main x-ray events. Since we have concentrated our efforts in the following chapters mainly on the CL-2 observations, the spectra from this flight are analyzed in great detail.

Note that the x-ray data in the energy channels forming the spectra have been corrected for the detector efficiency as a function of energy and opening cone or the solid angle of acceptance. The efficiency values are shown in Figure 2.5, Chapter 2. The differential x-ray counts have also been corrected for the dead-time of the PM tubes according to equation 2.4, Chapter 2 and the background.

3.3 X-Ray Observations During CL-2 Balloon Flight

3.3.1 Overview of Flight, October 14, 1982

The balloon was launched on October 14, 1982, at 06:42 UT (00:42 LT). An early launch, so as to reach floating altitude before midnight, was not permitted at this time due to the scheduled flying maneuvers of the Canadian Air Force. The drift path of the balloon was monitored by the radar stations of Canadian Air Force throughout the whole flight. Shortly after launch the balloon drifted steadily in the SE direction as shown in Figure 3.1. The altitude of 100 000 feet was reached at 08:15 UT, while the float altitude of 109 000 feet as per radar information was reached at 08:42 UT. The flight termination occurred at 12:45 UT shortly after local sunrise.

The compass onboard the payload reveals that the orientation of the x-ray package was quite steady throughout the flight as shown in Figure 3.2. The plot here refers to the orientation of detector #4; the azimuth of 0 deg. corresponds to magnetic North. The azimuth of the detector #2 is that of the detector #4 but shifted by 120° in the anti-clockwise direction.

The payload experienced some rotation after 11:54 UT (Figure 3.2); in general, note that detector #4 was oriented mostly in the NW-N direction; thus that of detector #2 was in the S-SW direction.
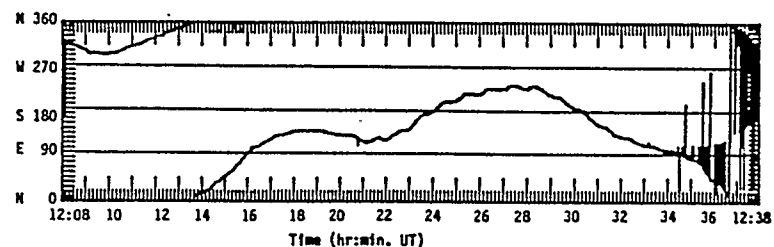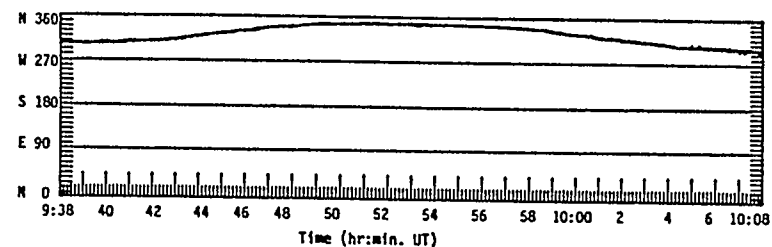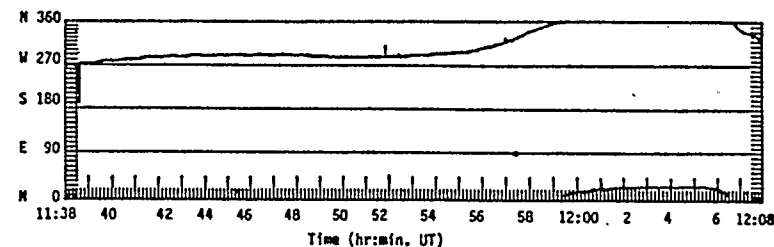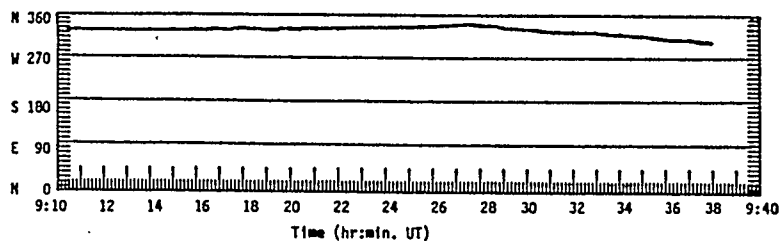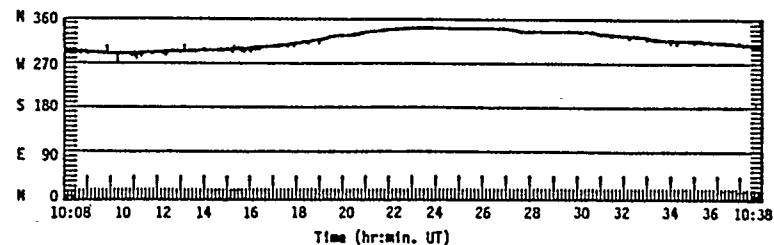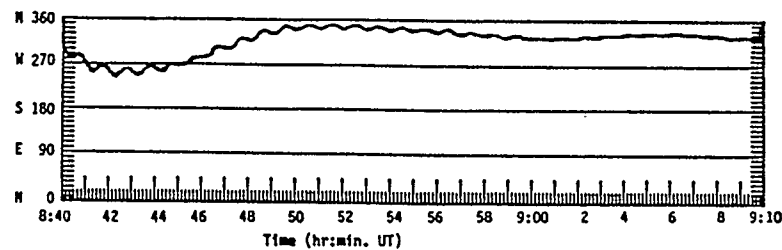
Figure 3.2 Azimuthal orientation of the inclined detector #4 during the major X-ray
events of CL-2 balloon flight.The inclined detector #2 is lagging detector #4
by 120 degrees (see Figure 2.1 for relative orientation of directional detectors)

Visual auroral activity onset was observed at 03:00 UT (09:00 LT); it continued varying in intensity till the morning hours after which the sunrise obscured any further observations. The visual auroral activity during this flight is presented in greater detail in Chapter 5.

3.3.2 X-Ray Detectors of the CL-2 Flight, October 14, 1982

During the CL-2 balloon flight, the x-ray data have been collected by only three detectors, one of the inclined detectors (detector #3) having failed shortly after launch. Unfortunately, the first three lowest energy channels of the inclined detector #4 (20-40 keV, 40-60 keV, and 60-80 keV) also had some problems. The counting rates in the 60-80 keV channel was at an anomalously high level and the other two lower energy channels registered identical counting rates. The data could be salvaged somewhat; this is discussed later on. The data from the 40-60 keV channel fits well with the exponential spectrum. This demonstrates that the 20-40 keV channel is the one that is malfunctioning. Bad soldering at the input pins of the digital counters is suspected to be the cause of the problem. Division of the count rate in the 60-80 keV energy channel of detector #4 by a factor of 2.8 has provided a solution. This factor is based on the relative magnitudes of the count rates observed in the 60-80 keV energy channels of all the three detectors during the Pfotzer maximum. This on occasions has turned out to be a satisfactory procedure since the data could be fitted with

an exponential spectrum. Nevertheless, the data from detector #4 are utilized mainly for comparison purposes.

3.3.3 Motion of Electrojet and Location of Observatory

The relative position of the electrojet and its motion with respect to the location of the magnetic observatory has been dealt with earlier (Varga, 1982). Here we deal with it briefly for the sake of completeness. The sign and the magnitude of the Z and H components at the observatory provide the necessary information for this.

If the electrojet is to the south of the station, the sign of the Z component will be positive (+), and hence above the base line. As the electrojet begins to move Northward toward the magnetic station, the Z component perturbation will decrease. At zenith, the Z component perturbation will be zero and becomes negative (-) as the electrojet moves to the north of the station.

The H component perturbation will have a negative sign for the westward, and positive for the eastward electrojet. If the intensity of the electrojet stays the same during the motion from the South to the North, the magnitude of the H component will be maximum when the electrojet is at the zenith of the station; the magnitude decreases as the electrojet moves either N or S of the station.

3.3.4 X-Ray Activity During Interval 08:10-08:50 UT

Figure 3.4 indicates a magnetically active period from 7 a.m. However, the balloon reached floating altitude only at 08:10 UT; during the interval under study, the AE index registered a value ≥ 500 nT. Figure 3.3a, b shows the H and Z components for a number of magnetic observations, for the interval 08:13 UT, October 14, 1982. The magnetic coordinates of the stations are given in Table 3.1. BL refers to the base level. From this figure, it can be seen that most of the magnetic storm activity at this time was concentrated well to the East of Cold Lake as the Leirvorgur magnetic observatory experiences bay activity of 600nT. The nagative value of Z component at Leirvorgur indicates that the main portion of the electrojet is situated to the south of the station.

The profiles of the x-ray count rates of three channels of detector #1 during this flight are shown in Figures 3.4. Similarly, Figures 3.5 and 3.6 show the differential x-ray activity for the detectors #1, #2, and #4 in the eight energy channels indicated. From 08:15UT (the balloon was already at float altitude) to 08:30 UT no significant x-ray activity is seen above the background level. Only a small increase is observed after 08:30 UT in all the energy channels; this is coincident with the observed south-westward shift of the magnetic bay activity seen from Figure 3.3a, b. At the Leirvorgur station, the increase in

TABLE 3.2

LIST OF MAGNETIC OBSERVATORIES USED IN CONNECTION WITH COLD LAKE FLIGHTS.

MAGNETIC OBSERVATORY	GEOMAGNETIC COORDINATES		GEOGRAPHIC COORDINATES		MAGNETIC SHELL NUMBER
	LAT. (^{O}N)	LONG.(^{O}E)	LAT. (^{O}N)	LONG.(^{O}E)	(L)
LEIRVORGUR	70.22	71.04	64.18	338.30	6.3
NARSSARSSUAQ	71.21	36.79	61.20	314.16	7.4
GREAT WHALE RIVER	66.58	347.36	55.27	282.22	6.9
FORT CHURCHILL	68.70	322.77	58.80	265.90	8.5
YELLOWKNIFE	69.00	292.80	62.40	245.60	7.8
COLLEGE	64.63	256.52	64.87	212.17	5.0
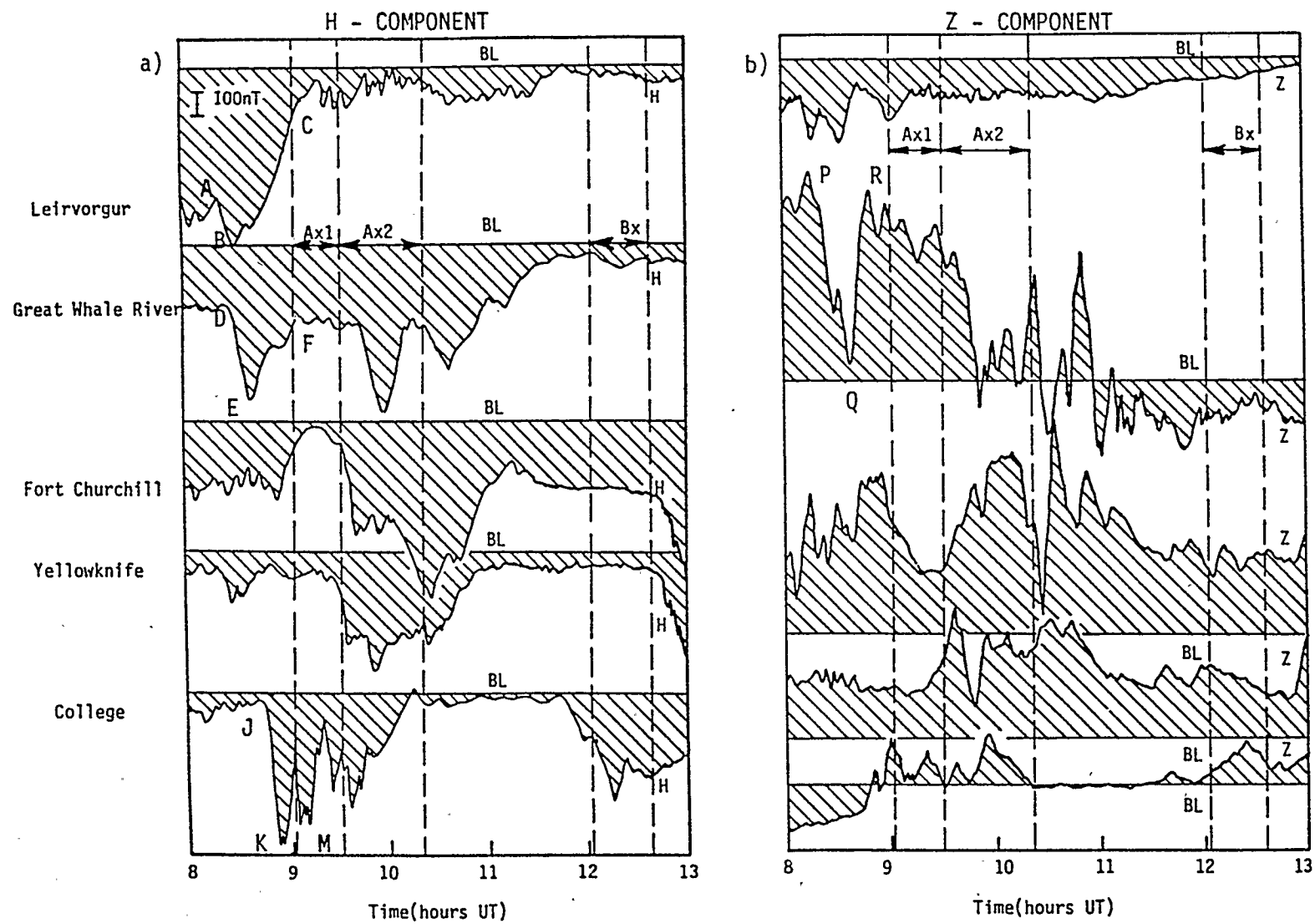
Figure 3.3 Auroral zone magnetic data from October 14. 1982.

the magnitude of negative value of the H component from A to B is seen after which the magnitude of the H component decreases from B to C. The Z component remains negative throughout.

At the Great Whale River Observatory, note that the H component which remained at a certain constant negative value suddenly starts to increase in magnitude (more negative), from D to E, followed by a decrease in magnitude (becoming less negative). Looking at Figure 3.3b, it can be seen that in the same period there is a decrease in the positive value of the Z component from P to Q and subsequent increase from Q to R. This increase in magnitude from D to E in the H component while at the same time there is a decrease from P to Q in the Z component indicates the net current movement toward the magnetic station (see for example Clark and Anger, 1967). Note that at College, the increase in the magnitude of the H component from J to K occurs later than at Great Whale River indicating south-westward movement of the electrojets.

3.3.5 X-Ray Activity During Interval 08:50-11:40 UT

In this time interval two major x-ray events, Ax1 and Ax2, have been observed in association with the magnetospheric substorm which began at 08:50 UT and decayed at 11:40 UT (Figures 3.4, top). These x-ray events are marked in Figure 3.4 by dotted lines. First, a sudden intensification of magnetospheric activity occurs at 08:50
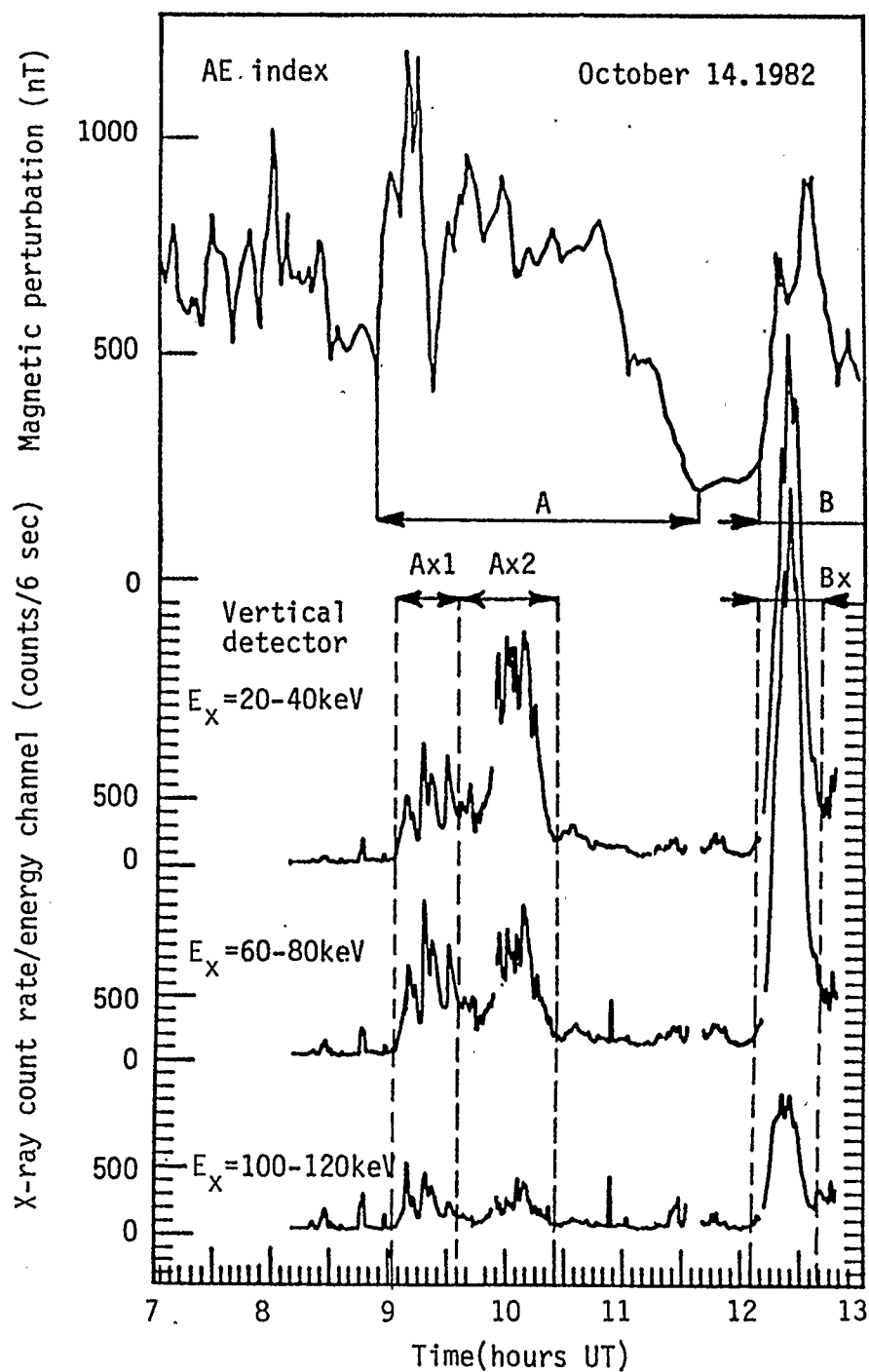
Figure 3.4 Observed AE index (top) and X-ray activity profiles during the CL-2 balloon flight.
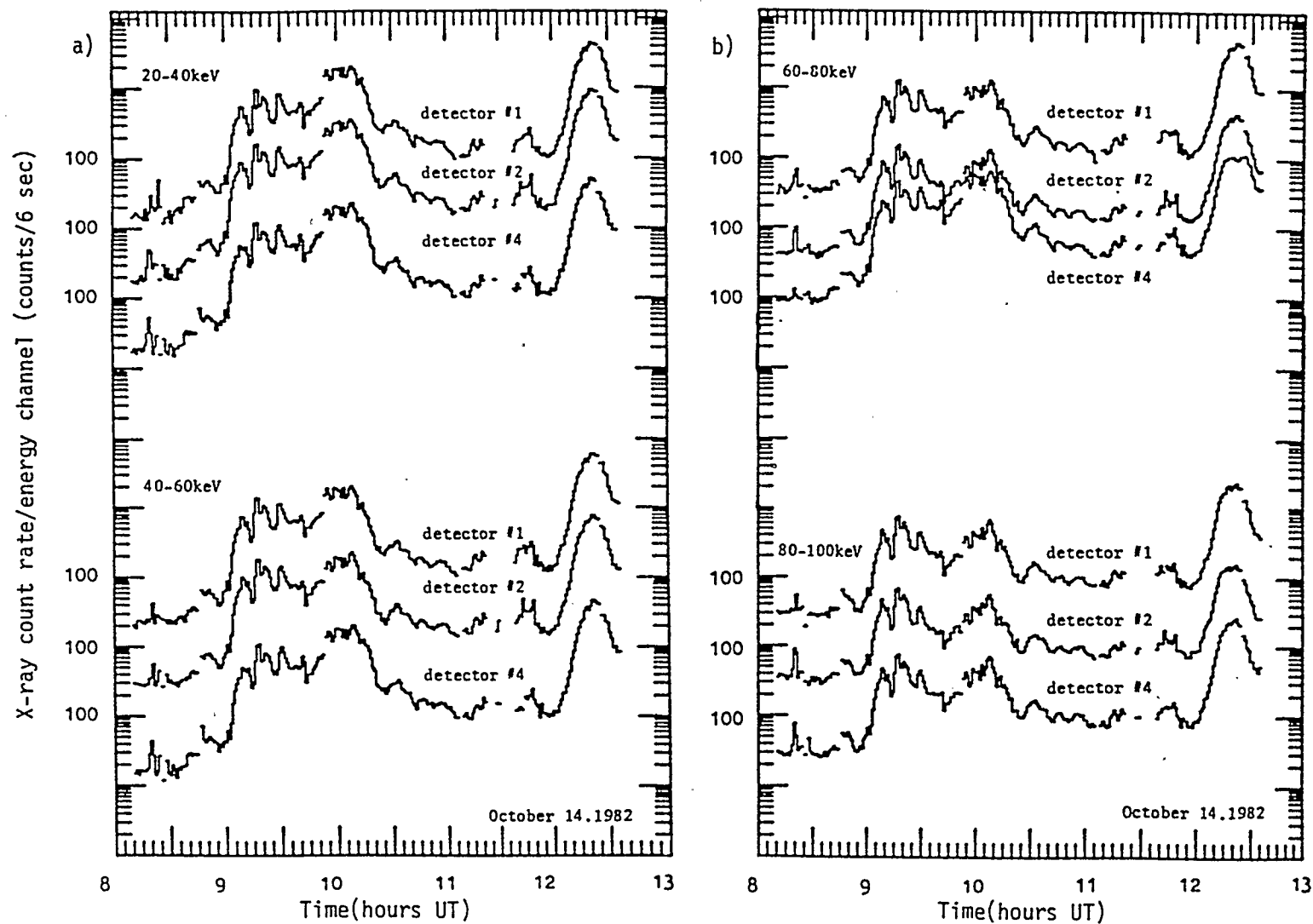
Figure 3.5 Observed differential X-ray activity over the energy region of 20keV-100keV by the vertical(detector #1) and the two functioning inclined detectors.
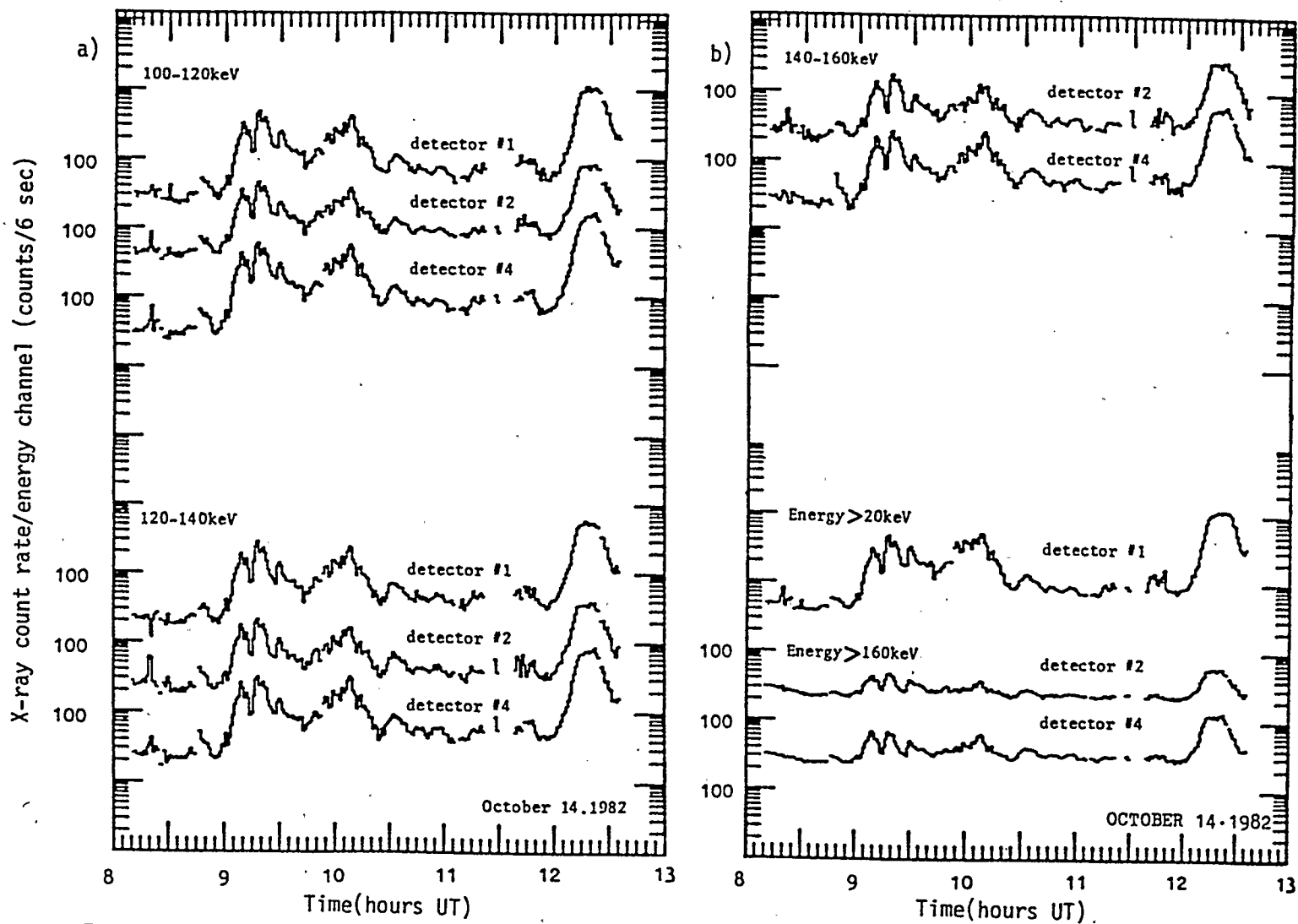
Figure 3.6 Observed differential X-ray activity over the energy region of 100keV-160keV.The integral count rate profiles over E_x>20keV and E_x>160keV are shown in panel (b).

UT seen as a sharp peak in the AE index. At this time the magnetic activity appears in the form of sharp spikes (identifiable at M in Figure 3.3) seen by the magnetic station College (L = 5) located west of the balloon. The electrojet activity is concentrated at L = 5; thus we see why Yellowknife (L=8) and Churchill (L=8.5) magnetic stations do not observe much evidence of the presence of the electrojet at this time.

The onset of the first x-ray event Ax1 occurs at 09:02 UT as indicated by the dotted line in Figure 3.3a; this onset coincides with the intensification of the second magnetic bay at College (see Point M in Figure 3.3a). As Figures 3.5 and 3.6 show, the x-ray activity appears simultaneously in all the three detectors and all the energy channels. Figure 3.4 shows that this event consists of three smaller impulsive events, each of 10 minutes duration. The temporal variation of the Ax1 event resembles the impulsive characteristic x-ray events which are generally observed in the midnight sector (22:00-02:00 LMT) as discussed in Chapter 1. This sporadic intensity variation may not, however, be due to the temporal variations of the precipitating high energy electrons; spatial movement of the x-ray source could also produce the observed impulsive nature of this event. This topic is further discussed in Chapter 5.

The onset of event Ax2 occurs at 09:35 UT and identified by the dotted line in Figure 3.4. Again, it

coincides with the magnetic bay intensifications at College, Yellowknife, and Fort Churchill (Figure 3.3a). The following points can be made about Figure 3.4. This event is much softer than the previous one as is evident from a comparison of the relative x-ray intensifications in the low (20-40 keV), medium (60 -80 keV) and high energy (100-120 keV) channels. Compared to Ax1, the event Ax2 is less structured, but with a few distinct spikes superimposed over the broad base. After 10:10 UT this event decays fast and by 10:25 UT the x-ray count rate, for example in the 20-40 keV regions, has dropped by a factor of 10. Although still significantly above the background rate, the x-ray activity remains low till 12:05 UT at which time the onset of event Bx is observed. The onset and the decay of Ax2 coincide with those of the magnetic bay activity at College as seen from Figure 3.3. Apparently when the balloon and the magnetic station are located at comparable values of L, the association between the magnetic bay and x-ray activity seems to be dominant. Note that College is 45° west of Cold Lake; their L values are 5.0 and 4.8 respectively.

Again Figures 3.3a, b show that during the interval 10:20 UT-11:40 UT the magnetic bay activity at College is low and another enhancement of magnetic storm activity is observed only after 11:40 UT. However, during that same time period, the stations Yellowknife (L=7.8), Fort Churchill (L=8.0), and Great Whale River (L=6.8) experience the magnetic storm activity indicating the Northward motion

of the electrojet after 10:20 UT. The Northward motion of the electrojet activity followed by the gradual decay can be associated with the recovery phase of the substorm (Kisabeth and Rostoker, 1971). This motion of the bay activity could be responsible for the observed decay of Ax2 event at 10:25 UT, in association with the onset of the substorm's recovery phase (estimated at 10:10 UT). The motion of the x-ray source away from the detectors at 10:25 UT is discussed later in Chapter 5.

3.3.6 X-Ray Activity During Interval 12:00-12:40 UT

Impulsive intensification of AE index and x-ray activity are observed shortly after 12:00 UT (Figure 3.4) in connection with the onset of a second substorm during the CL-2 balloon flight. The onset in x-ray activity can be placed at 12:05 UT and is observed simultaneously by all the three detectors #1, #2, and #4 over the whole range of energies sampled (Figures 3.5 and 3.6). The x-ray count rate peaks at 12:25 UT followed by a sharp drop of x-ray activity; within a 10 minute time interval the count rate drops to 20 percent of its peak value. Similarly, as in the case of the first two x-ray events, the observed x-ray activity in this time interval is coincident with the observed bay activity at College.

3.3.7 Spectra During Interval 08:10-11:40 UT

Figures 3.7a, b and 3.9a show the spectral plots in five minute time increments (solid lines) as well as spectra at some intermediate times (dotted lines) for the detector #1 (vertical). Samples of spectra seen by the inclined detector #2 are shown in Figures 3.8a and 3.9 b and those of inclined detector #4 in 3.8b.

The background spectrum (1) in Figure 3.7a, has been subtracted from the other observed spectra. The spectra 2, 3, and 4 prior to the onset (09:02 UT) of the intense x-ray activity do not show the clear-cut exponential characteristics that are typical of those seen at the increased x-ray count rate (See spectra 6-14 in Figure 3.7a, and 1-3 in Figure 3.7b). The points with x-ray energy Ex > 70 keV can be well-fitted by a single straight line, using a linear regression method. Note that the 30 keV and 50 keV points lie below this straight line indicating the effect of the atmospheric absorption. Some of the important characteristics of the spectrum can be qualitatively discussed in terms of the observed count rate ratios such as given in Equation 3.1; this procedure is often adopted.

$$\text{Log (R1)} = \text{Log} \frac{C(20 - 40)}{C(40 - 60)} = \text{Log } C(20-40) - \text{Log } C(40-60)$$

$$\text{Log (R2)} = \text{Log} \frac{C(40 - 60)}{C(60 - 80)} = \text{Log } C(40-60) - \text{Log } C(60-80)$$

$$\text{Log (R3)} = \text{Log} \frac{C(60 - 80)}{C(80 - 100)} \text{ and so on}$$

(3.1)

TABLE 3.3

SPECIFIC TIMES OF OBSERVATION

Spectrum number	Time(UT)	Spectrum number	Time(UT)
1	background	8	9:09
2	8:47	9	9:10
3	8:50	10	9:15
4	8:55	11	9:18
5	9:00	12	9:20
6	9:05	13	9:23
7	9:07	14	9:25

Numbers relate to the spectral plots in panel (a) of Figure 3.7 and coresponding observation during interval 08:47UT - 09:25UT + background.

TABLE 3.4

Spectrum number	Time(UT)	Spectrum number	Time(UT)
1	9:30	7	9:55
2	9:35	8	10:00
3	9:37	9	10:05
4	9:40	10	10:10
5	9:45	11	10:15
6	9:50	12	10:20
		13	10:25

Numbers relate to the spectral plots in panel (b) of Figure 3.7 and coresponding observation during interval 09:30UT - 10:25UT.
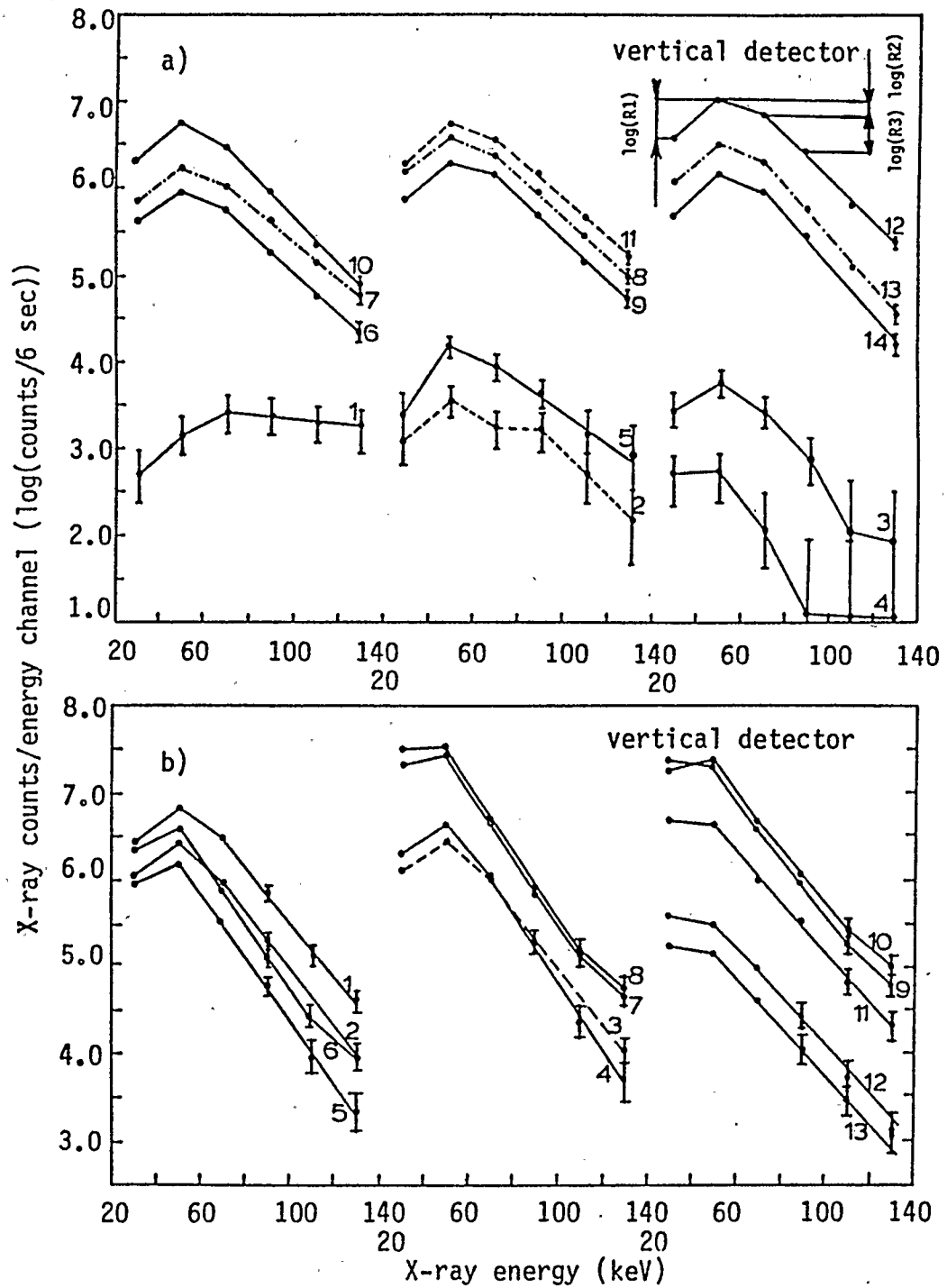
Figure 3.7 Observed X-ray spectra in the time interval 8:47UT-10:25UT during CL-2 balloon flight. See Tables 3.1 and 3.2 for specific times of observation.

where C(20-40) for example is the count rate in the 20-40 keV energy channel, duly corrected for efficiency of detector, background and the dead time of the PM tube. Figure 3.7a, b for example show that during most of Axl event the value of log(R1) is less than zero and log(R2) is less than log(R3). This is true for the vertical as well as the inclined detector #2 (see Figure 3.8a, spectral plots 1, 2, and 3). After 09:35 UT however, the shapes of the observed spectra begin to change.

First the count rate in the 40-60 keV energy channel begins to increase as shown by the increase of log(R2) in relation to log(R3) (see spectra 5-13 in Figure 3.7b). This is even more visible in case of inclined detector #2 (Figure 3.8a, spectra 4, 5, 6, and 7). We have given in Figure 3.8b the spectra for the inclined detector #4 but do not discuss the same for reasons discussed earlier. Such an increase of the count rate in the 40-60 keV energy window signals the appearance of a second, softer spectrum dumping softer x-rays into the low energy channels. At the same time (spectrum 4, Figure 3.8a) a break develops in the spectrum of detector #2. Appearance of a similar break (both in the 100-120 keV energy channel) is observed at 09:50 UT (spectrum 6, Figure 3.7b) in the case of the vertical detector. This is further discussed in connection with Figure 3.13 in Section 3.3.9. Breaks in the x-ray spectra at the balloon altitude are not unusual and have been reported previously (e.g. Pilkington, 1970 and Vij, 1973).
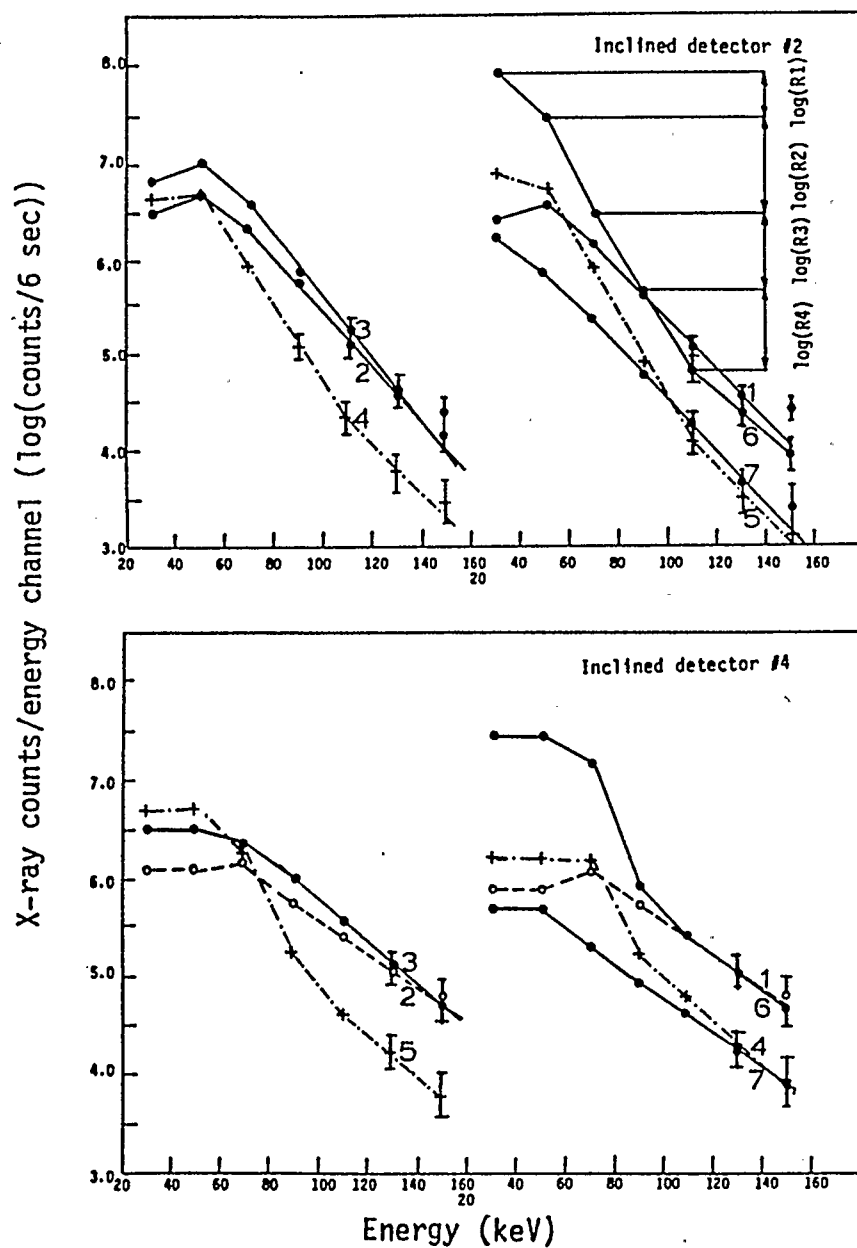
Figure 3.8 Observed X-ray spectra by the inclined detectors during CL-2 balloon flight. Distortions at the low energy region of detector #4 spectra are evident.

Figure 3.9 Observed X-ray spectra during CL-2 flight shortly after the main events.
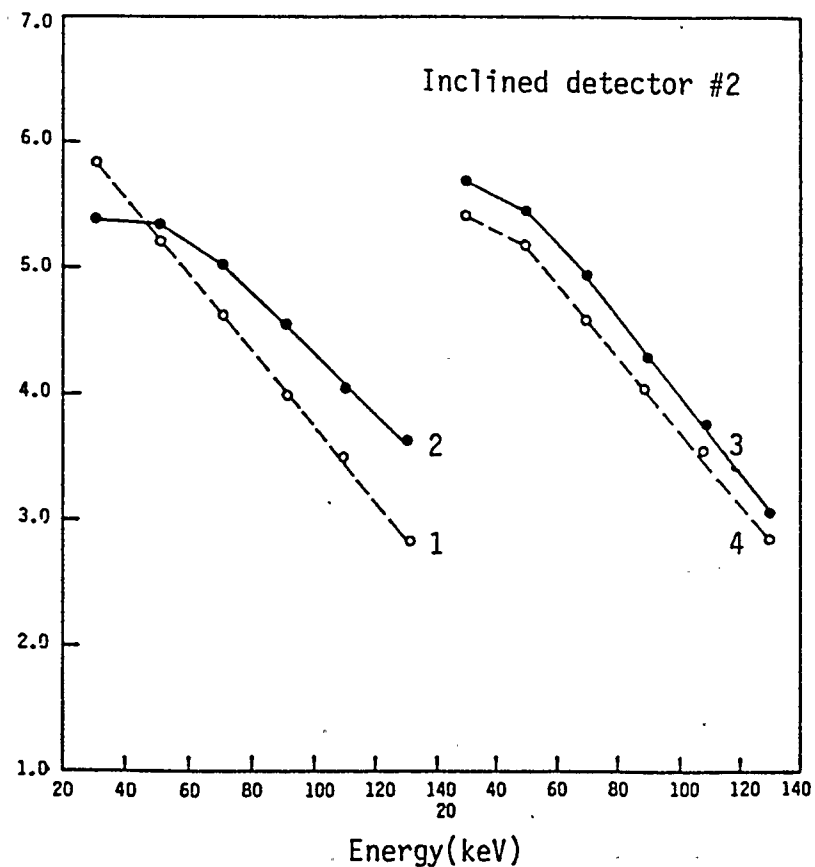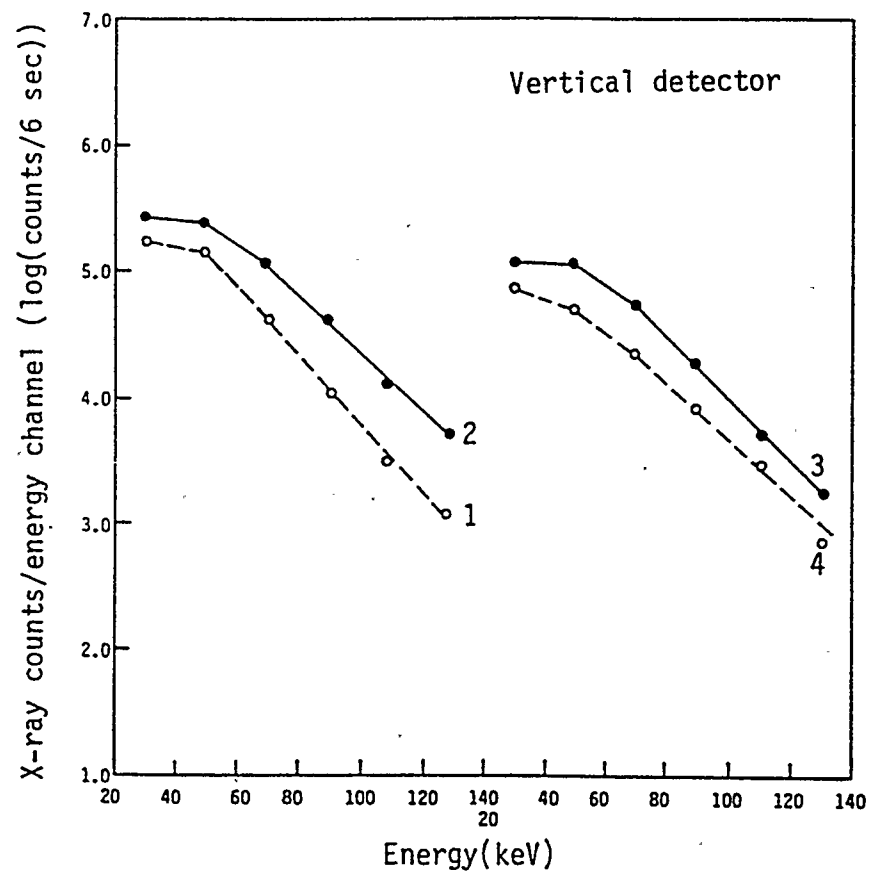
Spectrum number	Time(hr:min. UT)
1	10:25
2	10:35
3	10:45
4	10:50
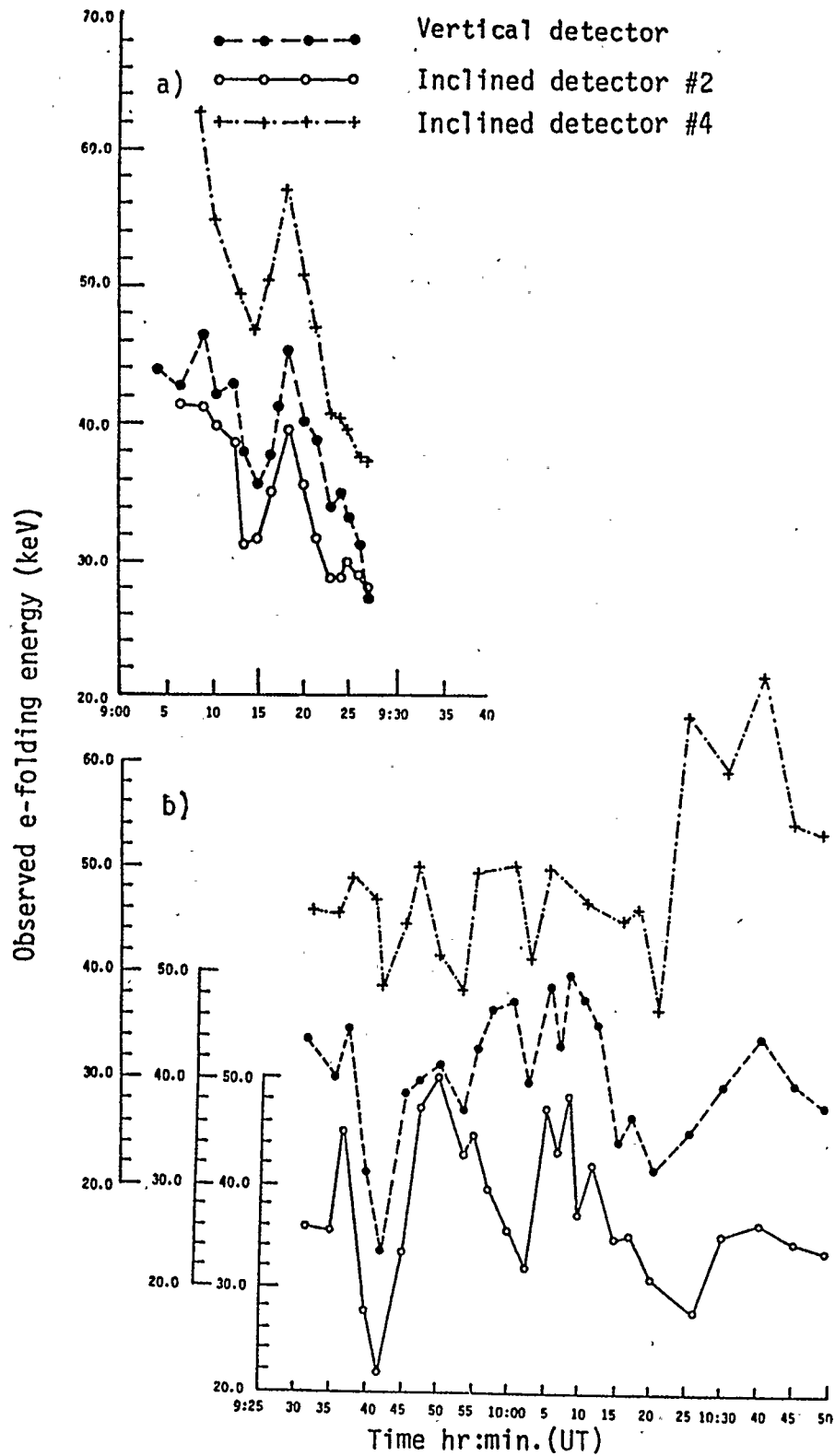
Figure 3.10 Summary of observed e-folding energy variation during and shortly after the first main X-ray events. In the case of a double spectrum, the e-folding energy value relates to the hard component only.

These breaks are caused by a softer spectrum being superimposed over the harder one. The softer spectrum component decays by 10:15 UT as noted from the disappearance of the break. After this time for $E_x > 70$ keV only single exponential spectra are observed in Figures 3.7b, 3.8a, b and 3.9a and b.

Another very important spectral feature observed in the case of both the vertical and the inclined detector #2, is the increase of ratio R1 above the value of unity after 09:40 UT (detector #2) and 09:55 UT (vertical detector). The implication of this aspect of the observations are discussed further in Chapter 5.

The observed variation in the e-folding energy during and after Ax1 and Ax2 events is summarized in Figure 3.10. In the case of a double spectrum, such as that during the time interval between 09:30 UT-10:15 UT, the e-folding energy values refer to the hard component only. As for the inclined detector #4, the data points in the 60-80 keV energy channel are not included in the linear regression method for calculation of the e-folding energy for reasons discussed earlier about problems in the channel. The results of Figure 3.10 are discussed further in Chapter 6.

3.3.8 Spectra in Interval 12:00-12:30 UT

The x-ray spectra generated by the Bx event are shown in Figure 3.11 (vertical detector) and 3.12a, b (inclined detectors #2 and #4). The observed e-folding energy values

Spectrum number	Observed Eo(keV)	Time(hr:min. UT)
1	66.7	12:00
2	57.1	12:05
3	44.3	12:10
4	40.0	12:15
5	33.3	12:20
6	33.3	12:25
7	33.3	12:30
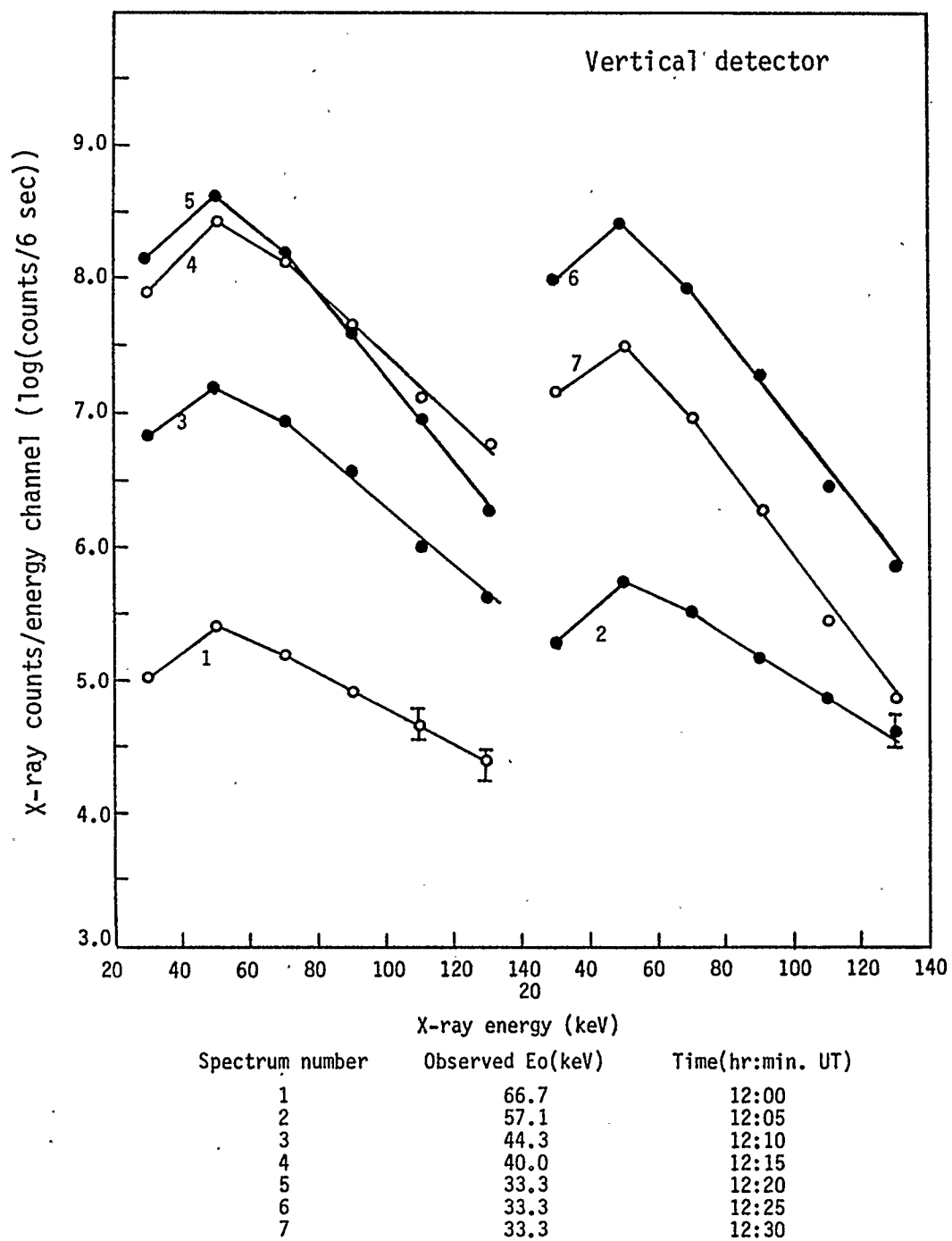
Figure 3.11 Examples of observed X-ray spectra during the Bx
event (time interval 12:05 - 12:40 UT). The
e-folding energy(E_0) observed are also given for
the seven spectra.
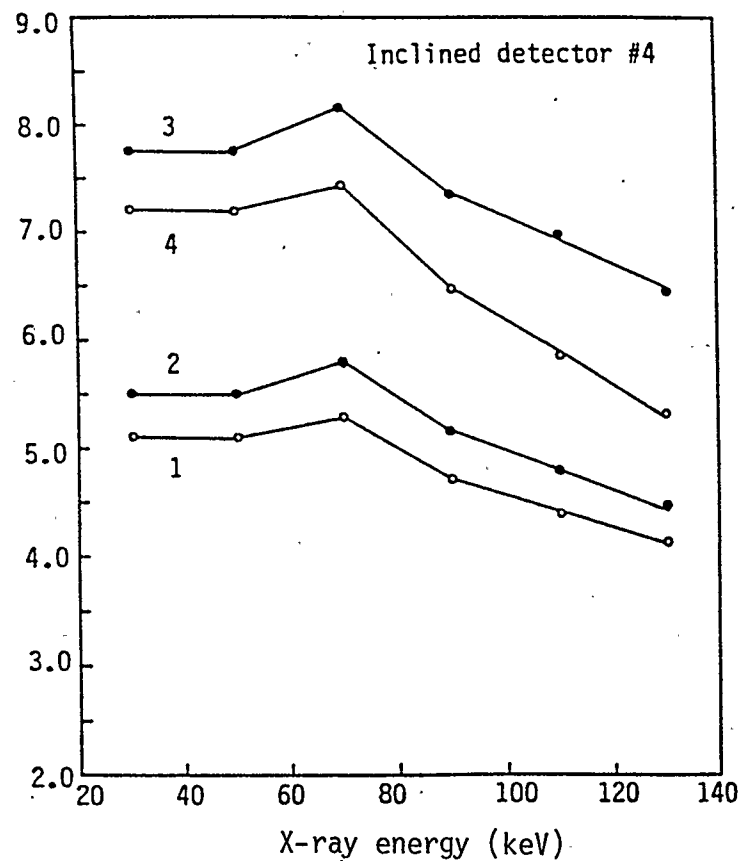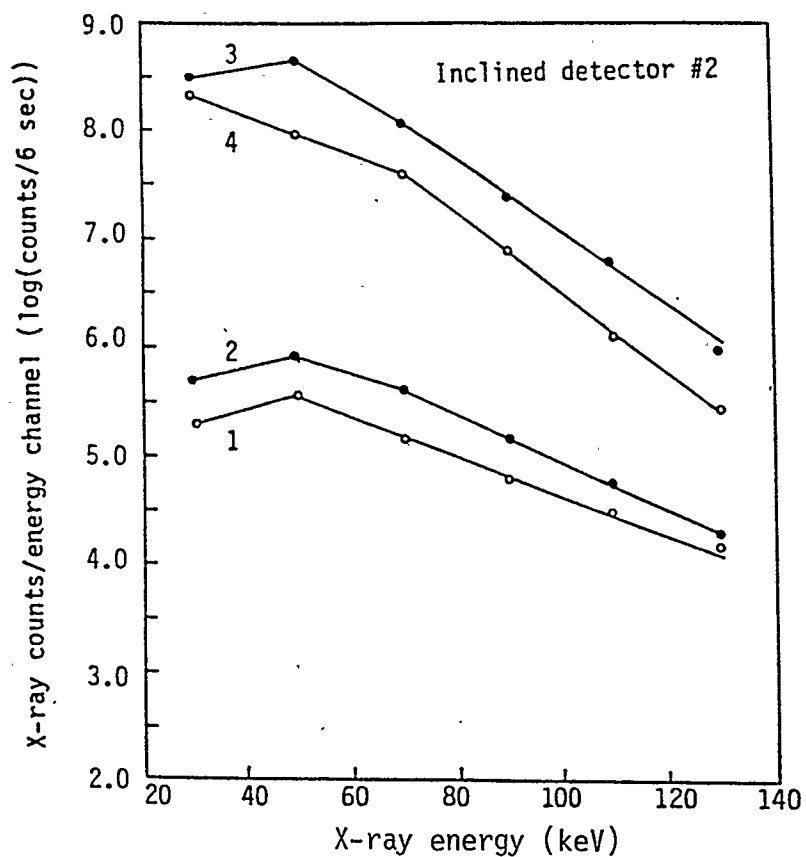
Spectrum number	Observed Eo(keV)	Observed Eo(keV)	Time(hr:min. UT)
1	57.1	74.1	12:00
2	50.0	60.6	12:05
3	30.7	41.7	12:15
4	26.7	30.7	12:30

Figure 3.12 Examples of observed X-ray spectra by the inclined detectors and the e-folding energy(E_0) during the Bx event.

during this x-ray event are also provided at the bottom of these same figures; they were obtained by fitting a single exponential function to the points $E_x > 70$ keV (detector #1 and #2) and to the points $E_x > 90$ keV (detector #4) and not less than 70 keV because of the problem in the 60-80 keV channel pointed out earlier. At first glance, it is evident that substantial spectral softening has occurred during the progress of the Bx event. At the event onset (12:05 UT) the observed values of e-folding energy were large, being 57.1 keV, 50.0 keV and 60.0 keV respectively for detectors #1, #2, and #4. Progressively, these decrease to 33.3 keV, 26.7 keV and 30.7 keV by 12:30 UT (Figures 3.11 and 3.12a,b). Figure 3.11 also shows that the softest spectrum (Eo = 33.3 keV) is observed at the maximum intensity of Bx event (12:20 UT) and no further change in Eo is observed during the event decay.

3.3.9 Soft Spectral Component and the Fast X-Ray Pulsations

Figure 3.13 shows the onset and the decay of fast x-ray pulsations observed during the Ax1 and Ax2 events. The plots are one-second-accumulated counts observed by the vertical and the two inclined detectors #2 and #4 respectively. Unfortunately, there is a data gap during 09:25 to 09:26 UT. Hence, it is estimated that x-ray pulsations appeared somewhere in the time interval between 09:23 UT and 09:26 UT (Figure 3.13a) and decayed between
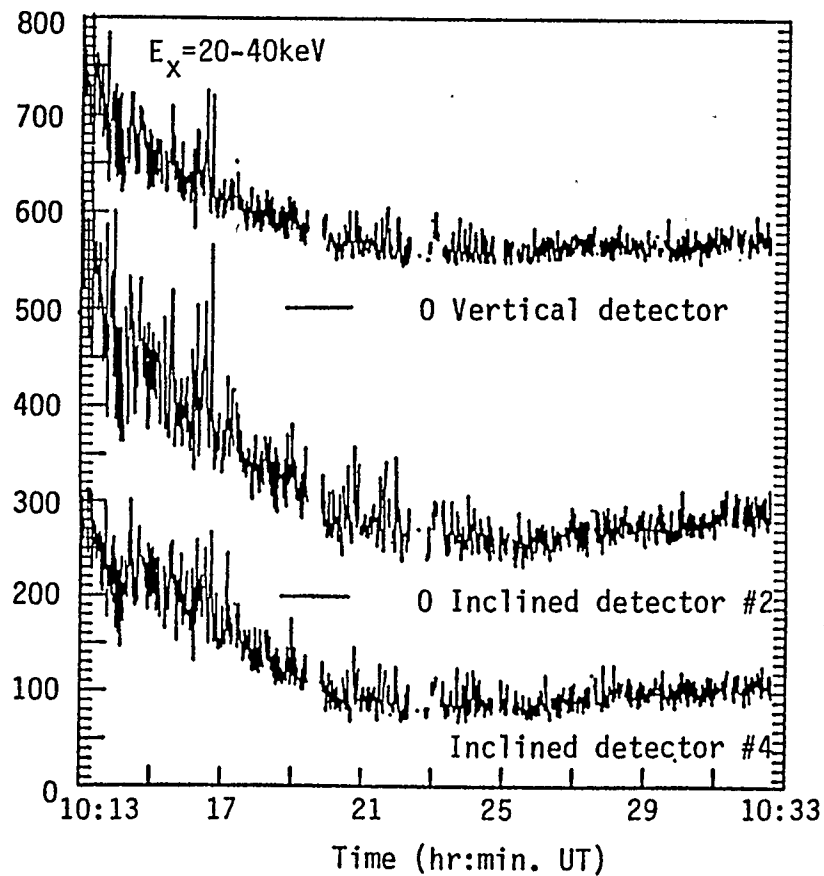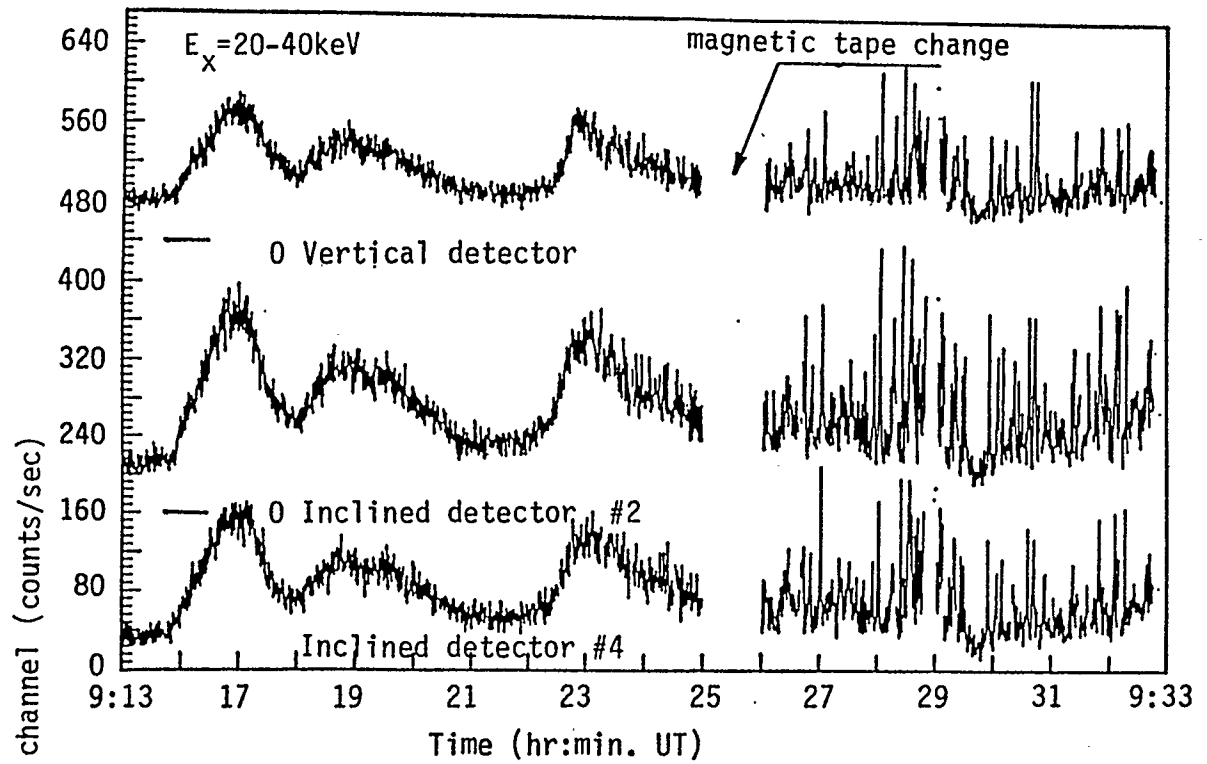
Figure 3.13 The onset(9:23-9:26) and the decay(10:21-10:25) of the fast pulsating X-ray activity.

10:21 UT and 10:25 UT (Figure 3.13b). We are not particularly concerned here with the details of the characteristics of the pulsations. We merely with to point out that their appearance coincides with the time after which the linear regression method, used to obtain the e-folding energy of the spectrum, begins to show persistently poorer fit (namely the sum of residues increases by a factor of 10 or more).

Such a deterioration of the goodness of fit is not purely coincidental but can be associated with the break in the spectrum observed in the 100-120 keV energy channel (see Figure 3.7b and 3.8a). The goodness of fit improves if the points are separated into two groups, specifically, points in the 70-120 keV energy region and the points in 100-160 keV energy region, the point in the 100-120 keV channel being common to both groups.

Treating the points in the high energy tail of the spectrum as the hard component of the observed spectrum, the activity of the soft component is calculated. The results are plotted in Figure 3.14a, b for the vertical and inclined detector #2 respectively. The calculated e-folding energy (E_O) values of the soft component are given in Table 3.5 for the specific times shown by the numbers 1 to 7. The e-folding energy variation of the hard component between 09:23-10:25 UT are shown in Figure 3.10b. The resulting e-folding energy of the soft component is less than 50 % of

TABLE 3.5

E-FOLDING ENERGY VALUES OF THE SOFT COMPONENT

SPECTRUM NUMBER	TIME (UT)	E-FOLDING ENERGY (keV)	
		VERTICAL DETECTOR	INCLINED DETECTOR #2
1	09:37	17.09	12.57
2	09:47	16.26	11.40
3	09:55	13.15	14.11
4	10:00	15.75	13.88
5	10:02	18.34	12.34
6	10:07	20.23	15.74
7	10:12	21.50	15.08

The spectrum numbers relate to the numbers shown in panels (a) and (b) of Figure 3.14.
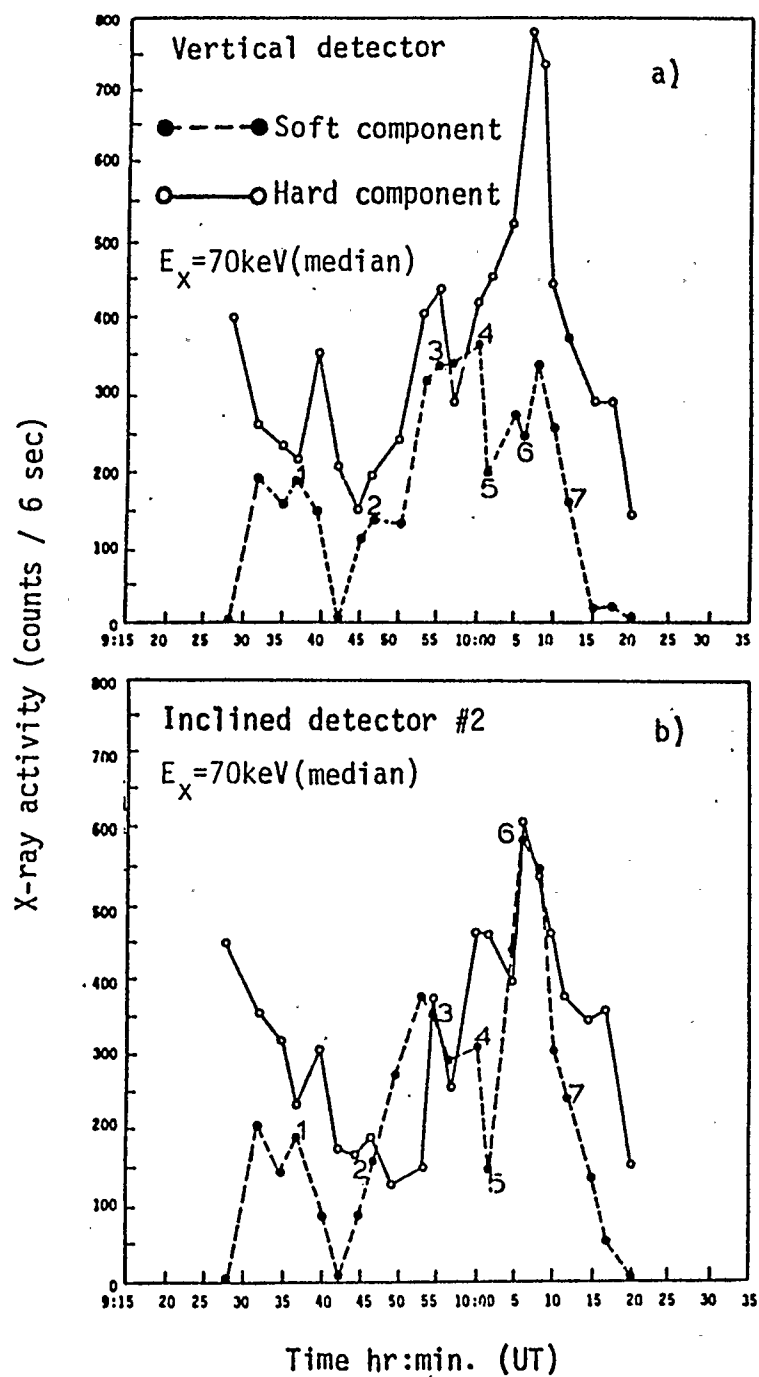
Figure 3.14 Calculated intensity variation of the soft and the hard
         X-ray component from the observed double spectrum.
         Examples of e-folding energy values of the soft component
         are given in Table 3.4.

the e-folding energy value of the harder spectrum; the inclined detector #2 sees generally a softer spectrum.

Evidently, the duration as well as the occurrence of maximum intensity of the soft component correlates with the duration and the maximum activity of the fast x-ray pulsations. It therefore seems reasonable to assume that the pulsating x-ray source is the observed soft component of the spectrum present during the interval between 09:23 UT-10:25UT. Note that the early x-ray auroral investigations have reported a pronounced coincidental spectral softening with the appearance of pulsating activity (Barcus and Rosenberg 1966).

3.4 CL-1 Balloon Flight

3.4.1 Flight Overview

The balloon was launched on September 17, 1982, at 04:53 UT. One hour after the launch at the altitude of 7700 feet the pressure transducers failed and thus after this altitude the means of monitoring the ascent was lost. Based on the average ascent velocity of 1300 feet min^{-1}, the estimated time of reaching the float altitude has been placed at 06:30UT. The only radar trace available at 08:42 UT gave float altitude of 105 000 feet. Visual auroral activity has been observed during most periods of this flight. Based on the flight log-book data, the visual auroral activity can be described with respect to launch
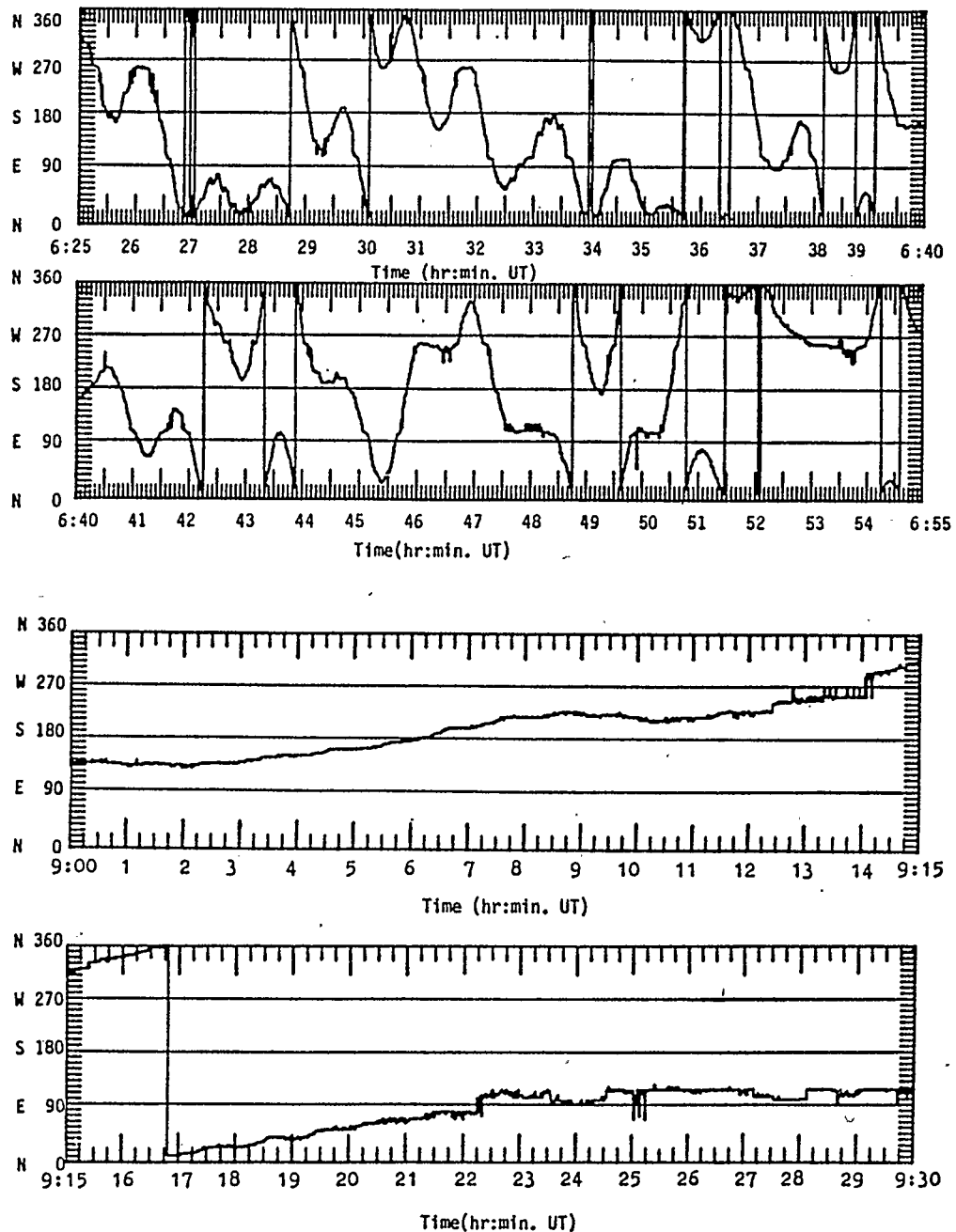
Figure 3.15 Samples of orientation of the inclined detector #4
during CL-1 flight. The orientation of the inclined detector
#3 is that of detector #4 plus 120 degrees. Between 06:25UT
and 06:55UT (panels (a),(b)) the payload executed several
rotations with periods varying between 90 seconds to 5 minutes.
During the main X-ray event (panels (c),(d)) the observed
rotation period was approximately 30 minutes.

site as follows:

05:55 UT-06:40 UT	diffuse aurora located to the North
08:25 UT	Green (5577A) discrete aurora observed to the West
09:15 UT	discrete aurora (green) with red lower border observed to the South of Cold Lake
09:21 UT	flickering aurora (green) to the south of Cold Lake
10:00 UT	faint discrete green auroral features to the South and East of Cold Lake
10:05-10:30 UT	faint discrete green auroras observed in all directions
11:43 UT	no visual auroras observed
12:30 UT	sunrise

Cut-down occurred at 13:27 UT where at this time (based on the cut-down transmitter) the balloon was located at a distance of 165 miles from Cold Lake in an azimuthal direction of 90 degrees.

3.4.2 X-Ray Detectors of the CL-1 Flight

Out of the four x-ray detectors, one of the inclined detectors (detector #4) failed completely. The vertical (#1) and the inclined #2 and #3 detectors however showed periods of spurious counts with no similarity from one

detector to another (see Figures 3.18 and 3.19). For example, during the interval of 06:25-06:55 UT (Figure 3.15a, b) the payload executed several rotations during which the inclined detector #3 registered an impulsive count rate peak. If this peak originated from some high intensity x-ray region scanned by detector #3, then this peak should also appear in the inclined detector #2 as the payload rotates. However, this was not the case, as seen in Figures 3.18 and 3.19. Similarly, detectors #1 and #2 observe activity during 07:00-08:30 UT not observed by detector #3. Since the payload has been rotating during this time as well (from compass data not shown here) it has to be concluded that these observed count rates were not genuine. The source of these spurious counts is not obvious, but the high voltage power supply of the PM tubes is suspected to be a possible cause. The inclined detector #3 is considered as providing the most reliable x-ray data. This is supported by the fact that the x-ray features (shaded) over interval 08:00-11:30 UT are seen to exhibit common features in all the three detectors and thus are considered to be more reliable.

3.4.3 Temporal Profile of the X-Ray Aurora During
Flight CL-1

The overall features of the observed x-ray activity during this flight are shown in Figures 3.17b, 3.18, and 3.19. Only the shaded portion of the x-ray profile is
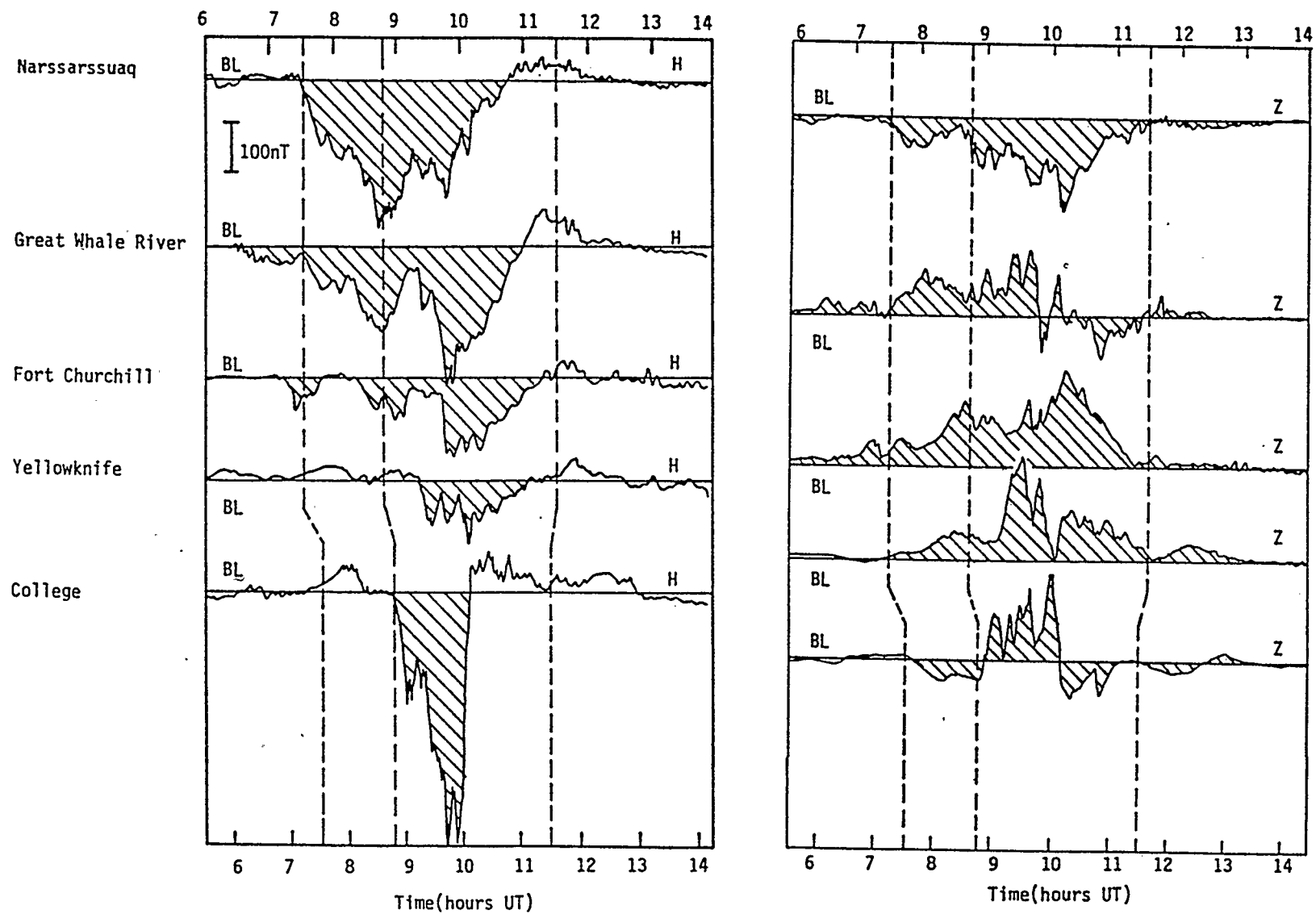
Figure 3.16 Auroral zone magnetic data from September 17. 1982.
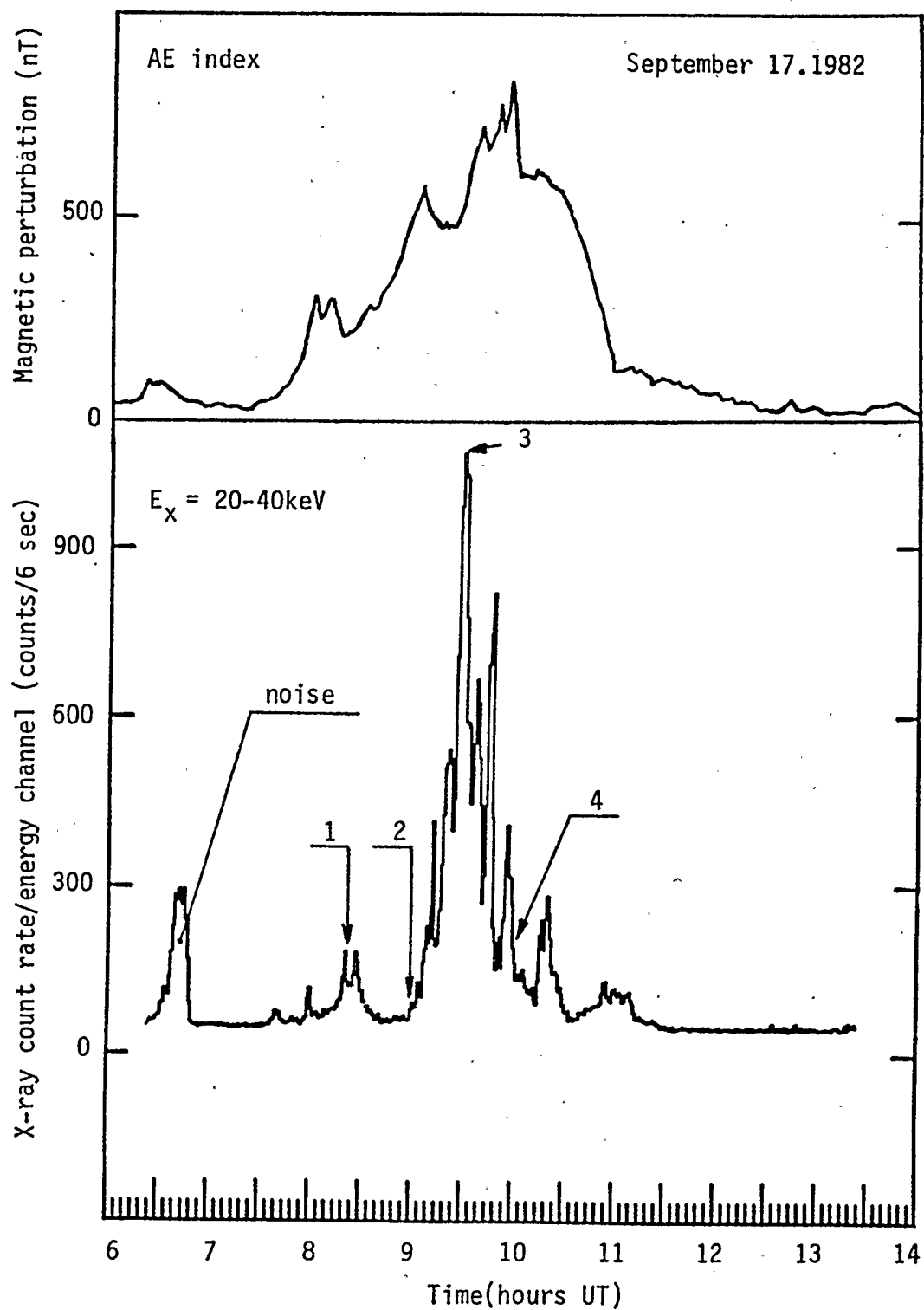
Figure 3.17 Observed AE index (top) and X-ray activity profiles
during CL-1 balloon flight. The numbers relate to
spectrum plots in Figure 3.20

considered relevant.   Shortly after the balloon reaches the float altitude (estimated   time 06:30 UT),   no 'significant x-ray activity is   observed.   First appearance of x-ray activity   occurs   at   08:15   UT; however, the event   is   not intense the decay is   observed   by   08:40 UT.   This peak is clearly observed .in all the energy plots of detector #3 but is partially buried by high x-ray activity observed in the count rate profiles of detector #1 and #2 for energies E_x < 80 keV (Figure 3.18).   The main feature   in   the x-ray profile common to all the three detectors is the broad highly-structured peak observed between 09:00 UT and 10:00 UT (see also Figure 3.17).   This peak dominates all other x-ray structures in the energy range between 20-80 keV (Figures 3.18 and 3.19). ·The decrease in the magnitude of the peak with increasing energy suggests the exponential nature of the x-ray spectrum.   The onset of this event and its duration coincides with the onset and duration of the impulsive bay activity at College (see Figures 3.16 and 3.17).

This, main event is softer than the first x-ray episode (08:15 UT-08:40 UT) which is clearly observed if one compares the relative intensities of the two events over the low and high energy domains of the spectrum (Figures 3.18 and 3.19).   For example for E_x less than 80 keV, the main event clearly dominates in intensity over the first x-ray event but for E_x greater than 80 keV the intensities of the two events are comparable.   This is again very similar
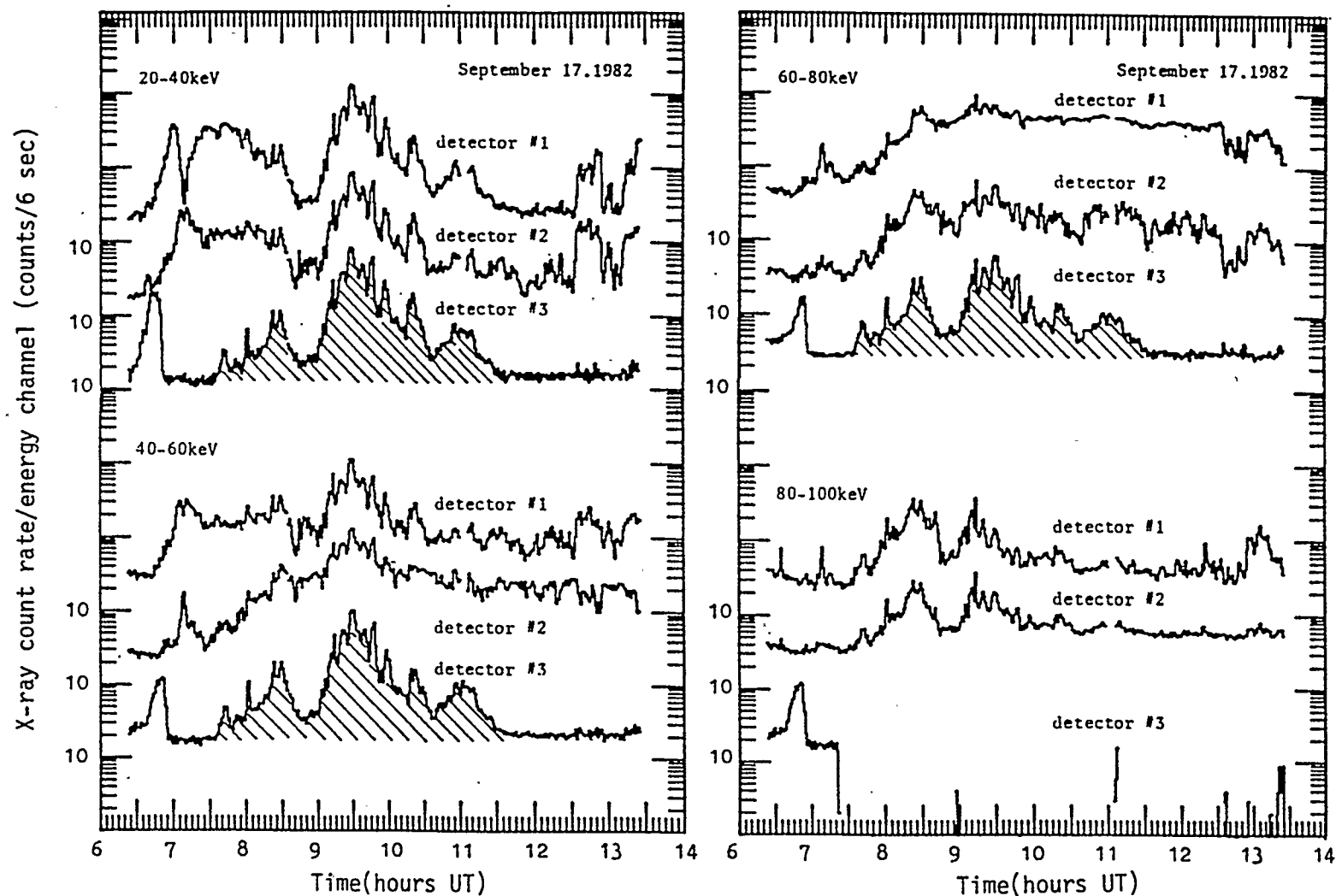
Figure 3.18 Observed differential X-ray activity over the energy region of 20keV-100keV by the vertical(detector #1) and the two inclined detectors.Only the shaded portion of the plot appears to be free of noise and hence is taken to represent the observed X-ray activity during the CL-1 flight.
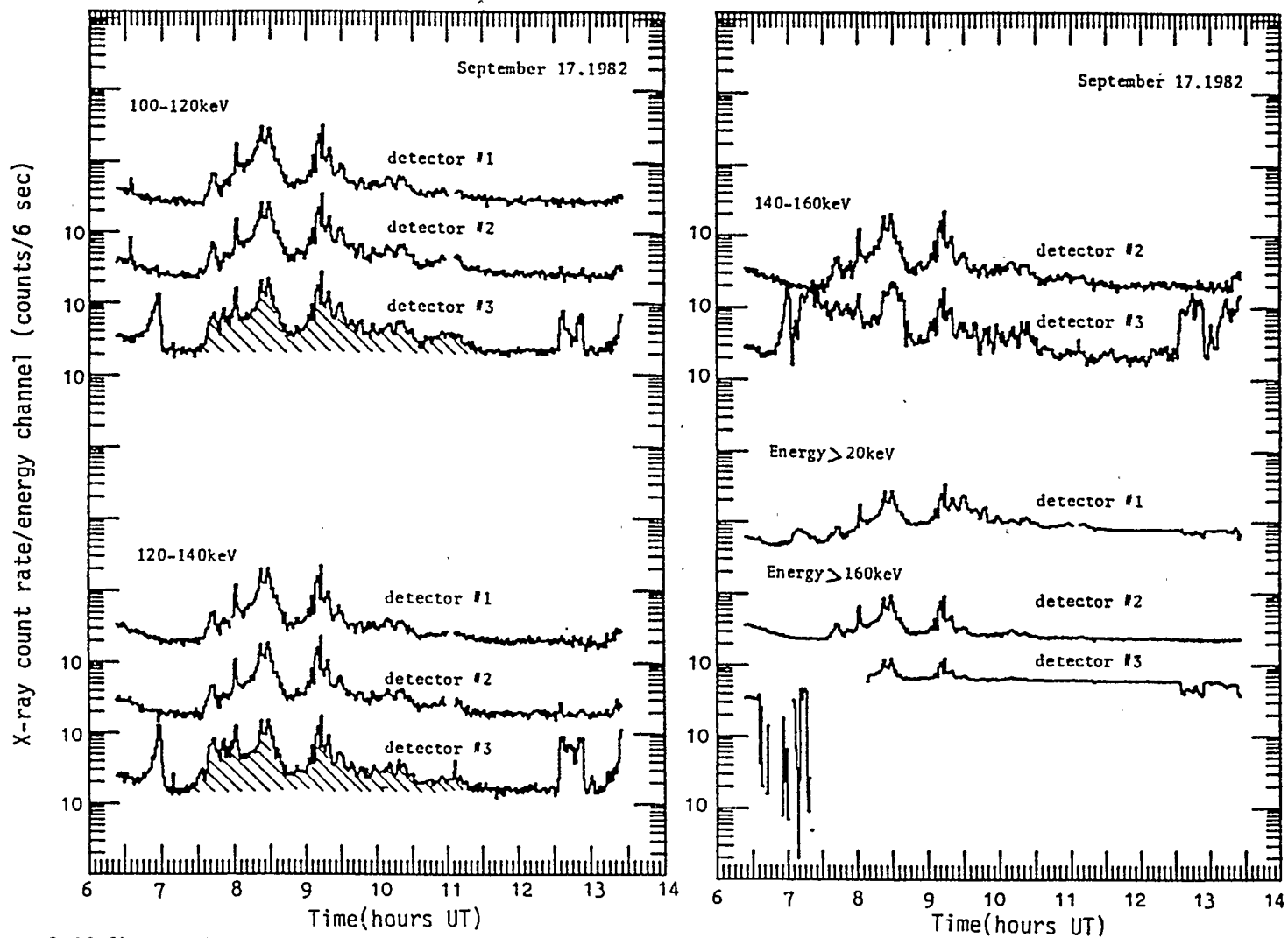
Figure 3.19 Observed differential X-ray activity over the energy region of 100keV-160keV by the vertical (detector #1) and the two inclined detectors.The integral count rate profiles for Ex 20keV and Ex 160keV are shown in panel (b).The shaded areas represent the X-ray profiles in this energy region.

to the observations during the CL-2 flight, where the Ax2 event dominated the Ax1 event in the low energy region of the spectrum.

3.4.4 Observed X-Ray Spectra During CL-1 Flight

Examples of measured x-ray spectra during the observed x-ray events are shown in Figure 3.20. It has already been pointed out that in case of detectors #1 and #2 spurious counts have been observed mainly in the 40-60 keV and 60-80 keV energy channels; these are excluded thus leading to incomplete spectra. During the first x-ray episode (08:15-08:40 UT) the x-ray spectra observed are hard (Figure 3.20). In addition, the maximum x-ray flux, usually observed in the 40-60 keV energy channel, is shifted to higher energy (plots #1). Hard spectrum is also observed just at the onset of the main x-ray event (plot #2, detector #3) followed by softening (plots #3 and #4).

Qualitatively, the spectral variations can be investigated by forming the ratios R_1, R_2, R_3, R_4 of count rates from neighboring energy channels. These have been computed only for detector #3 which has reliable data over the energy range of 20-140 keV and plotted in Figure 3.21. The data points in the plots have been smoothed by taking moving averages over the minute.

Obvious spectral softenings are observed during the main x-ray event. Note that the softening seems to follow the intensity variation of x-ray profiles. Several cases of

Figure 3.20 Examples of observed X-ray spectra during the CL-1 flight. See Figure 3.14 relating the spectrum number to the position on the X-ray profile. Data points contaminated by noise are not included in the spectra.
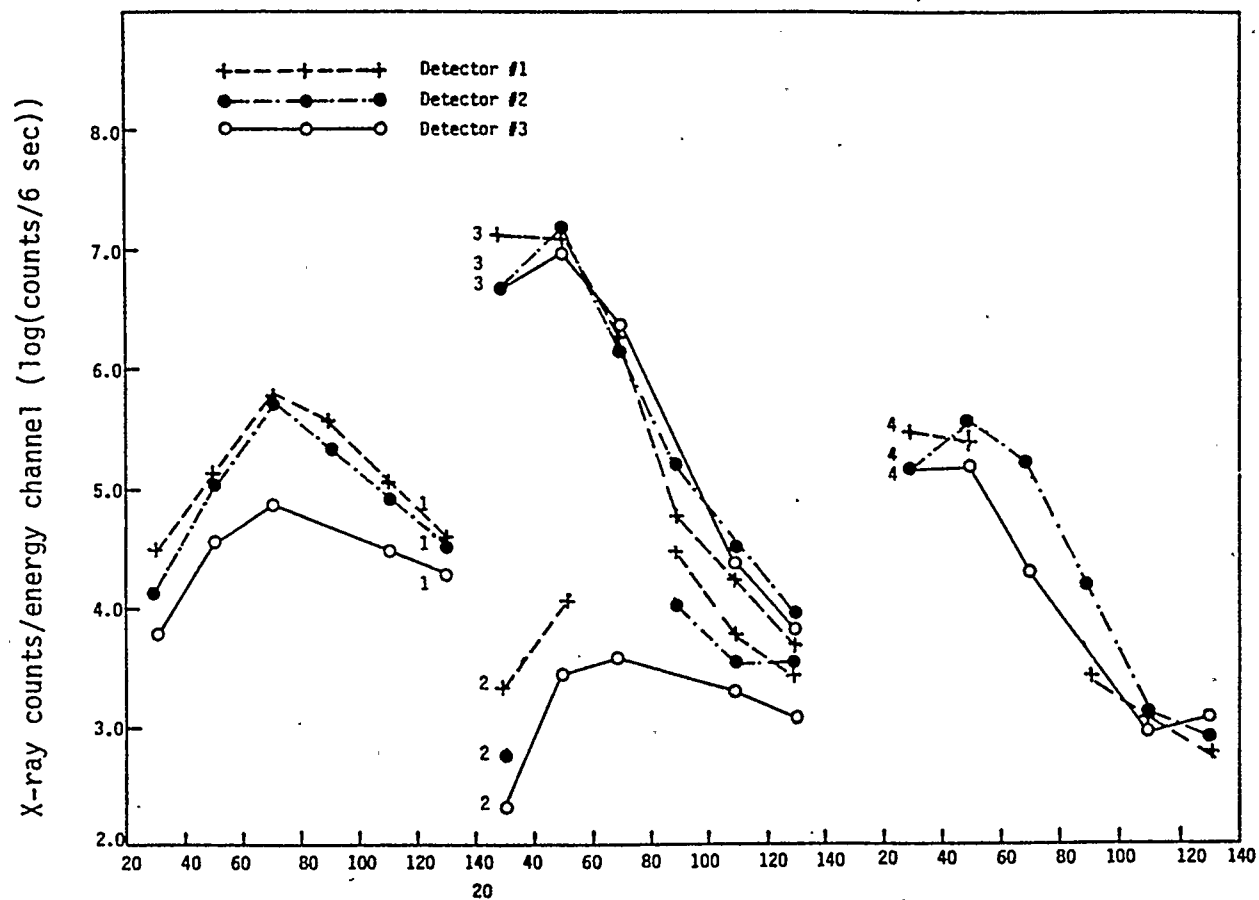
Spectrum number	Time(UT)	Spectrum number	Time(UT)
1	08:20	3	09:30
2	09:00	4	10:00
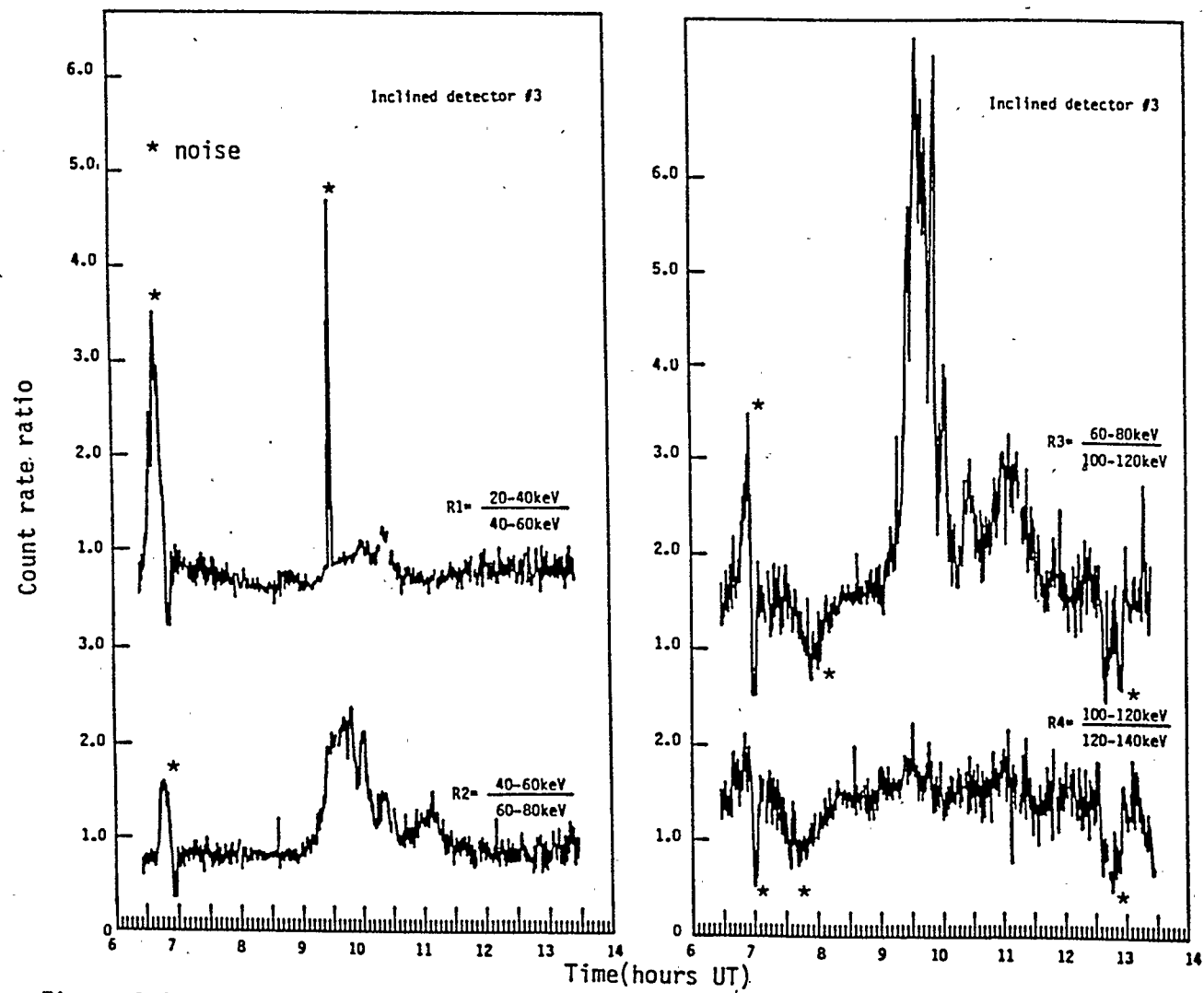
Figure 3.21 Plot of ratios formed from observed differential count rates. The increase of the ratios after 9:00UT indicate spectrum softening during the main X-ray event.

this association can be seen; good examples are observed at 10:00, 10:20, and 11:00 UT wherein intensification of x-ray activity (Figure 3.17) are accompanied with spectral softening (Figure 3.20).

The ratio R1 also increases, however its variation does not exactly follow the same trend as R2 and R3. R1 reaches a value greater than 1 at 10:00 UT and 10:20 UT (Figure 3.21) indicating a higher x-ray activity in the energy region E_x less than 40 keV.

3.5 CL-3 Balloon Flight

3.5.1 General Description

Due to problems encountered with the x-ray detectors and magnetic tapes the results of this flight CL-3 (launch, October 2, 1983, 04:41 UT) will be presented only briefly. Similar to CL-1 flight, both the high and the low altitude pressure transducers in this flight also failed during the ascent. The float altitude of 33.3 km as provided by radar information was reached at 06:20 UT; the drift path of the balloon during various stages of the flight is shown in Figure 3.1. The detector assembly in this payload consisted of four vertical detectors collimated to a 2.0π, 0.36π, 0.26π, and 0.18π opening solid angles.

3.5.2 Description of X-Ray Activity

During the first segment of the flight at float

(06:00-09:00 UT) the magnetic activity was essentially concentrated well to the East of Cold Lake, where a large magnetic bay activity (300 nT) was observed by Narssarsuaq (61.15°N, 314,5°E). Some impulsive bay activity between 07:15 UT and 08:00 UT was also observed by Fort Churchill. After the bay activity decayed at Narssarsuaq 09:00 UT, only a small (< 150 nT) magnetic activity was registered by the Yellowknife station. The onset of x-ray activity was observed at 06:15 UT shortly after the balloon had reached float altitude. The observed x-ray profiles reveal impulsive peaks ranging in duration from 10 minutes to 1 hour; also the x-ray profiles appear the same in all the energy channels.

The x-ray activity subsided at 10:00 UT; the rest of the period till cut-down (12:10 UT) revealed no x-ray features.

3.6 Summary of Observations

3.6.1 CL-2 Balloon Flight

During the course of CL-2 balloon flight, two magnetospheric substorms were observed as evident from the AE index profile (Figure 3.4, top). The first substorm occurred at 08:50 UT and decayed at 11:40 UT. Within this time period, two major x-ray events were observed.

The onset of the first major x-ray activity (Ax1) at 09:02 UT occurs simultaneously in all the three detectors

and in all the energy channels; it coincides with a second intensification of the magnetic bay activity at College. The x-ray profile of this event shows the presence of three impulsive intensifications (Figure 3.4) each lasting nearly 10 minutes in duration.

The observed x-ray spectra during this event had shown exponential characteristics, the inclined detector #2 showing the softest spectra during the course of the whole event. By the end of the Ax1 (09:35 UT) a net spectral softening occurred with some intermittent softening and hardening during the event (Figure 3.10).

The second major x-ray event (Ax2) started at 09:35 UT, coinciding with another large intensification of the magnetic bay activity at Fort Churchill and Yellowknife and a smaller one at College. Positive Z component of the magnetic perturbation profiles at Yellowknife and Fort Churchill indicate that the majority of the auroral electrojet was situated to the south of these stations while the electrojet was centered above College (L = 5) as indicated by Z = 0.

The intensity of Ax2 peaked between 09:55 UT and 10:10 UT after which all the three detectors simultaneously observed a rapid drop in the x-ray intensity, and this drop again coincided with the decay of the magnetic bay activity observed at College. The count rate after this event remained low although still above the background (observed at 08:30 UT). During the whole event the inclined detector

#2 again observed the softest spectrum while the inclined detector #4 measured the hardest spectrum (see Figure 3.10).

Figure 3.2 shows that the payload orientation during these two major x-ray events was steady with the inclined detector #4 pointing in the magnetic N-NW direction and the inclined detector #2 in the SW-S direction. Breaks in the observed exponential spectra develop at 09:35 UT (inclined detector #2) and at 09:50 UT (vertical detector) in the 100-120 keV energy channel; the break is due to a softer spectrum being superimposed over the harder one. The appearance of pulsating x-ray activity seems to coincide with the development of the break. Similarly, the end of the pulsating activity (Figure 3.13) is accompanied by the disappearance of the break in the 100-120 keV at 10:15 UT. After separation of the two spectral components, the e-folding energy values of the soft component is found to lie between 13 and 22 keV in the case of the vertical and between 11 and 16 keV in the case of the inclined detector #2.

The onset of the third major event (Bx) is observed at 12:00 UT; the intensity of this event dominates the two previous ones. This x-ray event can be associated with the onset of the second substorm which occurred at 12:05 UT. The activity peaks between 12:15 UT and 12:25 UT after which a rapid drop of x-ray activity is observed in all the three detectors. The observed spectra during this event again have exponential characteristics with e-folding energy

softening during the course of the event (Figures 3.11 and 3.12).

3.6.2 CL-1 Flight

The first x-ray event during this flight is observed to occur between 08:15 UT and 08:40 UT appearing as a small intensification in the x-ray count rate profile. The onset of the second and also major x-ray event occurs at 09:00 UT and clearly dominates the former one (Figure 3.17). Similar to that observed during the CL-2 flight, this event is associated with the magnetic bay activity at College (Figure 3.16). The temporal profile of this event shows the presence of impulsive spikes superimposed on the main broader base. Prior to 09:00 UT, the observed spectra were hard with subsequent softening during the development of the main event and hardening again during the decay of the main x-ray activity.

CHAPTER 4

STUDY OF X-RAY REGION DYNAMICS-MONTE CARLO SIMULATION

4.1 Introduction

In order to interpret the x-ray data collected by the detectors onboard balloon-borne payloads, the Monte Carlo method of simulating the passage of x-rays through the atmosphere from the production layer (90 km; 0 g cm^{-2}) down to the balloon altitude (33 km; 9 g cm^{-2}) has been utilized.

The computer program has been adopted from Pilkington (1970), modified and adopted to the Multics computer system. The program listing is given in the appendix. With respect to the original version, the modified version now separates the direct and the scattered x-rays and thus the relative amount of these components can be monitored during the passage through the atmosphere.

The program assumes an isotropic x-ray point source with an exponential energy spectrum. The output format of the program allows us to obtain the count rate at concentric annular distances of 15 km increments with the x-ray counts discriminated into 5 keV wide energy windows starting at 10 keV and continuing up to 200 keV. The output can be utilized for omnidirectional as well as the collimated detectors as the program also keeps track of the zenith angle interval at which x-rays cross the particular annulus

118

at the desired atmospheric depth. Since the vertical and the inclined detectors onboard are sampling the x-ray flux in the zenith angle intervals of 0-30 degrees and 0-60 degrees respectively, the zenith angle intervals of the program have been set to 0-30, 30-60, and 60-90 degrees to accommodate the zenith angle intervals in which the measurements were carried out. The output of the Monte Carlo program is then utilized in a secondary program which simulates the motion of various x-ray sources with respect to the detectors. The effect of the moving sources on the relative count rates and e-folding energies of both the inclined and the vertical detectors is explored. The technique of generating moving x-ray sources from a uniform extended source is described in the next section. The simulation enables us to investigate the imaging capability of the detector assembly employing directional detectors.

4.2 The Method of Generating and Moving the X-Ray Sources

Figure 4.1 shows schematically the geometry involved in the Monte Carlo program between the source at the production altitude and the observed x-ray flux at the detection altitude. The source S_1 located at 0 g cm^{-2} emits N x-rays from which n_j will pass through the area of the annulus L_j having average radius of $1/2(R_{j-1} + R_j)$. As pointed out in the previous section n_j is provided by the output of the program. This is drawn in solid lines. The principle involved in the generation of the extended

X-ray production altitude

$0^o - 30^o$

a)

S_3

S_2

U_j

S_n

S_1

$30^o - 60^o$

U_1

$60^o - 90^o$

D

L_j

X-ray detection altitude

b)

Θ_j

R_j

d

U_1

U_j
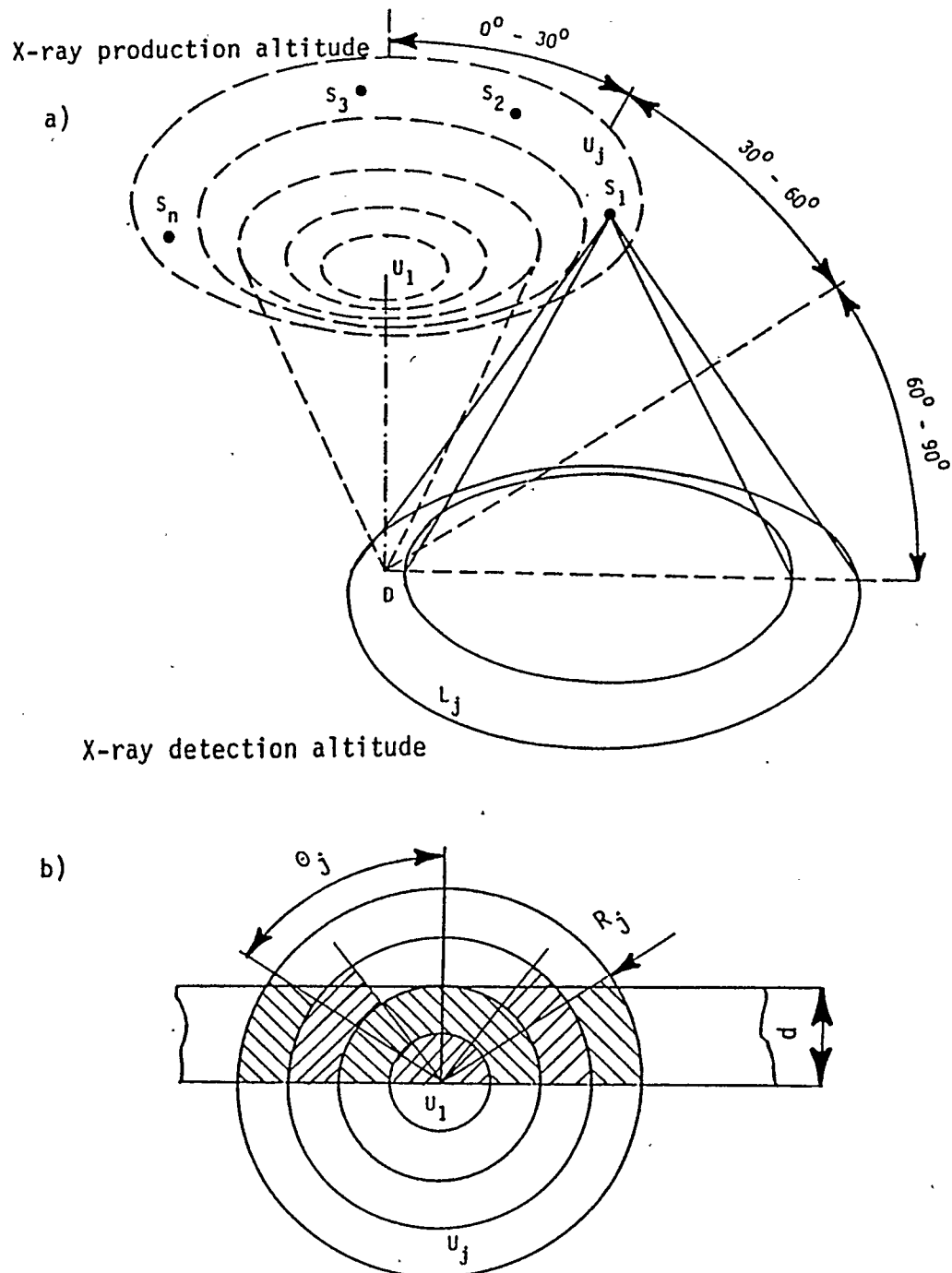
Figure 4.1 a) Schematic diagram showing the geometry involved in the Monte Carlo program between the X-ray source S_1 at the production altitude and the annulus L_j located at the detection (balloon) altitude. The source S_1 is emitting N X-rays from which n_j will pass through the annulus L_j. This is shown with solid lines. The dotted lines relate to the method of generating uniform extended X-ray source as given in section 4.2.

b) Method of generating band-like source from the uniform extended source(after Pilkington,1970).

uniform x-ray source is shown with dotted lines (see also Pilkington, 1970).

The number of counts observed by a flat detector D of unit area (1 cm^2) located in annulus L_j is

$$C_j = \frac{n_j}{A_j} \qquad (4.1)$$

where A_j is the area of annulus L_j. It can be assumed that the source S_1 itself (also having area of 1 cm^2) is located in the annulus U_j having the same area as the annulus L_j at the detection altitude. Filling the annulus U_j uniformly with x-ray sources S_i each emitting N x-rays will generate count rate at D given by

$$A_j \cdot C_j = A_j \cdot \frac{n_j}{A_j} = n_j \qquad (4.2)$$

Note that for example the geometrical configuration between S_3 and D is the same as between S_1 and D.

Generating the extended uniform source, the contribution from all annular rings must be summed up, giving the total count at D

$$C_{TOTAL} = \sum_{all\ j} n_j \qquad (4.3)$$

The total count observed by the detector D from the extended uniform source emitting N x-rays cm^{-2} is thus numerically equal to the sum of the count rates from each annulus given

by the output of the Monte Carlo program.

The band-like source used in this study has been generated as shown in Figure 4.1b from concentric annular rings where only the shaded portions of the rings contribute to the count rates at detector D. The contribution to the count rate from annular ring j is

$$C_j = \frac{1}{2} n_j \left(1 - \frac{\theta_j}{90} \right)$$
(4.4)

where the angle θ_j (in degrees) shown in Figure 4.1b is

$$\theta_j = \cos^{-1} \left(\frac{2d}{R_{j-1} + R_j} \right)$$
(4.5)

The total count observed due to contribution of all the annular rings is

$$C_{TOTAL} = \frac{1}{2} n_1 + \frac{1}{2} \sum_{\text{all } j \geqslant 2} n_j \left(1 - \frac{\theta_j}{90} \right)$$
(4.6)

As the value of d is an integral multiple of 15 km, the contribution from the central circle is either $1/2 \, n_1$ for all values of d or 0 when d = 0. In this study it has been found that after a distance of 180 km from zenith the contribution from the source to the count rate is negligible and the value of j has been truncated at 12. The above calculations are performed by a secondary program using as
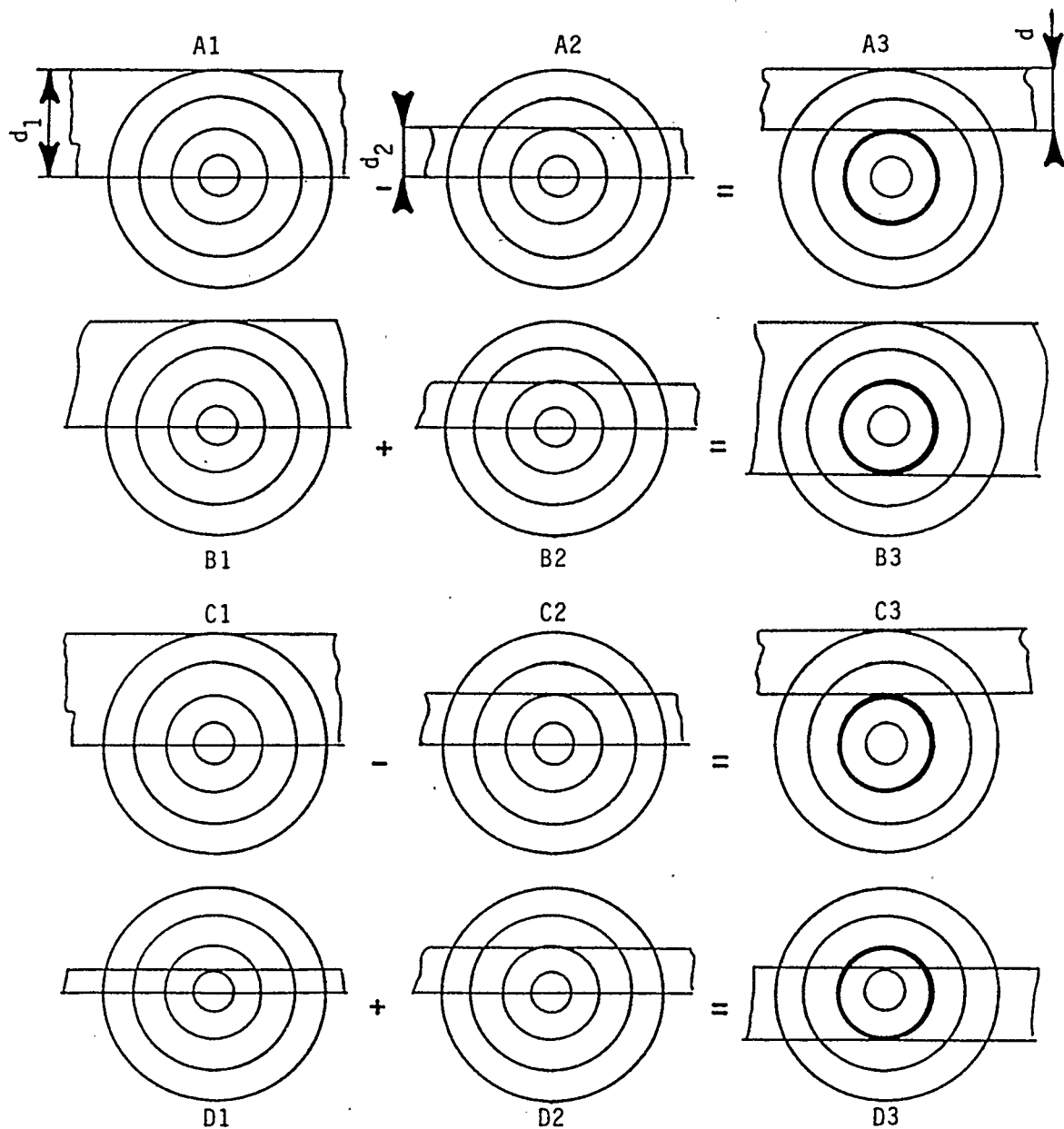
Figure 4.2 Method used to expand the X-ray source over the field of view of the detector(configurations A and B). Configurations C and D pertain to method of moving a band-like source. The heavy circles depict the illumination area of the detector.

The radius of the smallest circle is 15km;the radii of the larger circles are increments of 15km.

input the output from the Monte Carlo program, the input being in the form of a 2-dimensional array keeping track of the x-ray energy and the distance R_j. The method used to expand and move the source is shown in Figure 4.2.

As shown in Figure 4.2, the expansion of the source has been accomplished by adding or subtracting the smaller band-like source from the larger one according to

$$C_{A3} = C_{A1} - C_{A2} \qquad\qquad (4.7)$$

and

$$C_{B3} = C_{B1} + C_{B2} + C_{DIRECT} \qquad\qquad (4.8)$$

where C_{A3} and C_{B3} pertain to the final count rate in source configuration A3 and B3 respectively while C_{A1}, C_{B1}, C_{A2}, and C_{B2} are count rates related to source configuration shown by their appropriate subscripts. C_{DIRECT} is the contribution to the total count rate of the direct component from the fractions of the annular rings situated in the field of view of the detector.

The value d_1 in the case of configurations A and B is 165 km while d_2 is varied from 0 to 150 km. In the case of the moving source (configurations C and D) the values of d_1 and d_2 are related according to the following, as appropriate

$$d = d_1 - d_2$$

or $\qquad d = d_1 + d_2 \qquad\qquad\qquad\qquad$ (4.9)

where d is the desired width of the band-like source. Similarly, as in the case of the expanding x-ray source, the direct component is added whenever the source is moved into the field of view of the detector.

4.3 The Effect of Scattered X-Rays on the Observed Count Rate Profiles at Depth of 9 g cm^{-2}

The simulated count rate for the inclined detector has been generated by summing 50 % of the x-ray flux from the 0°-30° and 50 % of the flux from the 30°-60° zenith angle intervals, since the detector samples equal amounts of x-ray flux from both intervals.

The opening solid angle of the vertical detector is situated entirely in the 0°-30° zenith angle interval. All the simulated count rates prior to the summation have been normalized to counts per unit solid angle as the magnitude of the solid angle in the 30°-60° angle interval is 3 times (0.73π) that in the 0°-30° (0.26π) interval.

The results of the Monte Carlo simulation indicate that at the atmospheric depth of 9 g cm^{-2} (33 km altitude), the approximate altitude of the CL-1, CL-2, and CL-3 balloon flights, the effect of scattered x-ray component on the observed count rate profiles becomes significant. This is
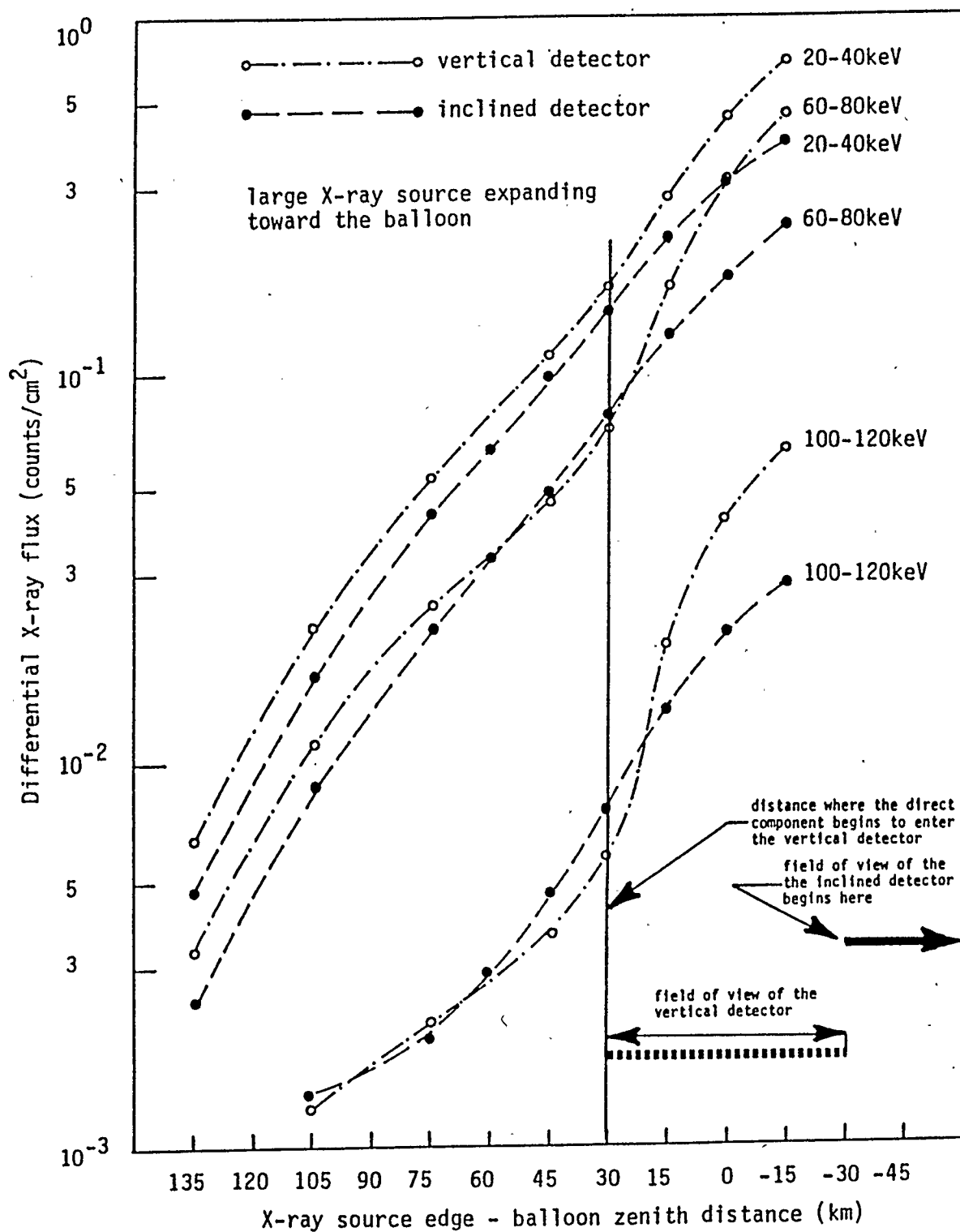
Figure 4.3 The effect of scattered X-rays on the count rate profiles of two detectors at the atmospheric depth of 9 g cm. The inclined detector observes the scattered component only.The source is moving in from the left.
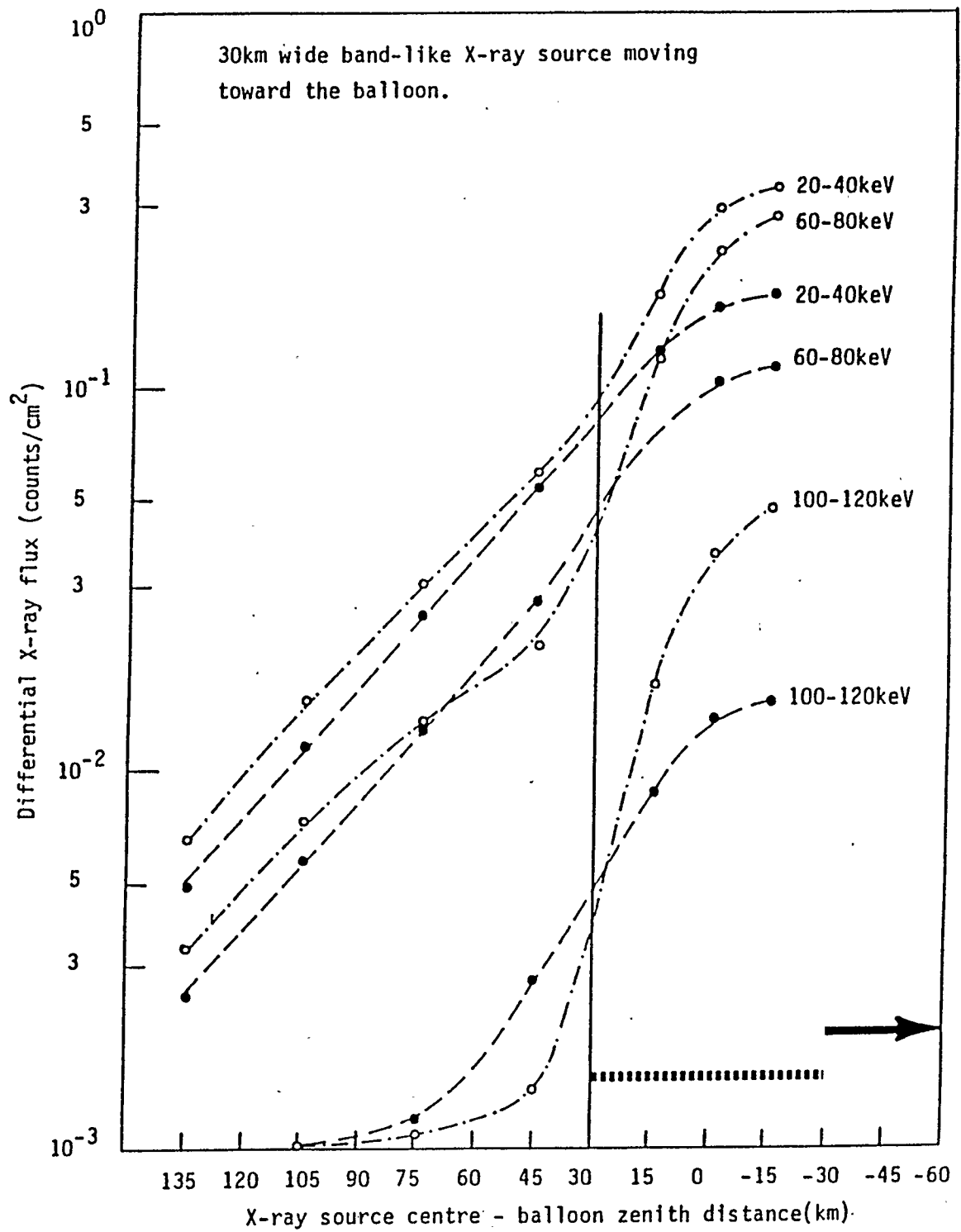
Figure 4.4 Same as Figure 4.3 but smaller X-ray source.

illustrated in Figures 4.3 and 4.4 showing the simulated x-ray count rate profiles of the vertical and the inclined detectors as the extended (Figure 4.3) and the smaller 30 km wide band-like (Figure 4.4) x-ray sources move towards the balloon's zenith. Three energy levels are considered namely 20-40 keV, 60-80 keV, and 100-120 keV as shown. The heavy lines depict the illumination areas of the vertical and the inclined (only a portion of it) detectors at the x-ray production layer. As the x-ray source begins moving towards the detectors, both the vertical and the inclined detector will observe increasing x-ray activity due to increasing flux of scattered component only. The net result is that, due to the presence of the large scattered component, the count rate profiles at this point will give an impression of a large x-ray source covering the fields of view of all the detectors.

At the distance of 30 km from the zenith, the direct x-ray component begins to enter the vertical detector; thus it experiences an increase of count rate relative to that of the inclined detector as it is still registering only the scattered component. Note however that, although the inclined detector does not measure any direct x-rays, the count rate of this detector still rises in response to the approaching source. The net result of scattering is that the x-ray peak caused by the approaching source will be observed simultaneously by all the detectors, the count rate

profiles thus showing good correlation from one detector to another. This is what has actually been observed in the x-ray activity plots from the Cold Lake flights.

4.4 Study of X-Ray Auroral Dynamics Using Relative Count Rate Ratios of Detectors

With directional detectors onboard the payload, the motion of the x-ray source relative to the fields of view of the detectors can be studied by means of the ratio formed from the count rate ratios of the two detectors. The entry of the x-ray source into the field of view of one detector will, due to the presence of direct x-ray components, change its count rate relative to that of the detector observing only the scattered component.

4.4.1 The Energy Dependence of the Count Rate Ratio

Figure 4.5 represents the result of an investigation concerning the dependence upon energy of the count rate ratios. The x-ray source considered for this study is one which expands from the zenith and eventually covers the field of view of the inclined and the vertical detectors. The shaded illumination areas of the vertical (small circle) and the inclined detectors (small ellipse) show the orientation of the detectors with respect to the velocity vector (heavy arrow) of the moving x-ray source edge. The heavy lines in the figure show the extent of the field of view of the detectors. Figure 4.5 shows that as the x-ray
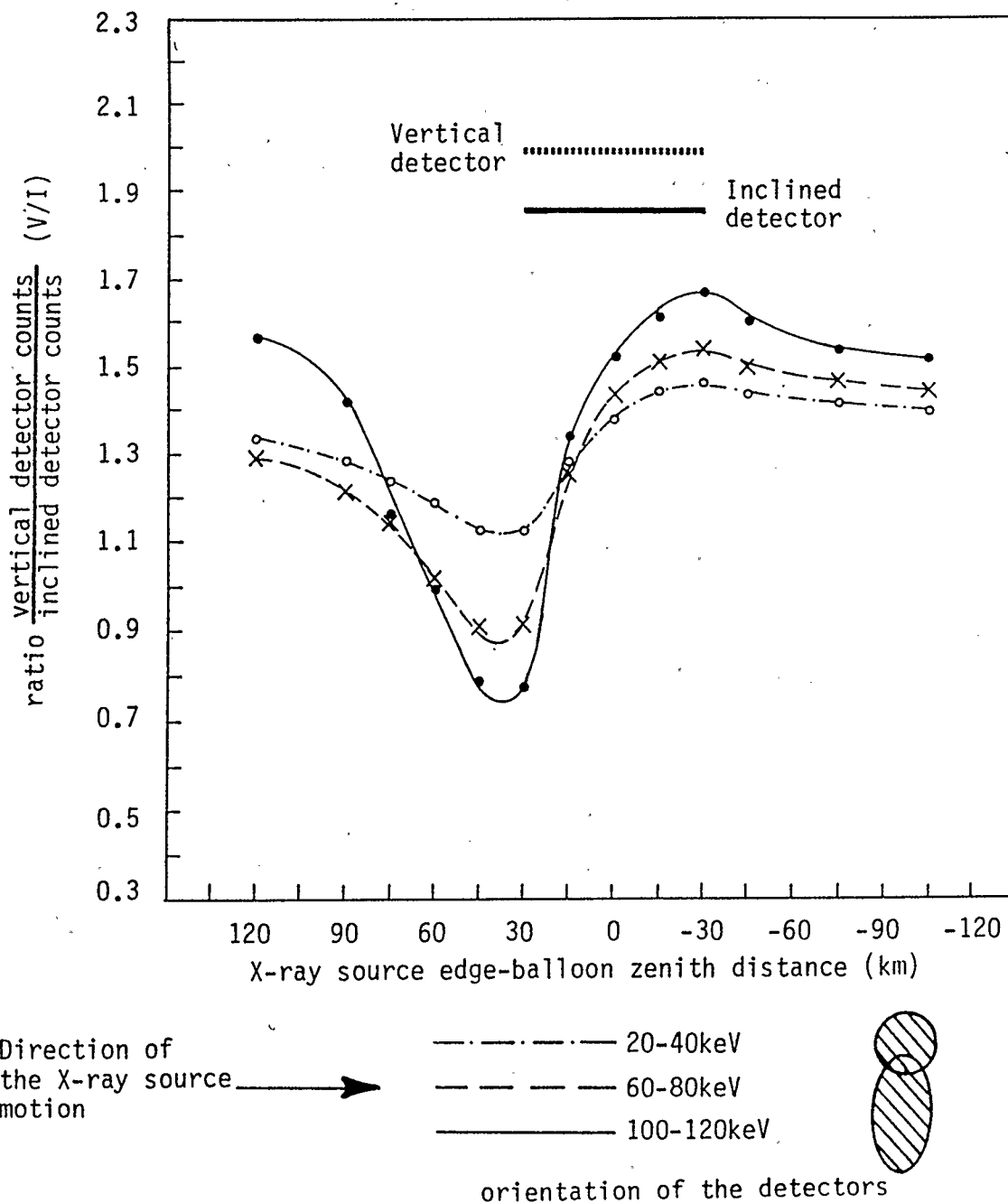
Figure 4.5 The energy effect on the ratio variation observed as the
large X-ray source expands toward and over the fields of
view of the detectors.The ratios are formed from the count
rates of the vertical versus inclined detector.The energy
levels considered are shown above.The heavy lines show the
extent of the detector's fields of view for the orientation
shown. The ratio produced at the higher energy level shows
larger variation and is thus more sensitive to the movements
of the X-ray source.

energy level increases, the ratio variation also increases. This direct relationship between variation in the ratio and the energy level being sampled can be interpreted as the higher energy x-rays have relatively fewer scattered components thus increasing the significance of the direct x-rays contributing to the total count rate. The result thus suggests that when analyzing real data, one should use ratios at higher energy levels as they are more sensitive to motion of the x-ray source.

4.4.2 The Effect of X-Ray Source Size and Orientation of Detectors on the Count Rate Ratio

The effect of the orientation of detectors relative to the motion of the x-ray source, and the effect of the source size on the ratio formed from the count rates of the vertical and the inclined detectors is studied here.

Based on the results from the previous section the ratios are formed from count rates observed in the 100-120 keV energy region. The x-ray sources utilized are:

i)   A large x-ray source expanding towards and over the detectors from the distance of 120 km (Figure 4.6).

ii) A 90 km wide, band-like x-ray source approaching and crossing over the detectors (Figure 4.7).

iii) Same as ii, but only 30 km wide x-ray source (Figure 4.8).

iv) a small, point-like x-ray source (Figure 4.9).

Three azimuthal orientations of the inclined detectors are
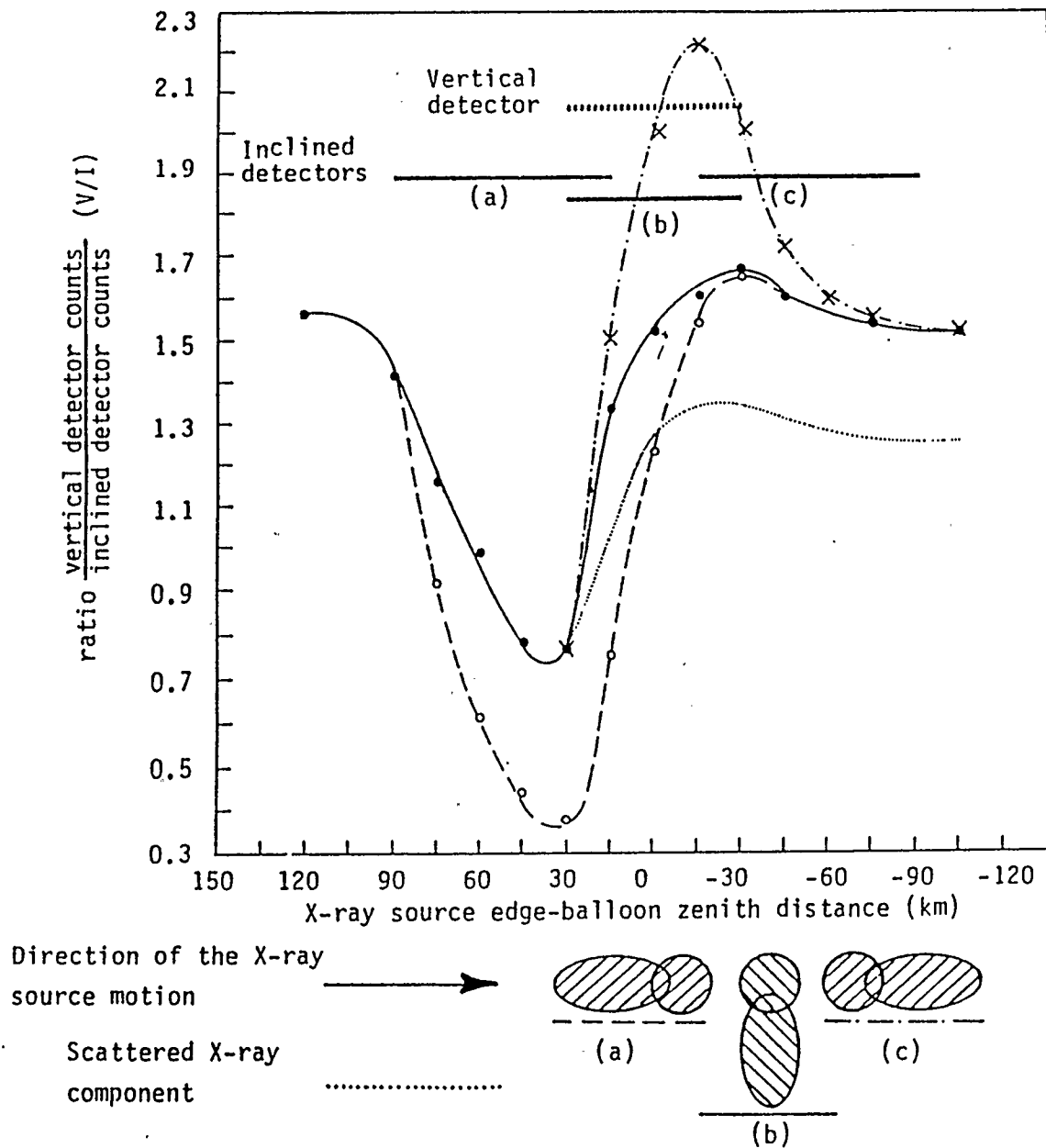
Figure 4.6 Calculated variation of the ratio made from count rates of the
vertical versus inclined detector as the X-ray source expands
toward and over the fields of view of both detectors.
The heavy lines show the extent of the detector's fields of view
for a particular orientation.The orientations labelled as
(a),(b) and (c) are shown above.The small ellipse and the circle
represent the fields of view of the inclined and the vertical
detector respectively.
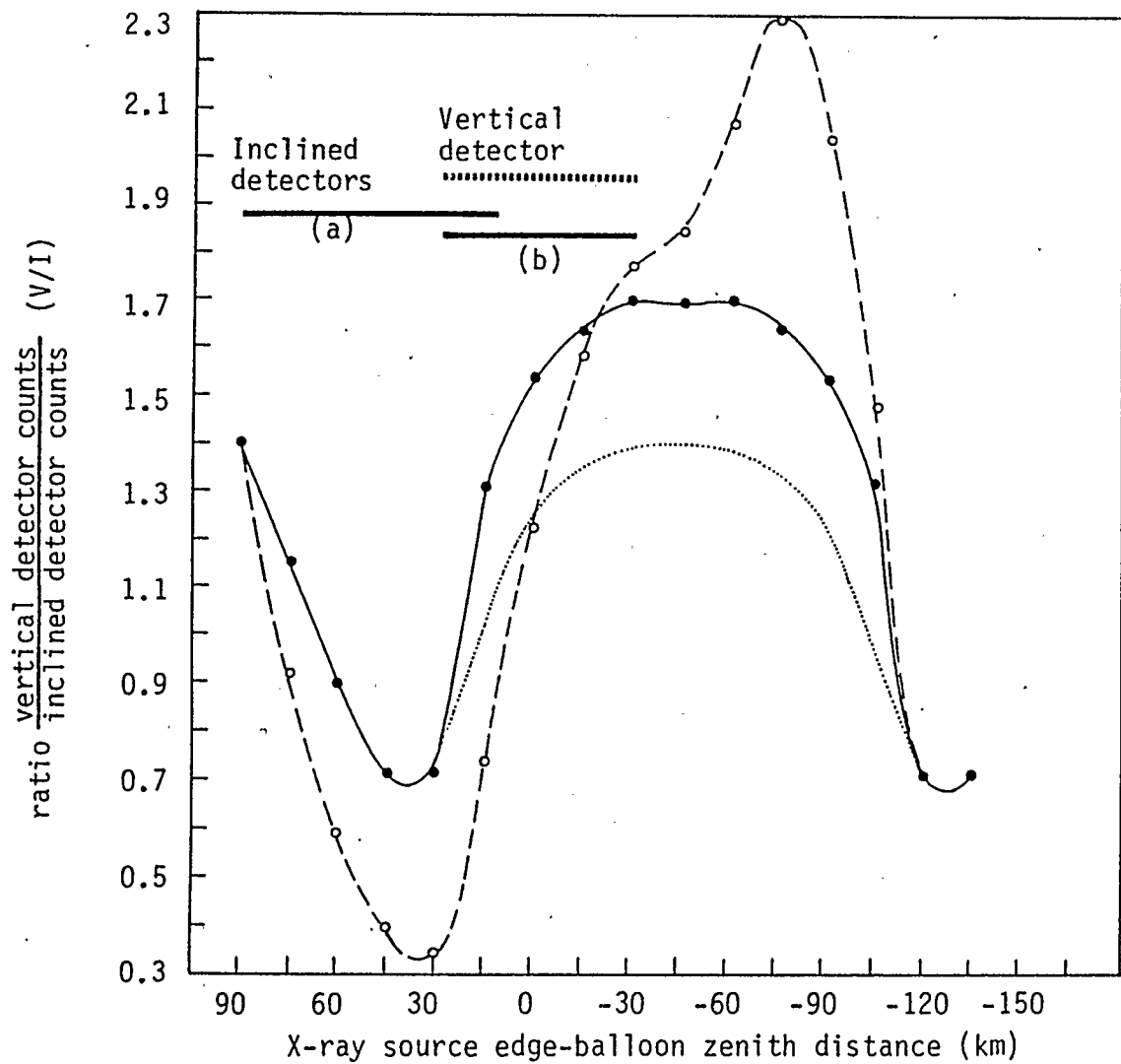
Figure 4.7 Calculated variation of the ratio made from count rates of the
vertical versus inclined detector as the 90km wide band-like
X-ray source moves toward and over the fields of view of both
detectors. Only two orientations, namely (a) and (b) are shown
since the orientations (a) and (c) are symmetrical for this
source. Refer to Figure 4.6 for labelling.

considered for the case (i) (Figure 4.6), where the angle of orientation is measured between the velocity vector of the moving source and the vector oriented along the semi major axis of the ellipse representing the field of view of the inclined detector. The vector associated with the semi major axis is directed from zenith outward. Just as in Figure 4.5, these orientations are shown with the shaded illumination area of the inclined and the vertical detector. These orientation angles are 180° and 90° or 270° and 0° labelled in Figure 4.6 as (a), (b), and (c) respectively. Only two orientations, namely (a) and (b) are considered in Figures 4.7 and 4.8 because the orientations (a) and (c) are symmetrical for these sources.

One orientation is considered for the point-like source (Figure 4.9) since this particular orientation can represent the other two as well. The heavy lines in Figures 4.6-4.9 show the extent of the detectors' fields of view in the particular orientation.

The result of this study, shown in Figures 4.6-4.9 indicates that the magnitude of the variation of the ratio is inversely proportional to the area of the x-ray source moving across the detectors' fields of view. The x-ray source entering the field of view of one detector produces change in the ratio, where the larger change occurs for smaller sources. This is observed for example when comparing the ratio in Figures 4.6, 4.7, 4.8, and 4.9 for orientation (a). In each case, the ratio changes from the <
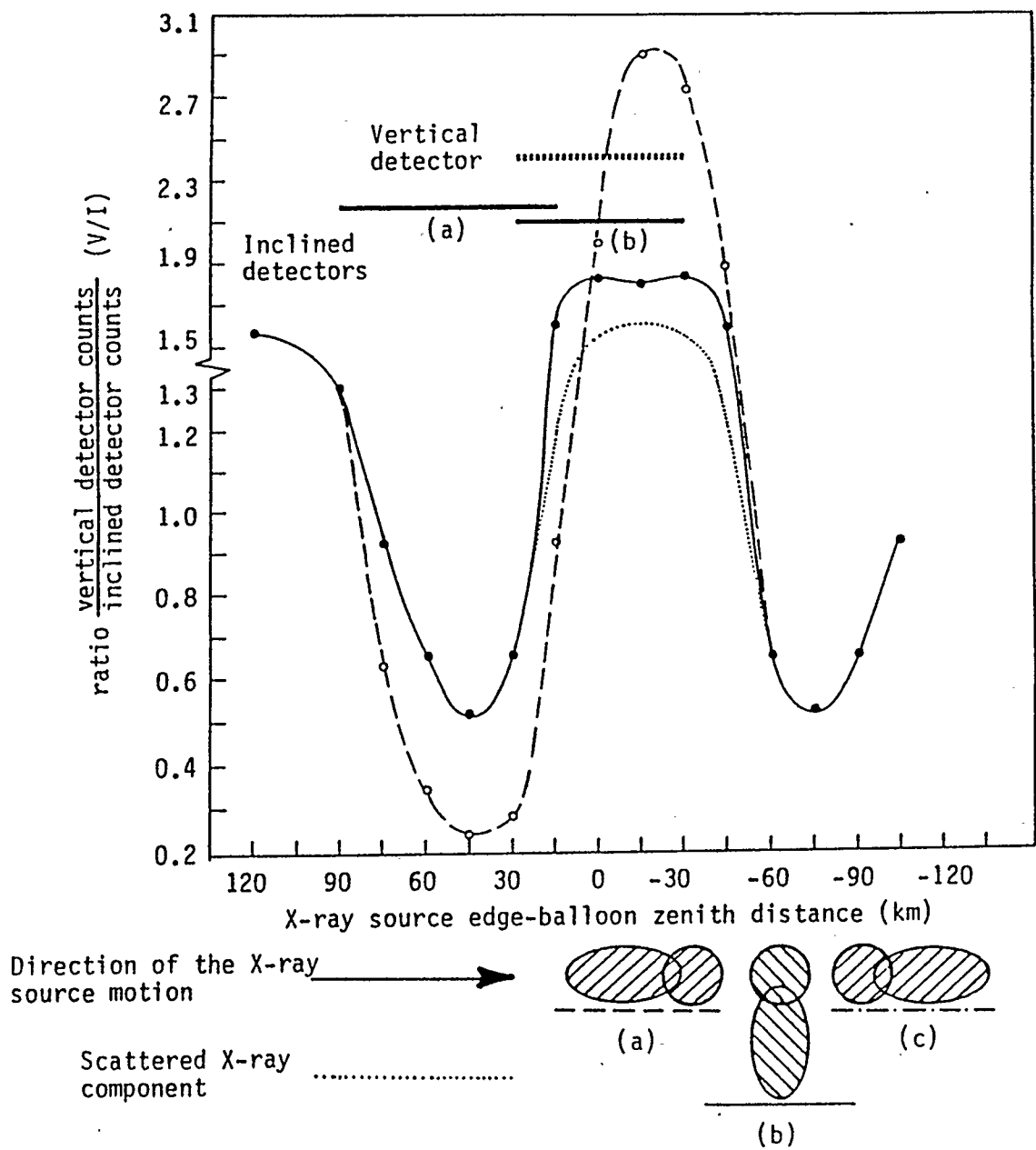
Figure 4.8 Calculated variation of the ratio made from count rates of the vertical versus inclined detector as the 30km wide band-like X-ray source moves toward and over the fields of view of both detectors. Orientations (a) and (b) are considered for the same reason as given in Figure 4.7.
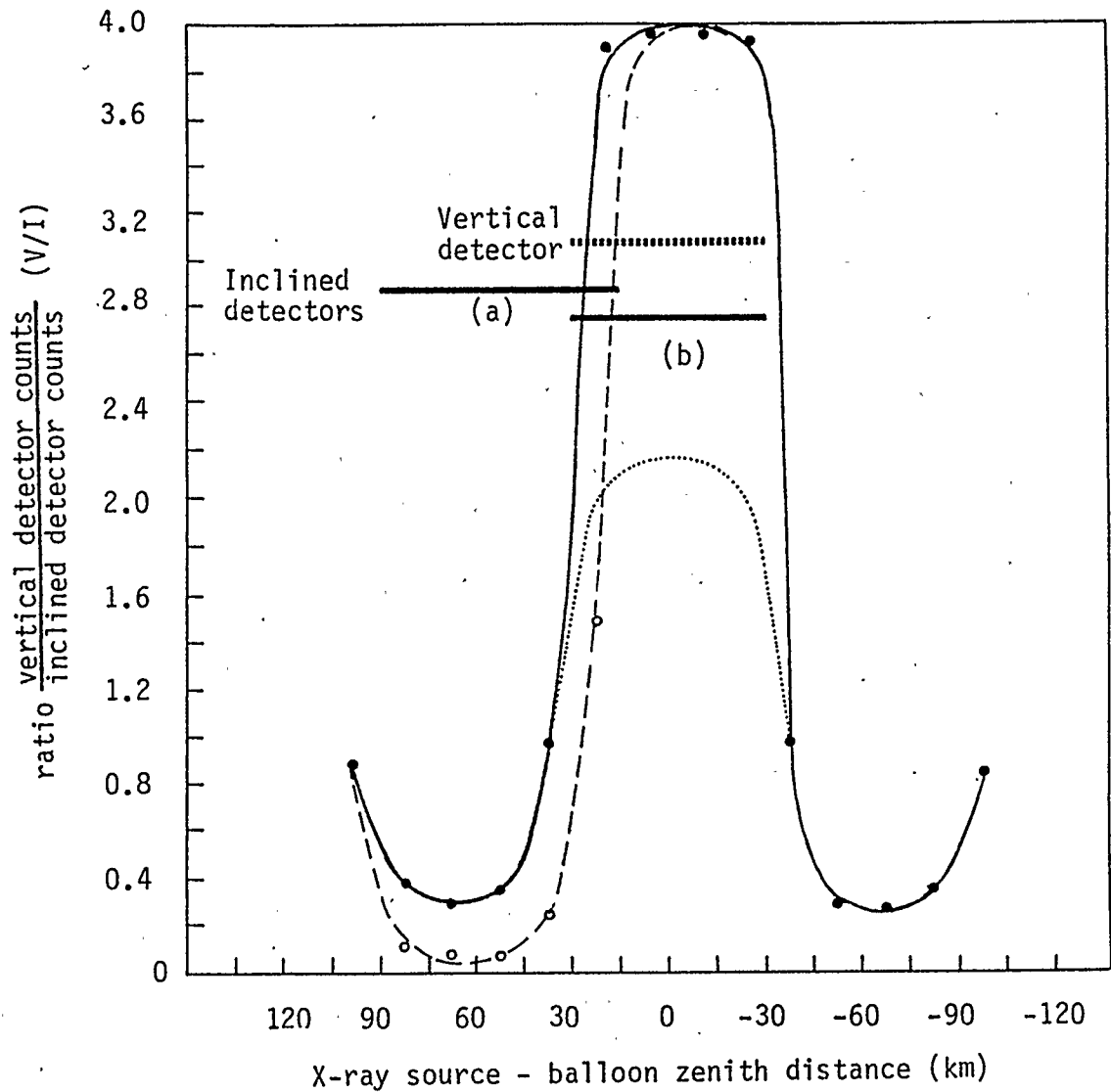
Figure 4.9 Calculated variation of the ratio made from count rates of the vertical versus inclined detector as the small point-like X-ray source moves toward and over the fields of view of both detectors. Only two orientations,namely (a) and (b)are shown since the orientations (a) and (c) are symmetrical for this source. Refer to Figure 4.8 for labelling.

1 value to the > 1 value as the source gradually leaves the field of view of the inclined detector and covers the field of view of the vertical detector. For example for the largest source (Case i) the ratio changes from 0.35-1.64 while for the point-like source, the observed change is from 0.08 to 3.79. The other two sources (Case ii and iii) produce ratio changes which fall between these two extrema (see Figure 4.7 and 4.8). The ratio variations also depend on the relative orientation of the detectors' fields of view with respect to the velocity vector of the moving source. This is observed if one compares the ratio variations for cases (a) and (b) in Figures 4.6, 4.7, and 4.8. Evidently, the difference between the two ratio profiles is due to the fact that the x-ray source at the particular distance from zenith will, for different orientations, cover a different fraction of the inclined detector's field of view.

The ratios of the scattered component shown in Figures 4.6-4.9 indicate that the inclined detector is sensitive to indirect x-rays originating from distances between 30-75 km while the vertical detector is sensitive to scattered x-rays, from within 30 km radius. This is illustrated in Figures 4.6, 4.7, 4.8, and 4.9 as the ratio V/R of the scattered component reaches minimum between 30-75 km and maximum at distance < 30 km. Evidently, these x-rays are actually scattered only through a small angle from the original direction of emission and hence from the distance of 60 km these x-rays will enter into the opening angle

TABLE 4.1
(EXPANDING X-RAY SOURCE)

Distance from zenith (km)	$V/I_{(a)}$	$V/I_{(b)}$ ($V/I_{(120°)}$)	$V/I_{(c)}$	$I_{(a)}/I_{(b)}$
120	1.56	1.56 (1.55)	1.56	1.0
90	1.41	1.41 (1.41)	1.41	1.0
75	0.92	1.15 (1.15)	1.15	1.25
60	0.61	0.94 (0.94)	0.94	1.59
45	0.44	0.78 (0.78)	0.78	1.77
30	0.38	0.77 (0.77)	0.77	2.02
15	0.76	1.33 (1.39)	1.49	1.75
0	1.23	1.52 (2.0)	2.0	1.23
-15	1.53	1.60 (1.96)	2.23	1.04
-30	1.65	1.66 (1.72)	2.0	1.0
-45	1.60	1.59 (1.63)	1.72	1.0
-75	1.54	1.54 (1.54)	1.61	1.0
-105	1.52	1.52 (1.52)	1.52	1.0

TABLE 4.2
(90KM WIDE BAND-LIKE X-RAY SOURCE)

Distance from zenith (km)	$V/I_{(a)}$	$V/I_{(b)}$	$I_{(a)}/I_{(b)}$
90	1.40	1.40	1.0
75	0.91	1.15	1.26
60	0.59	0.9	1.52
45	0.40	0.72	1.80
30	0.34	0.71	2.08
15	0.74	1.32	1.78
0	1.23	1.54	1.25
-15	1.58	1.63	1.03
-30	1.77	1.70	0.96
-45	1.85	1.68	0.91
-60	2.08	1.70	0.82
-75	2.32	1.63	0.70
-90	2.04	1.54	0.75
-105	1.49	1.32	0.89
-120	0.71	0.72	1.01

The ratios $V/I_{(a)}$, $V/I_{(b)}$ and $V/I_{(c)}$ relate to the orientations (a),(b) and (c) as given in Figure 4.6. The ratio $V/I_{(120)}$ applies to the orientation for which the angle between the velocity vector of the source and the inclined detector is 120 degrees. The ratio $I_{(a)}/I_{(b)}$ is calculated from $V/I_{(a)}$ and $V/I_{(b)}$ and represent the relative counts between the two inclined detectors in orientation (a) and (b).

TABLE 4.3

(30KM WIDE BAND-LIKE X-RAY SOURCE)

Distance from zenith (km)	$V/I_{(a)}$	$V/I_{(b)}$	$I_{(a)}/I_{(b)}$
120	1.55	1.55	1.0
90	1.30	1.30	1.0
75	0.63	0.92	1.46
60	0.34	0.65	1.91
45	0.24	0.51	2.12
30	0.28	0.65	2.32
15	0.92	1.6	1.73
0	1.98	1.83	0.94
-15	2.89	1.80	0.62
-30	2.71	1.83	0.68
-45	1.85	1.6	0.86
-60	0.65	0.65	1.0
-75	0.51	0.51	1.0
-90	0.65	0.65	1.0

Refer to Tables 4.1 and 4.2 for captions.

TABLE 4.4

(SMALL POINT-LIKE X-RAY SOURCE)

Distance from zenith (km)	$V/I_{(a)}$	$V/I_{(b)}$	$I_{(a)}/I_{(b)}$
97.5	0.88	0.88	1.0
82.5	0.10	0.39	3.90
67.5	0.08	0.33	4.13
52.5	0.07	0.33	4.71
37.5	0.25	1.0	4.0
22.5	1.32	3.73	2.83
7.5	3.76	3.76	1.0
-7.5	3.76	3.76	1.0
-22.5	3.73	3.73	1.0
-37.5	1.0	1.0	1.0
-52.5	0.33	0.33	1.0
-67.5	0.33	0.33	1.0
-82.5	0.39	0.39	1.0
-97.5	0.88	0.88	1.0

located between 30°-60°.

. The observed values of ratios for the source Cases i-iv as a function of source edge-balloon zenith distance are given in Tables 4.1-4.4. Table 4.1 also gives ratio values for the relative orientation between the source velocity vector and the vector along the semi-major axis of the ellipse at 120°. It is evident that for the given distance, each source produces a particular set of ratios for the same set of detector orientations. Such a unique set of ratios can in principle be applied to the set of ratios formed from real data in order to estimate the position and the size of the x-ray source.

4.5 Variations of X-Ray Spectrum

Figures 4.10 and 4.11 show the e-folding energy variations observed by both the vertical and the inclined detectors as a function of x-ray source-detector distance. The cases shown here are:

i) Large x-ray source approaching and expanding over the balloon from a distance of 150 km (Figure 4.10)

ii) 30 km wide band-like source moving across the field of view of the detectors (Figure 4.11)

The spectrum of the x-ray source considered is exponential with e-folding energy of 20 keV as given in Figure 4.10. The value of the observed e-folding energy at the atmospheric depth of 9 g cm^{-2} strongly depends on the distance between the source and detector. The spectral
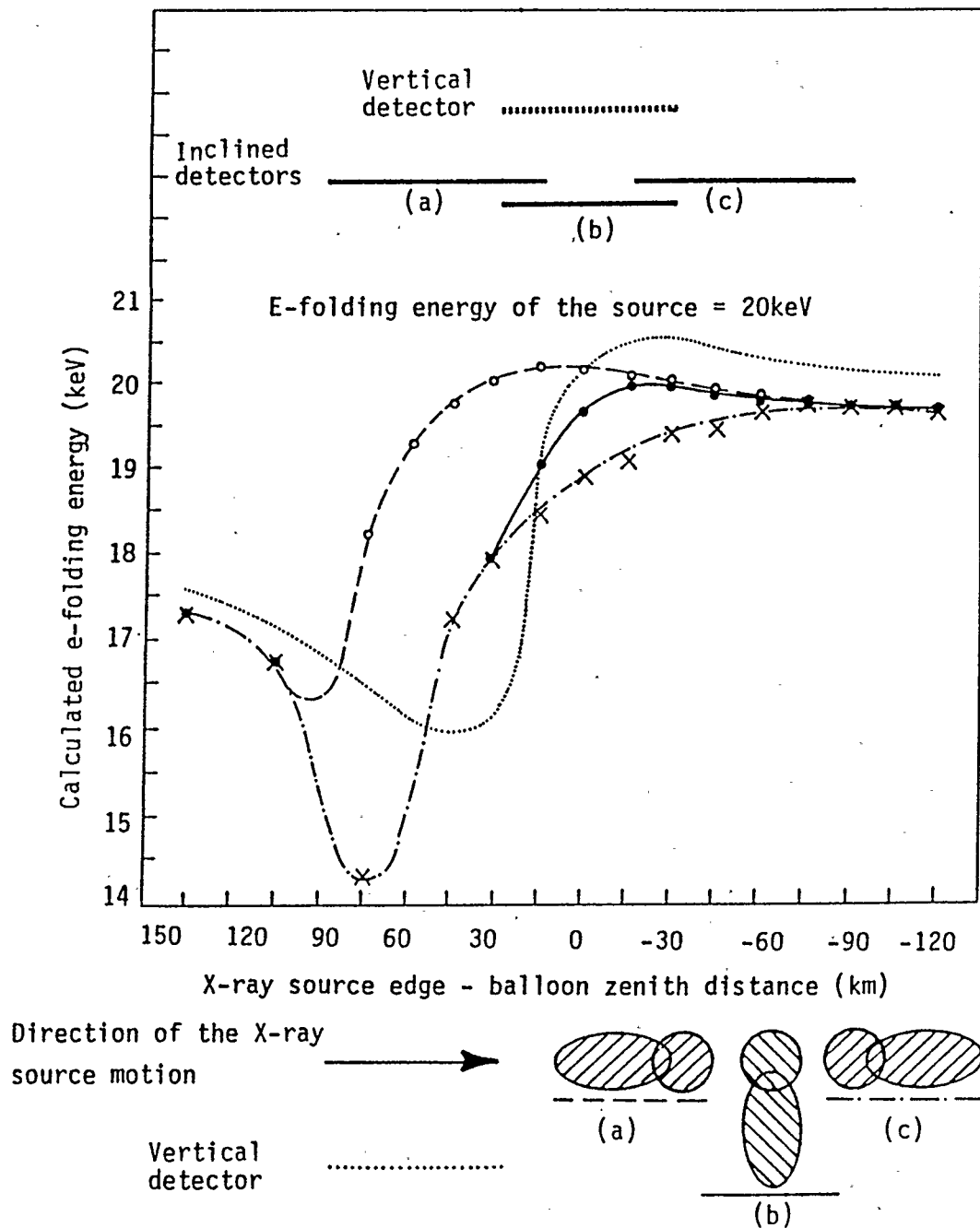
Figure 4.10 Calculated e-folding energy variation of the inclined and the vertical detector as the large X-ray source expands toward and over the fields of view of the detectors. The atmospheric depth of observation is $9g/cm^2$, the altitude of the X-ray source is $90km(0g/cm^2)$. The assumed orientations of the inclined detector are shown above. The heavy lines show the extent of the detectors fields of view for the orientations (a),(b) and (c).
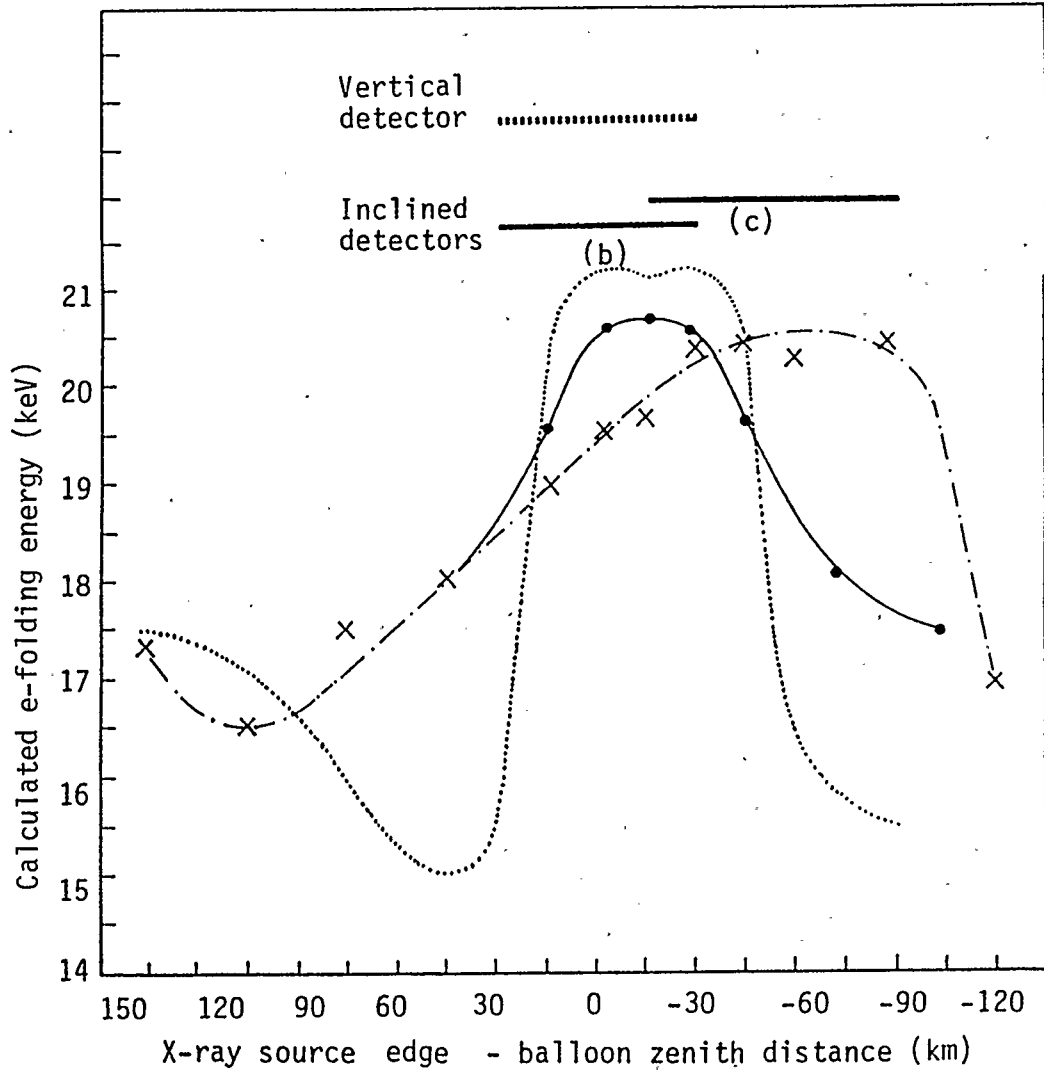
Figure 4.11 Calculated e-folding energy variation of the inclined and the vertical detector as the 30km wide band-like X-ray source moves toward and over the fields of view of both detectors. Only two orientations,namely (b) and (c) are shown since the orientations (a) and (c) are symmetrical for this source. See Figure 4.10 for labelling.

variation (Figure 4.10 and 4.11) depend on the size and the movement of the source with respect to the field of view of the detectors.

In all cases considered, the observed spectrum at the atmospheric depth of 9 g cm^{-2} is softer then the spectrum of the source at 0 g cm^{-2} whenever the x-ray source is located outside the field of view of the detectors. At this point the detectors are sampling only the scattered x-ray component and hence the observed e-folding energy is less than that of the source. As the x-ray source enters the illumination area of the detectors, the spectrum hardens due to the contribution of direct x-rays to the total flux sampled by the detector. For example, in case of orientation (a) (Figure 4.10) the abrupt spectral hardening at the source-detector distance of 90 km is caused by direct x-rays entering the inclined detector, while spectral softening trend is observed by the vertical detector. As the edge of the x-ray source crosses the 30 km source-detector distance, the vertical detector begins to register direct x-rays which produces sharp spectral hardening (Figures 4.10 and 4.11) by 25 percent and 30 percent respectively. The amount of spectral hardening increases with decreasing area of the source. Note the symmetrical variation (Figure 4.11) of the e-folding energy as the 30 km wide x-ray source moves in and out of the field of view of the vertical detector.

4.6 Study of the Dynamics of X-Ray Aurora Using

Observations

Using the method of ratios described earlier, the morphology of the x-ray aurora observed during the CL-2 balloon flight will be examined.

The ratios formed from the observed count rates of detectors #1, #2, and #4 during the CL-2 flight are shown in Figure 4.12. The energy region selected is 100-120 keV because of a larger sensitivity of the ratio at this energy level to the source movement. To aid data interpretation, the x-ray intensity profile and the e-folding energy variation of the vertical detector (detector #1) are also given. For convenience, some of the events in Figure 4.12 are highlighted with capital letters A to I. These events appear to indicate the movement of the x-ray source with respect to the fields of view of the detectors as based on the analysis done on the simulated x-ray sources in the previous sections.

Events such as A, C, and G for example show the increase in the ratio R_{12} accompanied by an increase of x-ray intensity and spectral hardening. Referring to the results from previous sections, the increase of the ratio R_{12} can be interpreted that the x-ray source had moved closer to the balloon and covered up a larger portion of the field of view of detector #1. This is accompanied by the spectral hardening due to the fact that a larger
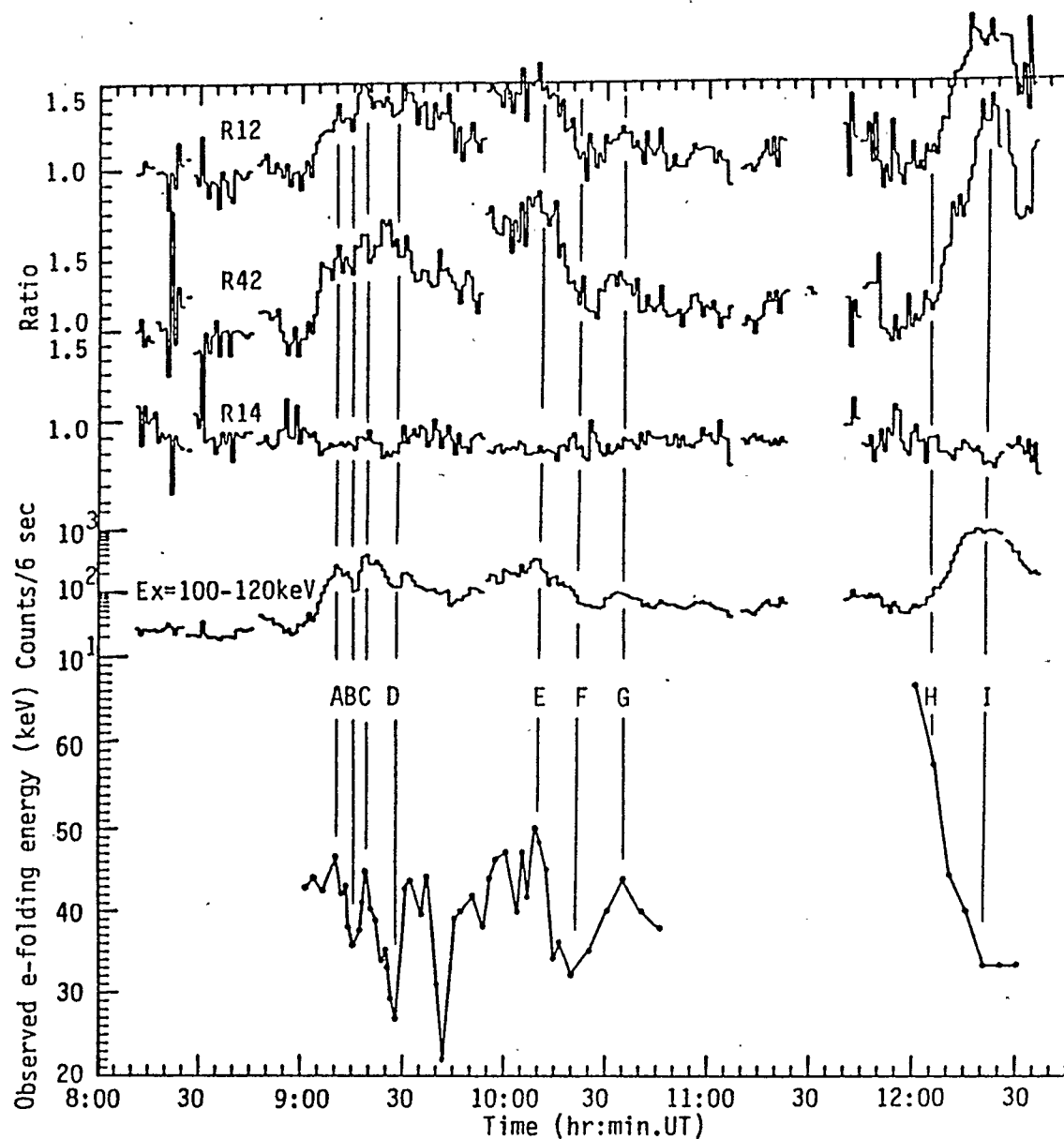
Figure 4.12 Variation of ratios R12,R42 and R14(formed in the 100-120 keV
energy region) during the CL-2 flight (October 14.1982).
The X-ray count rate profile(Ex=100-120keV) and the observed
e-folding energy variation of the vertical detector is shown
at the bottom. The smaller events highlighted with letters
are discussed in the text.

fraction of direct x-rays are now entering the detector as well. The third effect is increase of x-ray intensity since the x-ray source is now closer. The partial retreat of the source from the field of view of the detector #1 can be observed in events B and D indicated by the decrease of R_{12} ratio, decrease of x-ray intensity and spectral softening. Event F for example is even more interesting since the ratios R_{12} and R_{42} drop to 1 indicating that the x-ray source had moved out of the field of view of all the detectors completely.

Evidently thus, the impulsive x-ray events observed during Ax1 (see Figure 3.4 for the labeling and Section 3.3.4 for discussion of the x-ray activity) were caused by the motion of the x-ray source. Similar x-ray intensity variation caused by the movement of the source had been reported for example by Clark and Anger (1967) as deduced from the motions of the auroral electrojet. The e-folding energy variation observed for example during the Ax1 event can be considered as apparent only, caused by the motion of the x-ray source.

Events H and I on the other hand seem to indicate a true spectral softening as both the ratio R_{12} and the x-ray intensity increase, while at the same time the spectrum softens. Expansion of the x-ray source would produce apparent spectral softening (Pilkington, 1970) and x-ray intensity increase but at the same time the ratio R_{12} would decrease.

The average values of R_{14}, R_{42}, and R_{12} between 09:10 UT and 09:30 UT can be used to approximate average source edge-zenith distance during the AXl event. Using Figure 4.12, these average values for R_{14}, R_{12}, and R_{42} are 0.85 ± 0.05, 1.45 ± 0.15, and 1.5 ± 0.1 respectively. Also refering to Figure 3.2 (Chapter 3), the inclined detector #4 during this time interval was pointing in NW-N direction while the inclined detector #2 was at the same time pointing in the S-SW direction respectively. In Figure 4.6 for example the geometrical relationship between detectors #1 and #4 can be approximated by the orientation (a) while orientation (b) can be used for detectors #1 and #2. For detectors #4 and #2 the ratio can be calculated by eliminating the vertical detector simply by dividing the ratio of orientation (b) by the ratio of orientation (a). Using Tables 4.1-4.3 we find that the sets of ratios at the distance of 15 km between the zenith and the edge of the source is 0.76, 1.33, 1.75 (Table 4.1); 0.74, 1.32, 1.78 (Table 4.2); and 0.92, 1.6, 1.73 (Table 4.3) which are the sets closest to the one calculated from real data. Based on this result, and noting that other distances do not give such a close set of ratios, we conclude that the source was probably located somewhere in the vicinity of this distance from the zenith. The size of the equivalent source is difficult to estimate from tables alone and one should refer to Figure 4.6-4.9. For example, in Figure 4.6 at the distance of slightly less than 15 km, the ratio for

orientation (a) is 0.85 while for orientation (b) is 1.38. Decreasing the source size (Figures 4.7-4.9) and keeping the ratio for orientation (a) at 0.85, we obtain the ratios for orientations (b) 1.38 (Figure 4.7), 1.7 (Figure 4.8), and 2.8 (Figure 4.9) indicating that the larger x-ray source at this time produces a better fit.

On the other hand, during the peak of Bx event (12:20 UT) the ratios R_{14}, R_{42}, and R_{12} are 0.7, 2.4, and 1.9 respectively requiring one ratio of the vertical versus inclined detector to be small (0.7) while at the same time with respect to the other inclined one, the ratio must be large (1.9). In Tables 4.1-4.4 looking for the combination 0.7 and 1.9 we exclude x-ray sources relating to Tables 4.1-4.3. Table 4.4 indicates that between the distance of 22.5 and 37.5 km the combination could be formed.

Using Figure 4.9 and setting orientation (a) at 0.7 we find the corresponding value for orientation (b) to be 2.1 resembling the R_{14} and R_{42} ratios. The calculated ratio for the two inclined detectors is 3.0. Although higher than the ratios from real data, the net result indicates that the x-ray source during the Bx event at 12:20 was relatively small. The inclined detector #4 at this time was pointing in the SE direction (Figures 3.2, Chapter 3) suggesting that the source was located to the east or southeast of the balloon zenith.

Further rotation of detector #4 after 12:20 UT (see Figure 3.2) to the S and SW could have caused the ratio

R_{12} and R_{42} to drop somewhat (see Figure 4.12) as the source has also entered the field of view of the inclined detector #2 which by 12:28 UT was also pointing to the East.

4.7 Discussion of the Monte Carlo Simulation

The motion of the x-ray source can be detected by introducing a ratio formed from count rates measured by the individual x-ray detectors in the payload.

It is observed that the relative magnitude of scattered x-ray flux entering the zenith angle intervals of 0°-30° and 30°-60° will depend on the source-detector distance. The vertical detector having the solid angle of acceptance located entirely in the 0°-30° zenith angle interval shows maximum sensitivity at the source-detector distance within ± 30 km. This high sensitivity of the collimated vertical x-ray detector within a small source-detector distance had also been pointed out by Pilkington (1970). On the other hand, . the inclined detector also sampling the x-ray flux in the 30°-60° zenith angle interval shows maximum sensitivity at the source-detector distance between 45 to 75 km.

The result of the simulation study indicates that the ratio formed from the count rates of inclined and vertical detectors can in principle monitor the motion of the x-ray source. The sudden change of the count rate ratio will be due to the entry or exit of the x-ray source into the field

of view of one of the detectors.

The sensitivity of the ratio to the x-ray source variation increases with energy of the x-rays and decreases with the increasing area of the source. In real data application it is thus advantageous to look preferentially at the ratios formed from higher energy x-rays.

Due to the preferential depletion of x-rays at the soft end of the spectrum, the e-folding energy of direct x-rays is larger than that of the source itself. The net result is that the observed spectrum can actually become harder even with the scattered component present. This is more so for the smaller x-ray source because the contribution of scattered component to the total measured x-ray flux decreases with the area of the source.

On the other hand, when the x-ray source is located outside the detector's field of view, the measured spectrum will be softer than the original spectrum. Depending on the relative source-detector distance, the measured e-folding energy can be up to 30 percent less then that of the source itself.

When a uniform x-ray source covers the field of view of both the inclined and the vertical detectors, the vertical detector will measure a harder spectrum. The results from the simulation study were applied to real data collected during the flight of October 14, 1982.

The ratios R_{12}, R_{42}, and R_{14} have shown that during the main x-ray events (described in Chapter 3) the x-ray source

has entered only the fields of view of detectors #1 and #4 but not of detector #2. In addition a smaller variation in the ratios with similar variation of x-ray intensity and e-folding energy have shown that the source is not stable in position, but moving. The x-ray source during the AX1 event for example has been estimated to be large, deduced from the relative magnitudes of ratios while probably a small source was in the fields of view of the detectors #1 and #4 during the Bx event. It has also been determined that the decay of x-ray activity during the Ax2 event is due to the exit of the x-ray source from the field of view of all the detectors thus producing only apparent decay of x-ray activity. The exact geometry of the x-ray source cannot however be determined using this detector system and thus reference should be made to the so-called equivalent x-ray source only. The method provides the opportunity to deduce the changes of the x-ray source position with respect to the fields of view of the detectors, even at greater atmospheric depths. The improvement, for example, would be to simulate more sources with different sizes and geometry so that the relative magnitudes of ratios can be matched for more situations.

CHAPTER 5

STUDY OF X-RAY AND OPTICAL AURORAL EMISSIONS

This chapter explores the association between the x-ray and optical auroral emissions during the magnetospheric substorm on October 14, 1982.

The first section deals with the morphology of the optical auroral substorm during the CL-2 balloon flight as observed by the ground-based all-sky CCD camera. This is compared with the temporal and spatial variations of the x-ray aurora as determined from the previous two chapters. Observations of the anomalously high flux of soft x-rays appearing predominantly in the 20-40 keV energy channel during the various time intervals of the CL-2 flight is given in Section 2. Sections 3 and 4 deal with the nature of the x-ray source producing the observed soft x-ray flux at the atmospheric depth of 9 g cm^{-2}. In section 5 the association between the source of soft x-rays and auroral electrons is explored. A quantitative comparison between the intensities of the optical and the soft x-ray emissions during the CL-2 flight is given in Section 6.

5.1 The Comparison of 5577A Optical and X-Ray Auroral

Substorms During the CL-2 Flight

After the balloon reaches the float altitude, the first
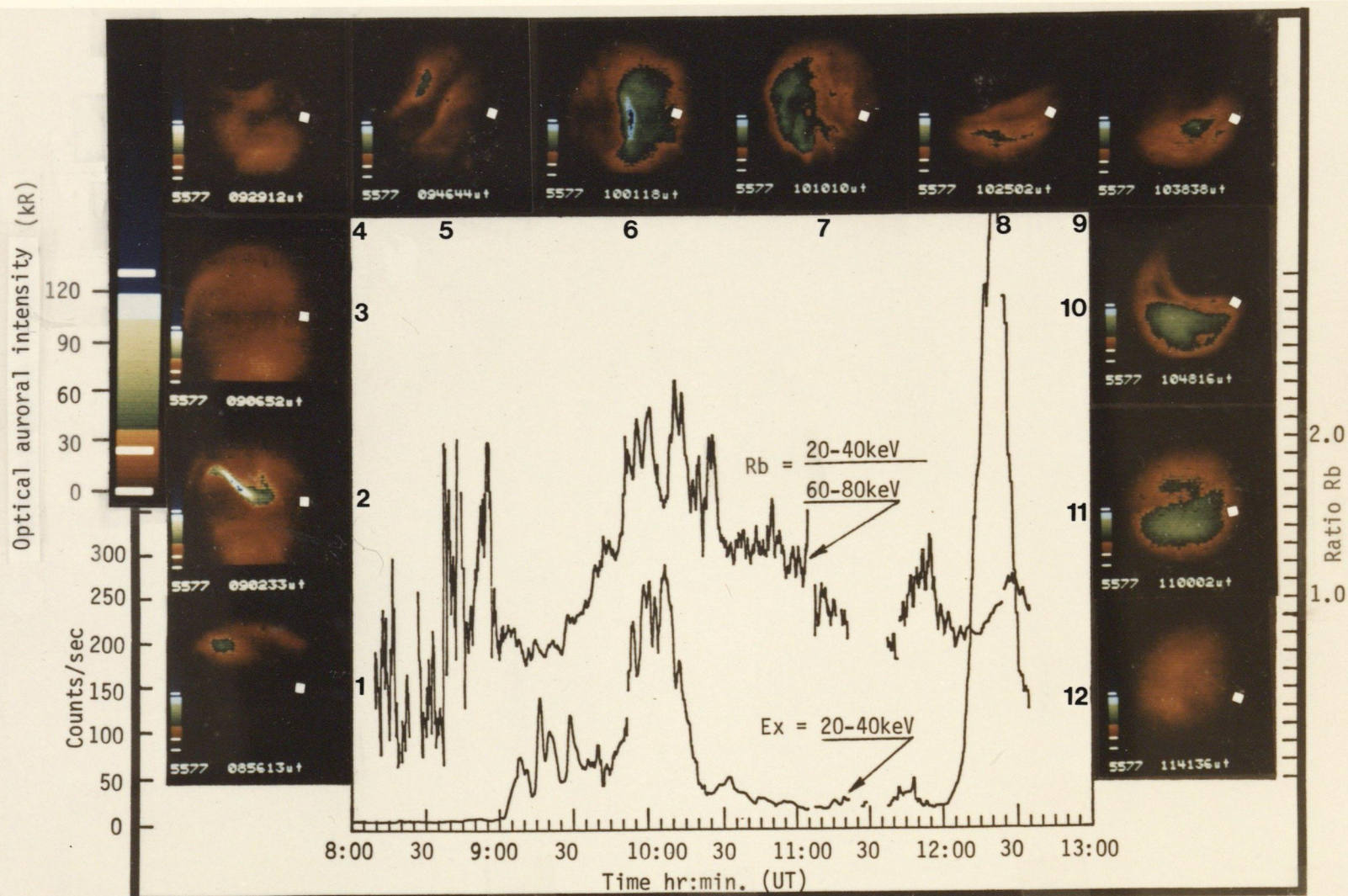
Figure **5.1** X-ray intensity (E_x=20-40keV) and R_b ratio variation during CL-2 flight. The all-sky photographs show the auroral activity in 5577 Å wavelength. The white dots show balloon zenith.

sign of more intense visual auroral activity is observed at 08:50 UT (Frame #1, Figure 5.1) showing as intensification of the auroral arc to the North of Cold Lake. To the South, the optical aurora is relatively structureless with estimated intensity of 5 kR. The white dot shows the zenith of the balloon.

Intensification of the auroral activity after 08:50 UT continues as the expansive phase of the first magnetospheric substorm during the CL-2 flight unfolds. Frames #1 and #2 show the expansion of the auroral activity which is typically associated with the expansive phase of the substorm. The auroral arc located to the North develops into a curl structure reaching intensity of 100 kR (Frame #2). As evident from Figure 5.1, a rapid increase of x-ray activity (onset of the Ax1 event) is observed at the same time when the optical aurora covers the whole sky (Frame #2). The onset of the x-ray activity is, however, delayed by 12 minutes with respect to the auroral activity. The delay could be actually a spatial effect only since, according to Bewersdorff et al. (1968), the x-ray precipitation starts at $L = 6.5$ and then spreads equatorward to lower L values (L value of the balloon's location $\cong$ 4.9). In general, the optical activity remains high until 09:05 UT after which the discrete auroral activity disappears and by 09:07 UT (Frame #3) there is only diffuse aurora covering the whole field of view with estimated intensity of 25-30 kR. Strong x-ray activity is observed

at this time (see Frame #3 and the bottom plot in Figure 5.1). Between 09:07 UT and 09:28 UT there is a period of low optical activity. In the same time interval, however, the x-ray activity is high, showing the presence of impulsive events (Figure 5.1, bottom plot). This temporal variation of the x-ray activity, as established in Chapter 4, was due to the movement at the x-ray source in the fields of view of the detectors. Frame #4 (09:29 UT) shows some patchy aurora with intensity 25-30 kR; the optical activity begins to intensify after this time and the patches in Frame #4 develop into two distinct curl-like structures, one directed in the NW-SE and the other in the SW-NE direction. The peak intensity of these structures is 90 kR and the estimated length is between 300-400 km. This is followed by the period of gradual decay, the relative optical x-ray activity minima being reached at 09:42 UT.

Recovery of the optical and the x-ray (the Ax2 event) activity after 09:42 UT is evident in Figure 5.1 from Frames #5 and 6 and from the x-ray plot. It also should be pointed out that after the time 09:50 UT the intensity of the optical aurora could not be monitored since the optical data are missing between 09:50 UT and 10:00 UT. It appears that there is a rapid increase of optical activity between 09:50 UT and 10:00 UT, reaching the peak intensity at 10:01 UT as shown in Frame #6. The maximum intensity reaches 120 kR with 60 kR in the vicinity of the balloon, as strong 60-90 kR aurora covers 30 percent of the field of view of the
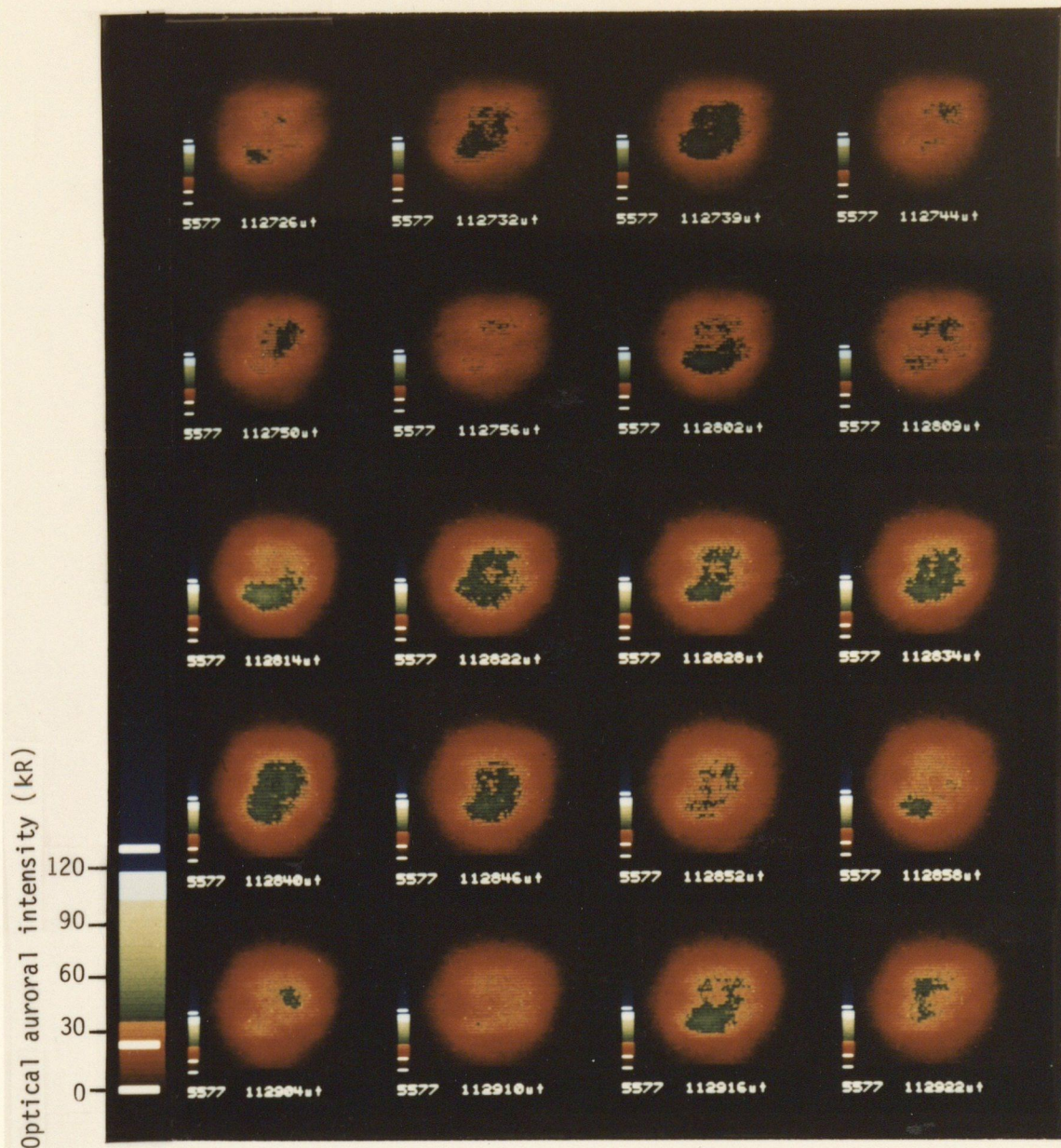
Figure 5.12 A good example of the optical auroral pulsations observed in
the local morning sector.The observed intensity variations
are   10kR. The time interval shown is from 11:27:26UT-
11:29:22UT.

camera. Prior to this time, as the optical Frames #1-#5 show, the optical activity in the vicinity of the balloon was < 30 kR.

The optical activity remains high up to 10:10 UT after which the activity begins to subside, the decrease in intensity being more rapid to the north of balloon's latitude. This is shown in Frames #8, #9, and #10 where the strong optical activity generally thrusts to the south of the balloon while to the north the activity is much lower. The general decrease of the optical activity is accompanied by a similar decrease of the x-ray activity, shown as a rapid intensity drop after 10:10 UT. However, as determined in Chapter 4, the x-ray activity after 10:10 UT actually moved Northward; no such a movement of optical activity is evident during the same time. On the contrary, the strong aurora with maximum intensity in the vicinity of 80 kR remains situated to the South and expands northward only by 11:00 UT (Frame #11). The observation seems to indicate that the net movements of the optical and x-ray auroral features do not correlate with each other. Frames #8, #9, and #10 also show that the optical intensity in the vicinity of the balloon was 25-30 kR.

The morphology of the aurora after 11:00 UT remains essentially the same as that shown in Frame #11, only the intensity of the green patch shows some intensity variations suggesting the presence of pulsating activity. This is shown in Figure 5.2 using the all-sky images between the

time period of 11:27:26 UT and 11:29:22 UT, with estimated variation in intensity of 10 kR. The last frame (#12) in Figure 5.1 shows the optical auroral activity at 11:41:36 UT indicating a relatively low intensity featureless glow after the recovery phase of the substorm. Due to the sunrise, the optical images were taken only up to 12:00 UT, the Frame #12 representing the typical auroral display till the end of the optical data gathering.

5.2 Detection of the Extra X-Ray Counts in the 20-40 keV Energy Channel

Spectrum plots during the Ax1 event (flight CL-2) as well as at various time periods of the CL-1 flight indicate that the observed count rate in the 20-40 keV energy channel was lower than the count rate observed in the next higher energy channel of 40-60 keV. The smaller count rate in the 20-40 keV energy channel is due, as pointed out in Chapter 1 (Section 1.2), to photoelectric absorption preferentially operating on the low energy end of the spectrum, resulting in the removal of x-ray photons below 50 kev from the spectrum and thus generating a hump on the spectral plot in the 50-60 keV energy interval. Reports from earlier balloon observations (for example, Barcus and Rosenberg, 1966; Vij, 1974; and Parks et al., 1979) have shown similar absorption effects at the low energy end of the spectrum. However, it should be pointed out that the observed count rate in 20-40 keV energy channel was not always below the count rate of
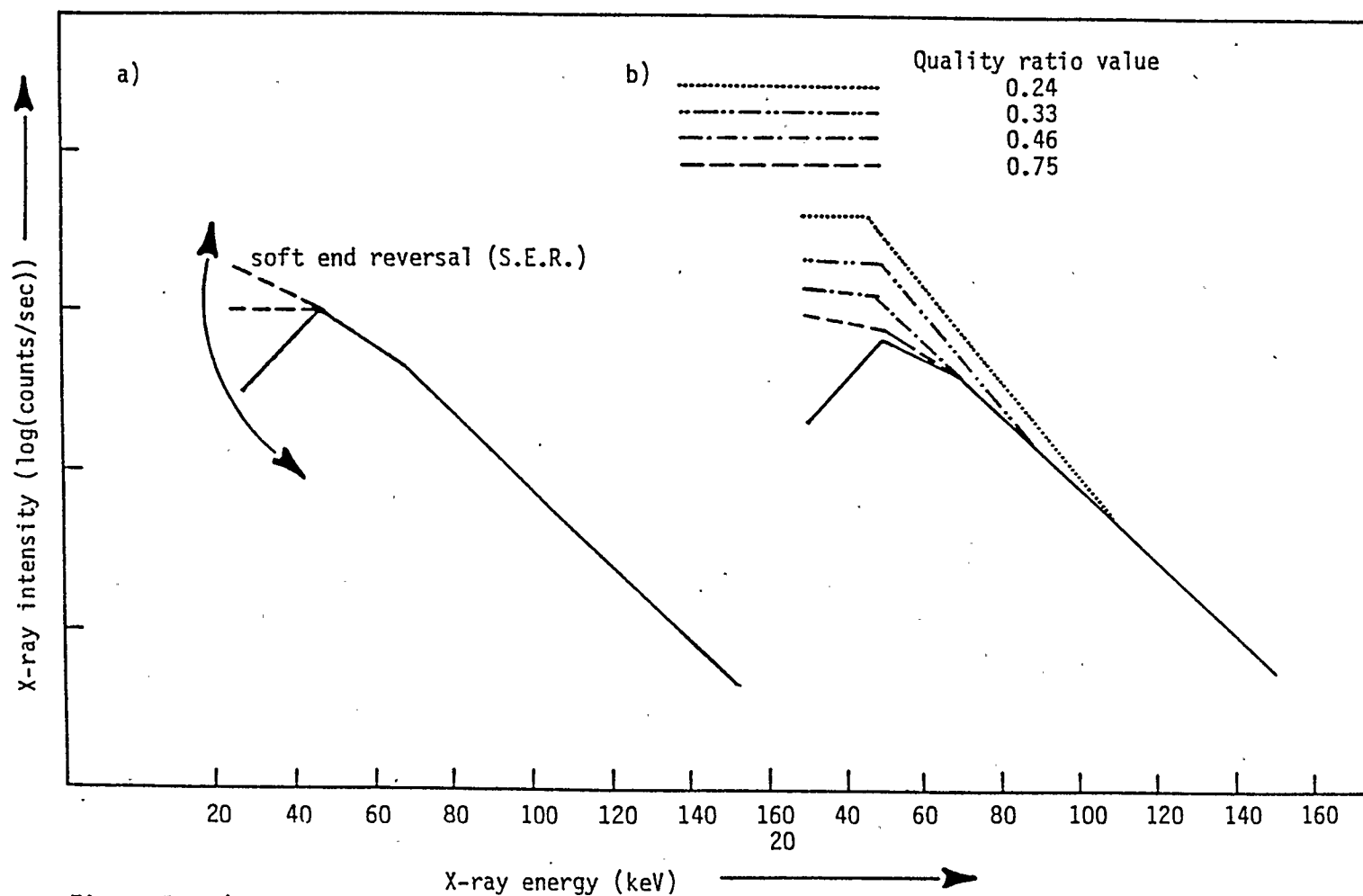
Figure 5.3 a) Flapping motion at the low energy end of the spectrum is caused by the extra amount of
X-rays entering into the 20-40kev energy channel.The dotted lines show the soft end
effect(S.E.R).

b) The soft X-ray sources having low quality ratio will produce a break in the observed
composite spectrum.

the 40-60 keV energy channel. The spectral plots exhibit the extensive up and down motion at the lowest energy end of the spectrum as indicated in Figure 5.3 a. Spectra observed for example after 09:45 UT during CL-2 flight (see spectral plots in Chapter 3, Figures 3.6, 3.7, and 3.8) show that the count rate in the 20-40 keV energy channel has increased on numerous occasions to values exceeding the count rate in the 40-60 keV energy channel. This indicates that there must be an additional source supplying soft x-rays into the 20-40 keV energy channel. This special event, (count rate in the 20-40 keV energy channel equals or exceeds the count rate in the 40-60 keV energy channel) will hereafter be referred to as the soft end reversal (S.E.R.) effect. In Figure 5.4, the S.E.R. effect during CL-2 flight is shown as a shaded region above the horizontal line at which the ratio equals unity.

On several occasions, the S.E.R. effect has been observed during CL-1 flight (see Figure 3.11, Chapter 3). The vertical axis in Figure 5.4 is the ratio (R_a) between the count rate observed in the 20-40 keV energy channel (C(20-40)) and count rate in the 40-60 keV energy channel (C(40-60)). The ratios shown in Figure 5.4 have been smoothed by taking moving averages. The large fluctuations in the value of R_a observed prior to 09:00 UT are due to large statistical errors in the low background count rates. Shortly after 09:00 UT the values of R_a, for both the inclined detector #2 and the vertical detector, are seen to
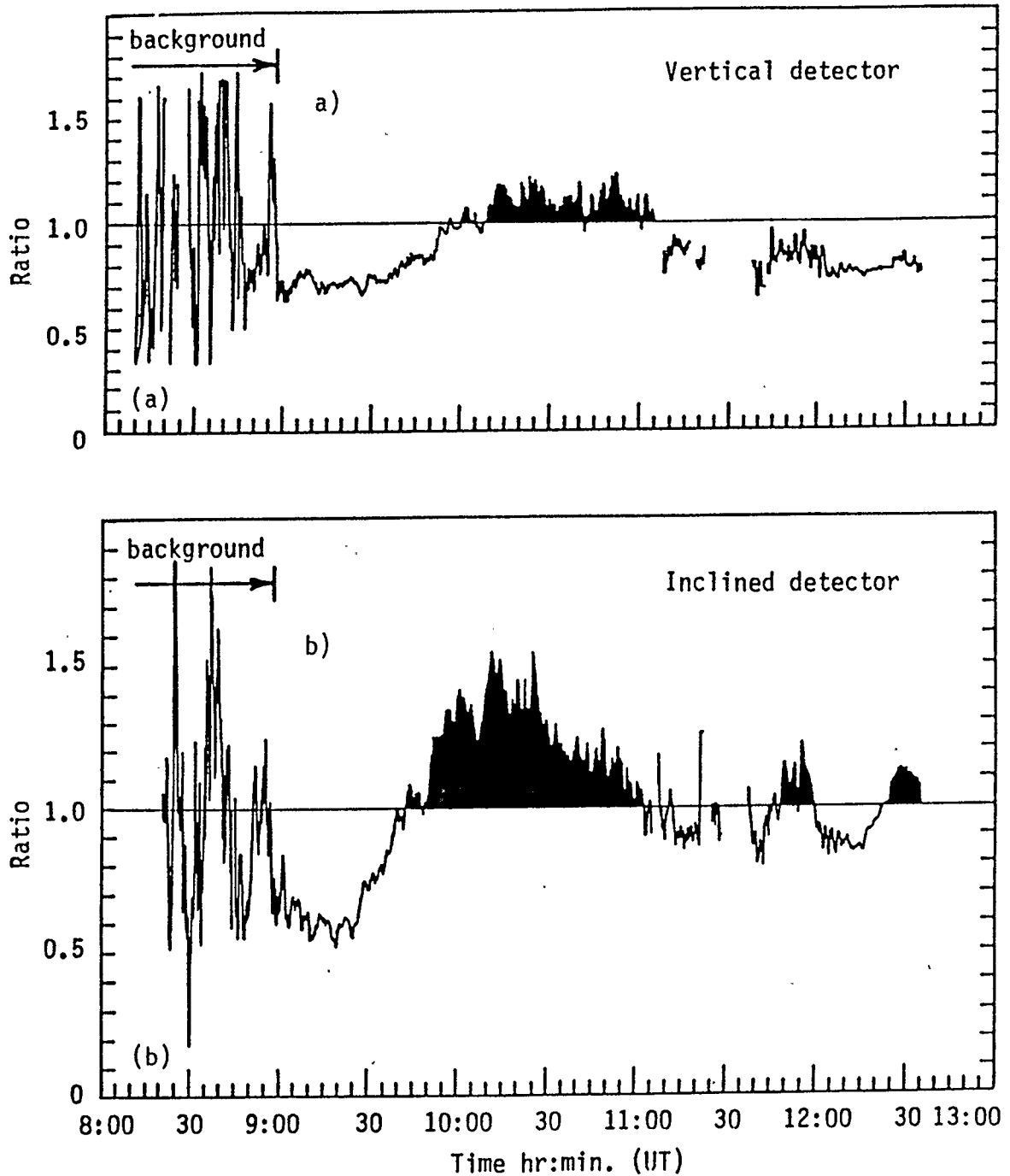
Figure 5.4   Ratio $\frac{20\text{-}40\text{keV}}{40\text{-}60\text{keV}}$ during CL-2 flight showing the soft end reversal(S.E.R.) events as the shaded region above the unity. The large ratio fluctuations(prior 09:00) occurs when the count rate is at the background level.

be 0.6 and 0.7 respectively, showing the effect of photoelectric absorption operating on x-rays in the 20-40 keV energy region. After 09:35 UT, the value of R_a begins to increase, the observed increase being steeper for the inclined detector #2 (panel b, Figure 5.4). The ratio (R_a) exceeds the value of unity only moderately in case of the vertical detector but as panel b (Figure 5.4) shows, the observed countrate in the 20-40 keV energy channel of the inclined detector #2 exceeds the countrate in the 40-60 keV channel by up to 50 percent. The nature of the parent x-ray source capable of producing the S.E.R. effect and the association of this extra soft x-ray flux with the optical aurora are explored in the following sections.

5.3 Parent X-Ray Source Producing S.E.R. Effect

Monte Carlo simulations of x-rays passing through the atmosphere have been performed in order to determine the spectrum of the x-ray source capable of producing the S.E.R. effect at the balloon altitude of 9 g cm^{-2}, assuming the parent x-ray source situated at an altitude of 90 km (0 g cm^{-2}) and having an exponential spectrum given by:

$$\frac{dN(Ex)}{d(Ex)} = \frac{1}{2\pi} \ I_o \ \exp(-E_x/E_o) \ (counts \ sec^{-1} \ ster^{-1} \ keV^{-1})$$
$$(5.1)$$

where I_o ranges from 1×10^5 counts to 1×10^6 counts. For softer spectra, high values of I_o are needed to minimize the counting errors in the final output of the

program. The e-folding energy (E_0) values for the parent x-ray sources considered were 20 keV, 15 keV, 12 keV, 10 keV, 8 keV, 6 keV, and 5 keV respectively. Two independent runs for each e-folding energy case have been carried out so the results have been generated from the sum of the two runs. The results of the simulation indicate that only small e-folding energy values are appropriate for the soft parent x-ray source. Specifically, only x-ray sources with e-folding energies of less than 12 keV will, at the balloon altitude (9 g cm^{-2}), have a higher count rate in the 20-40 keV energy channel than in the 40-60 keV channel. To begin with, only a small or negligible amount of x-rays in the energy region greater than 40 keV is present. These results indicate that, even though the photoelectric absorption still affects the softest part of spectrum most dramatically, in the case of these soft x-ray sources, nevertheless the highest count rate is still in the 20-40 keV energy region.

Denoting the x-ray sources for which at the balloon altitude C(20-40) is greater than C(40-60) as "soft" and sources for which C(20-40) is less than C(40-60) as "hard", during the soft end reversal (S.E.R.) effect observed, the relation

$$C(20-40)Hard + C(20-40)Soft > C(40-60)Hard + C(40-60)Soft$$

$$(5.2)$$

or

C(20-40)Soft - C(40-60)Soft > C(40-60)Hard - C(40-60)Hard

$$(5.3)$$

holds. For use in specific real cases, it is convenient first to express the relative magnitudes of C(20-40)Soft and C(40-60)Soft for a particular soft source in terms of the ratio

$$\frac{C(20-40)Soft - C(40-60)Soft}{C(20-40)Soft + C(40-60)Soft} \qquad (5.4)$$

named here as "quality ratio". The magnitude of the quality ratio has a upper limit equal to unity and is independent of the intensity of the soft source.

Figures 5.5a and 5.5b show in simulation the variations of the quality ratio for the radially expanding soft x-ray sources and soft x-ray sources located at a gradually increasing distance from zenith. The e-folding energy values of cases considered are shown in Figure 5.5a. Figures 5.5a and b show that the quality ratio increases with decreasing e-folding energy of the source, increasing area of the source and increasing source-detector distance. X-ray sources with negative quality ratio will not produce the S.E.R. effect on the composite spectrum. Note, for example, that the x-ray source with e-folding energy = 12 keV located within a radius of less than 45 km will not produce the S.E.R. effect as the quality ratio of this source dips below the zero level as shown in Figure 5.5a.
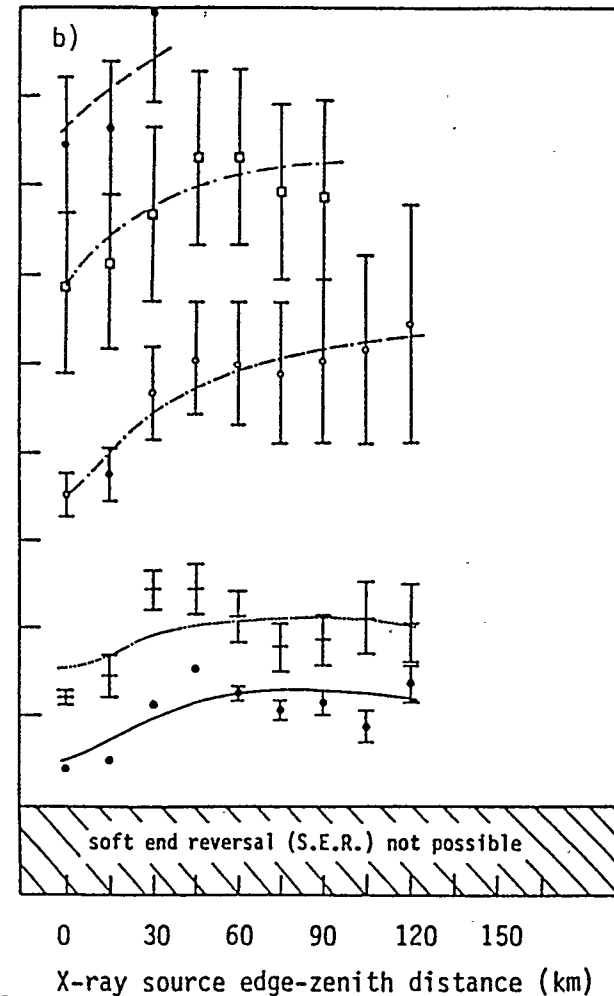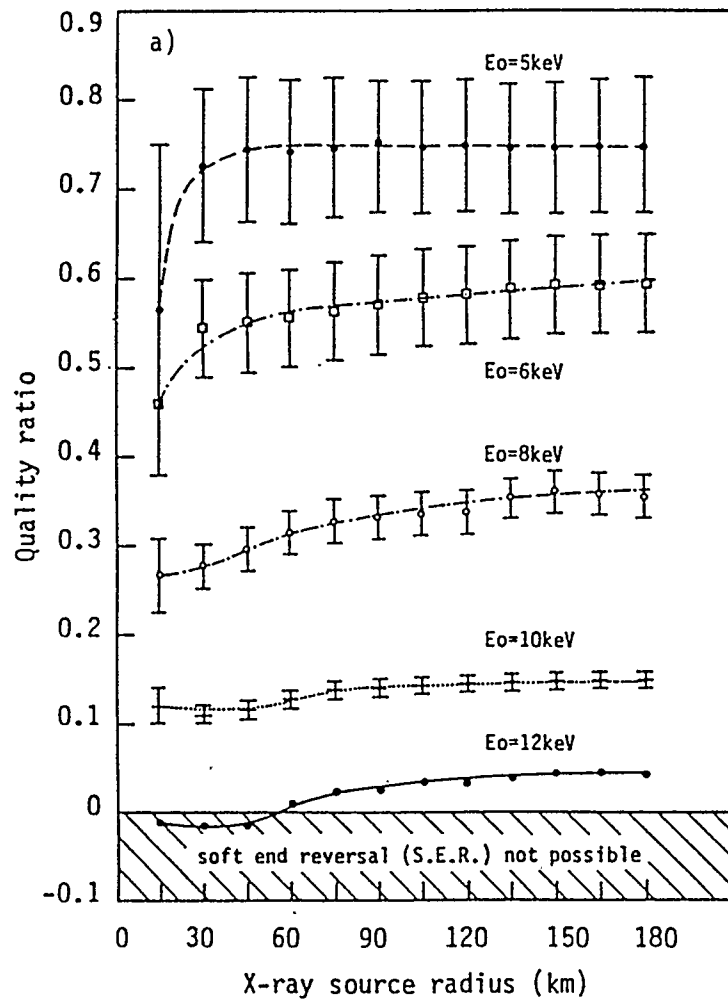
Figure 5.5 Originating from the soft X-ray source at 0 g cm^{-2}, the quality ratio(defined in the text) indicates the relative magnitudes of counts observed at 9 g cm^{-2} in the 20-40keV and the 40-60keV energy region. The heavy lines between the two panels relate to the spectrum case study done in section 5.5.
a) Radially expanding soft X-ray source
b) X-ray source receding from zenith

X-ray sources with low but positive quality ratio will produce the S.E.R. effect on the composite spectrum but will also produce breaks in the final spectrum due to a relatively significant count observed in the 40-60 keV or even 60-80 keV energy window. This is summarized in Figure 5.3b which shows a break development on the composite spectrum as the quality ratio decreases.

5.4 Method of Obtaining the e-folding Energy of the Soft X-Ray Source - A Case Study

During the S.E.R. event observation, the count rate in the 20-40 keV and 40-60keV energy channels are related by equation 5.2 and so in order to determine the spectrum of the soft component, the entries on the left and the right hand sides of equation 5.2 must be separated. Example of the spectrum during the observed S.E.R. event is shown in Figure 5.6 with the soft and the hard components separated. Here, the spectrum is plotted on a linear scale to show better their relative magnitudes. It is the (i) portion of the composite spectrum which is always observed, the soft end of the hard component is buried.

In the next few paragraphs, a specific spectral case observed at 10:45 UT during CL-2 balloon flight is considered. The aim here is to determine the spectrum and the intensity of the soft x-ray source and hence the cause producing these S.E.R. events.

Figure 3.9 (Chapter 3) shows that the particular
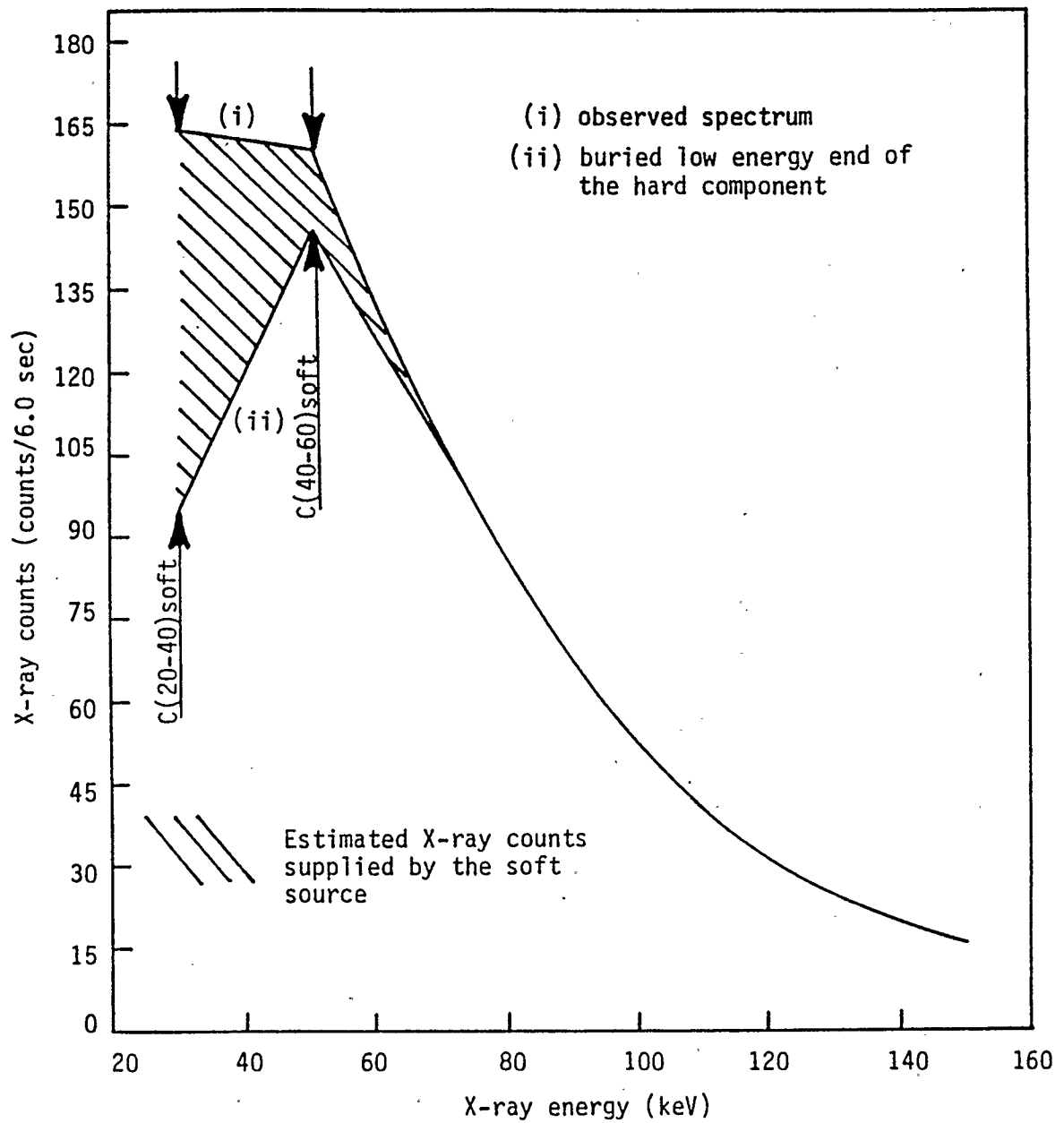
Figure 5.6 Schematic diagram showing the low-energy end of the
hard spectrum(curve(ii)) buried with the soft X-ray
flux(curve(i)). The spectrum is plotted on the linear
scale to show better the magnitude of the soft flux.

spectrum is showing the S.E.R. effect; the e-folding energy of the hard component is 40 keV.

In order to obtain the x-ray intensity at the low energy end of the hard component, two cases for the hard source are considered. These are:

I) x-ray source with e-folding energy equal to 60 keV located outside the detector's field of view. The apparent e-folding energy of this source at the balloon's altitude is 40 keV.

II) x-ray source with e-folding energy equal to 40 keV covering the detector's field of view.

The x-ray counts from the soft source are then obtained by first matching the intensities of the I and II spectra with the observed spectrum at 10:45 UT (CL-2 flight) over the energy region $E_x > 70$ keV. Then the soft ends in the region $E_x < 60$ keV are subtracted as shown in Figure 5.6 and the required C(20-40)Soft and C(40-60)Soft were determined for the two cases. The values obtained are given in Table 5.1

TABLE 5.1

CALCULATED SOFT X-RAY FLUX IN THE 20-40KEV AND 40-60KEV ENERGY
REGION AT 10:45 UT FOR THE TWO CASES OF THE HARD SPECTRUM.

HARD SPECTRUM COMPONENT	REQUIRED $C(20-40)_{SOFT}$	REQUIRED $C(40-60)_{SOFT}$
CASE I	14.2 ± 1.37	2.69 ± 0.59
CASE II	12.9 ± 1.30	2.10 ± 0.53

Evidently, at this particular time the soft source is supplying x-ray flux ranging between 10 to 14 counts sec^{-1} cm^{-2} $ster^{-1}$ into the 20-40 keV channel of the detector while supplying 2 to 3 counts sec^{-1} cm^{-2} $ster^{-1}$ into the 40-60 keV energy channel.

The quality ratios associated with these quantities in Table 5.1 are 0.69 ± 0.10 and 0.72 ± 0.11 for Case I and II respectively. The results from Chapter 4 indicate that the hard x-ray source at this time was located outside the fields of view of the detectors and hence Case I seems to be the more appropriate choice. The e-folding energy of the equivalent source can be determined from Figure 5.5 where the quality ratios for Cases I and II are shown with heavy lines. The simulated sources matching the quality ratios of the real source can in principle supply the correct relative
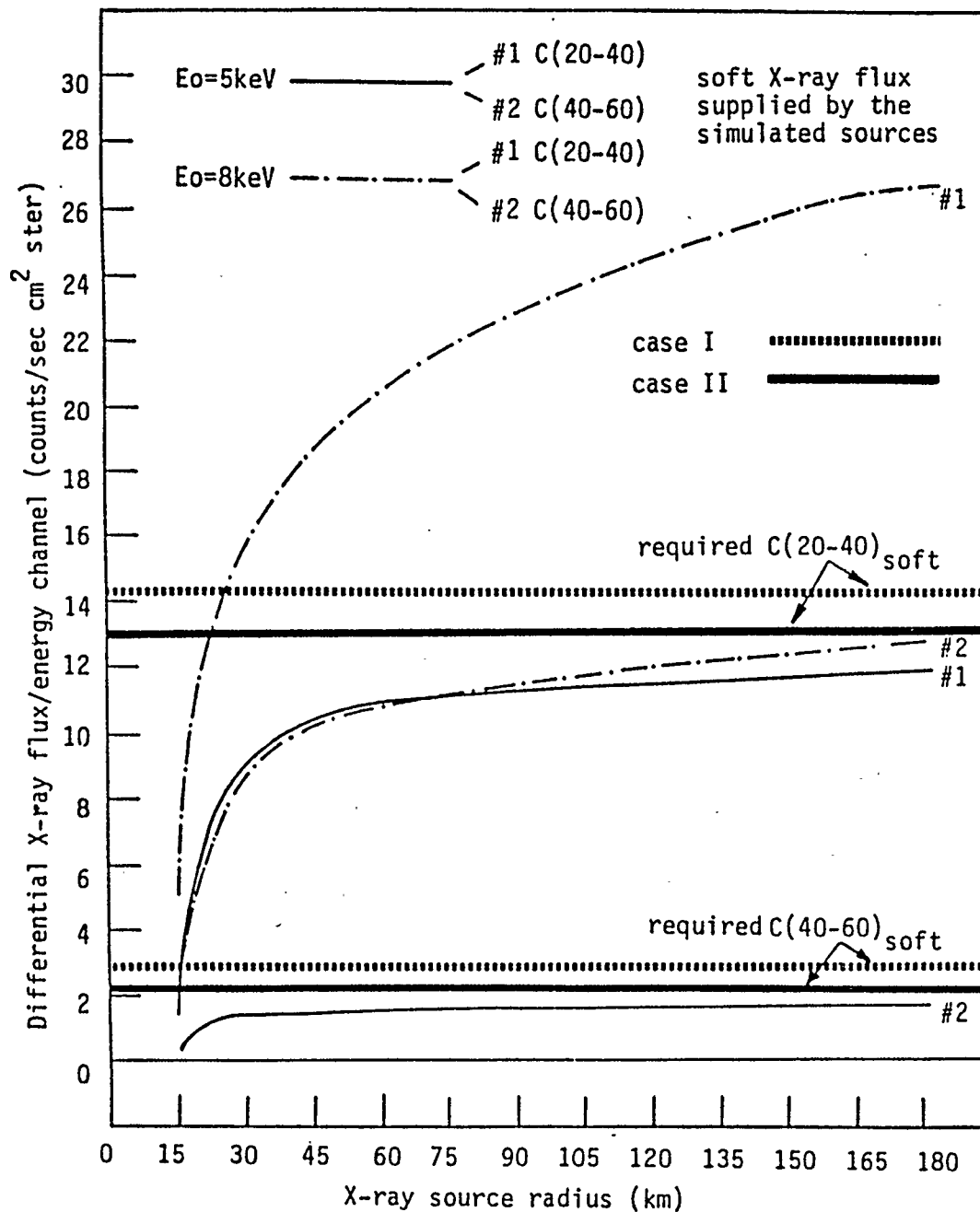
Figure 5.7 The relative magnitudes between 20-40keV and 40-60keV X-ray flux at the atmospheric depth of 9 gcm^{-2} supplied by the simulated X-ray sources (0gcm^{-2}) with increasing radius(light curves).The e-folding energies of the sources are shown above. The heavy lines show the required soft X-ray flux (taken from Table 5.1) for the cases I and II(see text).
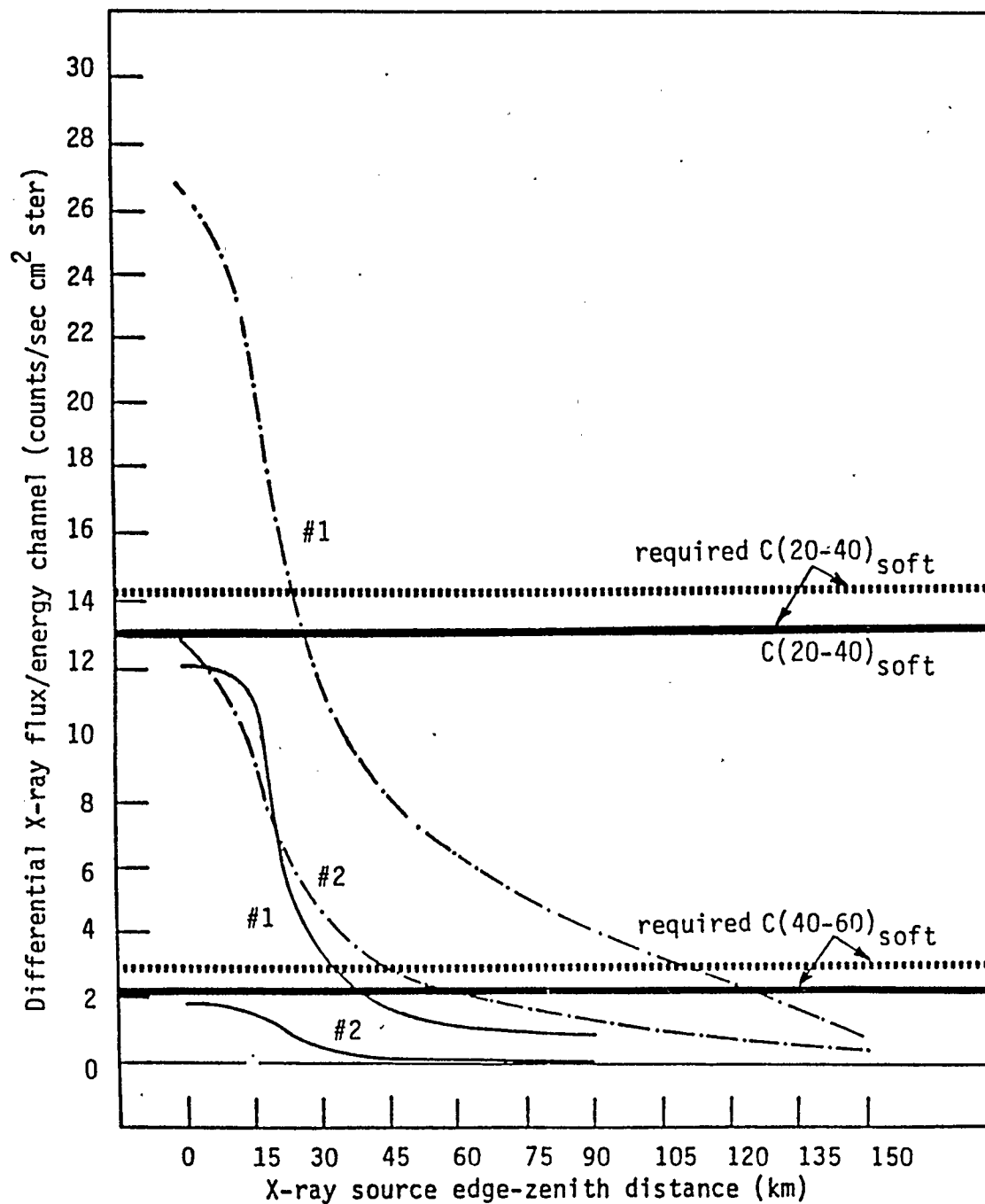
Figure 5.8 The same as Figure 5.7 but now the simulated X-ray
sources are being gradually moved to a larger
distance from zenith.

counts into the 20-40 keV and 40-60 keV energy channels. As Figures 5.5a, b, show, these sources have e-folding energies 5-6 keV depending on the location of the source in relation to the detector. The sources with e-folding energies of 8, 10, and 12 keV must be rejected as their quality ratios (Figures 5.5a and b) are too low and would not supply the proper amount of x-rays into the 20-40 keV and 40-60 keV channels. Quantitatively, this is shown in Figures 5.7 and 5.8. In Figures 5.7 and 5.8 the light lines are the graphically smoothed relative magnitudes of the x-ray flux into the 20-40 keV energy channel and 40-60 keV energy channel, which the soft sources with e-folding energies 8 keV and 5 keV and intensity at zero energy of 6.7×10^3 and 3.3×10^4 photons cm^{-2} sec^{-1} respectively can supply. The lines can be moved vertically up and down which would correspond to changes of soft source intensity. The heavy lines represent the required counts into 20-40 keV and 40-60 keV energy channels as presented in Table 5.1 in connection with Case I and II.

Examination of, for example, the soft source with E_O = 8 keV in Figures 5.7 and 5.8 shows that it supplies too many x-rays into the 40-60 keV energy channel and not enough into 20-40 keV energy channel. This is evident as the light line #2 for this harder source will always cross the lower heavy line before the light line #1 crosses the upper heavy line for each specific Case I or II. The situation for example is good in case of the source with e-folding energy

equal to 5 keV, because the light lines #1 and #2 can cross the heavy lines simultaneously. Using Figure 5.5a it is evident that the size of source cannot be determined exactly, only the lower and (or) upper limit on the radius can be imposed. In the case of the source with E_0 = 5 keV, the estimated lower limit is 30 km while in case of harder source (E_0 = 6 keV) the lower limit is 180 km. It also should be pointed out here that the radius of 180 km also represents a distance from beyond which the contribution to the observed x-ray flux becomes insignificant. For sources removed further from the zenith, (Figure 5.5b) the one with E_0 = 6 keV is more suitable, the softer source (E_0 = 5 keV) has a quality ratio which is too high, meaning that such a source will be supplying too many x-rays into the 20-40 keV energy channel with respect to the 40-60 keV channel.

The calculated electron spectrum producing the S.E.R. event at 10:45 UT shows a good general agreement with the observed auroral electron spectra made by rockets (McIllwain, 1960 and Ulwick et al., 1967 to name a few). Based on this calculation apparently the high-energy end of the auroral electron spectrum can produce a sufficient amount of soft x-rays which will be detectable at balloon's altitudes. The detection of these x-rays is not however straightforward, as they appear at the low-energy end of the hard x-ray spectrum in the form of the S.E.R. event. Since the electrons producing the S.E.R. event are the auroral

electrons, they originate in the plasma sheet. More specifically, the presence of diffuse aurora above the balloon at 10:45 UT suggests that the balloon at this time is located under the equatorward portion of the auroral oval and hence the electrons, producing the S.E.R. event and the diffused glow, originate in the central plasma sheet region (CPS) as discussed in Chapter 1, Section 1.3.4.

5.5 Optical Auroral Electrons as a Source of the Soft X-Ray Flux Producing the Observed S.E.R. Events

The intensity of the soft x-ray source was estimated from Figure 5.7a for Case I hard component; the radii of the soft source considered were 30 km and 180 km. For the 30 km radius, the spectrum of the soft x-ray source supplying at atmospheric depth of 9 g cm^{-2} 14.2 $\pm$ 1.37 counts sec^{-1} $ster^{-1}$ cm^{-2} into 20-40 keV channel and 2.69 $\pm$ 0.59 counts sec^{-1} $ster^{-1}$ cm^{-2} into the 40-60 keV energy channel can be represented by

$$\frac{dN(Ex)}{d(Ex)} \quad 5.03 \times 10^4 \exp(-Ex/5) \quad (\text{x-rays } cm^{-2} \ sec^{-1} \ keV^{-1}) \quad (5.5)$$

while for the source with 180 km radius the differential spectrum is

$$\frac{dN(Ex)}{d(Ex)} \quad 3.91 \times 10^4 \exp(-Ex/5) \quad (\text{x-rays } cm^{-2} \ sec^{-1} \ keV^{-1}) \quad (5.6)$$

The intensities at zero energy were obtained by shifting the light line #1 vertically upward to 14.2 (Case I heavy line). This involves multiplication of the intensity at zero energy

(3.33 x 10^4 as given in the previous section) by a factor of 1.58 (30km radius) and by a factor of 1.20 (180 km radius).

Using relativistic thick target bremsstrahlung (Evans 1955) as given in Chapter 1, Section 1.2 the exponential electron spectrum producing the above x-ray fluxes was calculated and is given by

$$\frac{dN(E)}{d(E)} \quad (8.60 \times 10^8 - 1.41 \times 10^9) \exp(-E/6.0) \qquad (5.7)$$

for 180 km and 30 km radius respectively using the photon to electron conversion factor of 1 x 10^5 (Anderson, 1964).

The electron spectrum calculated from the equivalent soft source observed at 10:45 UT fits well with the in-situ observed range of electron spectra during active auroras using rockets and satellites. As discussed in Chapter 1, Section 1.4, many of the observed electron spectra were exponential with observed e-folding energy values between $E_0 \cong 5$ keV to $E_0 \cong 9$ keV.

The calculated soft electron flux between 1 and 20 keV at 10:45 UT is 7.20 x 10^9 electrons cm^{-2} sec^{-1} and between 20-60 keV is only 3.00 x 10^8 electrons cm^{-2} sec^{-1} i.e. only 4 percent of this flux is capable of producing bremsstrahlung to be detected at balloon altitude. The integral electron spectrum obtained here, viz.,

$$(2.88 \times 10^9 - 4.72 \times 10^9) \exp(-E/6) \qquad (5.8)$$

is comparable with that observed by McIlwain (1960) (see Chapter 1, Section 1.4) who gives value of 2.5×10^9 exp (-E/5) in the energy region between 3 keV and 30 keV. The energy flux J(w) due to an exponential spectrum over the energy region E_{min} to E_{max} is

$$J(w) = N_0 \int_{E_{min}}^{E_{max}} E \exp(-E/E_0) \, dE \tag{5.9}$$

where N_0 is the electron intensity at zero energy and E_0 is the e-folding energy of the electron spectrum. Belon et al. (1966) have determined that the optical auroral intensity is most sensitive to electron intensity variation between 0.7 keV and 6 keV. Using the calculated electron spectra given by equation (5.7) the calculated energy flux over this energy region is 11-19 ergs cm^{-2} sec^{-1}. Vallance Jones (1971) has obtained the value of energy deposition by the auroral electrons during IBC I type aurora (emission intensity 1 kR) to be 0.5-1.5 ergs cm^{-2} sec^{-1}. Based on these values and on calculated energy deposition at 10:45 UT, the calculated intensity of the aurora for the two spectra is 7.3-22 kR and 12.6-38 kR, the latter intensity showing better agreement with the observed optical auroral intensity of 26 kR (see Figure 5.9 and/or 5.1).

5.6 Intensity of the Optical Aurora and the Soft X-Ray Component

Continuous monitoring of the soft x-ray component intensity producing the S.E.R. effect on the composite spectrum can to some extent be done by following the ratio

$$R_b = \frac{C(20-40)\text{Total}}{C(60-80)\text{Total}} \qquad (5.10)$$

where $C(20-40)$Total and $C(60-80)$Total represent the measured counts into the 20-40 keV and 60-80 keV energy channels. The ratio R_b is suitable for monitoring the soft component intensity because the x-rays from such a soft source will be mainly deposited in the 20-40 keV energy channel. Unless the soft component e-folding energy is located above 8 keV, the x-rays in the 60-80 keV energy channel will be essentially contributed from the hard component.

Temporal variations of R_b, optical auroral intensity and the x-ray activity in the 20-40 keV energy region is shown in Figure 5.9, 5.10, and 5.11. The 5577A intensity profile represents the averaged optical aurora intensity above the balloon. Figure 5.9 represents the whole flight while 5.10 and 5.11 are selected time intervals between 09:30 UT-09:49 UT and 09:58 UT-10:30 UT. The noisy R_b profile prior to 09:00 UT is due to the background noise.

Between 09:02 UT and 09:25 UT (Figure 5.9), both the 5577A and R_b intensity profiles are low, only the hard
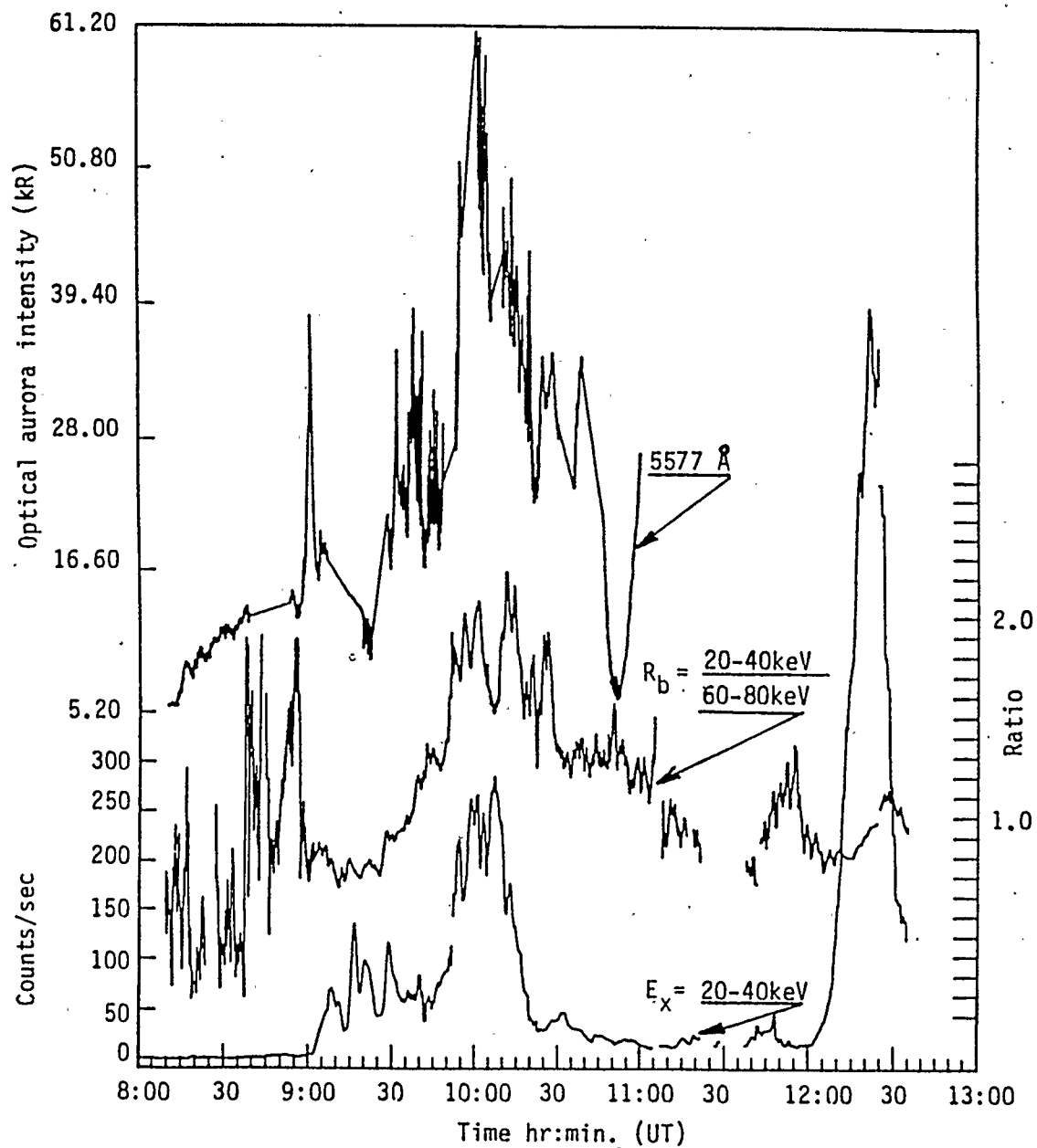
Figure 5.9 Variation of the X-ray activity (E_x=20-40keV), ratio R_b $(\frac{20-40keV}{60-80keV})$ and the optical aurora intensity(above the balloon, λ=5577Å) observed during CL-2 balloon flight.

TABLE 5.2

CORRELATION BETWEEN THE OPTICAL AURORAL INTENSITY, THE X-RAY INTENSITY
AND THE RATIO R_b DURING THE INDICATED TIME INTERVALS.

Time hr:min.(UT)	Correlated variables	Correlation coefficient	Percent linearity
10:10-10:26	5577Å & R_b	0.90	81.0
	5577Å & Ex=20-40keV	-0.49	24.0
10:00-10:05	5577Å & R_b	0.78	61.0
	5577Å & Ex=20-40keV	0.14	2.0
09:30-09:49	5577Å & R_b	0.0246	nil
	5577Å & Ex=20-40keV	0.11	1.2
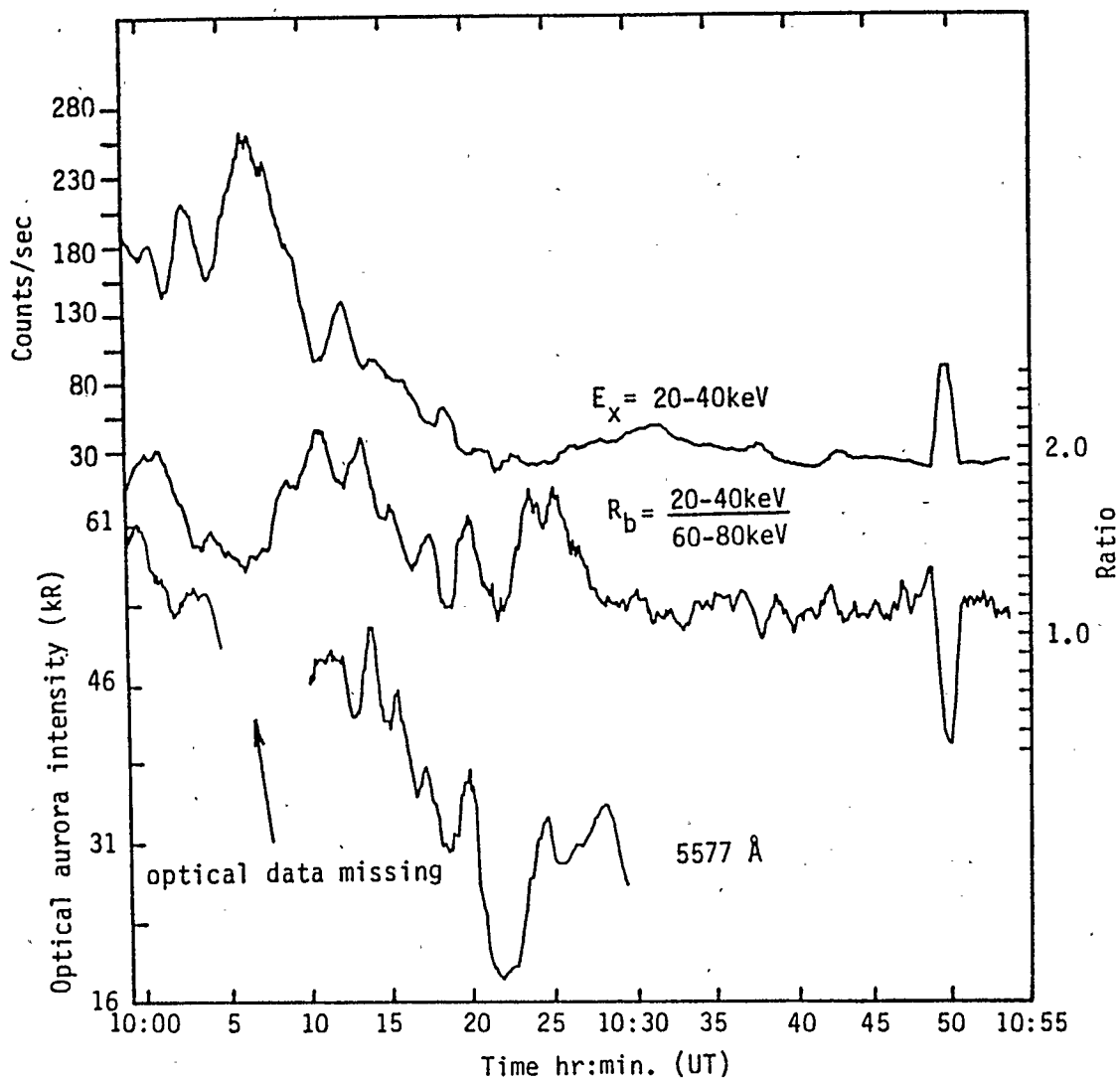
Figure 5.10 In the time interval 10:10UT - 10:26UT a good correlation exists
between the ratio R_b and the 5577Å emission intensity from the
aurora above the balloon(correlation coeff. = 0.90).Over the same
time interval the correlation between the X-ray intensity
(E_x=20-40keV) and the optical emission intensity is poor(correla-
tion coeff. = -0.49).
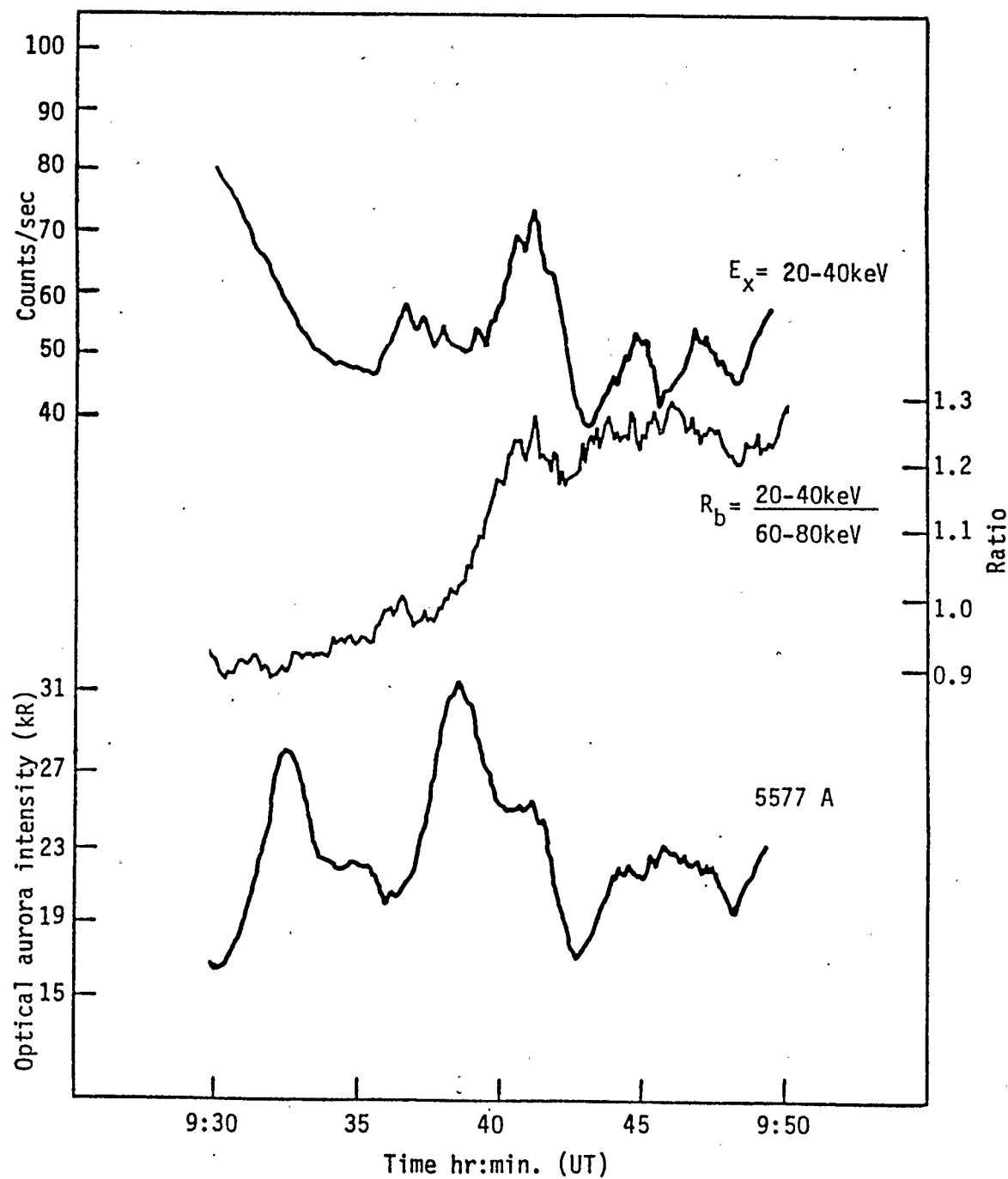
Figure 5.11 Example where both the ratio R_b and the X-ray intensity $(E_x = 20\text{-}40\text{keV})$ show poor correlation with the optical emission intensity ($\lambda=5577Å$) from the aurora above the balloon.

x-ray activity is observed. The small variations of the R_b intensity at this time are most likely due to the spectral variation and motion of the hard component only. Major increases in all the three profiles are observed after 09:50 UT and 30 minutes later only the hard x-ray component experiences a relatively large drop in intensity while both the 5577A emission and R_b intensities experience only a marginal drop.

Very good correlation between the R_b ratio and the 5577A optical emission intensity is observed between 10:10 UT and 10:30 UT. The following Table 5.2 gives examples of the linearity relationships (given by the square of the correlation coefficient), between the 5577A emission intensity and the intensity of x-rays between 20-40 keVand intensity of R_b.

Both very high and low linearity relationships are observed in the case of 5577A optical emission and R_b ratio while the case between 5577A emission intensity and hard x-ray component intensity always is low. It appears that the increase of optical auroral activity and the hard x-ray activity after 09:50 UT could be related only through the overall increase in polar substorm activity at this time, as the two features show a clear lack of detailed variation. Note, however, that R_b is not an ideal indicator of the soft x-ray component activity as the intensity of $C(20-40)Soft$ depends on the e-folding energy

variation of the auroral electrons. For example, changing the energy from 7 keV to 5 keV will reduce the flux of electrons in the energy region by a factor of 4 which will produce an apparent variation of C(20-40)Soft magnitude at the balloon level.

Also, there will be no increase of C(20-40) if the optical auroral feature is produced by a monoenergetic electron beam with energy below 20 keV threshold, as is often observed in the case of auroral arcs.

5.7 Summary of the Method and Discussion of the Results

The result of the correlation between the optical and the x-ray aurora indicates no clear association between the two polar substorm phenomena. On few occasions, both, strong optical and x-ray auroras were observed simultaneously. An occasion such as this occurred for example during the expansive phase of the first substorm. Large x-ray activity was observed when the optical auroral bulge had expanded in all directions, filling the sky with active auroras. The onset of the x-ray activity was, however, delayed by approximately 12 minutes with respect to the onset of the optical auroral activity.

Similar association between the optical and x-ray activity was observed during the Ax2 event which occurred just before on the onset of the substorm's recovery phase. As before, the wide-spread intense optical activity was again accompanied by intense x-ray activity. Although both

phenomena were active at this time the result of detailed correlation between the optical and x-ray intensities (Table 5.2) showed no one-to-one relation. This suggests that the intensities of the low and high energy electrons, producing the optical and x-ray auroras respectively, are modulated separately, possibly by two different mechanisms.

At the beginning of the recovery phase of the substorm (approximatly after 10:10 UT), the optical and the x-ray auroras became spatially separated. The optical activity retreated Southward, while apparently, the x-ray aurora has moved Northward following the electrojet. The Southward retreat of the optical aurora was followed by another expansion. However, at this time, the optical aurora appeared as a fairly intense diffuse glow which then gradually decayed. The x-ray aurora did not show any intensification with this expansion at all, since it apparently remained Northward of the balloon until the end of the substorm.

Spectral measurements during CL-2 balloon flight (and also during CL-1 flight) indicate an extra flux of soft x-rays being deposited into the 20-40 keV energy channel. This is observed by noting that the count rate in this channel often exceeds the count rate in the 40-60 keV energy channel, the observed event being named "Soft End Reversal" (S.E.R.). Due to the presence of photoelectric absorption acting on the beam of x-rays passing through the atmosphere, the count rate at the balloon altitude in the 40-60 keV

channel is usually higher.

Monte Carlo simulations have indicated that when the S.E.R. event is observed, there are actually two spectra present. The hard component can be identified from the count rates in the energy channels above 60 keV while the soft component produces the S.E.R. event in the 20-40 keV energy channel. It has been determined that the soft source must have e-folding energy (based on the assumption that the spectrum is exponential) below or equal to 12 keV since only these soft sources at balloon altitude will produce x-ray flux which in the 20-40 keV energy region is higher then in the 40-60 keV energy region. Spectrum and intensity identification of the soft x-ray source was done in three stages.

In the first stage, the two components of the composite spectrum were separated. The method first involved identification of the hard component spectrum shape using Monte Carlo simulation. This was followed by subtraction of the simulated from the observed spectrum. A specific real spectrum, that which was observed at 10:45 UT during the CL-2 flight, was selected for this purpose. The result of the subtraction yielded the x-ray counts contributed by the soft source into 20-40 keV and 40-60 keV energy channels.

The second step involved e-folding energy identification of the soft x-ray source. The identification involved formation of the ratio, called "quality ratio", the quantity describing the relative magnitudes of counts in the

20-40 keV and 40-60 keV energy channels. It should be pointed out that every x-ray source, depending on the size, the location distance relative to detection, and the e-folding energy, will have a specific quality ratio signature at the balloon altitude. The e-folding energy of the source is the most important parameter in this method. Identification of the e-folding energy thus involves matching the quality ratio of the real source with the quality ratio of the simulated source.

The third stage involved estimation of the soft x-ray source intensity necessary to produce the observed soft counts at the balloon altitude. These counts have been plotted in Figures 5.7 and 5.8 using heavy lines. The light lines in the same figures represented the observed counts at the 9 g cm^{-2} produced by the simulated soft x-ray sources with e-folding energies of 8 keV and 5 keV. Due to the result from the second step, the harder ($E_O = 8$ keV) x-ray source was then rejected. The intensity of the softer source was estimated by shifting the light curves (#1 and #2) upward by the correct amount so that they will just cross the two heavy lines. At this point then, the simulated soft source has the intensity necessary to produce the required soft x-ray flux by emitting 1.2×10^3 x-rays cm^{-2} sec^{-1} ster^{-1} over 20-40 keV and 3.8×10^1 x-rays cm^{-2} sec^{-1} ster^{-1} over the 40-60 keV energy intervals isotropically downward. The deduced electron spectrum capable of producing the required soft x-ray source

at 10:45 UT had an e-folding energy of 6 keV with integral intensity in the 3-30 keV energy region between 2.88×10^9 and 4.72×10^9 electrons cm^{-2} sec^{-1} and zero energy intensity (the intercept at E = 0) between 8.60×10^8 and 1.41×10^9 electrons cm^{-2} sec^{-1} showing good agreement with the observed electron spectra, using rockets and satellites, at the time of active optical auroras as presented in Chapter 1.

The method has yielded results indicating that the soft x-ray flux at the balloon altitude producing the observed S.E.R. events is likely created during the active optical auroras by the primary auroral electrons. The S.E.R. events were present only during active auroras but the presence of active auroras have not always indicated well defined S.E.R. events. The intensity of the soft x-ray source was monitored by forming the ratio R_b (see Section 5.6, Equation 5.10) because it is sensitive to the variation of the soft x-ray flux in the 20-40 keV energy region. The results have indicated that there is a period between 10:10 UT and 10:26 UT where the variation of the ratio R_b very closely follows the variation of the auroral intensity (λ = 5577A) in the field of view of the vertical detector. The situation is, for example, different during the time interval of 09:30 UT-09:49 UT where no relation between the optical intensity and the R_b magnitude was observed. The spectral variation of the auroral electrons during this period could produce an apparent variation in the intensity

of the soft source resulting in a poor relationship between the R_b value and the optical auroral intensity. For example, simply reducing the e-folding energy of the electron spectrum from 6 to 5 keV will reduce the intensity of the soft x-rays source by 66 percent. Except during specific time periods, visual inspection of Figure 5.9 indicates that the R_b variation in general compares well with intensity variation of the optical aurora.

Anderson and DeWitt (1963), based on observed close space-time association between optical and x-ray aurora, have explored the possibility that the low energy portion of the auroral electron spectrum contributed mainly to auroral glow while the high energy tail, penetrating deeper into the atmosphere, would produce x-rays detectable at the balloon level. They have estimated the primary electron spectrum by using the ratios of observed x-ray flux above 50 keV and 25 keV respectively thus using directly the observed x-ray events in the energy channels. More recently, Barcus et al. (1981) have conducted two rocket flights into energetic auroral events with x-ray (NaI) and particle (Geiger counters) detectors onboard payloads. The rotation of the payload provided the means of obtaining the spatial structure of the x-ray aurora. During one of the flights, two components of x-ray aurora were distinguished. The soft component ($E_x < 40$ keV) showed spatial correlation with optical aurora while the hard component ($E_x > 40$ keV) did not show any spatial correlation with the optical emission

region at all. The electron flux measured during this event for $E > 15$ keV was 6×10^7 cm^{-2} sec^{-1} with e-folding energy of 5 keV. Although Barcus et al. (1981) also concluded that the resolution of x-ray aurora into two components from balloon measurements cannot be achieved due to atmospheric absorption effect, apparently this is not the case. Observations here indicate that the soft x-ray flux produced by the soft electron spectrum, similar to that associated with optical auroras, cannot be observed by the main energy channels but appear only at the very low energy end of the hard spectral component in the form of the Soft End Reversal (S.E.R.) event.

CHAPTER 6

SUMMARY AND CONCLUSIONS

6.1 Study of X-Ray Aurora With Directional Detectors

The interpretation of the data from the directional and vertical detectors during the CL-2 and CL-1 balloon flights has been enhanced by the Monte Carlo technique of simulating x-ray sources moving with respect to the fields of view of the detectors. The relative count rates observed by these instruments have been studied for three orientations of the inclined detector taken with respect to the direction of the moving source velocity vector. The results of this simulation study are summarized below.

i) The effect of the scattered x-rays at the depth of 9 g cm^{-2} on the relative x-ray profiles of the vertical and the inclined detectors is significant. Intensity variations of the x-ray source lying outside the field of view of one detector while inside the field of view of the other will produce qualitatively identical temporal variations in both detectors, since significant amounts of scattered x-rays will be entering both detectors. The approaching or receding x-ray source located outside the field of view of a detector will produce apparent increase or decrease in x-ray intensity.

ii) The motion of an x-ray source with respect to the field of view of the detectors can be studied by forming ratios from the x-ray counts measured by two different detectors. The x-ray source entering the field of view of one detector will change the count rate ratio due to the presence of the direct x-ray component. The variation of the ratio of count rates increases with increasing energy and decreasing area of the source.

iii) The motion of the x-ray source produces an apparent variation in the observed e-folding energy, with abrupt hardening as the x-ray source enters the field of view of the detector. When a large x-ray source covers the field of view of the vertical and the inclined detectors, the inclined detectors will measure a softer spectrum.

iv) All three parameters viz., the ratio of the count rates, the e-folding energy, and the variations of x-ray intensity should be used when interpreting real data for positive identification of the dynamics of the equivalent x-ray source. Based on Monte Carlo simulation the ratios formed from data of the detector system onboard the CL-2 flight has enabled the estimation of the size of the x-ray source producing the Ax1 event. The detector system has also enabled us to detect the source movement with the simultaneous use of ratios, x-ray intensity, and variations of e-folding energy. Thus we have been able to discriminate

between the apparent and true spectral variations caused by the motion or expansion of the source. The system also has demonstrated the importance of scattering at atmospheric depth of 9 g cm^{-2} as indicated by the virtually identical x-ray profiles of all three detectors.

6.2 Association of Soft X-Ray Flux With Optical Aurora

Exploring the association between x-ray and optical aurora has yielded some interesting results which are summarized below.

i) Up and down "flapping motion" at the low energy end of the spectrum between 20-40 keV and 40-60 keV energy channels has indicated the presence of extra-soft x-rays at the balloon altitude. The ratio of the count rates, viz.,

$$\frac{C(20-40) \ keV}{C(40-60) \ keV}$$

has often exceeded the value of 1 for extensive periods of time. Such an event has been named "Soft End Reversal" (S.E.R.).

ii) Monte Carlo simulation has indicated that this soft x-ray flux observed at the balloon altitude can originate only from x-ray sources with e-folding energy of $\leq$ 12 keV.

iii) A method has been introduced for the separation and determination of the e-folding energy of the soft x-ray

source. The method has been applied to a specific spectrum observed at 10:45 UT during the CL-2 balloon flight. The calculated result has indicated that at this time the e-folding energy of the soft x-ray source was 5 keV, the e-folding energy of the associated electron spectrum being 6 keV. The intensity and the e-folding energy of the deduced electron spectrum has shown a good agreement with the observed electron spectra from previous rocket and satellite observations, thus suggesting that the extra-soft x-ray flux at the balloon altitude does indeed originate from the optical auroral region.

iv) The ratio R_b formed from count rates in the 20-40 keV and the 60-80 keV energy channels have been used to monitor the intensity of the soft x-ray flux. The selection of the 60-80 keV energy channel has been based upon observation that the simulated soft x-ray sources with $E_o \le 8$ keV had virtually no x-rays in the 60-80 keV energy region at the balloon altitude of 33 km (9 g cm^{-2}). At one instance the R_b variation (for 15 minutes) has been observed to follow very closely the intensity variation of the 5577A auroral optical emission situated in the vicinity of the balloon's zenith. However, at other time virtually no association between the two correlated quantities was evident. The lack of correlation was attributed to the spectrum variation of the auroral electrons, as such a variation could produce an apparent intensity variation of

the soft x-ray flux and hence of R_b magnitude.

v) The calculated results suggest that soft x-rays are emitted during the active optical auroras. If the intensity of the auroral electron flux is high enough, the high energy end of the auroral electron spectrum can produce a sufficient amount of soft x-rays that can be detected by balloon-borne x-ray detectors. However the detection of such soft x-ray flux is not a straight-forward matter. Due to their softness, they appear only at the low energy end of the hard component in the form of the S.E.R. event.

6.3 X-Ray and Optical Aurora at Cold Lake

i) The major x-ray events correlated with the magnetic bay activity at the College magnetic observatory, which is situated on approximately the same magnetic L-shell as Cold Lake, although separated considerably in longitude. Apparently, the similarity between the magnetic L-shell values of the balloon's position and the location of the magnetic observatory plays a dominant role in the association between the magnetic bay and x-ray activity.

ii) The ratio method, applied to x-ray data from CL-2 balloon flight, has revealed the x-ray source to be not stationary but moving in the fields of view of the detectors. It has also concluded that in the time interval 09:10 UT-09:30 UT, the x-ray source has approached to within

15 km of the zenith.

The equivalent x-ray source in this time interval extends from the North and covers totally the field of view of the inclined detector #4 (oriented between 09:10 UT and 09:30 UT in N-NW direction), partially the field of view of the vertical detector ($\sim$30%) while not or just slightly in the field of view of the inclined detector #2 (oriented between 09:10 UT and 09:30 UT in the SW-S direction).

A small x-ray source, similar to a point-like source apparently has been responsible for the high count rate at 12:20 UT during the Bx event. The location of this equivalent x-ray source is 30 km from zenith, situated in the field of view of the inclined detector #4.

iii) During the main x-ray events, the observed spectra have shown an exponential characteristic; the spectra during the time interval 09:30 UT- 10:15 UT (CL-2 flight) is actually composed of three components.

The e-folding energy variation of the hard component is between 25 keV and 70 keV. The softer spectrum, observed to be associated with pulsating x-ray activity, has shown an e-folding energy variation between 11 keV and 21 keV.

The very soft component is observed only at the low energy end of the composite spectrum in the form of S.E.R. event. In one specific case (spectrum at 10:45 UT, CL-2 flight) the e-folding energy of this very soft component was determined to be 5 keV.

iv) Both apparent (caused by the change in the x-ray source-detector geometry) and real e-folding energy variations have been observed during the CL-2 flight. For example in the time interval 09:10 UT-09:30 UT this apparent e-folding energy variation is superimposed over the real spectral softening. Evidently, a real spectral softening alone was observed during the Bx event.

v) No clear association between the optical and x-ray aurora has been observed although during the Ax2 event (CL-2 flight) both strong optical and x-ray auroras have been observed simultaneously. This association has however been offset by periods before and after this event during which virtually no correlation between the intensity of the two phenomena was seen. In addition, no clear association between the motions of the x-ray source and the optical auroral features were observed.

vi) Presence of a soft x-ray flux has been observed during CL-2 flight (see Figure 5.3) and CL-1 flight (10:30 UT see Figure 3.21) which appear to be associated with optical aurora as discussed in detail in the previous section.

6.4 Possibilities of Future Studies

To obtain more and better information about the morphology of the x-ray aurora, one needs to concentrate on

the improvement of the present x-ray detection system.

The first significant change would be the addition of three more inclined detectors; these are easily incorporated into the present system with only minor changes in the PCM bit frame. This would eliminate the " blind" spots located between the illumination areas of the inclined detectors.

The ratio method presented in the present work can be improved by simply expanding the variety of possible sources treated by the Monte Carlo simulation method. This would only involve extension of the software work presented in Chapter 4. The increased number of simulated ratios available would improve the estimation of the x-ray source size and the location when comparing the ratios from real and simulated data. Again, the comparison of the two types of ratios could be done by software.

A different way of utilizing the ratio method would be to build up the x-ray source from individual point-like sources instead of using a solid geometry source. This would involve the development of a computer program which would sum the contributions to the total count rate from individual points placed at appropriate positions until the set of ratios formed from the simulated count rates would match the set of ratios formed from the observed rates. A different approach to improve the spatial resolution of the x-ray detectors was presented by Mauk et al. (1981). The system was used during the actual balloon flight, showing some improvement over the presently used assembly of

directional x-ray detectors.

A new concept in x-ray imaging was recently proposed by Lieu et al. (1985). Although not developed yet, this system is worthy of consideration as a future replacement for presently used x-ray detector system. The interested reader should refer to above-mentioned publications for the detailed descriptions and methods involved.

REFERENCES

Akasofu, S.I., The Development of the Auroral Substorm,
Planet. Space Sci., 12, 273, 1964.

Akasofu, S.I., Recent Progress in Studies of DMSP Auroral
Photographs, Space Sci. Rev., 19, 169, 1976.

Akasofu, S.I., "Distribution of Plasmas in the Magnetosphere",
Physics of Magnetospheric Substorms, D. Reidel
Pub. Co., 1977.

Akasofu, S.I., "Physics of Auroral Arc Formation",
Geophysical Monograph 25, Ed. S.I. Akasofu and
J.R. Kan, Pub. AGU, Washington, D.C., 1981.

Anderson, K.A. and D.C. Enemark, Balloon Observations of
X-Rays in the Auroral Zone, 2, J. Geophys. Res.,
65, 3521, 1960.

Anderson, K.A. and R. DeWitt, Space-Time Association of
Auroral Glow and X-Rays at Balloon Altitude, J.
Geophys. Res., 68, 2669, 1963.

Anderson, K.A., A Review of Balloon Measurement of X-Rays
in the Auroral Zone, Proc. Jan. 1964 Lockheed

Auroral Symp., Stanford Univ. Press, Stanford,
1964.

Anger, C.D., Advances in Auroral Imaging from Space, *Adv.*
Space Res., 2, 97, 1983.

Arnoldy, R.L., Auroral Particle Precipitation and
Birkeland Currents, *Rev. Geophys. Space Phys.,*
12, 217, 1974.

Ashour-Abdalla, M., and C.F. Kennel, "Diffuse Auroral
Precipitation", Auroral Processes, Ed.,
C.T. Russell, Japan Scientific Societies Press,
p. 73, 1977.

Babey, S.K., J.S. Murphree, E.P. King, L.L. Cogger, and
C.D. Anger, An Intensified CCD Imager for Auroral
Studies, Optical Engineering, Oct., 1986.

Banks, P.M., C.R. Chappell, and A.F. Nagy, A New Model
for the Interaction of Auroral Electrons with the
Atmosphere: Spectral Degradation, Backscatter,
Optical Emission and Ionization, *J. Geophys.*
Res., 79, 1459, 1974.

Barcus, J.R. and T.J. Rosenberg, Energy Spectra for
Auroral Zone X-Rays, *J. Geophys. Res.,*

<u>71</u>, 803, 1966.

Barcus, J.R. and R.A. Goldberg, X-Ray Scanning of
   Overhead Aurorae from Rockets, <u>J. Atmos. Terr.
   Phys.</u>, <u>43</u>, 1003, 1981.

Belon, A.E., G.J. Romick, and M.H. Rees, The Energy
   Spectrum of Primary Auroral Electrons
   Determined from Auroral Luminosity Profiles,
   <u>Planetary Space Sci</u>., <u>14</u>, 597, 1966.

Berger, M.J. and S.M. Seltzer, Bremsstrahlung in the
   Atmosphere, <u>J. Atmos. Terr. Phys.</u>,
   <u>34</u>, 85, 1972.

Bewersdorff, A., G. Kremser, J. Stadsnes, H. Trefall and
   S. Ullaland, Simultaneous Balloon Measurements
   of Auroral X-Rays During Slowly Varying
   Ionospheric Absorption Events, <u>J. Atmos. Terr.
   Phys.</u>, <u>30</u>, 591, 1968.

Bjordal, J., H. Trefall, S. Ullaland, A. Bewersdorff, J.
   Kangas, P. Tankskanen, G. Kremser, K. H.
   Saeger and H. Specht, On the Morphology of
   Auroral Zone X-Ray events, <u>J. Atmos. Terr.
   Phys.</u>, <u>33</u>, 605, 1971.

Bryant, D.A., H.L. Collin, G.M. Courtier, and A.D. Johnstone, Evidence for Velocity Dispersion in Auroral Electrons, Nature, 215, 45, 1967.

Clark, T.A. and C.D. Anger, Morphology of Electron Precipitaion During Auroral Substorms, Planet. Space Sc., 15, 1287, 1967.

Davis, T.N., T.J. Hallinan and H.C. Stenback-Neilsen, "Auroral Conjugacy and Time Dependent Geometry of Auroras", The Radiating Atmosphere, Ed., B.M. McCormac, D. Reidel Pub. Co., 1971.

Davis, T.N., Observed Characteristics of Auroral Forms, Space Sci. Rev., 22, 77, 1978.

Deehr, C.S., A. Egeland, K. Aarsnes, R. Amundson, H.R. Lindalen, F. Soraas, R. Dabziel, P.A. Smith, G.R. Thomas, P. Stauning, H. Borg, G. Gustafsson, L.A. Holmgasen, W. Riedler, J. Raift, G. Skovli, T. Wedde, and R. Jaeschke, Particle and Auroral Observations from the ESRO 2/Auroral Satellite, J. Atmos. Terr. Phys., 35, 1973.

Eather, R.H., and S.B. Mende, Airborne Observations of Auroral Precipitation Patterns, J. Geophys.

Res., <u>76</u>, 1746, 1971.

Evans, R.D., "The Atomic Nucleus", McGraw Hill, 1955.

Fairfield, D.H., and A.F. Vinas, The Inner Edge of the
Plasma Sheet and the Diffuse Aurora, <u>J. Geophys.
Res.</u>, <u>89</u>, 841, 1984.

Feldstein, Y.I., Some Problems Concerning the Morphology of
Auroras and Magnetic Disturbances at High Latitudes,
<u>Geomagn. and Aeronomy</u>, <u>3</u>, 1963.

Freeman, J.W. Jr. and J.J. Maguire, "Particle Dynamics at
the Synchronous Orbit", Physics of the
Magnetosphere, D. Reidel Pub. Co., p. 586,
1968.

Hartz, T.R. and N.M. Brice, The General Pattern of
Auroral Particle Precipitation, <u>Planet. Space
Sc.</u>, <u>15</u>, 301, 1967.

Hofmann, D.J., and R.A. Greene, Balloon Observations of
Simultaneous Auroral X-Ray and Visible Bursts,
<u>J. Geophys. Res.</u>, <u>77</u>, 776, 1972.

Imhof, W.L., G.H. Nakano, R.G. Johnson, and J. B. Reagan,
Satellite Observations of Bremsstrahlung from

Widespread Energetic Electron Precipitation
Events, J. Geophys. Res., 79, 565, 1974.

Imhof, W.L., G.H. Nakano, and J.B. Reagan, Satellite
Observations of Impulsive Bremsstrahlung X-Ray
Events Associated with Substorms, J. Geophys.
Res., 83, 4237, 1978.

Imhof, W.L., H.D. Voss, D.W. Datlowe, and J. Mobilia,
Bremsstrahlung X-Ray Images of Isolated Patches
at High Latitudes, J. Geophys. Res., 90,
6515, 1985.

Imhof, W.L., J. Stadsnes, J.R. Kilner, D.W. Datlowe,
G.H. Nakano, J.B. Reagan, and P. Stauning,
Mapping of Energetic Electron Precipitation
Following Substorms Using the Satellite
Bremsstrahlung Technique, J. Geophys. Res.,
87, 671, 1982.

Kan, J.R., and L.C. Lee, "Formation of Auroral Arcs and
Inverted V Precipitations: An Overview", Physics
of Auroral arc formation Geophysical Monograph 25,
1981.

Kangas, J., L. Lukkari, P. Tamskanen, H. Trefall, J.
Stadness, G. Kremser and W. Riedler, On the

Morphology of Auroral Zone X-Ray Events - IV.
Substorm Related Electron Precipitation in the
Local Morning Sector, J. Atmos. Terr. Phys.,
37, 1289, 1975.

Kisabeth, J.L. and G. Rostoker, Development of Polar
Electrojet During Polar Magnetic Substorms,
J. Geophys. Res., 76, 6815, 1971.

Kremser, G., K. Wilhelm, W. Riedler, K. Bronstad, H.
Trefall, S.L. Ullaland, J.P. Legrand, J. Kangas
and P. Tanskanen, On the Morphology of Auroral
Zone X-Ray Events - II. Events During the
Early Morning Hours, J. Atmos. Terr. Phys.,
35, 713, 1973.

Lieu, L., L. Varga, R.B. Hicks, and L.I. Yin, "A New
Approach to Position Sensitive Gamma-Ray
Spectroscopy", J. Phys. E: Sci. Instrum., 19,
1986.

Luhmann, J.G., Auroral Bremsstrahlung Spectra in the
Atmosphere, J. Atmos. Terr. Phys., 39, 595,
1976.

Lui, A.T.Y., and C.D. Anger, A Uniform Belt of Diffuse
Auroral Emission Seen by the ISIS-2 Scanning

Photometer, <u>Planet Space Science</u>, <u>21</u>, 799, 1973.

Lui, A.T.Y., Multi-Satellite Studies of Magnetospheric Phenomena, Ph.D. Thesis, University of Calgary, 1974.

Lui, A.T.Y., D. Venkatesan, C.D. Anger, S.I. Akasofu, W.J. Heikkila, J.D. Winningham and J.R. Burrows, Simultaneous Observations of Particle Precipitation and Auroral Emissions by the ISIS-2 Satellite in the 19 - 24 MLT Sector, <u>J. Geophys. Res.</u>, <u>82</u>, 2210, 1977.

Maral, G.K. Bronstad, H. Trefall, G. Kremser, H. Specht, P. Tanskanen, J. Kangas, W. Riedler and J.P. Legrand, On the Morphology of Auroral Zone X-Ray Events - III. Large Scale Observations in the Midnight-to-Morning Sector, <u>J. Atmos. Terr. Phys.</u>, <u>35</u>, 735, 1973.

Mauk, B.H., J. Chin, and G. Parks, Auroral X-Ray Images, <u>J. Geophys. Res.</u>, <u>86</u>, 6827, 1981.

McIlwain, C.E., Direct Measurements of Particles Producing Visible Auroras, <u>J. Geophys. Res.</u>, <u>65</u>, 1960.

Meng, C.I., Electron Precipitations and Polar Aurora,

Space Sci. Rev., 22, 223, 1978.

Mozer, F.S., C.W. Carlson, M.K. Hudson, R.B. Torbert, B.
Parady, J. Yatteau and M.C. Kelley, Observations
of Paired Electrostatic Shocks in the Polar
Magnetosphere, Phys. Rev. Lett., 38, 292, 1977.

Meredith, L.H., L.R. Davis, J.P. Heppner, and O.E. Berg,
Rocket Auroral Investigations, IGY Rocket Rept.
Ser. 1, National Academy of Sciences, National
Research Council, Washington, D.C., 169, 1958.

Murphree, J.S., C.D. Anger, and L.L. Cogger, "ISIS-2
Observations of Auroral Arc System", Physics of
Auroral Arc Formation, Ed., S.I. Akasofu and J.R.
Kan, Geophysical Monograph 25, 1981.

Ogilvie, K.W., Auroral Electron Energy Spectra, J.
Geophys. Res., 73, 2325, 1968.

Oguti, T., "TV Observations of Auroral Arcs", Physics of
Auroral Arc Formation, Geophysical Monograph 25,
Ed. S.I. Akasofu and J.R. Kan, Pub. AGU,
Washington, D.C., 1981.

Omholt, A., "Particle Precipitation - Ionization and
Excitation", Cosmical Geophysics,

Universiteitsforlager, 1973.

Parks, G.K., D.W. Milton, and K.A. Anderson, Auroral Zone
X-Ray Bursts of 5 to 25 Millisecond Duration,
J. Geophys. Res., 72, 1967.

Parks , G.K., F.V. Coroniti, R.L. McPherron, and K.A.
Anderson, Studies of the Magnetospheric Substorm
1. Characteristics of Modulated Energetic
Electron Precipitation Occurring During Auroral
Substorms, J. Geophys. Res., 73, 1685, 1968.

Parks, G.K., G. Gurgiolo, and R. West, Relativistic
Electron Precipitation, Geophys. Res. Letters,
6, 1979.

Pfitzer, K.A., and J.R. Winckler, Intensity Correlations
and Substorm Electron Drift Effect in the Outer
Radiation Belt Measured with OGO3 and ATS1
Satellites, J. Geophys. Res., 74, 5005, 1969.

Pilkington, G.R., A Monte Carlo Calculation of Auroral
X-Ray Propagation in the Atmosphere with Application
to Balloon Observations, Ph.D. Thesis, University
of Calgary, 1970.

Pilkington, G.R. and C.D. Anger, A Monte Carlo Analysis

of the Passage of Auroral X-Rays Through the Atmosphere, <u>Planet Space Sci.</u>, <u>19</u>, 1069, 1971.

Price, W.J.J., "Nuclear Radiation Protection", p. 24 and 186, McGraw-Hill, 1964.

Rearwin, S., Rocket Measurements of Low-Energy Auroral Electrons, <u>J. Geophys. Res.</u>, <u>76</u>, 4505, 1976.

Rees, M.H., Auroral Ionization and Excitation by Incident Energetic Electrons, <u>Planet. Space Sci.</u>, <u>11</u>, 1963.

Rees, M.H., Ionization in the Earth's Atmosphere by Aurorally Associated Bremsstrahlung X-Rays, <u>Planet. Space Sci.</u>, <u>12</u>, 1964.

Rees, M.H., Auroral Electrons, <u>Space Sci. Rev.</u>, <u>10</u>, 413, 1969.

Rees, M.H., and R.A. Jones, Time Dependent Studies of the Aurora - II. Spectroscopic Morphology, <u>Planet Space Sci.</u>, <u>21</u>, 1213, 1973.

Rees, M.H., and D. Luckey, Auroral Electron Energy Derived from Ratios of Spectroscopic Emissions, 1. Model Computations, <u>J. Geophys., Res.</u>, <u>79</u>,

5181, 1974.

Rosenberg, T.J., J. Bjordal, H. Trefall, G.J. Kvifte, A. Omholt, and A. Egeland, Correlation Study of Auroral Luminosity and X-Rays, <u>J. Geophys. Res.</u>, <u>76</u>, 1971.

Runcorn, S.K., "Method and Technique in Geophysics", Volume 1, Interscience Pub. Inc., 1960.

Seltzer, S.M., M.J. Berger and T.J. Rosenberg, "Auroral Bremsstrahlung at Balloon Altitudes, NASA Spec. Rep., Sp - 3081, 1973.

Seltzer, S.M. and M.J. Berger, Bremsstrahlung in the Atmoshpere at Satellite Altitudes, <u>J. Atmos. Terr. Phys.</u>, <u>36</u>, 1974.

Sharp, R.D., J.E. Evans, W.L. Imhof, R.G. Johnson, J.B. Reagan and R.V. Smith, Satellite Measurements of Low-Energy Electrons in the Northern Auroral Zone, <u>J. Geophys. Res.</u>, <u>69</u>, 2721, 1964.

Sidney, R.F., "The Photographic Lens", Focal Press, London, 1979.

Sletten, A., J. Stadnes and H. Trefall, Auroral Zone

X-Ray Events and Their Relation to Polar Magnetic Substorms, <u>J. Atmos. Terr. Phys.</u>, <u>33</u>, 589, 1971.

Smith L., A Computer Controlled Optical Calibration system, M.Sc. Thesis, University of Calgary, 1981.

Sorensen, T., J. Bjordal, H. Trefall, G.J. Kvifte, and H. Pettersen, Correlation Between Pulsations in Auroral Luminosity Variations and X-Rays, <u>J. Atmos. Terr. Phys.</u>, <u>35</u>, 961, 1973.

Swift, D.W., "Substorm and Magnetospheric Energy Transfer Processes", Dynamics of the Magnetosphere, Ed., S.I. Akasofu, D. Reidel Pub. Co., 1980.

Thomas, I.L., The Geometrical Relations Between an Optical Ground Station, a Radar-Tracked Balloon, and the Aurora Both are Sensing, II-TV Technical Note No 2, University of Calgary, 1972.

Trefall, H., S. Ullaland, J. Stadnes, I. Singstad, T. Pytte, K. Bronstad, J. Bjordal, R.H. Karas, R.R. Brown and J.W. Munch, Morphology and Fine Time Structure of an Early-Morning Electron Precipitation Event, <u>J. Atmos. Terr. Phys.</u>, <u>37</u>, 83, 1975.

Ulwick, J.C., W.P. Reidy and K.D. Baker, Direct Measurements
of the Ionizing Flux in Different Types of Auroral
Forms, <u>Space Research</u>, <u>VII</u>, 656, 1967.

Valance Jones, A., Notes from the Summer Institute on
Planetary Magnetospheres and Auroras, National
Center for Atmospheric Research, Boulder, Colorado,
350, 1971.

Varga, L. and D. Venkatesan, "Auroral Electrojet and Auroral
X-Rays", Paper presented at Chapman's Conference
on Magnetospheric Currents, Irmington, Virginia,
April 5-8, 1983.

Varga, L., Study of Auroral X-Ray Events and Their
Relation to Polar Magnetic Substorms, M.Sc.
Thesis, University of Calgary, 1982.

Velchors, A.M. and W.R. Krickenberger, "Trigonometry with
Tables", P. 303, Ginn and Company, 1957.

Vij, K.K., Investigation of Bremsstrahlung X-Rays at Cold
Lake, Alberta, and Fort Churchill, Manitoba, by
Rocket and Balloon-Borne Scintillation Detectors,
Ph.D. Thesis, University of Calgary, 1973.

Vij, K.K. and D. Venkatesan, "Propagation of X-Rays Through

Terrestrial Atmosphere", International Conference
on X-Rays in Space, Paper presented at University
of Calgary, Calgary, Canada, August 14-21, 1974.

Vij, K.K., D. Venkatesan and C.D. Anger, Investigation
of Electron Precipitation During an Auroral
Substorm, J. Geophys. Res., 80, 3205, 1975.

Vij, K.K., J.S. Vogel and D. Venkatesan, Auroral X-Ray
Observations at 60 to 30 km Altitudes, J. Geophys.
Res., 85, 5096, 1980.

Wescott, E.M., H.C. Stenbaek-Neilsen, T.N. Davis, W.B.
Murcray, H.M. Peek, and P.J. Bottoms, The L =
6.6 Oosik Barium Plasma Injection Experiment and
Magnetic Storm of March 7, 1972, J. Geophys.
Res., 80, 951, 1975.

Wescott, E.M., H.C. Stenback-Neilsen, T.N. Davis and H.M.
Peek, The Skylab barium plasma injection
experiments 1. Convection Observations, J.
Geophys. Res., 81, 4495, 1976.

Westerlund, L.H., The Auroral Electron Energy Spectrum
Extended to 45 keV, J. Geophys. Res., 74,
351, 1969.

Winckler, J.R., L. Peterson, R. Hoffman and R. Arnoldy,
    Auroral X-Rays, Cosmic Rays and Related Phenomena
    During the Storm of February 10-11, 1958,
    J. Geophys. Res., 64, 597, 1959.

Winningham, J.D., F.Yasuhara, S.-I. Akasofu, and W.J.
    Heikkila, The Latitudinal Morphology of 10 eV to
    10 keV Electron Fluxes During Magnetically Quiet
    and Disturbed Times in the 21:00-03:00 Sector,
    J. Geophys. Res. 80, 1975.

APPENDIX

LISTING OF THE MONTE CARLO PROGRAM

1.fortran 12/13/85   0949.8 mst Fri

```
        program main_
c Monte carlo program to study the deep penetration of xrays
c into the atmosphere . The program starts with an isotropic
c point source at the top of the atmosphere , and detectors
c at four different depths . A flat (collimated) and omnidirectional
c detector are considered .
c
c               Variable Descriptions
c
c a,b,c,d             temporary variables to calculate new direction cosines
c angle               flat detector array coordinate for angle of xray detected
c ano                 number of xrays at zero kev,parameter for input spectrum
c coh                 1-probability of coherent scattering
c coh_angle           cosine of coherent scattering angle
c cosx                x axis direction cosine of current xray
c cosy                y axis direction cosine of current xray
c cosz                z axis direction cosine of current xray
c cosz_old            direction of original xray at the production layer
c count               current count of xrays at this energy
c dak                 distance travelled by xray to altitude interval considered
c depth               detector array coordinate for depth of penetration
c depth_int           altitude interval considered
c depth_max           maximum depth considered
c direct              array holding number of direct xrays reaching a given depth
c direct_xrays        array for detector that counts only direct xrays
c dist                total distance travelled by the current xray
c down                array holding number of down xrays reaching a given depth
c efolding            efolding energy
c electron_mass       electron rest mass
c en                  temporary variables to set new energy after a compton scatter
c energy              detector array coordinate for energy of detected xray
c energy_cnt          current initial energy of the xrays in Kev in floating point
c energy_counter      current initial energy of the xrays in Kev in fixed point
c energy_end          ending energy of the simulation
c energy_start        starting energy of the simulation
c flat_dn             array for collimated detector for down xrays
c flat_up             array for collimated detector for up xrays
c interp              fractional part of xenergy, used for linear interpolation
c ir                  temporary variables to calculate coherent scattering angle
c mfp                 xray total mean free path
c new_depth           latest array coordinate for depth of penetration
c new_xdepth          ending depth of current xray in gm/cm2
c num_xrays           number of xrays at this energy in the input spectrum
c omni_dn             array for omnidirectional detector for down xrays
c omni_up             array for omnidirectional detector for up xrays
c probc               probability of a compton scatter
c r                   uniformly distributed random number on the interval 0 to 1
c ra                  radial distance at which xray crosses interval
c range               detector array coordinate for range of penetration
c rr                  temporary variables to calculate coherent scattering angle
c up                  array holding number of up xrays reaching a given depth
c x1,y1,z1            starting coordinates of the current xray
c x2,y2,z2            ending coordinates of the current xray (collision point)
c xdepth              starting depth of current xray in gm/cm2
c xenergy             energy of current xray in terms of electron rest mass
c total               total number of xrays simulated
c
c          declare external routines here
```

```
      external random_$uniform
c
c          explicitly declare all variables here
c
      integer angle,count,depth,energy,ir,i
      integer new_depth,num_xrays,range
      integer direct(4),direct_xrays(4,20,42)
      integer omni_dn(4,20,42),omni_up(4,20,42),down(4),up(4)
      integer flat_dn(4,20,42,3),flat_up(4,20,42,3)
      real a,b,c,d,ano,cosx,cosy,cosz,cosz_old,dak,depth_int,depth_max
      real dist,efolding,electron_mass,en,energy_end,energy_start,energy_cnt
      real interp,new_xdepth,ra,r,rr,x1,y1,z1,x2,y2,z2,xdepth,xenergy,total
      real coh(44),coh_angle(21),mfp(44),probc(44)
c data statements initializing various parameters
c
      data mfp/0.026,0.202,0.649,1.344,2.096,2.924,3.584,4.107,
     &         4.545,4.878,5.128,5.376,5.550,5.721,5.880,6.024,
     &         6.170,6.290,6.410,6.490,6.618,6.741,6.850,6.939,
     &         7.008,7.079,7.145,7.212,7.277,7.397,7.464,7.532,
     &         7.598,7.667,7.735,7.804,7.872,7.941,8.078,8.149,
     &         9.349,10.490,11.500,12.420/
      data probc/.002,.027,.096,.209,.340,.476,.588,.670,.736,
     &         .785,.820,.854,.877,.892,.905,.915,.925,.937,
     &         .942,.948,.953,.957,.958,.964,.967,.970,.972,
     &         .974,.975,.976,.978,.979,.980,.981,.982,.983,
     &         .984,.985,.985,.986,.993,.996,.997,.998/
      data coh/.986,.953,.911,.878,.864,.859,.867,.879,
     &         .891,.903,.913,.923,.931,.938,.944,.949,
     &         .954,.958,.961,.964,.968,.970,.972,.974,
     &         .975,.977,.979,.980,.981,.982,.982,.983,
     &         .984,.985,.986,.986,.987,.987,.988,.988,
     &         .994,.996,.997,.998/
      data coh_angle/1.000,0.930,0.850,0.770,0.685,0.600,0.500,0.380,
     &         0.265,0.130,0.000,-0.130,-0.265,-0.380,-0.500,
     &         -0.600,-0.685,-0.770,-0.850,-0.930,-1.000/
      data electron_mass /510.0/
      data depth_int/3.0/
      data depth_max/20.0/
      data efolding/20.0/
      data ano       /100000/
      data altitude /90.0/
      data energy_start /20.0/
      data energy_end /200.0/
      data energy_inc /5.0/
      data total /0.0/
c
c format statements
c
100      format(2x,'angles between 0 and 30 degrees')
101      format(2x,'angles between 30 and 60 degrees')
102      format(2x,'angles between 60 and 90 degrees')
103      format(2x,'total xrays simulated= ',f12.2)
104      format(2x,6i6)
105      format(2x,'depth= ',i3,' gm/cm2 down xrays= ',i6,
     &          ' up= ',i6,' direct= ',i6)
106      format(2x,'depth=',i3,' gm/cm2',' range=',i3,' km')
107      format(2x,'efolding=',f4.1)
108      format(2x,'energy=',f6.1)
109      format(2x,'ano=',f10.2)
110      format(2x,'uncollimated detector')
111      format(2x,'collimated detector')
112      format(2x,'direct xrays')
113      format(f15.4)
114      format(1x,'absorbed xrays=',i6)
115      format(1x,'N(Ex)=',i6)
```

```
c read in appropriate parameters
c
c
c initialize space arrays
c
        do 201 depth=1,4
        down(i)=0.0
        up(i)=0.0
        direct(i)=0.0
        do 201 range=1,20
        do 201 energy=1,42
        direct_xrays(depth,range,energy)=0
        omni_dn(depth,range,energy)=0
        omni_up(depth,range,energy)=0
        do 201 angle=1,3
        flat_dn(depth,range,energy,angle)=0
        flat_up(depth,range,energy,angle)=0
        i=0
201     continue
c
c open file for data output
c
        open(1,file='output',form='formatted',carriage=.true.,
1               status='unknown')
c
c set up the energy looping and weigh the number
c of xrays according to spectrum here
c
        energy_cnt=energy_start-energy_inc
41      continue
        print 114,i
        print 115,count
        i=0
        energy_cnt=energy_cnt+energy_inc
        write(6,108)energy_cnt
        write(1,108)energy_cnt
        num_xrays=ano*exp(-energy_cnt/efolding)
        total=total+num_xrays
        count=0
1       continue
        count=count+1
c
c next statement weights flux at e according to spectrum
c
        if(count.gt.num_xrays) goto 61
c
c next few lines initialize parameters of the current xray
c
58      continue
        call random_$uniform (r)
        if(r.le..000001)goto 58
        cosz=r
        cosz_old=cosz
        cosx=sqrt(1.0-cosz*cosz)
        cosy=0.0
        x1=0.0
        y1=0.0
        z1=0.0
        z2=0.0
        xdepth=0.0
        xenergy=energy_cnt/electron_mass
2       continue
c       energy=energy_cnt/energy_inc+0.00001
        energy=xenergy*102.0+0.00001
        interp=xenergy*102.0-float(energy)
```

```
c next statement calculates mean free path for xray of energy e
c
        fpgm=mfp(energy)+(mfp(energy+1)-mfp(energy))*interp
        call random_$uniform (r)
c
c next routine calculates the actual distance travelled
c
        dgm=-fpgm*alog(r)
        new_xdepth=xdepth+dgm*cosz
c
c this section keeps track of the direct xrays
c
        if(xenergy.ne.energy_cnt/electron_mass) goto 6
        if(cosz.ne.cosz_old) goto 6
        if(new_xdepth.lt.depth_int) goto 6
        new_depth=new_xdepth/depth_int
        if(new_depth.gt.4) new_depth=4
        do 5 depth=1,new_depth
          dak=(altitude-6.5*alog(1030.0/(float(depth)*depth_int)))/cosz
          ra =cosx*dak
          range=ra/15.0+1.001
          if(range.gt.20) range=20
          if(depth.gt.4)write(6,327)depth
          if(range.gt.20) write(6,328)range
          if(energy.gt.42)write(6,329)energy
327       format(1x,'depth= ',i6)
328       format(1x,'range= ',i6)
329       format(1x,'energy= ',i6)
          direct_xrays(depth,range,energy)=direct_xrays(depth,range,energy)+1
5       continue
c
c this distance is distance travelled if cosz is very small
c
6       continue
        if(cosz*cosz.gt..000001) goto 7
        dist=dgm*(10.0**((75.0-z1)/16.5))
        goto 9
7       continue
        if(new_xdepth.gt.0.0)goto 8
        if(xdepth.le.depth_int) goto 1
        z2=0.0
        dist=-z1/cosz
        goto 9
8       continue
        z2=altitude-6.5*alog( 1030.0/new_xdepth)
        dist=(z2-z1)/cosz
c
c x2,y2,and z2 are coordinates of the next collision in km
c
9       continue
        x2=x1+dist*cosx
        y2=y1+dist*cosy
c
c if xray energy greater than 150 kev ignore next routines
c
        if(energy.gt.42)goto 24
c
c next routine prepares data for space array
c
        if(xdepth.lt.depth_max) goto 54
        if(new_xdepth.gt.depth_max) goto 24
54      continue
        depth=xdepth/depth_int
        new_depth=new_xdepth/depth_int
```

```
c check if xray has crossed an altitude interval
c
        if(depth-new_depth)13,24,14
13      continue
        depth=depth+1
c
c check if xray is below the lowest allowed depth
c
        if(depth.st.4.0)soto 24
        dak=(altitude-6.5*alos(1030.0/(depth*depth_int))-z1)/cosz
        ra=sart((x1+dak*cosx)*(x1+dak*cosx)+(y1+dak*cosy)*(y1+dak*cosy))
        range=ra/15.0+1.0001
        if(range.st.20)range=20
        if(cosz*cosz.lt..750)soto 72
        angle=1
        soto 75
72      continue
        if(cosz*cosz.se..250)soto 73
        angle=3
        soto 75
73      continue
        angle=2
c
c enter data into array for omnidirectional detector
c
75      continue
        omni_dn(depth,range,energy)=omni_dn(depth,range,energy)+int(1.0/cosz)
c
c enter data into array for collimated detector
c
        flat_dn(depth,range,energy,angle)=flat_dn(depth,range,energy,angle)+1
c
c next routines are similar to those above but for ascendins xrays
c
        if(depth-new_depth)13,24,14
14      continue
        if(depth.le.0)soto 1
        if(depth.st.4)soto 22
        dak=(altitude-6.5*alos(1030.0/(depth*depth_int))-z1)/cosz
        ra=sart((x1+dak*cosx)*(x1+dak*cosx)+(y1+dak*cosy)*(y1+dak*cosy))
        range=ra/15.0+1.0001
        if(range.st.20) range=20
        if(cosz*cosz.lt..750) soto 82
        angle=1
        soto 85
82      continue
        if(cosz*cosz.se..250)soto 83
        angle=3
        soto 85
83      continue
        angle=2
85      continue
        omni_up(depth,range,energy)=omni_up(depth,range,energy)-int(1.0/cosz)
        flat_up(depth,range,energy,angle)=flat_up(depth,range,energy,angle)+1
22      continue
        depth=depth-1
        if(depth-new_depth)13,24,14
c
c check if xray has left the atmosphere
c
24      continue
        if(new_xdepth.le.0)soto 1
c
c calculate prob. of compton scatter for xray of energy xenersy
```

```
              comp=probc(energy)+(probc(energy+1)-probc(energy))*interp
c
c determine the type of collision
c
        call random_$uniform(r)
        if(comp.ge.r)goto 26
c
c calc probability of coherent scatter and find type of collision
c
        coher=coh(energy)+(coh(energy+1)-coh(energy))*interp
        if(r.lt.coher)goto 23
        call random_$uniform(r)
        goto 25
23      i=i+1
        goto 1
c
c if coherent scattering find scattering angle
c
25      ir=20.*r+1.
        if(ir.eq.21)ir=20
        rr=ir
        rr=(rr-1.)*.05
        a=coh_angle(ir)+(coh_angle(ir+1)-coh_angle(ir))*(r-rr)*20.0
        goto 29
c
c if compton scattering find the new energy of scattered xray
c
26      continue
        sss=xenergy/(1.+.5625*xenergy)
        call random_$uniform(r)
        en=xenergy/(1.+sss*r+(2.*xenergy-sss)*r*r*r)
c
c if energy less than 10 kev choose another xray
c
        if(en.le..018)goto 1
c
c calculate the scattering angle for compton scattering
c
        a=1.0+1.0/xenergy-1.0/en
        a=((10000.0*a)-int(10000.0*a))/10000.0
        xenergy=en
29      continue
        b=sqrt(1.0-a*a)
        call random_$uniform(r)
c
c c is the azimuth angle of the scatter
c
        c=cos(3.14159*(2.0*r-1.0))
        if(r.ge..5)goto 31
        d=-sqrt(1.-c*c)
        goto 32
31       continue
        d=sqrt(1.0-c*c)
c
c   calculate the new direction cosines
c
```

```
32          continue
            if((cosz-1.0)*(cosz-1.0).st..000001)soto 34
            cosx=b*c
            cosy=b*d
            cosz=a*cosz
            soto 35
34          continue
            cosx=(b*c*cosz*cosx-b*d*cosy)/sart(1.0-cosz*cosz)+a*cosx
            cosy=(b*c*cosz*cosy+b*d*cosx)/sart(1.0-cosz*cosz)+a*cosy
            cosz=-b*c*sart(1.0-cosz*cosz)+a*cosz
            if(cosz.st.0.0)soto 35
c
c reinitialize the various parameters
c
35          continue
            x1=x2
            y1=y2
            z1=z2
            xdepth=new_xdepth
            soto 2
c
c this section determines when to end the prosram
c
61          continue
            if(enersy_cnt.se.enersy_end) soto 206
            soto 41
c
c end of the prosram , print out the data here
c
206          continue
            write(6,107)efoldins
            write(1,107)efoldins
            write(6,109)ano
            write(1,109)ano
            write(6,103)total
            write(1,103)total
            do 50 depth=3,3
            do 50 ranse=1,12
c           write(6,106) depth*int(depth_int),ranse*15
            write(1,106)depth*int(depth_int),ranse*15
c           write(6,110)
            write(1,110)
c           write(6,104)(omni_dn(depth,ranse,enersy),enersy=1,42)
            write(1,104)(omni_dn(depth,ranse,enersy),enersy=1,42)
c           write(6,112)
            write(1,112)
c           write(6,104)(direct_xrays(depth,ranse,enersy),enersy=1,42)
            write(1,104)(direct_xrays(depth,ranse,enersy),enersy=1,42)
c           write(6,111)
            write(1,111)
            do 50 ansle=1,3
c           if(ansle.ea.1) write(6,100)
            if(ansle.ea.1) write(1,100)
c           if(ansle.ea.2) write(6,101)
            if(ansle.ea.2) write(1,101)
c           if(ansle.ea.3) write(6,102)
            if(ansle.ea.3) write(1,102)
c           write(6,104)(flat_dn(depth,ranse,enersy,ansle),enersy=1,42)
            write(1,104)(flat_dn(depth,ranse,enersy,ansle),enersy=1,42)
```

```
50        continue
          do 400 i=1,4
          do 400 J=1,20
          do 400 k=1,42
                  down(i)=down(i)+omni_dn(i,J,k)
                  up(i)=up(i)+omni_up(i,J,k)
                  direct(i)=direct(i)+direct_xrays(i,J,k)
400       continue
          write(6,105)(int(depth_int)*i,down(i),up(i),direct(i),i=1,4)
          write(1,105)(int(depth_int)*i,down(i),up(i),direct(i),i=1,4)
          close(1)
          stop
          end
```